Physica B 647 (2022) 414367

Contents lists available at ScienceDirect

Physica B: Physics of Condensed Matter

journal homepage: www.elsevier.com/locate/physb

# Rare earth metal element doped g-GaN monolayer : Study of structural, electronic, magnetic, and optical properties by first-principle calculations

Sandhya Y. Wakhare, Mrinalini D. Deshpande *

*Department of Physics, H.P.T. Arts and R.Y.K. Science College, Nashik, Maharashtra 422 005, India*

ARTICLE INFO

*Keywords:*
Density functional study
g-GaN monolayer
Rare earth metal dopant
Magnetic and optical properties
Dielectric function

ABSTRACT

Using first-principle calculations, we have studied the structural, electronic, magnetic, and optical properties of the g-GaN monolayer doped with rare earth (RE) metal elements, where RE = La, Ce, Nd, Eu, Gd, and Dy. The substitution of Ga atom with RE leads to the structural deformation in g-GaN monolayer. The RE atom protrudes out from the plane of GaN monolayer. The La@GaN shows non-magnetic behavior similar to g-GaN. The induced magnetism of 1, 3, 6, 7, and 5 $\mu$B is observed with Ce, Nd, Eu, Gd, and Dy doped GaN monolayer, respectively. The band gap of g-GaN is 1.98 eV with indirect characteristics. The indirect band gap characteristics of g-GaN retains with La, Gd and Dy doping, while Nd@GaN shows direct band gap behavior. With Ce and Eu doping in GaN monolayer, transformation of semiconducting nature of g-GaN turns to metallic one. The decrease in the work function is observed with the RE doping in GaN monolayer reflects enhanced conductivity. For La, Nd, Gd, and Dy@GaN, the absorption spectrum show similar nature to that of g-GaN spectra. The addition of band edge states near the Fermi of g-GaN show significant red shift in absorption spectrum for Ce and Eu doped GaN monolayers as compared with g-GaN. The absorption spectra of g-GaN extended from UV to IR with the doping of Ce and Eu atom. The static dielectric constant and refractive index of g-GaN monolayer is 1.61 and 1.57, respectively. Overall enhancement in the dielectric constants and refractive indices is seen with RE doping in GaN monolayer as compared to that of g-GaN. This study provides the basis for the development of g-GaN monolayer based optoelectronic devices.

## 1. Introduction

GaN-based materials have attracted considerable attention of the researchers, and have been potentially utilized in optoelectronic devices [1,2]. GaN is a wide direct band gap semiconductor (3.4 eV) used to fabricate efficient light emitting diodes (LEDs) and room temperature laser diodes [1,2]. It exhibits high luminous efficiency, good thermal conductivity, high temperature resistance, and anti-radiation properties [1–4]. Recently, the interest in GaN nanostructures have significantly increased owing to their specific structures and properties, leading to number of potential applications [5–10]. Various nanostructures of GaN such as nanowires, nanotubes and nanospirals have also been successfully synthesized and characterized [5–8]. These novel nanostructures have shown great potential for fabricating wide-spectrum of LEDs and other nanoscale optical devices [9,10]. Similar to graphene, two dimensional (2D) pristine GaN (g-GaN) was recently proposed as a viable to use in semiconductor devices [1,3,4]. g-GaN was first synthesized by Balushi et al. by migration-enhanced encapsulated growth technique [11]. Recently, theoretical investigations confirmed that g-GaN monolayer is a stable nanostructure with an indirect band gap of 1.95 eV [3,4,9,10,12,13]. One of the earlier DFT study have shown that, the band gap of g-GaN can be tuned from 1.8 to 3.5 eV with the application of an external electric field [13]. Very recently, comparison between the metallic nitride (AlN, GaN, InN, and TIN) monolayers is studied using DFT formalism [14]. The results showed that, the optical gap of the GaN is in the energy of visible light region for parallel polarized electric field and it shifts to UV for perpendicular polarized electric field. The electronic and optical behavior of GaN monolayer effectively tuned with doping and defects [15–20]. The adsorption of alkali metal, alkaline and transition metal-doped 2D GaN monolayer have been investigated by first principle calculations [15–17]. With the adsorption of alkali metal elements on GaN monolayer, the doped systems showed metallic character. The alkali adsorption showed red shift in absorption spectra as compared with GaN monolayer [15]. The Tian et al. showed that, the absorption coefficient of GaN monolayer extended from UV to IR range after doping of Be, Mg and Zn at Ga site of g-GaN monolayer [16]. The modulation in band gap and induced magnetism in GaN monolayer is observed with the substitution of Ga atom by TM dopant (Sc, Ti, Cr, Ni, Y, Zr, and Pd) [17].

* Corresponding author.
*E-mail address:* d_mrinal@yahoo.com (M.D. Deshpande).

https://doi.org/10.1016/j.physb.2022.414367
Received 16 April 2022; Received in revised form 17 August 2022; Accepted 20 September 2022
Available online 24 September 2022
0921-4526/

An important requirement for the production of various optical devices is the modification of material properties by controlled introduction of impurities into the material during the synthesis process. Most of the optical materials exploit RE rather than TM dopants because RE doping produces greater efficiencies and lower lasing thresholds [21]. RE elements exhibit unique electronic, magnetic and optical properties, primarily governed by the occupancy of 4$f$ shell. The presence of 4$f$ shell and the large size of RE element influence the local structure, stability and magnetic properties of the host material. In bulk GaN, the band gap narrowing and a red shift of absorption edge were observed when it implanted with Ce, Nd, Eu, Er, and Tm elements [22–26]. Experimental studies have been conducted to understand the optical properties of the nanostructured GaN doped with RE element for nanoelectronic and optical applications [27–29]. The blue, green and red emissions were observed in amorphous GaN thin films doped with $Eu^{3+}$, $Er^{3+}$ and $Tm^{3+}$ ions [29]. The improved photocatalytic activities of Ce, Eu, Gd, and Tb doped GaN thin films were observed due to induced defects [30,31]. In GaN nanowires, RE elements (Ce and Dy) enriched the optical properties by creating isoelectronic trap with defect levels [27,28]. Sanna et al. studied RE (Eu, Er and Tm) related defect pairs in GaN using LDA+U approach and concluded that RE elements showed a strong preference for the Ga site either as isolated substitutional or complexes with intrinsic defects [32]. It is seen that, the performance of graphene, ZnO and nitrogen doped graphene monolayers were effectively modulated with RE elements [33–35]. The higher magnetism is observed in graphene and ZnO monolayer in presence of RE elements [33,34]. On this basis, it is interesting to understand the magnetic and optical properties of RE doped GaN monolayer.

In this work, we are going to explore the effects of the rare earth dopant on the structural, electronic, magnetic, and optical properties of RE doped GaN monolayer, where RE = La, Ce, Nd, Eu, Gd, and Dy. It is found that the band gap of g-GaN can be tuned by RE doping. Among the RE elements, mainly Ce and Eu doped GaN are the promising candidates for the development of g-GaN based optical devices.

## 2. Computational details

Spin-polarized density functional theory (DFT) based calculations are performed using the Vienna *Ab initio* Simulation Package (VASP) [36]. To calculate exchange correlation energy, the generalized gradient approximation (GGA) with Perdew–Burke–Ernzerhof (PBE) [37] and projected augmented wave (PAW) potential [38–40] is used. Here, the model of 4 × 4 supercell for g-GaN monolayer is considered to understand the effects of RE element on structural and electronic properties of g-GaN. The vacuum region is set as 15 Å along $z$ direction to avoid the interaction between the adjacent layer. For plane wave expansion of electron wave function with energy cut off of 500 eV is used. The Brillouin zone is sampled with 7 × 7 × 1 k-points within the Monkhorst scheme. The structural relaxation is carried out until the residual forces on each atom is less than 0.001 eV/Å and the convergence criteria for energy is $10^{-5}$ eV. We note that the inclusion of the Ga-3$d$ pseudopotential for GaN does not introduce significant changes in its electronic properties. To reduce the computational cost in the subsequent calculations, the Ga-3$d$ orbitals are therefore, included in the core part of the Ga pseudopotential. For RE elements, we have selected the standard pseudopotential for the calculations. The 6$s$, 5$s$, 5$p$, 5$d$, and 4$f$ orbitals of RE elements are treated as the valence states.

To understand whether the RE doping process is favorable or not in g-GaN, we have calculated the formation energy ($E_{form}$). The formalism used to calculate $E_{form}$ of RE doped GaN monolayer (RE@GaN) monolayer as follows :

$$E_{form} = E[RE@GaN] - E[GaN] + \mu[Ga/N] - \mu[RE], \quad (1)$$

where E[RE@GaN] is the total energy per atom of the RE@GaN monolayer, E[GaN] is the total energy per atom of g-GaN monolayer. The $\mu$[Ga] is the chemical potential of Ga, used when Ga element substituted by RE. The $\mu$[N] represents the chemical potential of N, when $N$ substituted by RE element. $\mu$[RE] represent the chemical potential of RE atom [34,41].

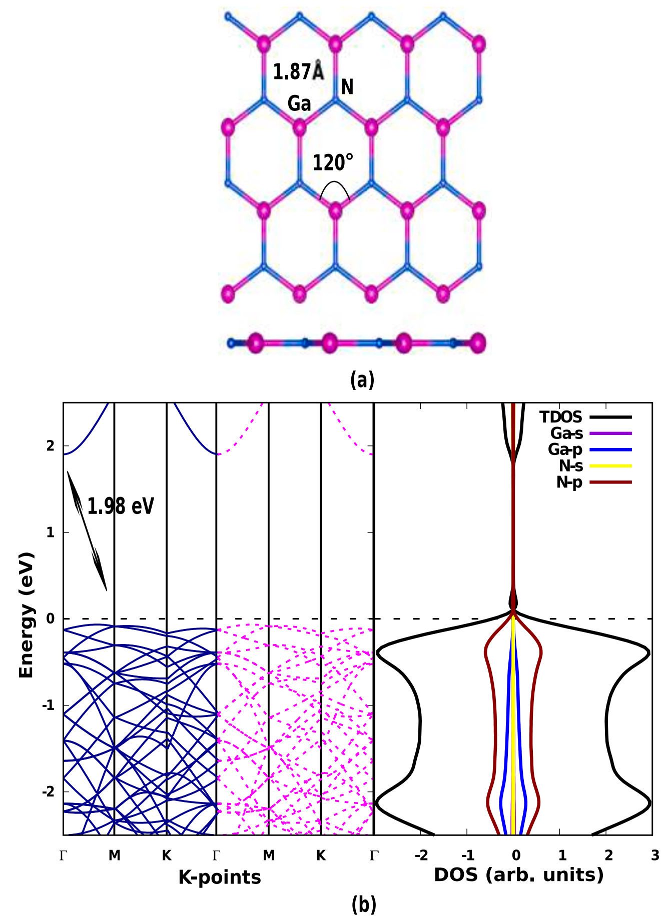


**Fig. 1.** (a) The optimized configuration of g-GaN monolayer with top and side views. The values in figure indicate Ga-N bond length (Å) and ∠ N-Ga-N (°). Pink and blue colors represent the Gallium and Nitrogen elements, respectively. (b) The spin-polarized band structure, total and projected density of states for g-GaN monolayer. In band structure plot, the blue solid lines on the left (pink dash lines on the right) represent the spin up (spin-down) channel. The value in the band structure Fig. 1(b) indicates the calculated band gap. The Fermi level is set at zero energy and indicated by black dashed horizontal line in band structure and DOS plots. In DOS plot, to identify projected DOS with total DOS on the same scale, we have scaled the total DOS at one fifth of its original value. (For interpretation of the references to color in this figure legend, the reader is referred to the web version of this article.)

To calculate electronic and optical properties of RE doped GaN, the Brillouin zone is sampled with 11 × 11 × 1 k-points mesh. The optical properties are determined by the frequency dependent complex dielectric functions. It is calculated using summation over conduction band method for self-consistent dielectric function evaluated from linear response theory [17]. These calculations are carried out by increasing the number of eigenstates by a factor of 3. We have also calculated the dielectric constant and refractive index from the real part and energy loss function from imaginary part of the dielectric function of RE doped GaN monolayer and compared with g-GaN.

## 3. Results and discussion

The optimized structure, 4 × 4 supercell of g-GaN is presented in Fig. 1(a). The optimized lattice parameters of g-GaN (a = b = 3.25 Å) are in excellent agreement with the earlier experimental [6,11] and theoretical results [3,4,15–20]. The calculated Ga-N bond length in

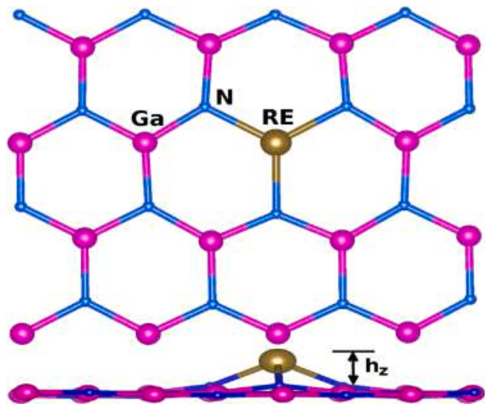


**Fig. 2.** The optimized configuration of RE@GaN monolayer with its top and side views are shown (RE = La, Ce, Nd, Eu, Gd, and Dy). Pink, blue and brown colors represent the Gallium, Nitrogen and RE element, respectively. The $h_z$ indicates the distance of RE atom from the planar GaN monolayer along $z$ direction. (For interpretation of the references to color in this figure legend, the reader is referred to the web version of this article.)

**Table 1**
The average bond lengths (Å), bond angles (°) and h$z$ is the distance of dopant from GaN monolayer along $z$ axis (Å) for RE@GaN monolayer (RE = La, Ce, Nd, Eu, Gd, and Dy).

| System | Bond lengths | Bond angles | $h_z$ |
|---|---|---|---|
| | RE-N (Å) | $\theta_{N-RE-N}$ (°) | (Å) |
| La@GaN | 2.23 | 98.7 | 1.20 |
| Ce@GaN | 2.18 | 101.2 | 1.40 |
| Nd@GaN | 2.19 | 100.0 | 1.43 |
| Eu@GaN | 2.22 | 98.7 | 1.55 |
| Gd@GaN | 2.15 | 101.9 | 1.30 |
| Dy@GaN | 2.12 | 103.8 | 1.05 |

GaN monolayer is 1.87 Å [17–20]. In bulk system, the Ga-N bond length is 1.94 Å [42]. The shorter bond lengths are observed in g-GaN monolayer, which indicates the stronger interaction in nanostructure form. The spin polarized band structure along with total and projected density of states (DOS) are presented in Fig. 1(b). The calculated band structure indicates that g-GaN monolayer is a semiconductor with indirect band gap of 1.98 eV. The reported experimental band gap of 2D GaN is 4.68 eV [9]. The experimental band gap of g-GaN is higher than bulk GaN (3.4 eV) [1]. The theoretical band gap is in the range of 1.76 to 2.95 eV [12,13,15,17,20]. It is well known that, the GGA-PBE functional of DFT method which underestimate the band gap in semiconductors. From total DOS, it is observed that the spin-up and spin-down components of the total DOS are symmetric, indicating nonmagnetic behavior of g-GaN. From projected DOS, it is found that the states near the Fermi are dominated by Ga-4$p$ and N-2$p$ states. All these results are consistent with the earlier theoretical studies [13,15,17–20]. This benchmark the methodology and model employed in the present study.

Further using spin-polarized calculations, the structures of RE metal doped GaN monolayer are optimized. Initially, to understand favorable doping site for RE dopant in g-GaN, we have considered both the substitutional sites, Ga as well as N. The calculated formation energy for La@GaN substituted for Ga and $N$ site is −1.61 and 6.48 eV, respectively. For Ce@GaN, the formation energy is −2.28 and 5.88 eV for Ga and $N$ substitutional site, respectively. Similar trend of formation energies are observed for other RE@GaN. Overall, it is found that, substitution of Ga site is more favorable for RE element as compared to $N$ in GaN monolayer. The earlier studies have also shown that the substitution of metal atom with RE element in GaN was more favorable [17,32,43]. Based on this analysis and literature

**Table 2**
The formation energy ($E_{form}$) (eV), magnetic moment (μB), band gap ($E_g$) (eV), Bader charge on Ga, N and RE atoms (e), and work function ($\phi$) (eV) for RE@GaN monolayer along with g-GaN (RE = La, Ce, Nd, Eu, Gd, and Dy).

| System | $E_{form}$ | Magnetic | $E_g$ | Bader charge | | | $\phi$ |
|---|---|---|---|---|---|---|---|
| | | moment | spin-up | Ga | N | RE | |
| | (eV) | (μB) | (eV) | (e) | (e) | (e) | (eV) |
| **g-GaN** | **–** | **0** | **1.98 M-$\Gamma$** | **+1.31** | **−1.31** | **–** | **5.06** |
| La@GaN | −1.61 | 0 | 2.05 M-$\Gamma$ | +1.40 | −1.44 | +1.81 | 4.74 |
| Ce@GaN | −2.28 | 1 | Metallic | +1.40 | −1.42 | +1.82 | 2.40 |
| Nd@GaN | −3.65 | 3 | 0.39 $\Gamma$ | +1.34 | −1.41 | +1.73 | 3.33 |
| Eu@GaN | −9.55 | 6 | Metallic | +1.34 | −1.39 | +1.63 | 4.54 |
| Gd@GaN | −10.77 | 7 | 2.05 M-$\Gamma$ | +1.33 | −1.42 | +1.80 | 4.79 |
| Dy@GaN | −6.85 | 5 | 2.02 M-$\Gamma$ | +1.32 | −1.43 | +1.78 | 3.84 |

survey here, we are going to present the results for the substitution of Ga atom with RE element. In Fig. 2, we have presented the optimized structure of RE@GaN monolayer. The structural parameters for RE@GaN monolayers are summarized in Table 1. Table 2 presents the formation energy, magnetic moment, band gap, Bader charge, and work function of RE@GaN along with g-GaN system. To understand the relative stability of RE in g-GaN, we have calculated the formation energy of RE@GaN monolayer. The negative formation energies for the doped systems, indicate the feasibility of RE element in GaN monolayer with exothermic reaction. Gd doping is most favorable among the selected RE elements. Earlier studies showed that, the substitution of Ga site with RE element is favorable in bulk as well in various nanostructures [24,32]. After optimization, it is found that RE atom induces significant structural deformations in the g-GaN planar structure. The RE atom protrudes out from the plane of the GaN monolayer. The ionic radius of $Ga^{3+}$ is 0.62 Å and RE elements for $La^{3+}$, $Ce^{3+}$, $Nd^{3+}$, $Eu^{3+}$, $Gd^{3+}$, and $Dy^{3+}$ are 1.16, 1.14, 1.11, 1.06, 0.94, and 0.97 Å, respectively. The large sized RE atom induces a distortion in the g-GaN by creating strain on the nearest Ga-N bonds. We have mentioned the distance of RE atom from the plane of g-GaN monolayer ($h_z$) in Table 1. The largest distance of Eu (1.55 Å) from GaN monolayer along $z$ axis reflects the weak interaction of Eu with GaN monolayer. The shortest distance of Dy from doped GaN system reflects the stronger interaction with GaN monolayer. Overall, Ga-N bond lengths increases with RE doping.

The Bader [44] charge analysis for RE@GaN along with g-GaN monolayer is summarized in Table 2. From the Bader charge analysis, it is found that in g-GaN, the charge transfer is from Ga (+1.31e) to $N$ (−1.31e) atom. With the substitution of Ga with RE, the RE element transfer more charge to nearest $N$ atoms as compared with Ga atom. Overall, the increased in charge transfer of GaN monolayer is observed in presence of RE atom.

Further, to understand the nature of bonding in RE@GaN along with g-GaN, we have calculated the electron density, Laplacian of charge density and critical points of charge density distribution by using AIM-UC package [45,46]. The contour plot of electron density gradient for Ce, Eu and Dy doped GaN system along with g-GaN are presented in Fig. 3. The topology of electron density and presence of critical points in the system defines the nature of bonding in the system. From the calculated ratio of potential energy and kinetic energy density at critical point shows the increase in covalent character for RE@GaN except for La doped GaN monolayer. In GaN monolayer, the gradient of electron density is localized around the $N$ atoms. It is seen that, with the doping of RE element in GaN monolayer the gradient of electron density is distributed in between RE and its neighboring N atoms. It is seen that, sharing interaction in between RE-N bonds increases as compared to that of Ga-N bonds. These observations are consistent with the Bader charge analysis. It is seen that, the electron density on the critical points of Ga-N bonds decreases with RE doping as compared with g-GaN monolayer. The decreased electron density and increased critical points in RE@GaN show the enhancement in interplanar interaction compared

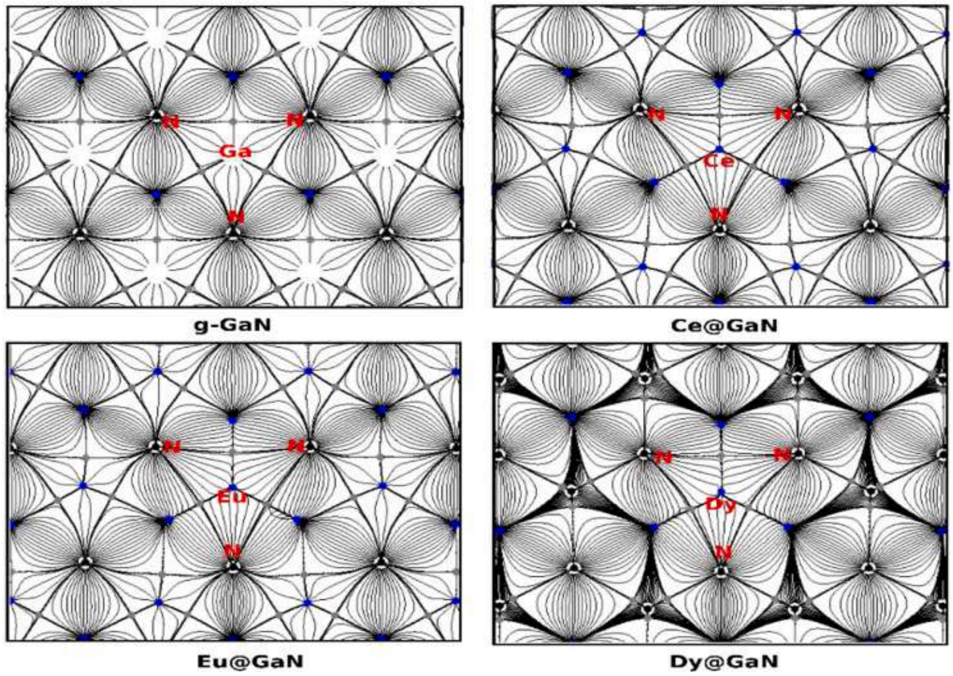


**Fig. 3.** Contour plot of $\Delta\rho$ showing the position of the critical points in RE@GaN along with g-GaN (RE = Ce, Eu and Dy). Gray dots stand for bond critical point and blue dots stand for ring critical point. Black solid lines across the bond critical point indicate the bond path.

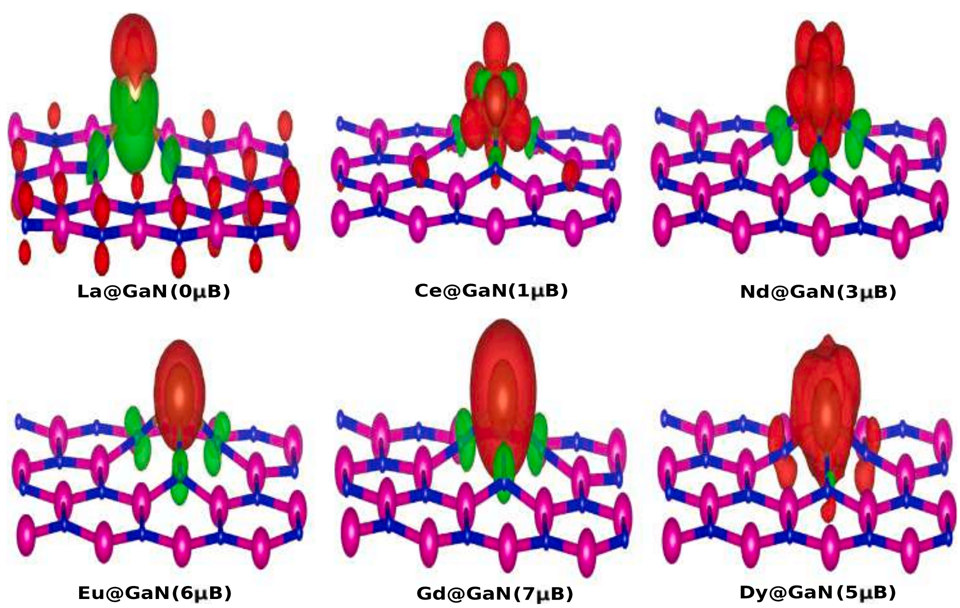


**Fig. 4.** The magnetization charge density isosurface of RE@GaN monolayers (RE = La, Ce, Nd, Eu, Gd, and Dy). The red and green color indicates the spin-up and spin-down charge density, respectively. The value in figure indicates the total magnetic moments of RE doped GaN systems. (For interpretation of the references to color in this figure legend, the reader is referred to the web version of this article.)

with g-GaN monolayer. It reduces the degree of ionicity with RE doping in GaN monolayer. The maximum electron density on bond critical points is observed for Ce@GaN and minimum for Eu@GaN system. It indicates that the interaction of Ce with GaN monolayer is stronger as compared to that of Eu.

From the spin-polarized DFT calculations, it is found that g-GaN is non-magnetic system. It is found that the La@GaN shows the non-magnetic behavior similar to g-GaN monolayer. The calculated magnetic moments of RE@GaN systems are presented in Table 2. The calculated local magnetic moment on RE atoms are 0.79, 3.03, 6.45, 6.90, and 4.86 $\mu$B for Ce, Nd, Eu, Gd, and Dy, respectively. From the magnetization charge densities, it is seen that the major contribution in the total magnetic moment is due to RE elements (Fig. 4). Small contribution from the total magnetic moment is also observed on the $N$ atoms nearer to RE atom. Similar magnetic behavior is observed for Ce, Nd, Eu, and Gd doped bulk RE@GaN [23,43]. The structural deformation and induced magnetism in RE@GaN monolayer shows its potential for spintronics and in other smart magnetic applications like data storage purpose. The higher magnetism is reported with adsorption of RE on graphene and nitrogen doped graphene monolayers as well as in RE doped ZnO monolayer [33–35]. To understand the effects of RE doping on the electronic structure of doped g-GaN, we have calculated the band structure for RE@GaN systems.

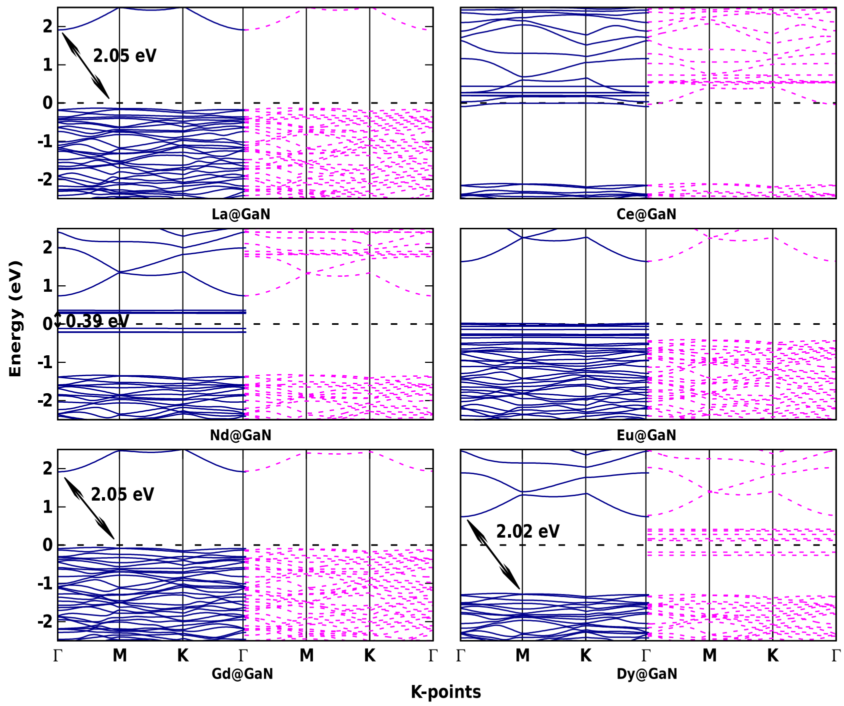


**Fig. 5.** The spin-polarized band structure for RE@GaN monolayer along with g-GaN (RE = La, Ce, Nd, Eu, Gd, and Dy). The blue solid lines on the left (pink dash lines on the right) represent the spin-up (spin-down) channel. The Fermi level is set at zero energy and indicated by black dashed horizontal lines. The value in figures indicate the calculated band gap. (For interpretation of the references to color in this figure legend, the reader is referred to the web version of this article.)

Fig. 5 presents the spin-up and spin-down band structure for RE@GaN monolayer. As noted earlier, g-GaN monolayer shows semi-conducting behavior with indirect band gap (1.98 eV) characteristics (Fig. 1(b)). The variation in band gap values for spin-up state of RE@GaN are noted in Table 2. The band structures of La and Gd@GaN are almost similar to g-GaN band structure. With Ce doping the spin-up and spin-down states of conduction band moves towards the Fermi. The inter bandgap states are found near Fermi level. The Ce@GaN system shows the metallic behavior. For Nd@GaN the narrow direct band gap (0.39 eV) is observed for spin-up state and spin-down state shows the semiconducting nature with indirect band gap of 2.04 eV. In case of Eu@GaN monolayer, the Fermi energy pass only through the spin-up states of valence band and the spin-down channel is semiconducting nature with indirect band gap of 2.05 eV. Here, also inter bandgap states are evidently seen at spin-up state. It shows half-metallic nature of Eu@GaN monolayer. With the doping of Dy in GaN monolayer, the spin-up band gap (2.02 eV) shows the semiconducting while spin-down band gap becomes narrow with the value 0.29 eV. Overall, the indirect band gap of g-GaN increases for La, Gd, and Dy@GaN. The semiconducting nature of g-GaN transforms to metallic in presence of Ce and Eu elements. The variations in band structure of RE@GaN is reflected in the work function of RE doped GaN.

The work function, $\phi$ is calculated by subtracting the Fermi energy from the electrostatic potential in the middle of vacuum [15,47]. The work function of the g-GaN monolayer is 5.06 eV. This result is consistent with the earlier reported values [15,47]. From Table 2, it is seen that the work function of RE@GaN is in between the range of 2.40 to 4.79 eV. It is found that, the work function of RE@GaN decreases as compared to the work function of g-GaN. This may be beneficial for field emission devices [35]. The decrease in work function reduces the amount of energy required to removal of electrons from highest filled level. It results in increased electron current density emission at lower temperature or light intensity or electric field. The decrease in work function reflects the enhancement in the conductivity.

Overall, with the doping of RE element, the band gap of the g-GaN monolayer can be tuned. The indirect semiconducting nature of g-GaN can be transformed to direct or metallic with the doping of RE element. It is excepted variations may affect the optical absorption of GaN monolayer. The imaginary and real parts of dielectric function for RE doped GaN systems in comparison with the pristine GaN monolayer are presented in Fig. 6.

The complex dielectric function is determined using real $\varepsilon_1(\omega)$ and imaginary $\varepsilon_2(\omega)$ part of dielectric function $\varepsilon(\omega)$,

$$\varepsilon(\omega) = \varepsilon_1(\omega) + i\varepsilon_2(\omega). \tag{2}$$

The imaginary part can be derived from the wave function of momentum matrix elements between the top of valence band and bottom of conduction band. The real part is calculated from imaginary part by the Kramers–Kronig transformation, respectively [48]. Due to 2D-hexagonal structure of g-GaN and RE@GaN, the isotropic dielectric function is observed along $x$ and $y$ directions. It is seen that, along $x$ and $y$ directions the dielectric function is similar. Here, we have plotted the $x$ component of dielectric function for the optical analysis. The absorption spectra of g-GaN is extended from UV towards visible range. As noted earlier, the calculated band gap of g-GaN is 1.98 eV comprehensive to the first optical transition. From DOS this peak is the result of interaction in between N-$p$ and Ga-$s$ states of valence and conduction band. Further, two dominant peaks are observed at 5.06 and 7.17 eV. These peaks are the result of interaction in between Ga-$p$ → N-$p$ and Ga-$s$ → N-$p$ states, respectively. All these findings are consistent with the earlier reports [3,4,15]. Onen et al. reported that, the transformation from bulk to 2D GaN shifts the optical coefficient from visible to UV [3]. For La, Nd, Gd, and Dy@GaN the spectrum show similar nature related to g-GaN with the variation in intensity. The significant red shift in the absorption spectrum is observed for Ce and Eu doped GaN monolayers as compared to that of g-GaN. Overall spectra is divided into two parts: below and above 2 eV. The dramatic variation in absorption spectrum below 2 eV is seen for Ce and Eu@GaN as compared with g-GaN. The dominant absorption peak is observed in IR range with the doping of Ce and Eu in GaN monolayer. This is mainly due to the addition of band edge states in Ce@GaN and Eu@GaN band structure. The band gap narrowing and

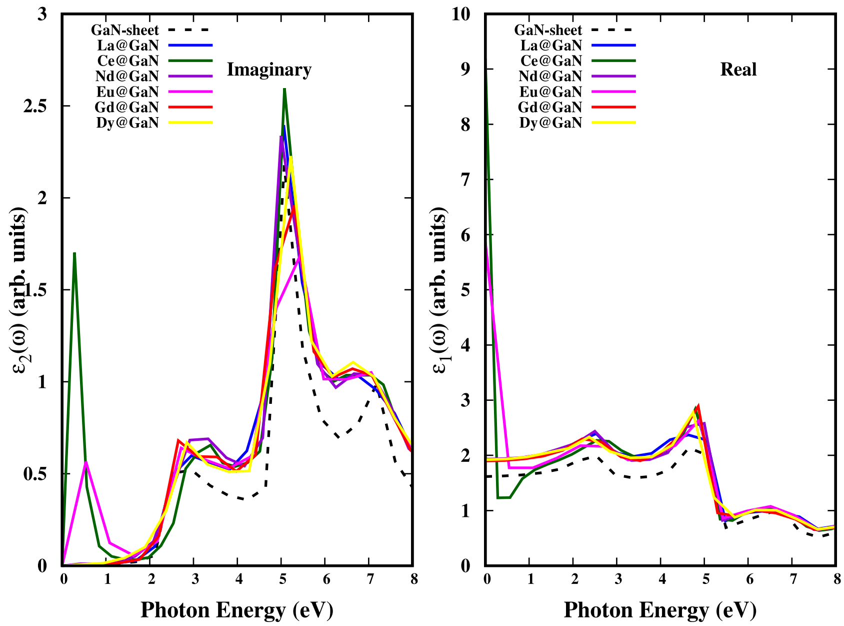


**Fig. 6.** Imaginary and Real parts of the dielectric function for RE@GaN monolayer along with g-GaN (RE = La, Ce, Nd, Eu, Gd, and Dy).

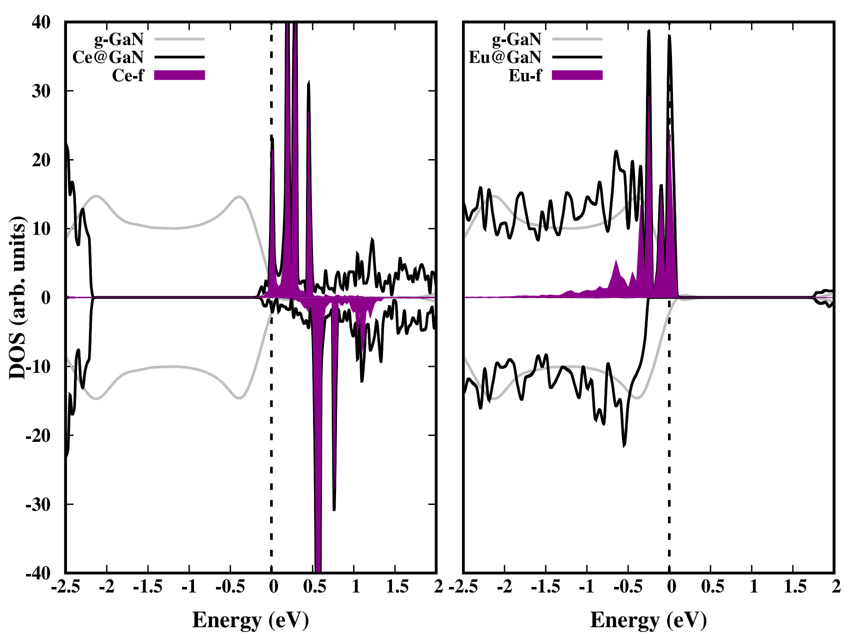


**Fig. 7.** The total DOS of Ce@GaN and Eu@GaN and projected DOS of Ce-$f$ and Eu-$f$ are also presented along with g-GaN. The Fermi level is set at zero energy and indicated by black dashed vertical lines.

a red shift of absorption edge were observed in GaN implanted with Ce [22]. On basis of these results, Ce@GaN and Eu@GaN monolayers can be applicable in the development of optical devices used in IR region. The spectrum above 2 eV, the nature of spectra of RE@GaN are similar to that of g-GaN monolayer spectra with the modulation in intensity. In bulk form, the electronic and optical properties of RE doped GaN are found similar with GaN system showed substitutional doping electronically and optically inert at room temperature [32,49].

To focus on the behavior of Ce and Eu@GaN and know more about the contribution of orbitals and its position we have presented the total DOS and projected DOS of Ce@GaN and Eu@GaN systems (Fig. 7). The delocalization of total DOS for RE@GaN compared with g-GaN shows the increased interaction of RE with GaN monolayer. It also reflects the enhanced stability of RE@GaN monolayer. The difference in spin-up and spin-down states of total DOS for RE@GaN show induced magnetism in RE@GaN except for La doping. The localized magnetization is due to RE-4$f$ states. The electronic states of Ce/Eu dispersed with conduction/valence band in the band edge. The delocalization of Ce and Eu-4$f$ states crossing the Fermi energy in spin-up channel induces the defect level peaks in absorption spectrum below 2 eV. The defect induced peaks of Ce and Eu below 2 eV is due to intraband transition of 4-$f$ states near the Fermi energy.

As seen earlier, the optical trend of La, Nd, Gd, and Dy@GaN are similar to g-GaN. Here, we have presented the total and projected DOS of Gd-$f$ and Dy-$f$ along with g-GaN in Fig. 8. With the addition of 4$f$ electrons in RE@GaN, the flat 4$f$ states emerge deep in the valence band. The energy spectra shifts towards lower energy side and bonding states move away from the Fermi energy. The dominant Gd-4$f$ states appear deep in the valence band while non-bonding Dy-4$f$

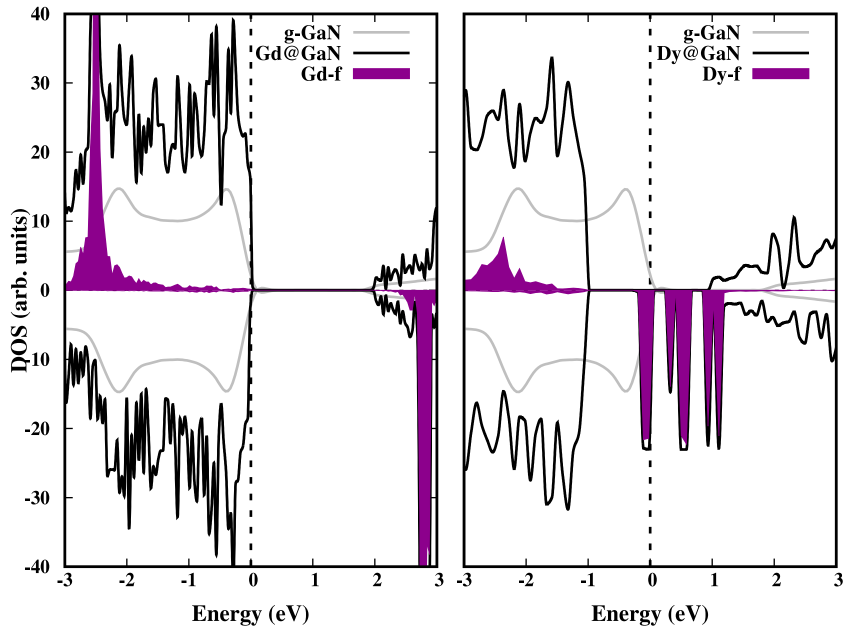


**Fig. 8.** The total DOS and projected DOS of Gd and Dy-$f$ orbitals for Gd and Dy@GaN along with g-GaN. The Fermi level is set at zero energy and indicated by black dashed vertical lines.

state appears in down-spin. For Nd@GaN, more localized Nd-$f$ states in band edge which does not disperse with electronic states of valence and conduction band (not shown). These states do not contribute in optical transition for Nd, Gd, and Dy@GaN as compared to that of g-GaN. Only results in enhancement of intensity for optical peaks. The effects of modulation in the spin-up state of band gap near Fermi is evidently observed in optical transition.

Further, we have studied the real part of the dielectric function. The real part of dielectric function gives us static dielectric constant, which present the ability to store electric field. The system with high dielectric constant exhibits only displacement current and ideal to develop capacitor for various applications such as MOSFET and memory devices. The dielectric constant of g-GaN monolayer in our result is 1.61. We used PBE as exchange and correlation functional. From the earlier reported study with PBE functional and CASTEP code, the value for dielectric constant for GaN monolayer is 1.40 [47]. The plane wave cutoff used in this study is 400 eV. With HSE functional and VASP code using 400 eV plane wave cutoff this value increases to 2.7 [4]. The value of dielectric constant in our result is in between the reported values is due to usage of methodology and change in plane wave cutoff. The dielectric constant of La, Ce, Nd, Eu, Gd, and Dy@GaN monolayer along $x$ axis is 1.91, 9.18, 1.95, 5.86, 1.78, and 1.92, respectively. Among all, Ce doped GaN monolayer has highest dielectric constant. This may emphasized on the basis of large concentration of electron density on Ce-N bond.

The optical properties, refractive index and energy loss function play efficient role while designing optoelectronic devices such as optical waveguide and photodetectors [26,50]. The refractive index and energy loss function of RE@GaN along with g-GaN for varying photon energy are represented in Fig. 9. The response of light through the material depends on the properties of material and defined in terms of refractive index n($\omega$). The refractive index n($\omega$)is evaluated from the calculated dielectric function [26,50].

$$n(\omega) = \sqrt{\epsilon_1(\omega) + i\epsilon_2(\omega)} \tag{3}$$

The static refractive index of GaN monolayer is 1.57 and in good agreement with the reported value 1.50 [50]. For La, Ce, Nd, Eu, Gd, and Dy@GaN, the static refractive index is 1.82, 3.99, 1.84, 1.96, 1.71, and 1.76, respectively. The considerable change in static refractive index is observed for Ce@GaN (3.99) and Eu@GaN (1.96) compared with g-GaN. The enhancement in refractive index for RE@GaN acts as a denser medium while traveling the light from the medium. It reduces the dispersion of light within the material and reflects high dielectric constant. The result gives the basis to explore the way towards the development of optical fiber and photodetector applications.

The energy loss while traveling the electrons from the material is defined in terms of the energy loss function L($\omega$).

$$L(\omega) = Im[-\frac{1}{\epsilon_1(\omega) + i\epsilon_2(\omega)}] \tag{4}$$

The peaks in energy loss function represent the properties of plasma resonance frequency. The high intensity energy loss peak for g-GaN is at 7.48 eV and is consistent with the reported value of 7.6 eV [50]. Overall the nature of spectra of RE@GaN similar to GaN but broad intense multiple energy loss peaks are observed for Ce and Eu doped GaN at lower energy side. It is the replication of intermediate states near the Fermi energy appeared in DOS plots for Ce and Eu@GaN monolayers. This results may help for the development of communication systems for IR range. The intensity of energy loss function decreases for RE@GaN above 5 eV except for Gd@GaN. For Gd doping shows ability towards UV transmitter. Overall, the tunable electronic, magnetic and optical properties of RE@GaN monolayer open up its way towards spintronic and optoelectronic applications.

## 4. Conclusions

The structural, electronic, magnetic, and optical properties of RE doped GaN monolayer (RE = La, Ce, Nd, Eu, Gd, and Dy) are systematically studied using first-principle calculations. The RE atom protrudes out from the plane of GaN monolayer for Ga substitution with RE. The negative formation energy implies the exothermic reaction. The band gap of g-GaN is 1.98 eV with indirect characteristic. Spin-polarized calculations showed that, with RE doping in g-GaN monolayer, the semiconducting nature of GaN monolayer turns towards the metallic behavior for Ce and Eu@GaN. For Nd@GaN the direct band gap behavior is observed. For La, Nd, Gd, and Dy doped GaN monolayers the absorption spectrum show similar nature but with increased intensity as compared to that of GaN spectra. The significant red shift in absorption spectrum is observed for Ce and Eu doped GaN monolayers compared to that of g-GaN. The delocalized Ce/Eu-4$f$ states near the band edge

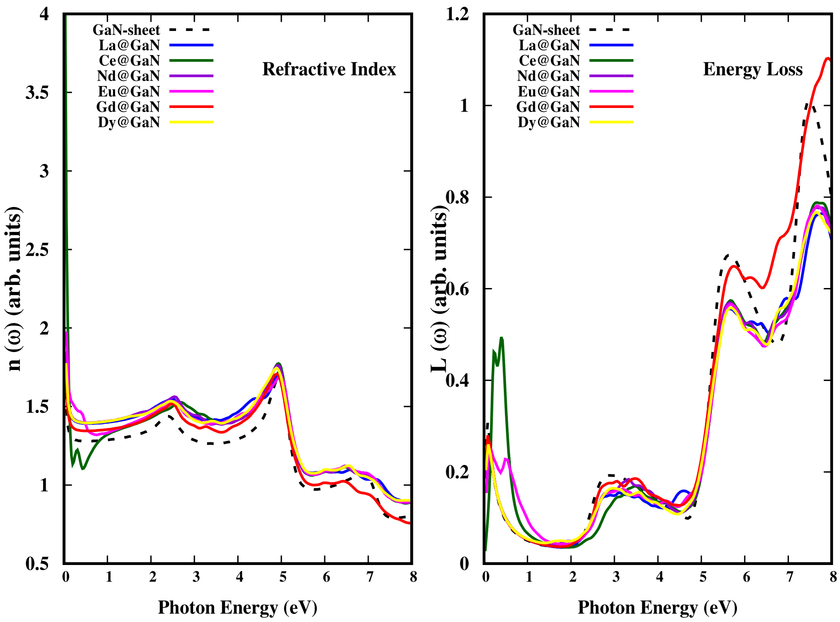


**Fig. 9.** The refractive index and energy loss function for RE@GaN monolayer along with g-GaN are presented (RE = La, Ce, Nd, Eu, Gd, and Dy).

are playing important role in the red shift of the absorption spectra. The static dielectric constant and refractive index of GaN monolayer is 1.61 and 1.57, respectively. RE doping enhances the dielectric constant of g-GaN in the range of 1.78 to 9.18 and refractive index from 1.71 to 3.99. The highest dielectric constant and refractive index is observed for Ce doped GaN monolayer. Our study demonstrates that RE metal-doped GaN monolayer possess tunable electronic, magnetic and optical properties and have potential application in the development of magnetic as well as optical devices.

## CRediT authorship contribution statement

**Sandhya Y. Wakhare:** Conceptualization, Methodology, Software, Data curation, Writing – original draft, Visualization, Investigation, Software, Validation, Writing – review & editing. **Mrinalini D. Deshpande:** Conceptualization, Methodology, Software, Data curation, Writing – original draft, Visualization, Investigation, Software, Validation, Writing – review & editing.

## Declaration of competing interest

The authors declare that they have no known competing financial interests or personal relationships that could have appeared to influence the work reported in this paper.

## Data availability

Data will be made available on request.

## Acknowledgments

SYW and MDD acknowledges the Center for Development of Advance Computing (CDAC), Pune, India and Bioinformatics Resources and Applications Facility (BRAF), India for providing the supercomputing facilities.

## References

[1] S. Strite, H. Morkoc, GaN, AlN, and InN: A review, J. Vac. Sci. Technol. B 10 (1992) 1237.
[2] S. Nakamura, Nobel Lecture: Background story of the invention of efficient blue InGaN light emitting diodes, Rev. Modern Phys. 87 (2015) 1139.
[3] A. Onen, D. Kecik, E. Durgun, S. Ciraci, GaN: From three- to two-dimensional single-layer crystal and its multilayer van der waals solids, Phys. Rev. B 93 (2016) 085431.
[4] M. Imran, F. Hussain, M. Rashid, H. Ullah, A. Sattar, F. Iqbal, E. Ahmad, Comparision of electronic and optical properties of GaN monolayer and bulk structure: A First principle study, Surf. Rev. Lett. 23 (2016) 1650026.
[5] R. Koester, J.-S. Hwang, D. Salomon, X. Chen, C. Bougerol, J.P. Barnes, D.L.S. Dang, L. Rigutti, A. de Luna Bugallo, G. Jacopin, M. Tchernycheva, C. Durand, J. Eymery, M-Plane core−−shell InGaN/GaN multiple-quantum-wells on GaN wires for electroluminescent devices, Nano Lett. 11 (2011) 4839.
[6] G. Suo, S. Jiang, J. Zhang, J. Li, M. He, Synthetic strategies and applications of GaN nanowires, Adv. Conden. Matter Phys. 2 (2014) 1.
[7] C.Y. Park, J.M. Lim, J.S. Yu, Y.T. Lee, Structural and antireflective characteristics of catalyst-free GaN nanostructures on GaN/sapphire template for solar cell applications, Appl. Phys. Lett. 96 (2010) 151909.
[8] G. Pinhal, N. Marana, G. Fabris, J. Sambrano, Structural, electronic and mechanical properties of single-walled AlN and GaN nanotubes via DFT/B3LYP, Theor. Chem. Account. 138 (2019) 2.
[9] X. Wang, X. Sun, M. Fairchild, S.D. Hersee, Fabrication of GaN nanowire arrays by confined epitaxy, Appl. Phys. Lett. 89 (2006) 233115.
[10] T. Zhou, J. Shi, M. Zhang, M. Yang, H. Zhong, X. Jiang, P. Huang, Band edge modulation and light emission in InGaN nanowires due to the surface state and microscopic indium distribution, J. Phys. Chem. C 117 (2013) 16231.
[11] Z. Balushi, K. Wang, R. Ghosh, R. Vila, S. Eichfeld, J. Caldwell, X. Qin, Y.-C. Lin, P. DeSario, G. Stone, S. Subramanian, D. Paul, R. Wallace, S. Datta, J. Redwing, J. Robinson, Two-dimensional gallium nitride realized via graphene encapsulation, Nature Mater. 15 (2016) 1166.
[12] N. Sanders, D. Bayerl, G. Shi, K. Mengle, E. Kioupakis, Electronic and optical properties of two-dimensional GaN from first principles, Nano Lett. 17 (2017) 7345.
[13] Q. Chen, H. Hu, X. Chen, J. Wang, Tailoring band gap in GaN sheet by chemical modification and electric field: Ab initio calculations, Appl. Phys. Lett. 98 (2011) 053102.
[14] N. Abdullah, B. Abdullah, V. Gudmundsson, Electronic and optical properties of Metallic Nitride: A comparative study between the MN (M=Al Ga, in, Tl) Monolayers, Solid State Comms. 346 (2022) 114705.
[15] Z. Cui, X. Wang, E. Li, Y. Ding, C. Sun, M. Sun, Alkali-metal-adsorbed g-gan monolayer: ultralow work functions and optical properties, Nanoscale Res. Lett. 13 (2018) 207.
[16] J. Tian, L. Liu, F. Lu, Theoretical research on p-type doping two-dimensional GaN based on first-principles study, Int. J. Energy Res. 44 (2020) 1.
[17] J. Li, H. Liu, Theoretical research of diluted magnetic semiconductors: GaN monolayer doped with transition metal atoms, Superlattices Microstruct. 18 (2018) 30647.

[18] N. Alaal, I. Roqan, Tuning the electronic properties of hexagonal two-dimensional GaN monolayers via doping for enhanced optoelectronic applications, J. Phys. Chem. C 119 (2015) 20911.
[19] Y. Mu, Chemical functionalization of GaN monolayer by adatom adsorption, J. Phys. Chem. C 119 (2015) 20911.
[20] Q. Zhao, Z. Xiong, Z. Qin, L. Chen, N. Wu, X. Li, Tuning magnetism of monolayer GaN by vacancy and nonmagnetic chemical doping, J. Phys. and Chem. Solids 91 (2016) 1.
[21] A. Steckl, Rare-earth-doped GaN: Growth properties, and fabrication of electroluminescent devices, IEEE J. Sel. Topic. Quantum Ele. 8 (2002) 749.
[22] Q. Li, Q. Hao, Y. Li, G. Liu, First principle study of ce doping and related complexes in GaN, Comput. Mater. Sci. 72 (2013) 32.
[23] A. Dar, A. Majid, Electronic structure analysis of rare earth ions Ce and Nd doped gallium nitride, J. Appl. Phys. 114 (2013) 123703.
[24] J. Filhol, R. Jones, M. Shaw, P. Briddon, Structure and electrical activity of rare -earth dopants in GaN, Appl. Phys. Lett. 84 (2004) 2841.
[25] A. Zaharo, A. Purqon, The calculation study of electronic properties of doped RE (Eu, Er and Tm)-GaN using density functional theory, J. Phys. Conf. Series 877 (2017) 012051.
[26] M. Khan, Z. Kanwal, N. Usmani, P. Akhtar, S. Hussain, Exploring optical properties of gd doped zincblende GaN for novel optoelectronic applications (A DFT+U study), Mater. Res. Express 6 (2019) 115916.
[27] J. Guo, J. Jian, Z. Zhang, H. Tao, R. Wu, J. Li, Synthesis and optical properties of Ce-doped GaN single-crystalline nanowires, J. Alloys Compounds 660 (2016) 220.
[28] Y. Cao, F. Shi, H. Sun, W. Liu, Y. Guo, C.S. Xue, Growth and properties of Dy-doped GaN nanowires, Eur. Phys. J. Appl. Phys. 50 (2010) 10602.
[29] Y. Wang, A. Steckl, Three-color integration on rare -earth-doped GaN electroluminescent thin films, Appl. Phys. Letter. 82 (2003) 4.
[30] B. Poornaprakash, U. Chalapathi, K. Subramanyam, S. Vattikuti, Y. Suh, S. park, Effects of ce incorporation on the structural morphological, optical, magnetic, and photocatalytic characteristics of ZnO nanoparticles, Mater. Res. Express 6 (2019) 125075.
[31] W. Fenwick, M. Kane, R. Varatharajan, T. Zaidi, Z. Fang, B. Nemeth, D. Keeble, H. El-Mkami, G. Smith, J. Nause, C. Summers, I. Ferguson, Transition metal- and rare earth-doped ZnO: a comparison of optical magnetic, and structural behavior of bulk and thin films, Proc. SPIE- Inte. Soc. Opt. Eng. 6474 (2007) 32.
[32] S. Sanna, B. Hourahine, Th. Frauenheim, U. Gerstmann, Theoretical study of rare earth point defects in GaN, Phys. Stat. Sol. C 5 6 (2008) 2358.
[33] Q. Zhou, Z. Fu, C. Wang, X. Yang, L. Yuan, Y. Tang, Electronic and magnetic properties of Rare-Earth atoms absorbed on graphene sheet: A theoretical study, Key Eng. Maters. 645 (2015) 40.
[34] C. Tan, D. Xu, K. Zhang, X. Tian, W. Cai, Electronic and magnetic properties of Rare-Earth metals doped ZnO monolayer, J. Nanomat. 329570 (2015) 8.
[35] C. Ouma, K. Obodo, M. Braun, G. Amolo, Ab initio insights on the effect of embedding lanthanide atoms on nitrogenated holey doped graphene (g-$C_2$N), J. Maters. Chem. C 6 (2018) 4015.
[36] Vienna *Ab Initio* Simulation Package, VASP, Technische Universitat Wien, 1999.
[37] J. Perdew, K. Burke, M. Ernzerhof, Generalized gradient approximation made simple, Phys. Rev. Lett. 77 (1996) 3865.
[38] P.E. Blochl, Projector augmented-wave method, Phys. Rev. B 50 (1994) 17953.
[39] G. Kresse, D. Joubert, From ultrasoft pseudopotentials to the projector augmented-wave method, Phys. Rev. B 59 (1999) 1758.
[40] G. Kresse, J. Furthmuller, Efficient iterative schemes for *abinitio* total-energy calculations for metals and semiconductors using a plane-wave basis set, Phys. Rev. B 54 (1996) 11169.
[41] D. Lide, CRC handbook of chemistry and physics (87th ed.), J. Am. Chem. Soc. 129 (2007) 724.
[42] Z. Qin, G. Qin, X. Zuo, Z. Xiong, M. Hu, Orbitally driven low thermal conductivity of monolayer gallium nitride (GaN) with planar honeycomb structure: a comparative study, Nanoscale 9 (2017) 4295.
[43] M. Shakil, A. Hussain, M. Zafar, S. Ahmad, M. Khan, M. Masood, A. Majid, Ferromagnetism in GaN doped with transition metals and rare -earth elements: A review, Chin. J. Phys. 56 (2018) 1570.
[44] W. Tang, E. Sanville, G. Henkelman, A grid-based bader analysis algorithm without lattice bias, J. Phys. Condens. Matter 21 (2009) 084204.
[45] D. Vega, D. Almeida, AIM-UC: an application for QTAIM analysis, J. Comp. Methods Sci. Eng. 14 (2014) 131.
[46] U. Saikia, M. Sahariah, R. Pandey, Stability of Cu-Nb layered nanocomposite from chemical bonding, Chem. Phys. Lett. 655 (2016) 59.
[47] J. Tian, L. Liu, S. Xia, Y. Diao, F. Lu, Optoelectronic properties of two-dimensional GaN adsorbed with H N and O: A first-principle study, Phys. Lett. A 383 (2019) 3018.
[48] L. Zhao, H. Chang, W. Zhao, Z. Luan, X. Tian, C. Tan, Y. Huang, Coexistence of doping and strain to tune electronic and optical properties of GaN monolayer, Superlatt. Microstr. 18 (2018) 32328.
[49] S. Song, W. Chen, C. Zhang, L. Bian, C. Hsu, L. Lu, Y. Zhang, J. Zhu, Electrical characterization of Er- and Pr-implanted GaN films, Appl. Phys. Lett. 86 (2005) 152111.
[50] Sh Valedbagi, S. Elahi, M. Abolhassani, A. Fathalian, A. Esfandiar, Effects of vacancies on electronic and optical properties of GaN nanosheet: A density functional study, Opt. Mater. 47 (2015) 44.

Chemistry Africa
https://doi.org/10.1007/s42250-023-00599-2

ORIGINAL ARTICLE

# Molecular Interactions in Muscle Relaxant Drugs and Sucrose Aqueous Solutions Studied from the Perspectives of Volumetric and Acoustic Parameters

**Meenakshi Virendra Rathi**[1]

Received: 25 August 2022 / Accepted: 19 January 2023


**Abstract**

The volumetric and acoustic properties of aqueous sucrose in the presence of muscle relaxant (MR) drugs such as guaifenesin/methocarbamol were investigated using a bicapillary pycnometer and an interferometer at various temperatures among T = (298.15, 303.15, 308.15, and 313.15) K for guaifenesin/methocarbamol concentrations ranging from 0.25 to 1.5 mol $kg^{-1}$ for each MR molecule. Density and ultrasonic velocity data were utilised to determine the apparent molar volume ($V_{\phi}$) and apparent molar isentropic compression ($K_{\phi,s}$) of the given solute–solvent system. The partial molar volume of transfer ($\Delta^{tr} V_{\phi}^{o}$) and isentropic compression of transfer ($\Delta^{tr} K^{0}_{\phi,s}$) of the examined solutions were also calculated using these data. Analysis of the data includes consideration of solute–solvent interactions and the significant impact on sucrose hydration, when co-solute, i.e. MR drugs, were added to the mixture. An increase in the solvent's electrostriction can also be observed when a drug is present in aqueous sucrose. Interactions between saccharides and added electrolytes modify the variety of physical as well as biological, catalytic, and medicinal properties. At least one of the mentioned MR drugs is injected in the blood stream so the obtained variation of the studied parameters mentioned above may be relevant in a medical, pharmaceutical point of view. The results of the experiment have been explained in terms of solute–solute and solute–solvent interactions along with the behaviour of the solutes in terms of making or breaking of structures.

**Keywords** Sucrose · Guaifenesin · Methocarbamol · Apparent molar volume · Apparent molar isentropic compression · Solvent's electrostriction

## 1 Introduction

Volumetric and acoustic parameters provide information on the strength and type of molecular interactions occurring inside the mixture since it is a non-destructive technique for characterising the solvent system. They also reveal information about the hydrogen bonding, dispersive forces, complex formation, and dipole–dipole intermolecular and intramolecular interactions present in the solute–solvent system. Saccharide is the unit structure of carbohydrates or sugars, which serve as the primary source of energy for a variety of metabolic processes. Sucrose is one of the most frequently used saccharide in medicated syrups as excipients for drug delivery in organisms and in order to formulate syrup properly, one must consider the properties of this basic drug delivery vehicle particularly its stability, and interaction with the other co-solutes (drugs).

Saccharide research and uses are very popular because saccharides and their derivatives play many biological roles: for instance, in cell biology, saccharides use their structural flexibility to signal, recognize, and communicate [1, 2]. Saccharides are known to stabilize proteins, and their presence in aqueous solution can provide insight into how glycoproteins and lipids contribute to the process of molecular recognition [3, 4].Ultra-high dehydration damages proteins and phospholipid bilayers. Saccharides modify fluid viscosity to prevent dehydration and freezing of the body fluids. Saccharides can be used to make a range of chemicals and biofuels, including bioethanol [5]. Glucose can reduce globular protein denaturation [6, 7].Therefore, aqueous saccharides determine biomolecules stability. These data can be utilised to examine thermophile and barophile catabolism [8].

✉ Meenakshi Virendra Rathi
meenakship2@gmail.com

[1] RNC Arts JDB Commerce and NSC Science College, Nashikroad, Nashik, Maharashtra, India

Saccharide-electrolyte interactions are also important in biology, catalysis, medicine, and environmental studies [9, 10]. The physical and thermal properties of saccharides are utilized to calculate their solute and solvent hydration characteristics [11–13]. They can store bioscience materials and perform several biological processes. Preserving drugs can be done with saccharides along with some other additives like ethanol, and salts in water [14, 15]. These additives alter viscosity, crystallization, and water content and also impact glass transition temperature [16, 17].

Guaifenesin, or glyceryl guaiacolate ether (GGE) is white to grey, crystalline solid, with slightly bitter aromatic taste and stable in light and heat. This drug is non hygroscopic, freely dissolves in ethanol, slightly soluble in benzene, chloroform, and does not dissolve at all in petroleum ether [18]. Temporary control of cough due to minor upper respiratory infections and related illnesses, such as sinusitis, pharyngitis and bronchitis as well as worsening of such conditions by viscous mucus and congestion can be treated by using guaifenesin as an expectorant [19–21]. It is thought that guaifenesin is a centrally acting muscle relaxant that inhibits or blocks nerve impulse transmission in the subcortical parts of the brain, brain stem, and spinal cord [22]. There are also sedative and analgesic effects [23]. In conjunction with the administration of anesthetics, the muscle relaxant guaifenesin is given to the patient via intravenous (IV) administration during brief medical procedures [24].The diaphragm and the ability to breathe normally are unaltered, despite the fact that the laryngeal and pharyngeal muscles have become more relaxed [25]. There is a possibility that temporary increases in heart rate and blood pressure may occur [26]. Equine exertion rhabdomyolysis and strychnine poisoning are also conditions that can be treated with this medication [27].

Methocarbamol (carbamate of guaifenesin) is a skeletal muscle relaxant [28]. Methocarbamol treats musculoskeletal discomfort by preventing nerve impulses (or pain sensations) from reaching brain [29, 30].Methocarbamol injection is sometimes used to treat tetanus (lockjaw), which causes painful muscle tightening [31].

According to a survey of the literature, the density and sound velocity of sucrose in aqueous solution with various solute additions have been examined. Usmani et.al studied the interactions of various amino acids in presence of aqueous glucose/sucrose. Nain AK et.al. investigated the solute–solute and solute –solvent interaction of l-threonine as well as isoniazid in aqueous sucrose solution. Tasneem S worked on the interaction between saccharides and varied solutes like bactericidal cefadroxil drug, diammonium hydrogen phosphate and glycine [32–38]. But no comparative studies on volumetric as well as acoustic properties with guaifenesin and methocarbamol have been undertaken till recently. Therefore, to investigate the effects of aqueous guaifenesin and methocarbamol solutions on sucrose, we designed volumetric and acoustic (compression) investigations. The reported data could be useful in terms of the viscosity parameter, Jones–Dole coefficients, specific and molar refraction, specific volume, and hydration numbers, which will provide insight into various intermolecular interactions occurring in aqueous solutions and provide an opportunity to further investigate the mixtures. It will aid in the analysis of various thermodynamic and physicochemical properties and enhancing characteristics of various drugs in the presence of excipients.

For this investigation, water + sucrose + guaifenesin/methocarbamol compositions were used to study density and sound velocity at temperature 298.15 K to 313.15 K and concentrations in the range of 0.25 to 1.5 mol-kg$^{-1}$. The obtained experimental data will be interpreted to discuss the solute–cosolute interactions and will be further used in terms of structure making/breaking nature of solutes.

## 2 Experimental Section

### 2.1 Materials

Guaifenesin and Methocarbamol (mass fraction purity > 0.99) were purchased from Sigma-Aldrich Laboratories, India and sucrose (mass fraction purity = 0.99) was acquired from SD Fine Chem. Ltd.India. All the chemicals studied in this research were used without further purification. However, before usage, all chemicals were vacuum-dried and stored over $P_2O_5$ for 3–4 h.

### 2.2 Methods

The solutions under study were prepared using triple-distilled, degassed water with a conductivity of $1 \times 10^{-6}$ S.cm$^{-1}$ as determined by the Systronics – 304 conductivity metre. Electronic Scientech SE-391 weighing balance with ± 0.01 mg precision was used for accurate weighing. Standard uncertainty in molality for the compound with purity more than 99% is 0.01. In order to prevent the samples from deteriorating over time, measurements were taken on the very same day.

A 20 cm$^3$ double arm pycnometer housed in a transparent glass water bath was used to measure aqueous solution density. Triple-distilled water and some organic solvents were used to calibrate the pycnometer. Density measurements were done in triplicate and the average density was calculated with $1.25 \times 10^{-4}$ g.cm$^{-3}$ precision. Ultrasonic Interferometer was used to measure sound velocity in aqueous sucrose and guaifenesin/methocarbamol systems (Model Number-F-81, Mittal Enterprises, and New Delhi, India). Each sound velocity measurement was done three times,

**Table 1** Chemical specifications list

| Chemicals | Mol.Wt.(g/mol) | Chemical formula | CAS number | Company | Purity (mass fraction) | Method of purification | Chemical structure |
|---|---|---|---|---|---|---|---|
| Sucrose | 342.3 | $C_{12}H_{22}O_{11}$ | 57-50-1 | SD fine chem. Ltd | > 99.0% | Vacuum dried | 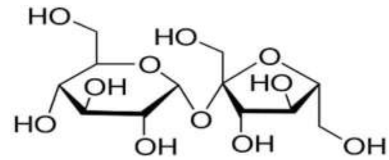 |
| Guaifenesin | 198.2 | $C_{10}H_{14}O_4$ | 93-14-1 | Sigma–Aldrich | > 99.5% | Vacuum dried | 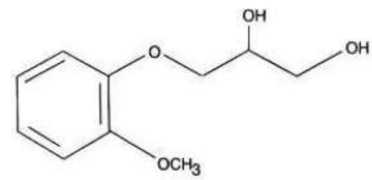 |
| Methocarbamol | 241.2 | $C_{11}H_{15}NO_5$ | 532-03-6 | Sigma–Aldrich | > 99.5% | Vacuum dried | 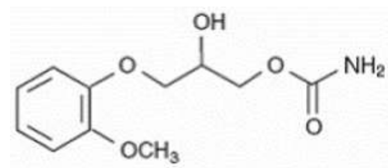 |

and the accuracy was within 0.5 m.s$^{-1}$. Because density and sound velocity are temperature-sensitive, demerstat with 0.1–0.2 K precision was used to control the thermostat temperature. It can adjust temperature to $\pm 1.0 \times 10^{-3}$ K. The measurements of density and sound velocity are accurate to within a range of $5.0 \times 10^{-3}$ kg.m$^{-3}$ and $3.0 \times 10^{-2}$ m.s$^{-1}$, respectively. The standard uncertinity for measurements of density and sound velocity is 0.4 kg m$^{-3}$ and 0.5 m.s$^{-1}$, respectively.

## 3 Results and Discussion

### 3.1 Density Measurements

#### 3.1.1 Apparent Molar Volume

Densities of mixed aqueous solutions of sucrose at four distinct molal concentrations of guaifenesin/methocarbamol (0.25, 0.50, 1.00, & 1.50) mol.kg$^{-1}$ at four different temperatures in the range of T = (298.15, 303.15, 308.15, and 313.15) K have been measured.

Using density data, apparent molar volumes ($V_\phi$) are computed using following Eq. 1 [39, 40]

$$V_\phi = (M/\rho) - \left\{(\rho - \rho^o)/m_1\rho\rho^o\right\} \quad (1)$$

Sucrose (solute) has a molecular mass of M, $m_1$ is the molality of sucrose in aqueous guaifenesin/methocarbamol (cosolute), ρ and ρo denote solution and solvent densities respectively. The density value $\rho^0$ is for the solvent, correspond to the one for the solution at solute, i.e. sucrose concentration equal zero but with content of muscle relaxant molecules. Sucrose density and apparent molar volume values for various aqueous solutions of guaifenesin and methocarbamol are shown in Table 2 and Table 3, respectively. The experimental density values for sucrose + water mixture are agreed well with the literature values [33, 34]. It shows that methocarbamol is denser than guaifenesin when the two are compared for the same concentration and temperature. The graphs comparing the densities of two drug molecules at the same temperature and concentration are reported in Figure S1 of supporting information. The positive apparent molar volumes, $V_\phi$ at various studied temperatures and drug molalities are obtained. As the temperature and concentration of the solute and cosolute increases, $V_\phi$ increases in parallel. The similar trend were noted in the literature [35]. Figure 1a–d and Fig. 2a–d show the apparent molar volumes of sucrose in aqueous guaifenesin and methocarbamol solutions respectively. All the plots reveal that the apparent molar volume $V_\phi$ for sucrose increases as the molality and concentration of both the MR, such as guaifenesin/methocarbamol, increases. This means that there is more interaction between the molecules of the solute (sucrose) and the molecules of the cosolute (MR drug). Also, the fact that the apparent molar volume increases as the temperature increases, it shows that sucrose molecules are more attracted to MR drug molecules, which makes the solute and cosolute molecules interact more. In Table 3, it can be seen that the $V_\phi$

**Table 2** Densities, ρ, and Apparent Molar Volumes, $V_\phi$ values of Sucrose in different concentrations of aq. guaifenesin solutions at experimental temperatures and pressure, p = 0.1 MPa

| T in K | $\rho \times 10^{-3}$ ($kg \cdot m^{-3}$) | | | | $V\phi \times 10^{6}$ ($m^3 \cdot mol^{-1}$) | | | |
|---|---|---|---|---|---|---|---|---|
| | 298.15 | 303.15 | 308.15 | 313.15 | 298.15 | 303.15 | 308.15 | 313.15 |
| $m_1$ ($mol \cdot kg^{-1}$) | | | | | | | | |
| Water + Sucrose | | | | | | | | |
| 0.0000 | 0.997058 | 0.99532 | 0.994047 | 0.99255 | | | | |
| 0.1001 | 1.00983 | 1.00803 | 1.00668 | 1.00511 | 212.17 | 213.04 | 213.92 | 214.79 |
| 0.2002 | 1.02207 | 1.02020 | 1.01876 | 1.01713 | 212.28 | 213.15 | 214.13 | 214.91 |
| 0.3008 | 1.03386 | 1.03192 | 1.03039 | 1.02868 | 212.39 | 213.26 | 214.24 | 215.12 |
| 0.4012 | 1.04514 | 1.04313 | 1.04153 | 1.03975 | 212.50 | 213.37 | 214.35 | 215.23 |
| 0.5016 | 1.05597 | 1.05389 | 1.05221 | 1.05036 | 212.61 | 213.48 | 214.46 | 215.34 |
| 0.6020 | 1.06636 | 1.06422 | 1.06246 | 1.06055 | 212.72 | 213.59 | 214.57 | 215.45 |
| 0.7024 | 1.07635 | 1.07415 | 1.07232 | 1.07034 | 212.83 | 213.70 | 214.68 | 215.56 |
| 0.25 $mol \cdot kg^{-1}$ Guaifenesin + Sucrose | | | | | | | | |
| 0.0000 | 1.026732 | 1.024879 | 1.023324 | 1.02132 | | | | |
| 0.1022 | 1.039152 | 1.037158 | 1.03547 | 1.03332 | 215.50 | 217.01 | 218.42 | 220.00 |
| 0.2021 | 1.050748 | 1.048625 | 1.04681 | 1.04452 | 215.62 | 217.10 | 218.51 | 220.10 |
| 0.3051 | 1.062174 | 1.059927 | 1.05798 | 1.05555 | 215.74 | 217.20 | 218.61 | 220.20 |
| 0.4032 | 1.072589 | 1.070233 | 1.06817 | 1.06561 | 215.86 | 217.29 | 218.70 | 220.29 |
| 0.4999 | 1.082431 | 1.079972 | 1.07779 | 1.07511 | 215.97 | 217.38 | 218.80 | 220.39 |
| 0.6025 | 1.092443 | 1.089895 | 1.08759 | 1.08477 | 216.10 | 217.46 | 218.89 | 220.50 |
| 0.7015 | 1.101704 | 1.099074 | 1.09665 | 1.09371 | 216.22 | 217.55 | 218.99 | 220.59 |
| 0.50 $mol \cdot kg^{-1}$ Guaifenesin + Sucrose | | | | | | | | |
| 0.0000 | 1.05422 | 1.05253 | 1.05098 | 1.04827 | | | | |
| 0.1035 | 1.06642 | 1.06457 | 1.06286 | 1.06001 | 216.17 | 217.74 | 219.30 | 220.88 |
| 0.2041 | 1.07773 | 1.07573 | 1.07387 | 1.07089 | 216.24 | 217.81 | 219.37 | 220.94 |
| 0.3053 | 1.08861 | 1.08646 | 1.08446 | 1.08134 | 216.31 | 217.88 | 219.44 | 221.00 |
| 0.403 | 1.09865 | 1.09637 | 1.09423 | 1.09099 | 216.38 | 217.95 | 219.51 | 221.07 |
| 0.5011 | 1.10832 | 1.10590 | 1.10363 | 1.10027 | 216.45 | 218.02 | 219.58 | 221.14 |
| 0.6025 | 1.11790 | 1.11534 | 1.11294 | 1.10947 | 216.52 | 218.10 | 219.65 | 221.20 |
| 0.7022 | 1.12693 | 1.12425 | 1.12171 | 1.11813 | 216.59 | 218.16 | 219.72 | 221.27 |
| 1.00 $mol \cdot kg^{-1}$ Guaifenesin + Sucrose | | | | | | | | |
| 0.0000 | 1.07960 | 1.07743 | 1.07585 | 1.07343 | | | | |
| 0.1038 | 1.09145 | 1.08913 | 1.08739 | 1.08484 | 216.74 | 218.24 | 219.72 | 221.19 |
| 0.2035 | 1.10230 | 1.09984 | 1.09796 | 1.09527 | 216.81 | 218.32 | 219.78 | 221.25 |
| 0.3051 | 1.11285 | 1.11025 | 1.10823 | 1.10541 | 216.88 | 218.39 | 219.84 | 221.33 |
| 0.4032 | 1.12259 | 1.11985 | 1.11771 | 1.11476 | 216.95 | 218.48 | 219.91 | 221.40 |
| 0.501 | 1.13189 | 1.12901 | 1.12675 | 1.12368 | 217.01 | 218.55 | 219.98 | 221.47 |
| 0.6026 | 1.14113 | 1.13813 | 1.13573 | 1.13256 | 217.09 | 218.61 | 220.06 | 221.53 |
| 0.7024 | 1.14982 | 1.14670 | 1.14418 | 1.14090 | 217.16 | 218.69 | 220.14 | 221.60 |
| 1.50 $mol \cdot kg^{-1}$ Guaifenesin + Sucrose | | | | | | | | |
| 0.0000 | 1.10204 | 1.10034 | 1.09781 | 1.09489 | | | | |
| 0.1032 | 1.11345 | 1.11158 | 1.10890 | 1.10583 | 217.30 | 218.86 | 220.41 | 221.99 |
| 0.204 | 1.12406 | 1.12203 | 1.11920 | 1.11598 | 217.38 | 218.93 | 220.50 | 222.09 |
| 0.3052 | 1.13421 | 1.13204 | 1.12905 | 1.12570 | 217.47 | 218.99 | 220.60 | 222.17 |
| 0.4034 | 1.14361 | 1.14130 | 1.13817 | 1.13469 | 217.56 | 219.06 | 220.68 | 222.25 |
| 0.501 | 1.15254 | 1.15010 | 1.14683 | 1.14323 | 217.64 | 219.14 | 220.76 | 222.32 |
| 0.6025 | 1.16143 | 1.15886 | 1.15545 | 1.15172 | 217.72 | 219.21 | 220.84 | 222.41 |
| 0.7024 | 1.16979 | 1.16709 | 1.16356 | 1.15971 | 217.80 | 219.29 | 220.90 | 222.48 |

The values are from calculation using Eq. 1

**Table 3** Densities, ρ, and Apparent Molar Volumes, $V_\phi$ values of Sucrose in different concentrations of aq. methocarbamol solutions at experimental temperatures and pressure, p = 0.1 MPa

| T in K | $\rho \times 10^{-3}$ (kg·m$^{-3}$) | | | | $V_\phi \times 10^{6}$ (m$^3$·mol$^{-1}$) | | | |
|---|---|---|---|---|---|---|---|---|
| | 298.15 | 303.15 | 308.15 | 313.15 | 298.15 | 303.15 | 308.15 | 313.15 |
| $m_1$ (mol·kg$^{-1}$) | | | | | | | | |
| 0.25 mol·kg$^{-1}$ Methocarbamol + Sucrose | | | | | | | | |
| 0.0000 | 1.03088 | 1.02853 | 1.026869 | 1.02453 | | | | |
| 0.09996 | 1.04289 | 1.04042 | 1.03864 | 1.03618 | 216.53 | 217.86 | 219.21 | 220.57 |
| 0.2004 | 1.05441 | 1.05181 | 1.04993 | 1.04736 | 216.63 | 218.05 | 219.29 | 220.66 |
| 0.3005 | 1.06540 | 1.06268 | 1.06069 | 1.05802 | 216.71 | 218.14 | 219.38 | 220.73 |
| 0.4006 | 1.07592 | 1.07309 | 1.07099 | 1.06821 | 216.79 | 218.21 | 219.46 | 220.81 |
| 0.5007 | 1.08600 | 1.08305 | 1.08086 | 1.07798 | 216.87 | 218.30 | 219.55 | 220.88 |
| 0.6008 | 1.09566 | 1.09261 | 1.09032 | 1.08734 | 216.95 | 218.38 | 219.62 | 220.96 |
| 0.6998 | 1.10484 | 1.10168 | 1.09930 | 1.09622 | 217.03 | 218.45 | 219.69 | 221.04 |
| 0.50 mol·kg$^{-1}$ Methocarbamol + Sucrose | | | | | | | | |
| 0.0000 | 1.06403 | 1.06233 | 1.06022 | 1.05857 | | | | |
| 0.1012 | 1.07571 | 1.07388 | 1.07164 | 1.06987 | 217.39 | 218.73 | 220.09 | 221.43 |
| 0.2011 | 1.08671 | 1.08475 | 1.08239 | 1.08050 | 217.46 | 218.81 | 220.18 | 221.50 |
| 0.301 | 1.09721 | 1.09514 | 1.09266 | 1.09064 | 217.55 | 218.88 | 220.24 | 221.57 |
| 0.4009 | 1.10725 | 1.10507 | 1.10247 | 1.10034 | 217.64 | 218.95 | 220.32 | 221.64 |
| 0.5008 | 1.11687 | 1.11456 | 1.11185 | 1.10962 | 217.71 | 219.03 | 220.40 | 221.71 |
| 0.6007 | 1.12607 | 1.12365 | 1.12084 | 1.11849 | 217.78 | 219.11 | 220.47 | 221.80 |
| 0.7005 | 1.13489 | 1.13236 | 1.12944 | 1.12697 | 217.85 | 219.19 | 220.55 | 221.89 |
| 1.00 mol·kg$^{-1}$ Methocarbamol + Sucrose | | | | | | | | |
| 0.0000 | 1.09524 | 1.09264 | 1.09051 | 1.08843 | | | | |
| 0.1027 | 1.10658 | 1.10385 | 1.10158 | 1.09937 | 218.23 | 219.64 | 221.02 | 222.38 |
| 0.2022 | 1.11704 | 1.11419 | 1.11178 | 1.10945 | 218.32 | 219.71 | 221.11 | 222.45 |
| 0.3028 | 1.12712 | 1.12415 | 1.12162 | 1.11917 | 218.41 | 219.80 | 221.19 | 222.51 |
| 0.4021 | 1.13662 | 1.13354 | 1.13088 | 1.12833 | 218.49 | 219.88 | 221.28 | 222.58 |
| 0.502 | 1.14578 | 1.14257 | 1.13979 | 1.13712 | 218.53 | 219.94 | 221.34 | 222.67 |
| 0.6018 | 1.15452 | 1.15117 | 1.14829 | 1.14552 | 218.59 | 220.04 | 221.42 | 222.73 |
| 0.7015 | 1.16288 | 1.15942 | 1.15641 | 1.15355 | 218.65 | 220.11 | 221.51 | 222.81 |
| 1.50 mol·kg$^{-1}$ Methocarbamol + Sucrose | | | | | | | | |
| 0.0000 | 1.11769 | 1.11493 | 1.11271 | 1.11079 | | | | |
| 0.1015 | 1.12847 | 1.12557 | 1.12321 | 1.12114 | 219.17 | 220.55 | 221.96 | 223.43 |
| 0.2038 | 1.13879 | 1.13577 | 1.13328 | 1.13105 | 219.26 | 220.62 | 222.03 | 223.52 |
| 0.305 | 1.14851 | 1.14537 | 1.14275 | 1.14036 | 219.33 | 220.70 | 222.10 | 223.61 |
| 0.4034 | 1.15752 | 1.15427 | 1.15152 | 1.14900 | 219.41 | 220.77 | 222.18 | 223.69 |
| 0.5016 | 1.16611 | 1.16275 | 1.15989 | 1.15723 | 219.49 | 220.85 | 222.24 | 223.77 |
| 0.6027 | 1.17456 | 1.17108 | 1.16811 | 1.16533 | 219.56 | 220.94 | 222.32 | 223.83 |
| 0.7012 | 1.18242 | 1.17885 | 1.17576 | 1.17285 | 219.65 | 221.01 | 222.40 | 223.92 |

The values are from calculation using Eq. 1

values for methocarbamol are higher than the $V_\phi$ values for guaifenesin. That makes it possible for more interactions to happen in case of methocarbamol. Moreover, as it can be seen at zero sucrose concentration, the methocarbamol density is higher than the one of guaifenesin and their respective values decrease in parallel with increasing temperature. (Tables 1 and 2). Therefore, the higher $V_\phi$ values for methocarbamol compare to guaifenesin is mainly due to the respective density of the muscle relaxant drugs [36].

### 3.1.2 Partial Molar Volume

Apparent molar volume $V_\phi$ can be fitted using Eq. (2) [40–43]

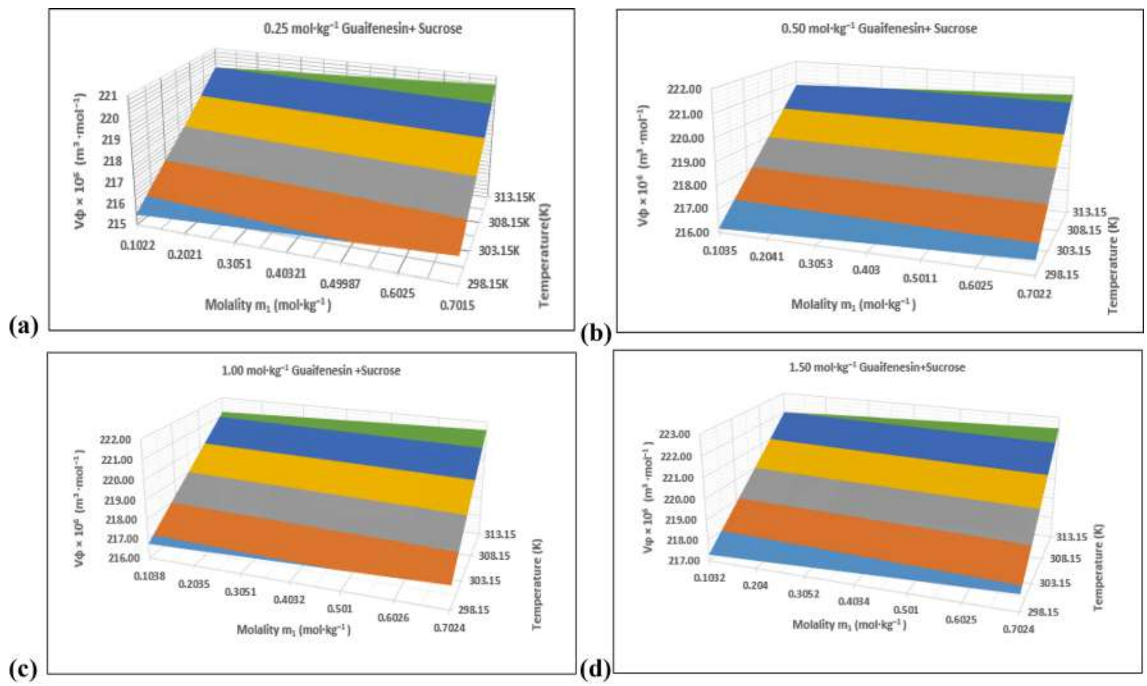


**Fig. 1** Apparent molar volumes, $V_{\phi}$ of sucrose as a function of its molality $m_1$ in **a** 0.25, **b** 0.5, **c** 1.0, and **d** 1.5 $mol{\cdot}kg^{-1}$ Guaifenesin aqueous solution at different temperatures (Values are coming from Table 2)

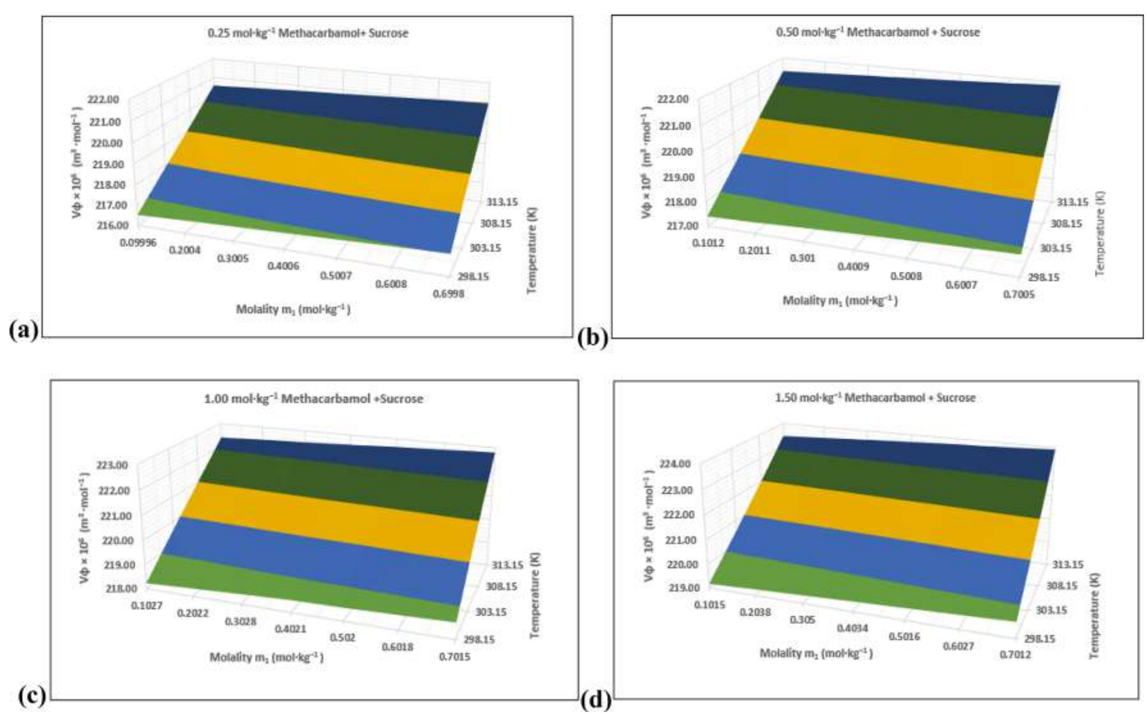


**Fig. 2** Apparent molar volumes, $V_{\phi}$ of sucrose as a function of its molality $m_1$ in **a** 0.25, **b** 0.5, **c** 1.0, and **d** 1.5 $mol{\cdot}kg.^{-1}$ Methocarbamol aqueous solution at different temperatures (Values are coming from Table 3)

$$V_{\phi} = V_{\phi}^{0} + Sv * m_1 \tag{2}$$

where $V_{\phi}{}^{o}$ is the partial molar volume, $S_V$* is the volumetric pairwise interaction coefficient, and $m_1$ is the sucrose molality in guaifenesin/methocarbamol aqueous solutions. Partial molar volumes, $V_{\phi}{}^{o}$ and experimental slopes, $S_V$*, of sucrose in guaifenesin /methocarbamol aqueous solutions at four different experimental temperatures obtained from Eq. 2 are shown in Table 4 along with standard errors.

As the temperature and concentration of guaifenesin/methocarbamol increase, the $V_{\phi}{}^{o}$ values increase as well [40]. A comparison of sucrose $V_{\phi}{}^{o}$ values in aqueous

**Table 4** Partial Molar Volumes, Vϕ°, and volumetric pairwise interaction coefficient, $S_V$*, of Sucrose in Water/Guaifenesin/Methocarbamol Aqueous Solutions at four Different experimental Temperatures

| T in K | $V\phi^o \times 10^6$ ($m^3 \cdot mol^{-1}$) | | | | $SV^* \times 10^6$ ($m^3 \cdot kg \cdot mol^{-2}$) | | | |
|---|---|---|---|---|---|---|---|---|
| | 298.15 | 303.15 | 308.15 | 313.15 | 298.15 | 303.15 | 308.15 | 313.15 |
| $m_2$ ($mol \cdot kg^{-1}$) | | | | | | | | |
| Sucrose + Water | | | | | | | | |
| 0.00 | 212.06 (±0.003) | 212.93 (±0.003) | 213.85 (±0.026) | 214.68 (±0.028) | 1.09 (±0.006) | 1.10 (±0.006) | 1.21 (±0.059) | 1.29 (±0.063) |
| Sucrose + Guaifenesin | | | | | | | | |
| 0.25 | 215.38 (±0.002) | 216.92 (±0.004) | 218.32 (±0.003) | 219.90 (±0.003) | 1.20 (±0.005) | 0.90 (±0.010) | 0.95 (±0.006) | 0.98 (±0.007) |
| 0.50 | 216.09 (±0.002) | 217.66 (±0.002) | 219.23 (±0.003) | 220.81 (±0.005) | 0.71 (±0.004) | 0.72 (±0.005) | 0.70 (±0.006) | 0.65 (±0.011) |
| 1.0 | 216.67 (±0.004) | 218.16 (±0.006) | 219.64 (±0.007) | 221.12 (±0.005) | 0.70 (±0.010) | 0.75 (±0.013) | 0.70 (±0.015) | 0.69 (±0.011) |
| 1.50 | 217.22 (±0.005) | 218.78 (±0.006) | 220.33 (±0.011) | 221.92 (±0.006) | 0.83 (±0.010) | 0.71 (±0.013) | 0.83 (±0.025) | 0.81 (±0.014) |
| Sucrose + Methocarbamol | | | | | | | | |
| 0.25 | 216.46 (±0.005) | 217.83 (±0.032) | 219.13 (±0.007) | 220.50 (±0.002) | 0.82 (±0.011) | 0.93 (±0.071) | 0.81 (±0.017) | 0.77 (±0.005) |
| 0.50 | 217.31 (±0.008) | 218.65 (±0.005) | 220.02 (±0.005) | 221.35 (±0.010) | 0.78 (±0.019) | 0.77 (±0.012) | 0.76 (±0.012) | 0.75 (±0.022) |
| 1.0 | 218.19 (±0.018) | 219.56 (±0.007) | 220.94 (±0.006) | 222.30 (±0.006) | 0.68 (±0.040) | 0.78 (±0.015) | 0.80 (±0.013) | 0.73 (±0.014) |
| 1.50 | 219.10 (±0.003) | 220.47 (±0.007) | 221.88 (±0.006) | 223.36 (±0.008) | 0.78 (±0.006) | 0.77 (±0.015) | 0.74 (±0.013) | 0.80 (±0.018) |

The values are from fits using Eq. 2

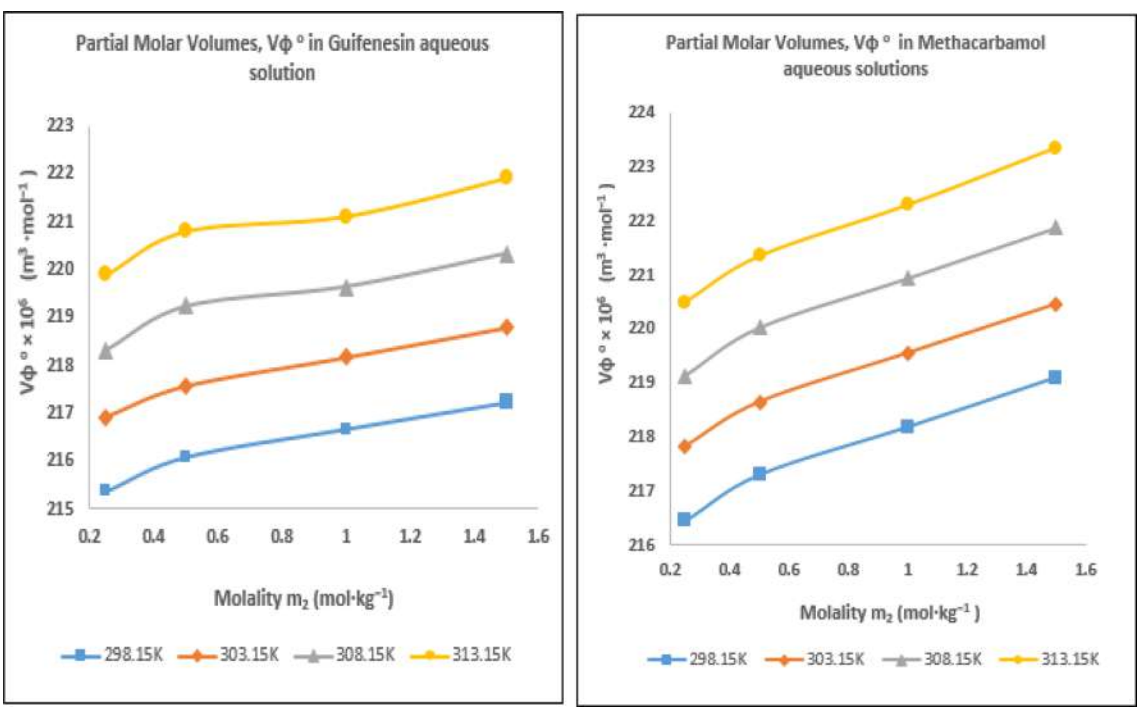


**Fig. 3** Partial molar volumes $V_{\phi}{}^{o}$ of sucrose at zero molality $m_1$ of sucrose as a function of aqueous Guaifenesin/Methocarbamol solutions molality $m_2$ ($mol \cdot kg.^{-1}$) at different temperature. (Values are coming from Table 4)

methocarbamol and guaifenesin solutions is shown in Fig. 3 and Figure S2 of supporting information (The values are coming from Table 4).The higher $V_\phi{}^o$ values for methocarbamol compare to guaifenesin, makes prior's solute–solvent and solute–cosolute interactions stronger [44].Viable interactions between guaifenesin/methocarbamol molecules and polar functional groups of sucrose, i.e. solute–cosolute and solute–solvent interactions can be demonstrated by employing positive $V_\phi{}^o$ values [45].

Due to higher solute –solvent interaction, each solute molecule is surrounded by solvent at infinite dilutions and thus $V_\phi{}^o$ is unaffected by solute–solute interactions [44–46]. This means that only information about interactions between solute–cosolute and solute–solvent can be gleaned from the partial molar volume [47]. The volume of the cosphere increases when two ionic species or hydrophilic sites are close together. On the other hand,volume decreases, when hydrophobic and ion-hydrophobic groups overlap [48, 49]. According to the $V_\phi{}^o$ values, hydrophilic-hydrophilic interactions between guaifenesin/methocarbamol with –OH group of sucrose appear to be responsible for sucrose's positive $V_\phi{}^o$ values [50]. Sucrose's hydrophilic regions get strongly attracted towards the MR drug molecule's polar groups (–OH or –O– groups) through H–bonds. The $V_\phi{}^o$ values increase with temperature and concentration can be attributed to the fact that the solubilized molecules are released into solution by soluble layers of the solute [51]. Guaifenesin, and Methocarbamol molecule's primary and secondary solvation layer depths have been shown to be dependent on temperature as well as $V_\phi{}^o$ values [52]. Furthermore the sucrose –OH groups bind with molecules of guaifenesin and methocarbamol (through -O$^-$, C=O, as well as –O–) to form H-bonds that increase $V_\phi{}^o$ values as the drug concentration increases [52]. $S_V$* values show no clear pattern, indicating that they are affected by other factors [53]. Besides that, all the Sv* values are positive. Weak solute–solute interactions are indicated by less positive values of Sv* [38, 39].

#### 3.1.3 Transfer Partial Molar Volume ($\Delta^{tr}V\phi^o$)

The transfer partial molar volume of sucrose from pure solvent i.e. water to aqueous guaifenesin and methocarbamol solutions at infinite dilution was calculated using Eq. 3.

$$\Delta^{tr}V\phi^o = (V\phi^o\,in\,aqueous\,solution\,of\,Guaifenes\,in\,/\,Methocarbamol) - (V\phi^o\,in\,water) \quad (3)$$

Tabulated values of $\Delta^{tr}V_\phi{}^o$ are found to be positive (Table 8). Increasing the concentration of guaifenesin and methocarbamol has been shown to result in an increase in positive $\Delta^{tr}V_\phi{}^o$ values [40]. The positive $\Delta^{tr}V_\phi{}^o$ values indicate strong hydrophilic-hydrophilic interactions among the guaifenesin/methocarbamol molecule and various polar groups of sucrose [54, 55].These solutes have structure-making ability, which is explained by the cosphere overlap model as a result of internal structure arrangement or contact between the co-spheres of solutes and solvophobic solvation. The polar groups that are present in the structural residues of both sucrose and MR drug molecules contribute to the enhancement of the structure-forming interactions that occur between drug and sucrose molecules. According to the cosphere overlap model interactions among the solute molecules, solute–solute interactions contribute less toward the partial volume of transfer; consequently, facts regarding solute–solvent and solute–cosolute interactions are provided here [56–58].Furthermore, the cosphere overlap model predicts that ion-hydrophobic interactions result in negative transfer volumes, while ion-hydrophilic interactions provide positive transfer volumes [59, 60].The positive $\Delta^{tr}V_\phi{}^o$ values reflect hydrophilic-hydrophilic interactions between guaifenesin/methocarbamol and sucrose in our investigation of sucrose + water + guaifenesin/methocarbamol along with partial molar volume dependence on temperature [61–64].

## 3.2 Sound Velocity

### 3.2.1 Apparent Molar Isentropic Compression

It is possible to compute the value of Ks, also known as the isentropic compressibility, by applying Eq. 4 to the values of u, also known as the speed of sound, and, ρ the density of the solution.

$$Ks = 1/u^2\rho \quad (4)$$

Table S2 and S3 of supporting information show the isentropic compressibility, Ks values of sucrose in guiafenesin / methocarbamol aqueous solutions respectively.

The apparent molar isentropic compression for sucrose in aqueous and guaifenesin /Methocarbamol aqueous solutions at different temperatures is computed using Eq. 5

$$K_{\phi,s} = \left(MK_{s\,/}\rho\right) - \{\left(K_{s,o}\rho - K_{s,}\rho_o\right)/m_1\rho\,\rho o\} \quad (5)$$

where M, $m_1$, ρo, and ρ have the similar connotations as in Eq. 1. $K_{s,o}$ and $K_s$ are the isentropic compressibilities of pure solvent and solution, respectively.Table 5 and 6 show sound velocity, u and $K_{\phi,s}$ apparent molar isentropic compression of sucrose in (0.25, 0.5, 1.0 and 1.5) mol·kg$^{-1}$ guaifenesin and methocarbamol solutions at T = 298.15, 303.15, 308.15, and 313.15 K. It is observed that the determined $K_{\phi,s}$ values of sucrose at all temperatures and concentrations of

**Table 5** Sound velocity, u, and apparent molar isentropic compression, Kϕ,s of Sucrose in guiafenesin aqueous Solutions at experimental temperatures and pressure, p = 0.1 MPa

| T in K | u ($m\cdot s^{-1}$) | | | | $K_{\phi,s} \times 10^6$ ($m^3\cdot mol^{-1}\cdot GPa^{-1}$) | | | |
|---|---|---|---|---|---|---|---|---|
| | 298.15 | 303.15 | 308.15 | 313.15 | 298.15 | 303.15 | 308.15 | 313.15 |
| $m_1$ ($mol\cdot kg^{-1}$) | | | | | | | | |
| Water + Sucrose | | | | | | | | |
| 0.0000 | 1497.05 | 1507.04 | 1519.9 | 1526.11 | | | | |
| 0.1001 | 1506.11 | 1515.71 | 1528.18 | 1534.02 | − 17.18 | − 13.99 | − 10.63 | − 7.83 |
| 0.2002 | 1515.09 | 1524.3 | 1536.46 | 1542.00 | − 16.15 | − 12.99 | − 9.82 | − 7.31 |
| 0.3008 | 1524.03 | 1532.88 | 1544.81 | 1550.13 | − 15.16 | − 12.09 | − 9.19 | − 6.85 |
| 0.4012 | 1532.86 | 1541.39 | 1552.97 | 1558.29 | − 14.21 | − 11.27 | − 8.35 | − 6.45 |
| 0.5016 | 1541.61 | 1549.92 | 1561.04 | 1566.41 | − 13.12 | − 10.58 | − 7.55 | − 5.97 |
| 0.602 | 1550.00 | 1558.12 | 1569.03 | 1574.52 | − 12.23 | − 9.66 | − 6.79 | − 5.50 |
| 0.7024 | 1558.16 | 1566.33 | 1576.88 | 1582.67 | − 11.14 | − 8.90 | − 6.04 | − 5.09 |
| 0.25 $mol\cdot kg^{-1}$ Guaifenesin + Sucrose | | | | | | | | |
| 0.0000 | 1534.68 | 1543.54 | 1555.9 | 1564.8 | | | | |
| 0.1022 | 1546.1 | 1554.8 | 1567.1 | 1575.9 | − 17.66 | − 15.49 | − 13.71 | − 11.91 |
| 0.2021 | 1556.9 | 1565.3 | 1577.6 | 1586.4 | − 16.08 | − 13.63 | − 12.05 | − 10.53 |
| 0.3051 | 1567.7 | 1575.8 | 1587.8 | 1596.6 | − 14.59 | − 12.10 | − 10.14 | − 8.75 |
| 0.4032 | 1577.5 | 1585.4 | 1597.5 | 1606.0 | − 13.04 | − 10.68 | − 9.02 | − 7.34 |
| 0.4999 | 1586.6 | 1594.6 | 1606.8 | 1615.1 | − 11.40 | − 9.43 | − 7.97 | − 6.23 |
| 0.6025 | 1596.5 | 1604.0 | 1616.1 | 1624.2 | − 10.31 | − 8.14 | − 6.67 | − 4.89 |
| 0.7015 | 1605.7 | 1613.1 | 1625.1 | 1632.6 | − 9.24 | − 7.21 | − 5.72 | − 3.66 |
| 0.50 $mol\cdot kg^{-1}$ Guaifenesin + Sucrose | | | | | | | | |
| 0.0000 | 1569.47 | 1579.2 | 1588.63 | 1599.1 | | | | |
| 0.1035 | 1580.6 | 1590.3 | 1599.9 | 1610.2 | − 8.19 | − 6.77 | − 6.25 | − 4.42 |
| 0.2041 | 1591.1 | 1600.9 | 1610.7 | 1620.9 | − 7.06 | − 5.97 | − 5.54 | − 3.89 |
| 0.3053 | 1601.5 | 1611.3 | 1621.4 | 1631.5 | − 6.20 | − 5.09 | − 4.87 | − 3.30 |
| 0.403 | 1611.3 | 1621.1 | 1631.6 | 1641.6 | − 5.37 | − 4.26 | − 4.27 | − 2.75 |
| 0.5011 | 1621 | 1630.95 | 1641.8 | 1651.7 | − 4.64 | − 3.68 | − 3.78 | − 2.30 |
| 0.6025 | 1630.5 | 1640.7 | 1651.7 | 1661.9 | − 3.68 | − 2.89 | − 2.92 | − 1.77 |
| 0.7022 | 1640 | 1650.5 | 1661.8 | 1672.1 | − 3.06 | − 2.44 | − 2.50 | − 1.46 |
| 1.00 $mol\cdot kg^{-1}$ Guaifenesin + Sucrose | | | | | | | | |
| 0.0000 | 1602.24 | 1612.4 | 1622.5 | 1632.6 | | | | |
| 0.1038 | 1612.3 | 1622.6 | 1632.8 | 1642.9 | 1.82 | 2.24 | 2.88 | 3.77 |
| 0.2035 | 1621.9 | 1632.3 | 1642.6 | 1652.8 | 2.19 | 2.68 | 3.28 | 3.95 |
| 0.3051 | 1631.7 | 1642.2 | 1652.6 | 1662.9 | 2.44 | 2.93 | 3.51 | 4.11 |
| 0.4032 | 1641.1 | 1651.7 | 1662.2 | 1672.6 | 2.71 | 3.21 | 3.75 | 4.31 |
| 0.501 | 1650.3 | 1661.2 | 1671.8 | 1682.3 | 3.06 | 3.39 | 3.91 | 4.44 |
| 0.6026 | 1659.78 | 1670.82 | 1681.6 | 1692.2 | 3.40 | 3.72 | 4.18 | 4.66 |
| 0.7024 | 1669.26 | 1680.44 | 1690.8 | 1701.9 | 3.57 | 3.88 | 4.62 | 4.85 |
| 1.50 $mol\cdot kg^{-1}$ Guaifenesin + Sucrose | | | | | | | | |
| 0.0000 | 1634.14 | 1644.5 | 1654.8 | 1663.9 | | | | |
| 0.1032 | 1644.5 | 1654.8 | 1665.2 | 1674.1 | 4.40 | 5.61 | 6.12 | 7.63 |
| 0.204 | 1654.6 | 1664.8 | 1675.3 | 1684.0 | 4.61 | 5.86 | 6.37 | 7.87 |
| 0.3052 | 1664.7 | 1674.9 | 1685.5 | 1693.8 | 4.82 | 5.96 | 6.46 | 8.17 |
| 0.4034 | 1674.5 | 1684.6 | 1695.3 | 1703.3 | 4.99 | 6.13 | 6.63 | 8.35 |
| 0.501 | 1684.2 | 1694.25 | 1704.9 | 1712.6 | 5.15 | 6.25 | 6.85 | 8.58 |
| 0.6025 | 1694.2 | 1704.2 | 1714.8 | 1722.2 | 5.32 | 6.40 | 7.06 | 8.79 |
| 0.7024 | 1704.1 | 1713.93 | 1724.6 | 1731.2 | 5.43 | 6.55 | 7.18 | 9.16 |

The values are from calculations using Eqs. 4 and 5

**Table 6** Sound velocity, u, and apparent molar isentropic compression, $K_{\phi}$,s of sucrose in methocarbamol aqueous solutions at experimental temperatures and pressure, p = 0.1 MPa

| T in K | u/(m·s $^{-1}$) | | | | Kϕ,s × $10^6$ /($m^3$ $mol^{-1}$ $GPa^{-1}$) | | | |
|---|---|---|---|---|---|---|---|---|
| | 298.15 | 303.15 | 308.15 | 313.15 | 298.15 | 303.15 | 308.15 | 313.15 |
| $m_1$ (mol·kg$^{-1}$) | | | | | | | | |
| 0.25 mol·kg$^{-1}$ methocarbamol + Sucrose | | | | | | | | |
| 0.0000 | 1544.7 | 1553.1 | 1563.9 | 1574.1 | | | | |
| 0.09996 | 1555.6 | 1564.0 | 1574.4 | 1584.3 | − 14.07 | − 12.93 | − 9.78 | − 7.25 |
| 0.2004 | 1566.0 | 1574.1 | 1583.9 | 1594.1 | − 12.12 | − 10.25 | − 6.73 | − 5.71 |
| 0.3005 | 1576.5 | 1584.5 | 1593.4 | 1603.9 | − 11.38 | − 9.65 | − 5.51 | − 5.01 |
| 0.4006 | 1587.1 | 1594.9 | 1602.9 | 1613.7 | − 10.94 | − 9.16 | − 4.73 | − 4.49 |
| 0.5007 | 1596.9 | 1604.6 | 1612.4 | 1623.5 | − 9.74 | − 8.05 | − 4.14 | − 4.07 |
| 0.6008 | 1607.2 | 1614.0 | 1622.1 | 1633.2 | − 9.21 | − 6.97 | − 3.84 | − 3.63 |
| 0.6998 | 1617.3 | 1624.2 | 1632.0 | 1643.1 | − 8.77 | − 6.78 | − 3.77 | − 3.46 |
| 0.50 mol·kg$^{-1}$ methocarbamol + Sucrose | | | | | | | | |
| 0.0000 | 1596.5 | 1606.1 | 1616.2 | 1626.1 | | | | |
| 0.1012 | 1607.9 | 1617.4 | 1627.7 | 1637.7 | − 6.87 | − 5.40 | − 5.11 | − 4.60 |
| 0.2011 | 1618.7 | 1628.3 | 1638.7 | 1648.9 | − 5.56 | − 4.53 | − 4.12 | − 3.80 |
| 0.301 | 1629.5 | 1639.2 | 1649.7 | 1660.1 | − 4.90 | − 4.06 | − 3.62 | − 3.37 |
| 0.4009 | 1640.3 | 1650.1 | 1660.7 | 1671.3 | − 4.46 | − 3.71 | − 3.27 | − 3.05 |
| 0.5008 | 1651.1 | 1661.0 | 1671.7 | 1682.5 | − 4.11 | − 3.42 | − 2.97 | − 2.80 |
| 0.6007 | 1661.9 | 1671.9 | 1682.7 | 1693.7 | − 3.82 | − 3.16 | − 2.73 | − 2.57 |
| 0.7005 | 1672.7 | 1682.8 | 1693.7 | 1704.9 | − 3.58 | − 2.95 | − 2.52 | − 2.37 |
| 1.00 mol·kg$^{-1}$ methocarbamol + Sucrose | | | | | | | | |
| 0.0000 | 1635.3 | 1645.7 | 1655.5 | 1664.9 | | | | |
| 0.1027 | 1646.1 | 1656.5 | 1666.3 | 1675.5 | 2.54 | 3.21 | 4.03 | 5.53 |
| 0.2022 | 1656.4 | 1666.6 | 1675.8 | 1685.4 | 2.96 | 4.04 | 5.94 | 6.33 |
| 0.3028 | 1666.7 | 1676.7 | 1685.3 | 1695.1 | 3.35 | 4.56 | 6.80 | 7.03 |
| 0.4021 | 1677.0 | 1686.8 | 1695.0 | 1704.9 | 3.48 | 4.74 | 6.97 | 7.18 |
| 0.502 | 1687.3 | 1696.9 | 1704.5 | 1714.5 | 3.61 | 4.92 | 7.28 | 7.51 |
| 0.6018 | 1697.6 | 1707.0 | 1713.9 | 1723.2 | 3.72 | 5.07 | 7.55 | 8.30 |
| 0.7015 | 1707.9 | 1717.1 | 1723.3 | 1732.8 | 3.81 | 5.17 | 7.76 | 8.34 |
| 1.50 mol·kg$^{-1}$ methocarbamol + Sucrose | | | | | | | | |
| 0.0000 | 1664.1 | 1673.5 | 1683.8 | 1692.9 | | | | |
| 0.1015 | 1675.1 | 1684.4 | 1694.6 | 1703.7 | 5.24 | 6.14 | 7.24 | 8.05 |
| 0.2038 | 1685.2 | 1694.8 | 1705.1 | 1714.4 | 6.95 | 7.20 | 7.95 | 8.42 |
| 0.305 | 1695.3 | 1704.6 | 1715.3 | 1724.6 | 7.43 | 8.14 | 8.41 | 8.98 |
| 0.4034 | 1704.6 | 1714.4 | 1724.9 | 1734.5 | 8.13 | 8.38 | 8.92 | 9.25 |
| 0.5016 | 1714.2 | 1724.0 | 1734.7 | 1744.3 | 8.34 | 8.65 | 9.10 | 9.52 |
| 0.6027 | 1724.1 | 1733.9 | 1744.5 | 1754.2 | 8.48 | 8.84 | 9.34 | 9.73 |
| 0.7012 | 1733.3 | 1743.6 | 1754.1 | 1764.0 | 8.79 | 8.92 | 9.49 | 9.85 |

The values are from fits using Eq. 6

guaifenesin and methocarbamol are negative except at higher molality i.e. 1.0 and 1.5 mol.kg$^{-1}$ aqueous solutions. $K_{\phi,s}$ increases with temperature, MR drugs, and sucrose concentration. Hydration of sucrose may lead to the negative values of $K_{\phi,s}$. which can be thought as a result of stronger resistance of water molecules around the MR drug moiety towards compression than in bulk [65, 66]. At higher molality i.e. 1.0 and 1.5 mol.kg$^{-1}$ positive values of $K_{\phi,s}$ may be attributed to the electrostriction reduction and thereby releasing of some of the molecules of water to the bulk causing stronger compression at higher concentrations [65].

#### 3.2.2 Partial Molar Isentropic Compression

Equation 6 effectively represents the variation of apparent molar isentropic compression $K_{\phi,s}$ of the sucrose with molal concentration [40]

**Table 7** Partial molar isentropic compression $K^0_{\varphi}$, s and isentropic compression pairwise interaction coefficient $\mathbf{S_K}$*, of sucrose in water / guaifenesin/methacarbamol aqueous solutions at four different experimental temperatures

| T in K | $K^0\varphi,s \times 10^6$ $m^3 \cdot mol^{-1} \cdot GPa^{-1}$ | | | | $S_K^* \times 10^6$ ($kg \cdot m^3 \cdot mol^{-2} \cdot GPa^{-1}$) | | | |
|---|---|---|---|---|---|---|---|---|
| | 298.15 | 303.15 | 308.15 | 313.15 | 298.15 | 303.15 | 308.15 | 313.15 |
| $m_2$ ($mol \cdot kg^{-1}$) | | | | | | | | |
| Sucrose + Water | | | | | | | | |
| 0.00 | − 18.17 (±0.036) | − 14.70 (±0.078) | − 11.40 (±0.040) | − 8.24 (±0.026) | 9.96 (±0.081) | 8.34 (±0.173) | 7.64 (±0.088) | 4.52 (±0.059) |
| Sucrose + Guaifenesin | | | | | | | | |
| 0.25 | − 18.95 (±0.212) | − 16.50 (±0.257) | − 14.64 (±0.298) | − 13.17 (±0.166) | 14.31 (±0.473) | 13.79 (±0.572) | 13.22 (±0.664) | 13.80 (±0.370) |
| 0.50 | − 8.88 (±0.111) | − 7.41 (±0.123) | − 6.84 (±0.075) | − 4.88 (±0.076) | 8.50 (±0.247) | 7.37 (±0.274) | 6.30 (±0.168) | 5.06 (±0.170) |
| 1.0 | 1.55 (±0.044) | 2.08 (±0.063) | 2.66 (±0.068) | 3.58 (±0.018) | 2.97 (±0.097) | 2.67 (±0.141) | 2.66 (±0.152) | 1.78 (±0.039) |
| 1.50 | 4.26 (±0.030) | 5.50 (±0.029) | 5.95 (±0.034) | 7.37 (±0.039) | 1.74 (±0.066) | 1.50 (±0.063) | 1.77 (±0.075) | 2.45 (±0.086) |
| Sucrose + Methocarbamol | | | | | | | | |
| 0.25 | − 14.23 (±0.379) | − 12.92 (±0.536) | − 9.10 (±0.874) | − 7.16 (±0.372) | 8.33 (±0.846) | 9.50 (±0.019) | 9.00 (±1.954) | 5.87 (±0.831) |
| 0.50 | − 6.78 (±0.329) | − 5.43 (±0.198) | − 5.08 (±0.238) | − 4.62 (±0.185) | 5.05 (±0.734) | 3.83 (±0.442) | 4.00 (±0.531) | 3.49 (±0.413) |
| 1.0 | 2.55 (±0.136) | 3.34 (±0.248) | 4.48 (±0.537) | 5.33 (±0.199) | 2.00 (±0.302) | 2.97 (±0.552) | 5.33 (±1.196) | 4.59 (±0.443) |
| 1.50 | 5.51 (±0.446) | 6.28 (±0.369) | 7.16 (±0.190) | 7.88 (±0.130) | 5.24 (±0.991) | 4.36 (±0.822) | 3.66 (±0.423) | 3.06 (±0.288) |

The values are from calculations using Eqs. 4 and 5

$$K_{\phi,s} = K^0_{\phi,s} + S_K * m_1 \tag{6}$$

where K0ϕ,s is the partial molar isentropic compression and SK* is the isentropic compression pairwise interaction coefficient, m1 is the molality of sucrose in aqueous guaifenesin / methocarbamol solutions. The least square fitting was applied to the deviation of the apparent molar isentropic compression Kϕ,s versus sucrose molality m1.

Table 7 reports the resulting fit parameters $K^0_{\phi,s}$ and $S_K$* as a function of the MR drug molality $m_2$ along with standard errors. As demonstrated in Table 7, negative $K^0_{\phi,s}$ values were determined for sucrose in aqueous drug solutions at all temperatures with the exception of sucrose in a 1.0 and 1.5 mol.kg$^{-1}$ guaifenesin /methocarbamol solution. The values of $K^0_{\phi,s}$ are depicted graphically in Fig. 4. Figure S2 of supporting information indicates that with rising temperature and concentration of guaifenesin/methocarbamol, the $K^0_{\phi s}$ increases, showing that ion-hydrophilic interactions prevail in sucrose + water + guaifenesin/methocarbamol solutions [67]. Due to the presence of polar ionic groups, the sucrose molecules have a net attraction toward the ions of MR medicines, resulting in dehydration of the sucrose molecules. As a result, the water molecules around sucrose are compressed more at greater MR drug concentrations than at lower drug concentrations. In consequence, when concentrations and temperatures increase, $K^0_{\phi,s}$ values become less negative [68].

#### 3.2.3 Partial Molar Isentropic Compression of Transfer

Using Eq. 7, the apparent molar isentropic compression of transfer at infinite dilutions from water to aqueous guifensin/methocarbamol solutions were elucidated.

$$\Delta^{tr} K^0_{\phi,s} = \left(K^0_{\phi,s}\ in\ aqueous\ solution\ of\ Guaifenes\ in\ /\ Methocarbamol\right) - \left(K^0_{\phi,s} in\ water\right) \tag{7}$$

The $\boldsymbol{\Delta^{tr}} K^0_{\phi,s}$ values are shown in Table 8 along with $\Delta^{tr}V_{\phi}$ ° values. Discussion and effect of $\Delta^{tr}V_{\phi}$° values have been already done in Sect. 1.c. Sucrose $\boldsymbol{\Delta^{tr}} K^0_{\phi,s}$ values are positive at all concentrations and temperatures except (0.25 mol. kg$^{-1}$) of guaifenesin aqueous solutions at studied temperatures. Table 8 demonstrates that when the drug ion concentration increases, so do the $\boldsymbol{\Delta^{tr}} K^0_{\phi,s}$ values. These positive $\boldsymbol{\Delta^{tr}} K^0_{\phi,s}$ values reflect the capacity of the molecule to form structures due to the dominant interactions between the polar

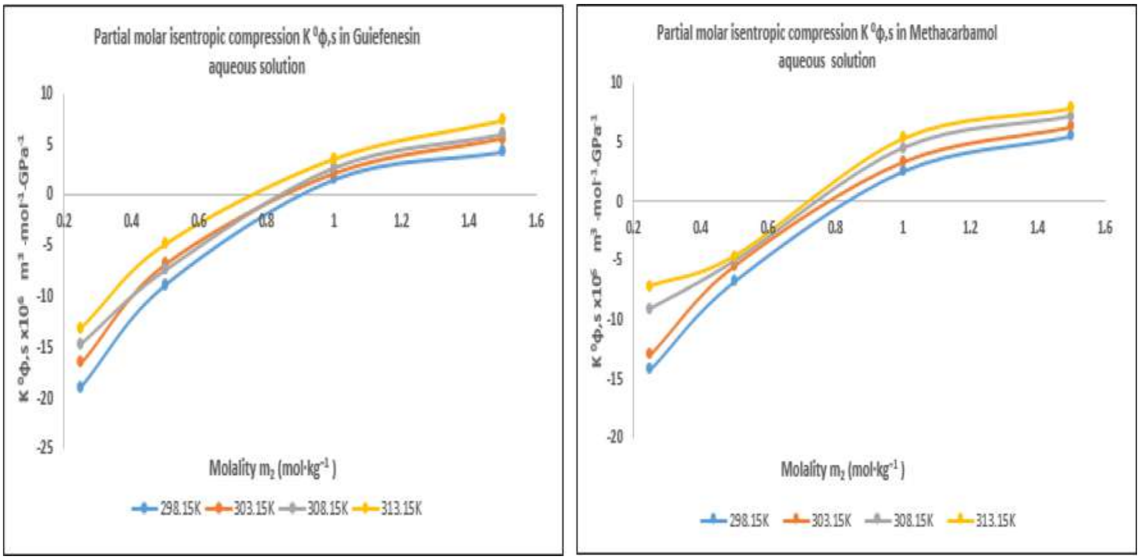


**Fig. 4** Partial molar isentropic compression $K^0_{\varphi,s}$ of sucrose at zero molality $m_1$ of sucrose as a function of aqueous guaifenesin /methocarbamol solutions molality $m_2$ (mol·kg.$^{-1}$) at different temperature. (Values are coming from Table 8)

groups of sucrose and the ions of guaifenesin/methocarbamol molecules, with increasing guaifenesin/methocarbamol concentration [69, 70]. Consequently, as the concentration and temperature of guaifenesin/methocarbamol increase, so does the electrostriction; consequently, the ability to form structures rises. This illustrates that bulk water is more compressible than electrostricted water with drug ions, and that compressibility decreases with increasing drug concentration [71]. The negative $\Delta^{tr}K^0_{\phi,s}$ values of guaifenesin suggest increase in the electrostriction around polar/hydrophilic groups and protonated group in it [72, 73].Results indicate that $K^0_{\phi,s}$ values are negative and $\Delta^{tr}K^0_{\phi,s}$ values are positive for sugar + water + MR drug solutions. Sucrose dehydration happens further due to interactions between the sucrose's hydrophilic sites and the drug polar groups, eventually results in release of less compressible water in to the bulk from the solute molecules' hydration shells.

## 4 Conclusions

Sucrose is widely used as excipients for drug delivery in organisms, since sucrose solutions provide sweetness, viscosity, as well as inherent stability. In this article sucrose and guaifenesin/methocarbamol (water + sucrose + guaifenesin/methocarbamol) aqueous solutions have been studied for their thermo-physical properties, such as the density, apparent molar volume, sound velocity and partial molar isentropic compression. From this information, we were able to determine the interactions between sucrose and MR

**Table 8** Partial molar volume of transfer, $\Delta^{tr}V^0_{\phi}$ and Partial molar isentropic compression of transfer, $\Delta^{tr}K^0_{\phi}$, s of sucrose in Guaiefenesin and Methocarbamol aqueous solutions of at different temperatures

| T in K | $\Delta^{tr}V_{\phi}^{o}\times10^6$ (m$^3$·mol$^{-1}$) | | | | $\Delta^{tr}K^0_{\phi,s}\times10^6$ (m$^3$·mol$^{-1}$·GPa$^{-1}$) | | | |
|---|---|---|---|---|---|---|---|---|
| | 298.15 | 303.15 | 308.15 | 313.15 | 298.15 | 303.15 | 308.15 | 313.15 |
| $m_2$ (mol·kg$^{-1}$) | | | | | | | | |
| Sucrose + Guaifenesin | | | | | | | | |
| 0.25 | 3.32 | 3.99 | 4.47 | 5.22 | − 0.78 | − 1.80 | − 3.24 | − 4.93 |
| 0.50 | 4.03 | 4.73 | 5.38 | 6.13 | 9.28 | 7.29 | 4.56 | 3.36 |
| 1.0 | 4.61 | 5.23 | 5.79 | 6.44 | 19.71 | 16.78 | 14.06 | 11.82 |
| 1.50 | 5.16 | 5.85 | 6.48 | 7.24 | 22.43 | 20.20 | 17.36 | 15.62 |
| Sucrose + Methocarbamol | | | | | | | | |
| 0.25 | 4.40 | 4.90 | 5.28 | 5.82 | 3.94 | 1.78 | 2.30 | 1.09 |
| 0.50 | 5.25 | 5.72 | 6.17 | 6.67 | 11.39 | 9.27 | 6.32 | 3.62 |
| 1.0 | 6.13 | 6.63 | 7.09 | 7.62 | 20.72 | 18.04 | 15.88 | 13.57 |
| 1.50 | 7.04 | 7.54 | 8.03 | 8.68 | 23.68 | 20.98 | 18.56 | 16.12 |

The values are from calculations using Eqs. 3 and 7 drugs i.e. guaifenesin/methocarbamol molecules. When the concentration of guaifenesin/methocarbamol solutions is increased, the degree of interaction increases, as determined by partial molar data and transfer volume characteristics. The obtained values of $V_\phi^o$ and $\Delta^{tr}V_\phi^o$ show positive and increasing trend with temperature as well as at higher concentration of MR drugs which indicates greater solvation and interaction amongst sucrose and MR drugs. From the result issued from the here presented investigation, it was demonstrated the presence of hydrophilic-hydrophilic and ion-hydrophilic interactions in the system composed of sucrose + water + pharmaceuticals MR drug solutions. Water is treated as a structured medium rather than as a continuum. These interactions are particularly interesting in view of the high degree of structure in aqueous solutions, both in the solvent itself and in the aggregates that can exist as a result of the structure of water. The trend observed in the values of $K_{\phi,s}$, $K^0_{\phi,s}$ and $\Delta^{tr} K^0_{\phi,s}$ leads to the inference that MR drugs (co-solutes) acts as structure-maker in aqueous-sucrose solvents. Medicated syrups typically have a high sucrose concentration, ranging from 60 to 80% and it is well known that sucrose in excess can cause Type 2 diabetes. Readers should be aware of the restricted use of this ingredient in a solution containing MR drugs.

**Supplementary Information** The online version contains supplementary material available at https://doi.org/10.1007/s42250-023-00599-2.

**Data availability** The datasets generated an analysed during the current study are available from the corresponding author on reasonable request.

## References


1. Gabius HJ, Siebert HC, Andre S, Jimenez-Barbero J, Rudiger H (2004) Chemical biology of the sugar code. Chem Bio Chem 5(6):740–764. https://doi.org/10.1002/cbic.200300753
2. Arda A, Jimenez-Barbero J (2018) The recognition of glycans by protein receptors Insights from NMR spectroscopy. Chem Commun 54(38):4761–4769. https://doi.org/10.1039/C8CC01444B
3. Gimeno A, Reichardt NC, Canada FJ, Perkams L, Unverzagt C, Jimenez-Barbero J, Arda A (2017) NMR and molecular recognition of N-glycans remote modifications of the saccharide chain modulate binding features. ACS Chem Biol 12(4):1104–1112. https://doi.org/10.1021/acschembio.6b01116
4. Lannoo N, Van Damme EJM (2015) Review/N-glycans: the making of a varied toolbox. In Plant Science 239:67–83. https://doi.org/10.1016/j.plantsci.2015.06.023
5. Wolfe J, Bryant G (2001) Cellular cryobiology: thermodynamic and mechanical effects. Int J Refrig 24(5):438–450. https://doi.org/10.1016/S01407007(00)00027-X
6. Agalya P, de Oliveira IP, Lescano CH, Caires AR, Velusamy V (2022) Effect of pH and cosolvent sucralose on the solvation profile of ovalbumin: Ultrasonic and molecular simulation studies. Food Hydrocoll 125:107386. https://doi.org/10.1016/j.foodhyd.2021.107386
7. Palaniappan L, Velusamy V (2013) Impact of cosolvent (glucose) on the stabilization of ovalbumin. Food Hydrocolloids 30(1):217–223. https://doi.org/10.1016/j.foodhyd.2012.05.020
8. Amend JP, Plyasunov AV (2001) Carbohydrates in thermophile metabolism: calculation of the standard molal thermodynamic properties of aqueous pentoses and hexoses at elevated temperatures and pressures. Geochim Cosmochim Acta 65(21):3901–3917. https://doi.org/10.1016/S0016-7037(01)00707-4
9. Teychene J, Balmann HR, Galier S (2021) Advances in the understanding of the transfer of saccharides through NF membranes in the presence of electrolytes by coupling quantum mechanics and thermodynamic methods. Membranes 11(5):341. https://doi.org/10.3390/membranes11050341
10. Teychene J, Roux-de Balmann H, Maron L, Galier S (2020) Interactions in saccharide/ cation/water systems: insights from density functional theory. Food Chem 327:127054. https://doi.org/10.1016/j.foodchem.2020.127054
11. Chalikian TV (2001) Structural thermodynamics of hydration. J Phys Chem B 105(50):12566–12578. https://doi.org/10.1021/jp0115244
12 Karimi S, Shekaari H, Ahadzadeh I (2020) The sweetness response and thermophysical properties of glucose and fructose in the aqueous solution of some deep eutectic solvents at T= (2881.5–3181.5)K. Carbohydr Res 495:108083. https://doi.org/10.1016/j.carres.2020.108083
13. Amirchand KD, Kaur S, Banipal TS, Singh V (2021) Volumetric and 1H NMR spectroscopic studies of saccharides-calcium lactate interactions in aqueous solutions. J Mol Liq 334:116077. https://doi.org/10.1016/j.molliq.2021.116077
14 Pittia P, Paparella A (2016) Safety by control of water activity: drying, smoking, and salt or sugar addition. Regul Safe Tradit Ethnic Foods. https://doi.org/10.1016/B978-0-12-800605-4.00002-5
15 Prakash V (2016) Introduction: the importance of traditional and ethnic food in the context of food safety, harmonization, and regulations. Regul Safe Tradit Ethnic Foods. https://doi.org/10.1016/B978-0-12-800605-4.00001-3
16. Kasaai MR (2014) Use of water properties in food technology: a global view. Int J Food Prop 17(5):1034–1054. https://doi.org/10.1080/10942912.2011.650339
17. Amit SK, Uddin MM, Rahman R, Islam SMR, Khan MS (2017) A review on mechanisms and commercial aspects of food preservation and processing. Agric Food Secur 6(1):51. https://doi.org/10.1186/s40066-017-0130-8
18. Williams M (2013) The Merck index: an encyclopedia of chemicals, drugs and biologicals. Drug Dev Res 74(5):339–339. https://doi.org/10.1002/ddr.21085
19. Albrecht HH, Dicpinigaitis PV, Guenin EP (2017) Role of guaifenesin in the management of chronic bronchitis and upper respiratory tract infections. Multidiscipl Respir Med 12(1):31. https://doi.org/10.1186/s40248-017-0113-4
20. United States Pharmacopeial Convention (2006) Usp di. Drug information for the health care professional, 26th edn. Thomson/Micromedex
21 Richter P (2014) Guaifenesin encyclopedia of toxicology, 3rd edn. Elsevier, pp 806–808
22. Tripathi S, Nikhare A, Sharma G, Shea T, Albrecht H (2019) Safety and tolerability of extended-release guaifenesin in patients with cough, thickened mucus and chest congestion associated with upper respiratory tract infection. Drug Healthcare Patient Safe 11:87–94. https://doi.org/10.2147/DHPS.S222109
23. Septimus EJ, Albrecht HH, Solomon G, Shea T, Guenin EP (2017) Extended-release guaifenesin/pseudoephedrine hydrochloride for symptom relief in support of a wait-and-see approach for the treatment of acute upper respiratory tract infections: a randomized,

double-blind, placebo-controlled study. Curr Ther Res Clin Exp 84:54–61. https://doi.org/10.1016/j.curtheres.2017.04.004
24. Lerche P (2013) Total intravenous anesthesia in horses veterinary clinics of North America. Equine Practice 29(1):123–129. https://doi.org/10.1016/j.cveq.2012.11.008
25. Ohar JA, Donohue JF, Spangenthal S, Ohar J (2019) Chronic Obstructive pulmonary diseases: journal of the COPD foundation the role of guaifenesin in the management of chronic mucus hypersecretion associated with stable chronic bronchitis: a comprehensive review. Stable ChronicBronchit J 6(4):341–349. https://doi.org/10.15326/jcopdf.6.4.2019.0139
26. https://www.mayoclinic.org/drugs-supplements/guaifenesin-oral-route/side-effects/drg-20068720. (2023).
27. Pruitt BN (2013) Methocarbamol suspension for the treatment of rhabdomyolysis in equines. Int J Pharmaceutical Compound 17(5):384–387
28. Corral C, Ashmawy MB, Lissavetzky J, Basilio A, Giraldez A (1987) Synthesis and central relaxant activity of thiophene analogs of mephenesin and methocarbamol. Eur J Med Chem 22(3):251–254. https://doi.org/10.1016/0223-5234(87)90057-2
29 Jung H, Chae H (2019) The safety and efficacy of methocarbamol as a muscle relaxant with analgesic action: analysis of current data. Innov Biosyst Bioeng 3(4):201–211. https://doi.org/10.20535/ibb.2019.3.4.183336
30. Beebe FA, Barkin RL, Barkin S (2005) A clinical and pharmacologic review of skeletal muscle relaxants for musculoskeletal conditions. Am J Ther 12(2):151–171. https://doi.org/10.1097/01.mjt.0000134786.50087.d8
31. Witenko C, Moorman-Li R, Motycka C, Duane K (2014) Considerations for the appropriate use of skeletal muscle relaxants for the management of acute low back pain. J Formul Manag 39(6):427–435
32. Riyazuddeen UMA (2012) Interactions in (l-alanine/l-threonine + aqueous glucose/aqueous sucrose) systems at (298.15–323.15) K. Thermochim Acta 527:112–117. https://doi.org/10.1016/j.tca.2011.10.013
33. Nain AK, Pal R, Neetu, (2013) Volumetric, ultrasonic and viscometric studies of solute–solute and solute–solvent interactions of l-threonine in aqueous-sucrose solutions at different temperatures. J Chem Thermodyn 64:172–181. https://doi.org/10.1016/j.jct.2013.05.012
34 Usmani R (2011) Densities, speeds of sound, and viscosities of (l-proline + aqueous glucose) and (l-proline + aqueous sucrose) solutions in the temperature range (2981.5 to 3231.5)K. J Chem Eng Data 56(9):3504–3509. https://doi.org/10.1021/je2000205
35. Ankita NAK (2019) Volumetric, acoustic and viscometric studies of solute-solute and solute-solvent interactions of isoniazid in aqueous-glucose/sucrose solutions at temperatures from 293.15 K to 318.15 K. J Chem Thermodyn 133:123–134. https://doi.org/10.1016/j.jct.2019.01.024
36. Tasneem S (2017) To study the interactions between saccharide/their derivatives and bactericidal cefadroxil drug: volumetric, acoustic and molecular docking studies. Z Phys Chem 231(11–12):1831–1847. https://doi.org/10.1016/j.jct.2021.106477
37 Tasneem S (2017) Study of the interactions of monosaccharides D(+)-glucose and D(−)-fructose in aqueous diammonium hydrogen phosphate over the temperature range T=(28815–31815) K. Z Phys Chem 231(11–12):1831–1847. https://doi.org/10.1016/j.jct.2022.106793
38. Tasneem S (2017) Effect of glycine on aqueous solution behavior of saccharides at different temperatures: volumetric and ultrasonic studies. Z Phys Chem 231(11–12):1831–1847. https://doi.org/10.1016/j.molliq.2014.03.004
39. Asghar Jamal M, Naseem B, Naz S, Arif I, Saeed M, Atiq S (2020) Thermo-acoustic properties of maltose in aqueous amino acids system. J Mol Liq 309:112932. https://doi.org/10.1016/j.molliq.2020.112932
40. Kumar H, Kaur K, Kaur SP, Singla M (2013) Studies of volumetric and acoustic properties of trisodium citrate and tripotassium citrate in aqueous solutions of N-acetyl glycine at different temperatures. J Chem Thermodyn 59:173–181. https://doi.org/10.1016/j.jct.2012.12.022
41 Masson DO (1929) XXVIII Solute molecular volumes in relation to solvation and ionization. Lond Edinb Dublin Phil Mag J Sci 8(49):218–235. https://doi.org/10.1080/14786440808564880
42. Desnoyers JE (1982) Structural effects in aqueous solutions: a thermodynamic approach. Pure Appl Chem 54(8):1469–1478. https://doi.org/10.1351/pac198254081469
43. Hedwig GR, Reading JF, Lilley TH (1991) Partial molar heat capacities and partial molar volumes of some N-acetyl amino acid amides, some N-acetyl peptide amides and two peptides at 25 °C. J Chem Soc Faraday Trans 87(11):1751–1758. https://doi.org/10.1039/ft9918701751
44. Tasneem S (2017) Hydration and solvation effect of glycine and glycylglycine molecules with β-Cyclodextrin in aqueous media a thermodynamic characteristic of interaction. Z Phys Chem 231(11–12):1831–1847. https://doi.org/10.22036/pcr.2016.12593
45. Shekaari H, Zafarani-Moattar M, Ghaffari F (2016) Volumetric, acoustic and conductometric studies of acetaminophen in aqueous ionic liquid, 1-Octyl-3-methylimidazolium bromide at T = 2931.5–3081.5 K. Phys Chem Res 4(1):119–141. https://doi.org/10.22036/pcr.2016.12593
46 Patil KR, Musale SP, Dagade DH (2020) Peptides in aqueous protic ionic liquid solutions: apparent and transfer volumes at 2981.5 K and at 0.1 MPa. J Mol Liq 317:113943. https://doi.org/10.1016/j.molliq.2020.113943
47. Mehrdad A, Hajikarimi M (2019) Volumetric, acoustic and viscometric investigation of ceftriaxone disodium in aqueous solutions of 1-propanol and 2-propanol. J Chem Thermodynamics 139:105880. https://doi.org/10.1016/j.jct.2019.105880
48. Kaur K, Arti S, Ghosh TK, Banipal TS, Banipal PK (2021) To study the interactions between saccharide/their derivatives and bactericidal cefadroxil drug: Volumetric, acoustic and molecular docking studies. J Chem Thermodynamics 159:106477. https://doi.org/10.1016/j.jct.2021.106477
49. Jamal MA, Ahmad Sajid T, Saeed M, Naseem B, Muneer M (2022) Explication of molecular interactions between leucine and pharmaceutical active ionic liquid in an aqueous system: volumetric and acoustic studies. J Mol Liq 360:119510. https://doi.org/10.1016/j.molliq.2022.119510
50. Kumar H, Behal I (2016) Thermodynamics of (solute + solute) and (solute + solvent) interactions of homologous series of amino acids with thiamine hydrochloride in aqueous medium at T = (305.15, 310.15, 315.15) K: a volumetric and acoustic approach. J Chem Thermodyn 102:48–62. https://doi.org/10.1016/j.jct.2016.06.026
51. Harries D, Rau DC, Parsegian VA (2005) Solutes probe hydration in specific association of cyclodextrin and adamantane. J Am Chem Soc 127(7):2184–2190. https://doi.org/10.1021/ja045541t
52. Kumar H, Behal I, Siraswar S (2019) Densities and speeds of sound for sucrose in aqueous solutions of ammonium phosphate salts at different temperatures through density and speed of sound measurements. J Chem Eng Data 64(9):3772–3780. https://doi.org/10.1021/acs.jced.8b01157
53. Rajagopal K, Mohamed Roshan M, Shailajha S, Roy Richi Renold G (2019) Volumetric approach to the interaction of L-proline in aqueous Metformin Hydrochloride solutions for temperature range 298.15–318.15 K. J Chem Thermodyn 133:312–319. https://doi.org/10.1016/j.jct.2019.02.012

54. Pal A, Chauhan N (2010) Interactions of diglycine in aqueous saccharide solutions at varying temperatures: a volumetric, ultrasonic and viscometric study. J Solution Chem 39(11):1636–1652. https://doi.org/10.1007/s10953-010-9620-z
55. Bhat R, Kishore N, Ahluwalia JC (1988) Thermodynamic studies of transfer of some amino acids and peptides from water to aqueous glucose and sucrose solutions at 2981.5 K. J Chem Soc Faraday Trans Phys Chem Condensed Phase 84(8):2651. https://doi.org/10.1039/f19888402651
56 Frank HS, Evans MW (1945) Free volume and entropy in condensed systems III. Entropy in binary liquid mixtures; partial molal entropy in dilute solutions; structure and thermodynamics in aqueous electrolytes. J Chem Phys 13(11):507–532. https://doi.org/10.1063/1.1723985
57. Gurney RW (1953) Ionic processes in solution. McGraw-Hill, New York
58. Friedman HL, Krishnan CV (1973) Studies of hydrophobic bonding in aqueous alcohols: enthalpy measurements and model calculations. J Solution Chem 2(2–3):119–140. https://doi.org/10.1007/bf00651969
59 Li S, Sang W, Lin R (2002) Partial molar volumes of glycine, l-alanine, and l-serine in aqueous glucose solutions at T=2981.5K. J Chem Thermodynamics 34(11):1761–1768. https://doi.org/10.1016/s0021-9614(02)00125-8
60. Kumar H, Behal I (2016) Volumetric and ultrasonic investigation of molecular interactions of l-serine and l-threonine in aqueous nicotinamide solutions at T= (288.15–318.15) K. J Mol Liq 219:756–764. https://doi.org/10.1016/j.molliq.2016.04.019
61. Gheorghe I, Stoicescu C, Sirbu F (2016) Partial molar volumes, isentropic compressibilities, and partial molar expansibilities of N-Methylglycine and d-Glucose in aqueous environments at temperatures between (298.15 and 323.15) K. J Mol Liq 218:515–524. https://doi.org/10.1016/j.molliq.2016.02.033
62. Gupta J, Nain AK (2019) Molecular interactions of gentamicin sulphate in aqueous-l-asparagine/l-glutamine solutions at different temperatures: Volumetric, acoustic and viscometric properties. J Mol Liq 293:111547. https://doi.org/10.1016/j.molliq.2019.111547
63. Mishra AK, Ahluwalia JC (1984) Apparent molal volumes of amino acids, N-acetylamino acids, and peptides in aqueous solutions. J Phys Chem 88(1):86–92. https://doi.org/10.1021/j150645a021
64. Iqbal MJ, Chaudhry MA (2010) Effect of temperature on volumetric and viscometric properties of some non-steroidal anti-inflammatory drugs in aprotic solvents. J Chem Thermodyn 42(8):951–956. https://doi.org/10.1016/j.jct.2010.03.009
65. Chandak AS, Zodape SP (2021) Insights into the temperature and concentration dependent studies of the anti-diabetic drug in aqueous binary and ternary (water + sucrose) mixtures at body temperature. Chem Phys Impact 3:100050. https://doi.org/10.1016/j.chphi.2021.100050
66. Ryshetti S, Gupta A, Tangeda SJ, Gardas RL (2014) Acoustic and volumetric properties of betaine hydrochloride drug in aqueous d(+)-glucose and sucrose solutions. J Chem Thermodyn 77:123–130. https://doi.org/10.1016/j.jct.2014.05.015
67. Jamal MA, Fatima J, Naseem B, Muneer M, Ibrahim M (2021) Molecular interaction studies of antidepressant drug with aqueous caffeine using volumetric and acoustic methods. J Mol Liq 329:115525. https://doi.org/10.1016/j.molliq.2021.115525
68. Kaur H, Chakraborty N, Juglan KC, Kumar H (2021) Volumetric and acoustic behavior of PEG-200 and PEG-600 in aqueous d-mannitol solutions at different temperatures. J Solution Chem 50(8):1079–1102. https://doi.org/10.1007/s10953-021-01105-3
69. Romero CM, Rodríguez DM, Ribeiro ACF, Esteso MA (2017) Effect of temperature on the partial molar volume, isentropic compressibility and viscosity of DL-2-aminobutyric acid in water and in aqueous sodium chloride solutions. J Chem Thermodyn 104:274–280. https://doi.org/10.1016/j.jct.2016.09.040
70. Devunuri N, Kancherla S, Chennuri BK, Gardas RL (2016) Apparent molar volume and isentropic compressibilities of antidepressant drugs (Citalopram HBr and Escitalopram oxalate) with water. J Mol Liq 216:347–353. https://doi.org/10.1016/j.molliq.2016.01.058
71. Chauhan S, Kumar K (2014) Effect of glycine on aqueous solution behavior of saccharides at different temperatures: volumetric and ultrasonic studies. J Mol Liq 194:212–226. https://doi.org/10.1016/j.molliq.2014.03.004
72. Arsule AD, Sawale RT, Deosarkar SD (2019) Temperature-dependent volumetric and ultraacoustic studies of α-amino acids in aqueous acetylsalicylic acid drug solutions. J Mol Liq 275:478–490. https://doi.org/10.1016/j.molliq.2018.10.122
73. Kumar H, Kumari S, Behal I, Sharma SK (2018) Analysing the molecular interactions of sucrose in aqueous triammonium citrate and trilithium citrate solutions at different temperatures T = (288.15–318.15)K through volumetric and ultrasonic investigations. J Chem Thermodyn 125:17–31. https://doi.org/10.1016/j.jct.2018.05.004

# Materials Today: Proceedings

## Acoustic, volumetric and viscometric study relative to inter-molecular interaction in aqueous KIO3 + 1% KH2PO4

--Manuscript Draft--

| | |
|---|---|
| **Manuscript Number:** | |
| **Article Type:** | SI: INPMA-2022 |
| **Keywords:** | KIO3; Jones-Dole constants; B-coefficient; adiabatic compressibility; Masson's Constant |
| **Corresponding Author:** | Meenakshi Virendra Rathi, Ph.D.<br>RNC Arts JDB Commerce and NSC Science College<br>Nashik, Maharashtra INDIA |
| **First Author:** | Meenakshi Virendra Rathi, Ph.D. |
| **Order of Authors:** | Meenakshi Virendra Rathi, Ph.D. |
| **Abstract:** | This research paper comprises of the effect of temperature and concentration on the acoustic volumetric and viscometric properties viz. ultrasonic velocity, density and viscosity of aqueous $KIO_3$ solutions in 1% $KH_2PO_4$ .The research findings is quite useful to expound the various inter molecular interactions like ion–ion, ion–solvent, and solvent–solvent between the chosen solute-solvent system. Based on the data obtained, various derived acoustical parameters viz, acoustic impedance(Z), adiabatic compressibility (β), intermolecular free length (Lf), free volume (Vf), Rao's constant (R),Wada's constant (W), density dependent apparent molar volumes ( [[EQUATION]] ) viscosity dependent viscosity B-coefficients for $KIO_3$ solutions in aqueous 1% $KH_2PO_4$ and pure water system have been determined at 298.15 to 313.15 K. Additionally Masson's constants, Jones-Dole constants are supported to study various molecular interactions. |
| **Suggested Reviewers:** | Dr.Arun Nikumbh, Ph.D.<br>Professor, Rayat Shikshan Sanstha's Annasaheb Awate College, Manchar<br>aob.nikumbh@gmail.com<br>Well Known Professor |
| | Dr.Raghunath Toche, Ph.D.<br>Professor, Dadasaheb Bidkar Arts,Science and commerce College Peth Dist Nashik Maharashtra<br>raghunath_toche@rediffmail.com<br>Great Reveiwer |

 

# Acoustic, volumetric and viscometric study relative to inter-molecular interaction in aqueous $KIO_3$ + 1 % $KH_2PO_4$

**Dr. Meenakshi Virendra Rathi ***

Department of Chemistry,
RNC Arts, JDB Commerce, NSC Science College, Nasik Road,
City: Nasik.
Postal Code: 422101
State: Maharashtra
Country: India
e-mail: meenakship2@gmail.com
Phone No. 9403510314

## Abstract:

This research paper comprises of the effect of temperature and concentration on the acoustic volumetric and viscometric properties viz. ultrasonic velocity, density and viscosity of aqueous $KIO_3$ solutions in 1% $KH_2PO_4$.The research findings is quite useful to expound the various inter molecular interactions like ion–ion, ion–solvent, and solvent–solvent between the chosen solute-solvent system. Based on the data obtained, various derived acoustical parameters viz, acoustic impedance(Z), adiabatic compressibility (β), intermolecular free length (Lf), free volume (Vf), Rao's constant (R),Wada's constant (W), density dependent apparent molar volumes ($\emptyset_V$) viscosity dependent viscosity B-coefficients for $KIO_3$ solutions in aqueous 1% $KH_2PO_4$ and pure water system have been determined at 298.15 to 313.15 K. Additionally Masson's constants, Jones-Dole constants are supported to study various molecular interactions.

**Keywords:** $KIO_3$, Jones-Dole constants, B-coefficient, adiabatic compressibility, Masson's Constant

## Introduction:

$KIO_3$ is a colourless crystalline solid that is widely used as an oxidising agent while Potassium dihydrogen phosphate, KDP ( $KH_2PO_4$) is the inorganic compound . Both are used in many different applications such as a food ingredient, fertiliser, and fungicide. (Depeng Meng, 2017) (Luo, 2018). Potassium iodate is occasionally used as a flouring agent in baking, (Paranthaman, 2021) , also used as a source for dietary iodine. It is also found in certain formula milk that is marketed to babies. (Gebreegziabher, 2017) KDP can be found in energy drinks, coffee creamers, cheddar cheese, and low-sodium foods..It supplies potassium and phosphorus nutrients. Incorporating the current research into multiple applications like the solutes for medical, food, and agricultural science encourages us to carry on the current investigation.

In food, medicine, and pesticide industries, molecular and ionic interactions of oxidising agents in presence of aqueous salts plays a vital role. The ion-water interactions in understanding the effects of oxidising agents, particularly their temperature dependence (Marcus, 2015) (Nikumbh & Rathi, 2016, Nikumbh & Rathi, 2014). The information gained from ultrasonic propagation parameters in liquid mixtures and solutions, such as ultrasonic velocity and its variation with concentration of one of the components, aids in betterunderstansing of how molecular interactions in a mixture affect each other and provides a way to test theories dealing with liquid structure. The transport and acoustic data will be very useful to understand solvolysis behaviour and ion-molecular interaction (Ganjare, 2020) of $KIO_3$ in used solvent systems.

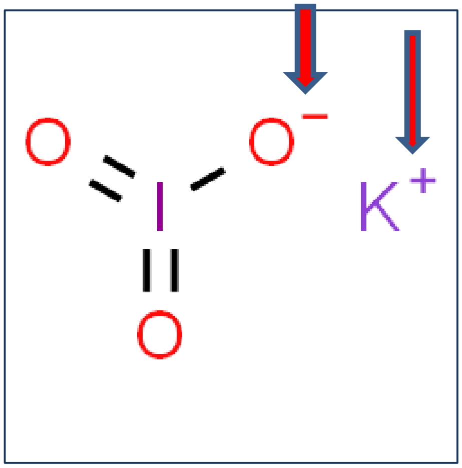


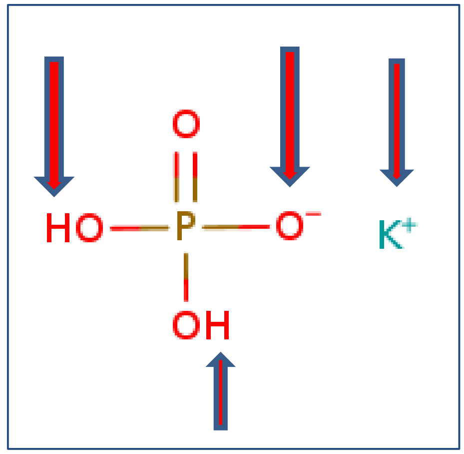


**Structure of $KIO_3$ and $KH_2PO_4$** (arrow shows the interacting sites)

## Experimental:

## Materials:

All chemicals were taken from Sigma Aldrich, Germany, with more than 99% purity and was further desiccated over anhydrous $CaCl_2$ before use. Tripally distilled water with a specific conductance of < $10^{-6}$ $S.cm^{-1}$ was used for the preparation of solutions at room temperature in a molality range (0.03-0.21) $mol.kg^{-1}$. The precision of balance used was ± $1\times10^{-5}$g.

**Table 1: Table 1: Chemical Specifications.**

| Chemicals | Source | Percentage Purity | Purification Method | CAS No. | Mol. Mass $g.Mol^{-1}$ | Chemical Formula |
|---|---|---|---|---|---|---|
| Potassium Iodate | Sigma Aldrich | ≥99.0% | desiccated over anhydrous $CaCl_2$ | 7758-05-6 | 122.55 | $KIO_3$ |
| Potassium phosphate monobasic | Sigma Aldrich | ≥98.0% | Used as obtained | 7778-77-0 | 136.1 | $KH_2$ $PO_4$ , |

### Measurements of Density:

Densities of aqueous solutions were determined using a 15$cm^3$ double arm pycnometer housed in a transparent glass walled water bath. The pycnometer was calibrated using triple distilled water. The densities of $KIO_3$ solutions in aqueous 1 % $KH_2$ $PO_4$ , and pure water were measured by bi-capillary pycnometer at different temperatures. The density was determined with an accuracy of ±1.28 $\times10^{-4}$ $g.cm^{-3}$ using an average of triple measurements. The thermostat temperature is maintained at the desired level using a demerstat with a 0.1 K precision.

**Measurement of Viscosity**

The viscosities of all seven concentration of $KIO_3$ solutions in aqueous 1 % $KH_2\ PO_4$ , were determined using an Ubbelohde viscometer at 298.15, 303.15, 308.15, and 313.15K. At least three times, measurements were taken to ensure the reproducibility of the results. Viscosity measurements were performed with an overall precision of ± $2.5\times10^{-4}$ mPa.s. The flow time is reliably measured at 0.01 second intervals. Before injecting each sample, the equipment was cleaned with distilled water and acetone and thoroughly dried.

**Measurement of ultrasonic velocity**

The Ultrasonic Interferometer (Model No. F-81, Mittal Enterprises, New Delhi, India) was used at a frequency of 2 MHz to measure the sound velocity in the aqueous systems and aqueous 1 % $KH_2\ PO_4$ , systems of $KIO_3$. In each case, the measurement was repeated three times, and the accuracy of the sound velocity measurement was found to be within 0.5 m/s . (Saxena, 2015) In the end, it all averages out.

## Data Evaluation:

The data on density and ultrasonic velocity were used to calculate acoustical parameters [45] viz., acoustic impedance (Z), adiabatic compressibility (β ), intermolecular free length (Lf ), free volume (Vf ), Rao's constant (R), Wada's constant (W), and partial molar volume (Vm) by the following equations: (Mohabansi, 2020)

1. Adiabatic compressibility (β) $=\frac{1}{u2\rho}$ $Kg^{-1}ms^{2}$

   u = velocity; ρ= Density of liquid

2. Specific Acoustic impedance (Z) = U x ρ $Kg^{-1}ms^{-3}$
3. Relative association (RA) = $\left[\frac{\rho}{\rho 0}\right]\left[\frac{U0}{U}\right]^{1/3}$

   Where ρ and ρ0 are the densities of solution and solvent respectively. U and U0 are the ultrasonic velocities of solution and solvent respectively.

4. Molar compressibility (W) $=\frac{(M.\beta)}{\rho}$

   Where ρ =density, M=Molecular weight, β = adiabatic compressibility

5. Rao's constant (R) = $\frac{M}{\rho}$ $[U]^{1/2}$

   Where, M = Molecular Weight, ρ = density

6. Free volume (Vf) = $[Meff.\ U\ K\eta]^{1/2}\ m^{3}$ ,

   Where M eff= effective molecular weight,

   K-temperature independent constant K = 4.28 $x10^{9}$ for all liquid) (Nori, 2019)

7. Intermolecular Free Length (Lf) =KT x $\sqrt{\beta}$

   Where, Jacobson's Constant, KT = (93.875 + 0.375 x T)

The apparent molar volumes $\emptyset_V$, were obtained from the density results using the following equation ( Hnedkovsky, Rasanen, Koukkari, & Hefter, 2020; Spitzer , Singh, & Olofsson., 1978)

$$\emptyset_V = \frac{1000(\rho_0-\rho)}{C\rho_0} + \frac{M2}{\rho}$$

Where $M_2$, C, $\rho$ and $\rho_0$ are the molar mass of the $KIO_3$, concentration (mol $kg^{-1}$ )and the densities of the solution and the solvent, respectively.

The apparent molar volumes ($\emptyset_V$) were plotted against the square root of concentration ($C^{½}$) in accordance with the Masson's equation ( Raundal, 2021; Roy, Dakua, & Sinha, 2007)

$$\emptyset_V = \emptyset_V^0 + S_v.C^{½}$$

Where $\emptyset_V$ is the limiting apparent molar volume $\emptyset_V^0$ and $S_v$ a semi-empirical parameter which depends on the nature of solute, solvent as well as temperature. When $\emptyset_V$are plotted against molality, the intercept onY axis and slope gives the values of the apparent molar volume, $\emptyset_V^0$ and Sv respectively.

The viscosity results were plotted in accordance with Jones-Dole equation (Jones, 1929; Pandey , Misra , Shukla , & Mushran, 1987)

$$\eta r-1 /C½ = A + BC½$$

Where $\eta_r = (\eta/\eta_o)$ and $\eta$, $\eta_o$ are viscosities of the solution and solvent respectively, C is the molar concentration.

The B-coefficients were obtained from the linear plots using the least-square fitting method. (Lomesh , Nathan, Bala , & Thakur, 2019) The A- coefficient reflects solute-solute interaction (Falkenhagen & Dole, 1929) and the B-coefficient reflect the solute-solvent interactions. Since in general, A/B <<1, the Jones –Dole equation reduces (Shakeel & Mahmood, 2020) to,

$$\eta_r = l + \beta.C,$$

The relative viscosity data of these solutions have also been fitted in Moulik equation (Tank , Sharma , & Sharma, 2019),

$$\eta_r{}^2 = M + K\,C^2$$

The density data of these solutions have also been fitted in Root's equation (Harsh, Katal, & Sharma, 2020) ,

$$(d - d_0) / C = R - SC^{½}$$

Where R and S are constants.

## Results and Discussion:

Density (ρ), viscosity(η ),ultrasonic velocity (u), acoustic impedance (Z), adiabatic compressibility (β), intermolecular free length (Lf ), free volume (Vf ), Rao's constant (R), Wada's constant (W), partial molar volume (VΦ) and Relaxation time for the solution of $KIO_3$ in 1 % $KH_2PO_4$ solvent systems and different temperatures are reported in table-1-4. Fig 1, Fig 2 and Fig 3 show that the values of densities and viscosities and ultrasonic velocities of $KIO_3$ solutions under investigation increases with increase in concentration. Similar observations were also made previously (Bhujbal, 2019; Khan, Farooqui, & Quadri, 2011) other solutions. At higher temperatures, the solution shows higher values of the ultrasonic velocity. (Kharat, 2010)

The positive values of $\emptyset_V$ decrease with concentration in 1% $KH_2$ $PO_4$ , and pure water solvent systems. The relative viscosities are found to increase with concentrations.

The apparent molar volumes at infinite dilution ($\emptyset_V^0 = V_2^0$ ) and slopes $S_V$, calculated using Masson equation (2) are given in table-5. The $\emptyset_V^0$ values of $KIO_3$ under investigation in 1% $KH_2$ $PO_4$ , and in pure water solvent systems are large and positive suggests presence of strong solute-solvent interactions promotes structure making effect. (Lu, 2020) .It is clear that the values of $\emptyset_V$ ($m^3.mol^{-1}$) are positive and more or less similar in water and in salt solutions at different temperatures. The slope $S_v$ is negative for $KIO_3$ solution in 1% $KH_2$ $PO_4$ , and in pure water. Since $S_v$ is measure of solute-solute interactions (Rathi & Nikumbh, 2019) These results indicate that there is presence of strong solute-solute interactions. $S_v$ values do not change systematically with change in temperature, and hence it suggests that the solute-solute interactions are insensitive to change in temperature. (Banipal, Arti, & Banipal, 2016). The acoustic impedance is the product of density and ultrasonic velocity (Z).and dependent on both concentration and temperature. Z increases gradually with increase in concentration and temperature. This reveals the structure making action via strong hydrogen bonding. (Chauhan, 2016) Adiabatic compressibility (β) varies inversely the molality of the solution, at all four studied temperature. (Ritesh R. Naik, 2015).This indicates the close packing of the molecules (Reena Roy, 2018). Values of intermolecular free length (Lf) is the indicator of the interactions between the solute and solvent due to association between the molecules through ionic interactions. With the increase in the concentration, the decrease in the Lf values reflects the strong solute- solvent interactions. The increases in the value of Vf with increase in the concentration may be due to the dispersive forces of the component molecules. The increase in the Rao's constant and Wada's constant values confirms that solute and solvents are associated in solution due to dipole–dipole interaction. (Reddy, 2016)

## Conclusions:

The physicochemical properties of $KIO_3$ solutions in water and 1 % KHD solutions at various temperatures are presented in this report in a systematic manner.

The density and viscosity parameters drop as the temperature increases. The reason would be that an internal molecular force decreases and thermal energy increases. In these systems, it has been observed that there are strong solute–solvent interactions. Positive $\emptyset_V^0$ values indicate the presence of ion-solvent interactions. For $KIO_3$, the Moulik, Roots, and Jones-Dole reduced equations are validated.

The higher densities of $KIO_3$ in 1 % $KH_2PO_4$ are due to the salts' relative salvation, corresponding relative volumes of system, and molar mass .Densities may increase with concentration due to the strengthening of solute-solvent interactions. (Iwadate & Ohkubo, 2020).By using values of acoustical parameters of the solute over the entire concentration range, it is interpreted that there is molecular interactions between solute and solvent.

**Acknowledgement:** I would like to sincerely acknowledge the guidance and help provided by Dr. Arun B. Nikumbh for compilation of this research report.

**Table 1:** Molality (m), density (ρ), viscosity(η ),ultrasonic velocity (u), acoustic impedance (Z), adiabatic compressibility (β), intermolecular free length (Lf ), free volume (Vf ), Rao's constant (R), Wada's constant (W), partial molar volume (VΦ) and Relaxation time for the solution of $KIO_3$ in $KH_2PO_4$ at 298.15 K and atmospheric pressure

| m, mol $kg^{-1}$ | ρ $kg/m^3$ | η × $10^{-3}$ Ns $m^{-2}$ | u, m $s^{-1}$ | Z × $10^{-5}$, kg $m^{-2}$ $s^{-1}$ | β × $10^{-10}$, $m^2$ $N^{-1}$ | Lf × $10^{-11}$, m | Vf × $10^6$ $m^3$ $mol^{-1}$ | R | W x $10^{-13}$ $m^{5/7}/N^{1/7}$ | VΦ × $10^{-6}$, $m^3$ $mol^{-1}$ | Relaxation Time |
|---|---|---|---|---|---|---|---|---|---|---|---|
| 0.03 | 1005.18 | 0.9289 | 1501.3 | 15.091 | 4.437 | 4.332 | 1390.756 | 0.00181 | 1.2759 | 3.163 | 5.4990 |
| 0.06 | 1006.66 | 0.9349 | 1512.8 | 15.229 | 4.362 | 4.296 | 1561.904 | 0.00195 | 1.3772 | 2.979 | 5.4378 |
| 0.09 | 1008.51 | 0.9417 | 1527.7 | 15.407 | 4.271 | 4.251 | 1677.296 | 0.00204 | 1.4422 | 2.820 | 5.3628 |
| 0.12 | 1010.73 | 0.9497 | 1539.6 | 15.561 | 4.197 | 4.214 | 1752.351 | 0.00211 | 1.4864 | 2.670 | 5.3141 |
| 0.15 | 1013.33 | 0.9592 | 1548.4 | 15.690 | 4.139 | 4.184 | 1797.759 | 0.00215 | 1.5176 | 2.535 | 5.2934 |
| 0.18 | 1016.49 | 0.9699 | 1559.7 | 15.854 | 4.067 | 4.148 | 1830.806 | 0.00218 | 1.541 | 2.425 | 5.2597 |
| 0.21 | 1018.45 | 0.9743 | 1571.3 | 16.003 | 3.996 | 4.111 | 1873.288 | 0.00221 | 1.5612 | 2.292 | 5.1907 |

**Table 2:** Molality (m), density (ρ), viscosity(η ),ultrasonic velocity (u), acoustic impedance (Z), adiabatic compressibility (β), intermolecular free length (Lf ), free volume (Vf ), Rao's constant (R), Wada's constant (W), partial molar volume (VΦ) and Relaxation time for the solution of $KIO_3$ in $KH_2PO_4$ at 303.15 K and atmospheric pressure.

| m, mol kg–1 | ρ kg/m3 | η × 10–3 Ns m–2 | u, m s–1 | Z × 10–5, kg m–2 s–1 | β × 10-10, m2 N–1 | Lf × 10-11, m | Vf × 106 m3 mol–1 | R | W x 10-13 m5/7/N 1/7 | VΦ × 10–6, m3 mol–1 | Relaxation Time |
|---|---|---|---|---|---|---|---|---|---|---|---|
| 0.03 | 1003.91 | 0.8461 | 1520.8 | 15.267 | 4.307 | 4.307 | 1610.849 | 0.00182 | 1.283 | 2.880 | 4.859 |
| 0.06 | 1005.31 | 0.8516 | 1534.8 | 15.429 | 4.223 | 4.265 | 1811.086 | 0.00196 | 1.386 | 2.759 | 4.795 |
| 0.09 | 1007.11 | 0.8586 | 1547.5 | 15.585 | 4.146 | 4.226 | 1937.609 | 0.00206 | 1.450 | 2.629 | 4.747 |
| 0.12 | 1009.25 | 0.8669 | 1558.6 | 15.730 | 4.079 | 4.192 | 2018.936 | 0.00212 | 1.495 | 2.532 | 4.715 |
| 0.15 | 1011.76 | 0.8767 | 1571.4 | 15.899 | 4.003 | 4.152 | 2074.958 | 0.00216 | 1.527 | 2.446 | 4.679 |
| 0.18 | 1014.76 | 0.8879 | 1589.8 | 16.133 | 3.899 | 4.098 | 2121.895 | 0.00220 | 1.553 | 2.380 | 4.616 |
| 0.21 | 1016.25 | 0.8924 | 1596.3 | 16.222 | 3.862 | 4.079 | 2158.602 | 0.00223 | 1.572 | 2.320 | 4.595 |

**Table 3:** Molality (m), density (ρ), viscosity(η ),ultrasonic velocity (u), acoustic impedance (Z), adiabatic compressibility (β), intermolecular free length (Lf ), free volume (Vf ), Rao's constant (R), Wada's constant (W), partial molar volume (VΦ) and Relaxation time for the solution of $KIO_3$ in $KH_2PO_4$ at 308.15 K and atmospheric pressure.

| m, mol $kg^{-1}$ | ρ $kg/m^3$ | η × $10^{-3}$ Ns $m^{-2}$ | u, m $s^{-1}$ | Z × $10^{-5}$, kg $m^{-2}$ $s^{-1}$ | β × $10^{-10}$, $m^2$ $N^{-1}$ | Lf × $10^{-11}$, m | Vf × $10^6$ $m^3$ $mol^{-1}$ | R | W x $10^{-13}$ $m^{5/7}/N^{1/7}$ | VΦ × $10^{-6}$, $m^3$ $mol^{-1}$ | Relaxation Time |
|---|---|---|---|---|---|---|---|---|---|---|---|
| 0.03 | 1002.64 | 0.7672 | 1534.6 | 15.387 | 4.235 | 4.30 | 1865.751 | 0.00183 | 1.288 | 2.642 | 4.332 |
| 0.06 | 1004.01 | 0.7742 | 1555.3 | 15.615 | 4.118 | 4.250 | 2102.814 | 0.00197 | 1.392 | 2.547 | 4.250 |
| 0.09 | 1005.72 | 0.7824 | 1568.9 | 15.779 | 4.040 | 4.209 | 2243.369 | 0.00207 | 1.458 | 2.479 | 4.214 |
| 0.12 | 1007.75 | 0.7924 | 1581.6 | 15.939 | 3.967 | 4.171 | 2329.952 | 0.00213 | 1.503 | 2.413 | 4.191 |
| 0.15 | 1010.18 | 0.8042 | 1596.5 | 16.128 | 3.884 | 4.127 | 2386.204 | 0.00218 | 1.536 | 2.359 | 4.164 |
| 0.18 | 1012.93 | 0.8177 | 1610.8 | 16.316 | 3.805 | 4.085 | 2415.863 | 0.00222 | 1.561 | 2.298 | 4.148 |
| 0.21 | 1014.25 | 0.8224 | 1625.8 | 16.490 | 3.730 | 4.045 | 2474.348 | 0.00225 | 1.583 | 2.250 | 4.090 |

**Table 4:** Molality (m), density (ρ), viscosity(η ),ultrasonic velocity (u), acoustic impedance (Z), adiabatic compressibility (β), intermolecular free length (Lf ), free volume (Vf ), Rao's constant (R), Wada's constant (W), partial molar volume (VΦ) and Relaxation time for the solution of $KIO_3$ in $KH_2PO_4$ at 313.15 K and atmospheric pressure.

| m, mol $kg^{-1}$ | ρ $kg/m^3$ | η × $10^{-3}$ Ns $m^{-2}$ | u, m $s^{-1}$ | Z × $10^{-5}$, kg $m^{-2}$ $s^{-1}$ | β × $10^{-10}$, $m^2$ $N^{-1}$ | Lf × $10^{-11}$, m | Vf × $10^6$ $m^3$ $mol^{-1}$ | R | W x $10^{-13}$ $m^{5/7}/N^{1/7}$ | VΦ × $10^{-6}$, $m^3$ $mol^{-1}$ | Relaxation Time |
|---|---|---|---|---|---|---|---|---|---|---|---|
| 0.03 | 1000.99 | 0.6834 | 1558.1 | 15.596 | 4.115 | 4.289 | 2238.271 | 0.00184 | 1.295 | 2.442 | 3.750 |
| 0.06 | 1002.38 | 0.6902 | 1574.4 | 15.781 | 4.025 | 4.242 | 2508.292 | 0.00199 | 1.399 | 2.347 | 3.704 |
| 0.09 | 1004.07 | 0.7011 | 1591.9 | 15.984 | 3.930 | 4.191 | 2664.792 | 0.00208 | 1.466 | 2.267 | 3.674 |
| 0.12 | 1006.15 | 0.7128 | 1610.6 | 16.205 | 3.831 | 4.139 | 2766.668 | 0.00215 | 1.513 | 2.193 | 3.641 |
| 0.15 | 1008.55 | 0.7263 | 1623.5 | 16.374 | 3.762 | 4.101 | 2810.691 | 0.00220 | 1.546 | 2.113 | 3.643 |
| 0.18 | 1011.01 | 0.7419 | 1642.4 | 16.605 | 3.667 | 4.049 | 2837.329 | 0.00223 | 1.573 | 2.056 | 3.627 |
| 0.21 | 1014.65 | 0.7624 | 1665.6 | 16.900 | 3.553 | 3.985 | 2833.837 | 0.00226 | 1.594 | 2.000 | 3.611 |

**Table 5:** Masson( $\phi_V^0$, $S_v$, ) Moulik( M,K) Jone-Dole (A,B,) Roots(R,S) parameters of of $KIO_3$ in 1% $KH_2PO_4$ at different temperatures.

| Temperature K | Masson Constant | | Jone-Dole Parameters | | Moulik Parameters | | Roots Parameter | | 'β' values |
|---|---|---|---|---|---|---|---|---|---|
| | $\phi_V^0$ | $S_v$, | A ($dm^{3/2}mol^{-/2}$) | B/ ($dm^3.mol^{-1}$) | K | M | R | S | β |
| **298.15K** | 213.4 | -12.8 | 0.28 | 0.54 | 71.27 | 1.08 | 0.74 | -2.36 | 1.5 |
| **303.15K** | 213.7 | -12.64 | 0.3 | 0.47 | 80.91 | 1.07 | 0.73 | -2.31 | 1.7 |
| **308.15K** | 214.1 | -13.12 | 0.28 | 1.14 | 108.8 | 1.08 | 0.73 | -2.21 | 2.27 |
| **313.15K** | 214.9 | -12.20 | 0.29 | 1.16 | 142.7 | 1.07 | 0.59 | -2.36 | 2.96 |

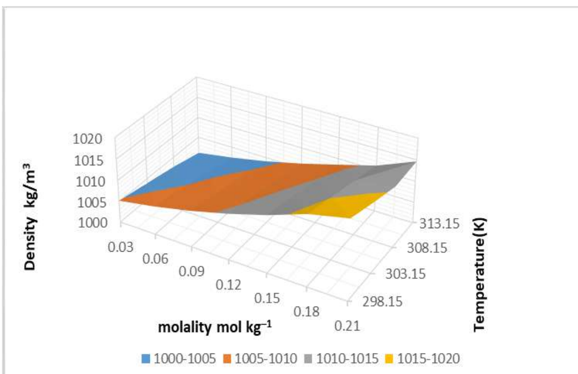


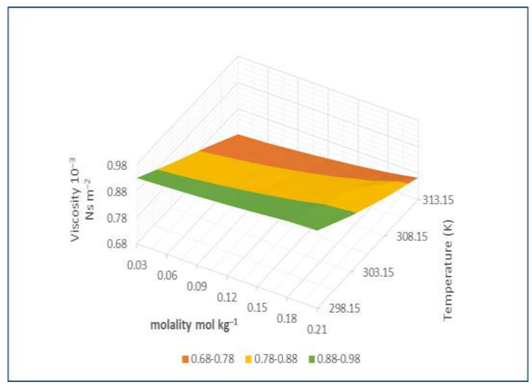


**Fig 1: 3-D plot of Density vs molality (*m* ) of** **Fig 2: 3-D plot of Viscosity vs molality (*m* )**
**$KIO_3$ in $KH_2PO_4$ at temperature 298.15 K,303.15 K,308.15 K and 313.15 K**

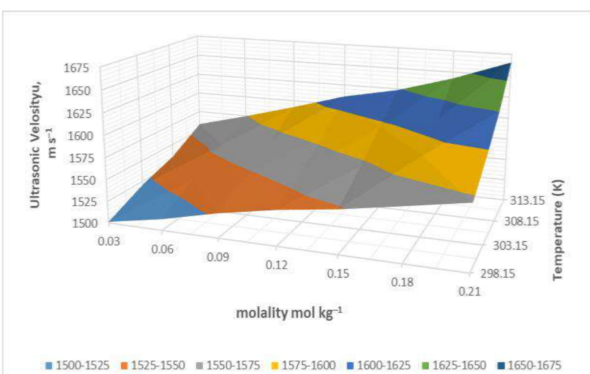


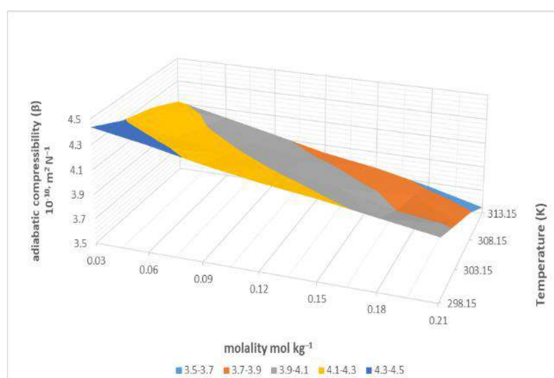


**Fig 3: 3-D plot of Ultrasonic Velosity vs molality (*m* )** **Fig 4: 3-D plot of adiabatic compressibility (β) vs molality (*m* )**

## References


Abraham, M., Acree, W., Fucaloro, A., & Zanella, A. (2017). Determination of molar refractions and Abraham descriptors for tris (acetylacetonato) chromium (III), tris (acetylacetonato) iron (III) and tris (acetylacetonato) cobalt (III). *New Journal of Chemistry,, 41*(23), 14259-14265. doi:10.1039/C7NJ02102J

Anji Babu , P., Omar Hattab , K., Aruna , I., & Mohan , R. (2017). COM PAR A TIVE STUDY OF PO TAS SIUM CHLO RIDE AND PO TAS SIUM CHLO RATE ON. *Progressive Research – An International Journal, 12*(03), 353-356.

Anupunt, P., & Sukhvibul, N. (2003). Lychee and longan production in Thailand. *In II International Symposium on Lychee, Longan, Rambutan and other Sapindaceae Plants, 665*, 53-60.

Banipal, P., Arti, S., & Banipal, T. (2016). Densities and Viscosities of Polyhydroxy Solutes in Aqueous Tetraethylammonium Bromide Solutions at Different Temperatures. *Journal of Chemical & Engineering Data, 61*(5), 1756-1776. doi:10.1021/acs.jced.5b00940

Bhujbal, R. C. (2019). Densitometric and Viscometric Study of Sodium Salicylate in Pure Water at Different Temperatures. *Current Pharma Research, 9*(2), 2824-2830. doi:DOI:10.33786/JCPR.2019.V09I02.015

Chauhan, S. P. (2016). Thermo-acoustical and optical studies of glycine and dl-alanine in aqueous furosemide solutions at different temperatures. *Journal of Molecular Liquids,, 221*, 755-762. doi:https://doi.org/10.1016/j.molliq.2016.06.025

Depeng Meng, P. X. (2017). Comparison of Foliar and Root Application of Potassium Dihydrogen Phosphate in Regulating Cadmium Translocation and Accumulation in Tall Fescue (Festuca arundinacea). *Water, Air, & Soil Pollution, 228*(3), 118. doi:https://doi.org/10.1007/s11270-017-3304-x

Dhingra, D., & Pandey, S. (2019). Effect of lithium chloride on the density and dynamic viscosity of choline chloride/urea deep eutectic solvent in the temperature range (303.15–358.15) K. *The Journal of Chemical Thermodynamics,, 130*, 166-172. doi:10.1016/j.jct.2018.10.003

Falkenhagen, H., & Dole, M. (1929). Viscosity of electrolyte solutions and its significance to the Debye theory. *Zeitschrift Für Physik, 30*, 611-616.

Ganjare, P. (2020). PREDICTION OF MOLECULAR INTERACTIONS IN LIQUIDS FROM DENSITY,. *Vidyabharati International Interdisciplinary Research Journal*, 479-499.

Gaware, M. R. (2021). Studies of molar refraction and polarizability constant of 6-(4-chlorophenyl)-1, 2, 3, 4-tetrahydro-2, 4-dioxopyrimidine-5-carbonitrile in 60% DMSO in the temperature range 298 to 313 K. *Indian Journal of Science and Technology,, 14*(2), 113-118. doi:10.17485/IJST/v14i2.2118

Gebreegziabher, T. &. (2017). Comparison of two sources of iodine delivery on breast milk iodine and maternal and infant urinary iodine concentrations in southern Ethiopia: A randomized trial. . *Food science & nutrition, 5*(4), 921-928. doi: https://doi.org/10.1002/fsn3.477

Harsh, K., Katal, A., & Sharma, P. K. (2020). Temperature-Dependent Thermodynamic Properties of Amino Acids in Aqueous Imidazolium-Based Ionic Liquid. *Journal of Chemical & Engineering Data, 65*(4), 1473-1487. doi:10.1021/acs.jced.9b00902

Hnedkovsky, L., Rasanen, L., Koukkari, P., & Hefter, G. (2020). Densities and Apparent Molar Volumes of Aqueous Solutions of Zinc Sulfate at Temperatures from 293 to 373 K and 0.1 MPa Pressure. *Journal of Chemical & Engineering Data, 66*(1), 38-44. doi:10.1021/acs.jced.

Huang, X., & Roth, C. B. (2016). Changes in the temperature-dependent specific volume of supported polystyrene films with film thickness. *The Journal of Chemical Physics, 144*(23), 234903.

Iwadate, Y., & Ohkubo, T. (2020). Densities and Refractive Indices of Molten Alkali Iodides: Estimation of Electronic Polarizability of an Iodide Ion. *Journal of Chemical & Engineering Data, 65*(11), 5240-5248. doi:10.1021/acs.jced.0c00411

Jagtap, V., Wadekar, M., & Hedaoo, D. (2017). Refractive Index, Density, Molar Refraction and Polarizability Constant of substituted1-phenyl-3-aryl-1H-pyrazol-4-carboxylic Acid Derivativesin Different Binary Mixture. *International Journal of Scientific Research in Science and Technology, 03*(08), 283-290.

Jones, G. &. (1929). The viscosity of aqueous solutions of strong electrolytes with special reference to barium chloride. *Journal of the American Chemical Society, 51*(10), 2950-2964.

Khan, J., Farooqui, M., & Quadri, S. (2011). VERIFICATION OF THE MOLAR REFRACTION AS AN ADDITIVE AND CONSTITUTIVE PROPERTY OF BINARY LIQUID MIXTURES OF WATER-ETHANOL AND BENZENE-ETHANOL. *Rasayan J Chem, 4*, 944-946.

Khan, S. N. (2017). Thermophysical properties of concentrated aqueous solution of N-methyldiethanolamine (MDEA), piperazine (PZ), and ionic liquids hybrid solvent for CO2 capture. *Journal of Molecular liquid, 229*, 221-229. doi:10.1016/j.molliq.2016.12.056

Kharat, S. J. (2010). Ultrasonic Velocity and Density Studies of Solutionsof Maleic Acid and Tartaric Acid in Waterat T = (298.15 and 308.15) K. *Int J Thermophys 31, 31*, 585–594. doi:DOI 10.1007/s10765-010-0736-6

Lomesh , S., Nathan, V., Bala , M., & Thakur, P. (2019). Volumetric and acoustic methods for investigating molecular interactions of antibiotic drug doxycycline hyclate in water and in aqueous solution of sodium chloride and potassium chloride at different temperatures (293.15–313.15) K. *Journal of Molecular Liquids, 284*, 241-251. doi:10.1016/j.molliq.2019.04.006

Lorentz, H. A. (1952). *Theory of Electrons* (2nd ed.).

Lu, X. X. (2020). Density, viscosity and electrical conductivity of alcohol solutions of 2, 2-diethyl-1, 1, 3, 3-tetramethylguanidinium bis (trifluoromethylsulfonyl) imide. *The Journal of Chemical Thermodynamics,, 151*, 106241. doi:10.1016/j.jct.2020.106241

Luo, L. N. (2018). Desuckering effect of KH2PO4 mixed with paclobutrazol and its influence on banana (Musa paradisiaca AA) mother plant growth. *Scientia Horticulturae, 240*, 484-491. doi:https://doi.org/10.1016/j.scienta.2018.06.033

Marcus, Y. .. (2015). *Ions in Solution and their Solvation.* John Wiley & Sons.

Mohabansi, N. P. (2020). Study of Excess Parameters and Partial Molar Volume for the Molecular Interactions of an aqueous 2-(tert-butylamino)-1-(3-chlorophenyl)Propan-1-one and NaCl Solution at Different Temperatures. *Journal of Scientific Research, 64*(2), 352-358. doi:10.37398/JSR.2020.640248

Mohamad, H., Wenil, S., & Cheng, Q. (2019). Modern pharmacological actions of Longan fruits. *Journal of Medicinal Plants Studies 2019;, 7*(4), 179-185. doi:10.5897/JMPR

Nikumbh, A., & Rathi, M. (2014). STUDY OF MOLAR REFRACTION AND POLARISABILITY CONSTANT OF AQUEOUS SOLUTIONS OF KCL AND KBRO3 AT DIFFERENT TEMPERATURES. *Int. J. Technical Res. Appl, 2*(6), 116-122. doi:10.21474/IJAR01/3872

Nikumbh, A., & Rathi, M. (2016). Densities, Viscosities and Apparent Molar Volumes of KClO3 in Water and Some Aqueous Electrolyte Solutions at Different Temperatures. *SSRG International Journal of Applied Chemistry (SSRG-IJAC), 3*(3), 1-6. doi:10.14445/23939133/IJAC-V3I5P102

Nori, T. S. (2019). Characteristic IR-acoustical analysis and surface tension variations in organic liquid mixtures at different temperatures. *Materials Today: Proceedings,, 18*, pp. 2060-2064.

Pandey , J., Misra , K., Shukla , A., & Mushran, V. (1987). Apparent molal volume, apparent molal compressibility, verification of jones-dole equation and thermodynamic studies of aqueous urea and its derivative. *Thermochimica Acta,, 117*, 245-259. doi:10.1016/0040-6031(87)88119-4

Paranthaman, R. M. (2021). Development and Validation of a Screening Method for Simultaneous Detection of KBrO3 and KIO3 in Baking Ingredients and Additives Using Powder XRD. Journal of Food Composition and Analysis,. *Journal of Food Composition and Analysis,, 102*, 104007. doi:https://doi.org/10.1016/j.jfca.2021.104007

Prutton, Samuel , H., Maron , H., & Carl , F. (1972). *'Principle of Physical Chemistry'.* Amerind publishing Co. Pvt.Ltd.

Rahman, W. M. (1988). Refractive index of solutions at high concentrations. *Applied optics,, 27*(16), 3341-3343. doi:10.1364/AO.27.003341

Rathi, M., & Nikumbh, A. (2019). INTERACTIONS OF KIO3 IN AQUEOUS 0.1%. *Journal of Emerging Technologies and Innovative Research, 6*(1), 167-175.

Raundal, P. G. (2021). STUDY THE TEMPERATURE EFFECT ON APPARENT MOLAR VOLUMES AND VISCOSITY (JONES DOLE COEFFICIENT) OF MAGNESIUM SULPHATE, ALUMINIUM AMMONIUM SULPHATE AND POTASSIUM ALUMINIUM SULPHATE IN BINARY MIXTURE OF AQUEOUS DMF AND AQUEOUS DMSO. *Journal of Advanced Scientific Research, 12*(1), 99-105.

Reddy, S. S. (2016). The study of solute–solvent interactions in 1-ethyl-3-methylimidazolium ethylsulfate+ 2-ethoxyethanol from density, speed of sound and refractive index measurements. *Journal of Molecular Liquids, 218*, 83-89. doi:10.1007/s10973-015-5205-9

Reena Roy, S. M. (2018). Acoustic Data on Molecular Interactions in Mixtures of Nitromethane and Nitroethane in Acetone at 303–318 K. *Russian Journal of Physical Chemistry A, 92*, 2606–2611. doi:https://doi.org/10.1134/S0036024418130253

Ritesh R. Naik, S. V. (2015). Acoustical studies of molecular interaction in the solution of propranolol hydrochloride drug at different temperatures and concentrations. *Russian Journal of Physical Chemistry A volume, 89*, 2149–2154. doi:https://doi.org/10.1134/S003602441511014X

Roy, M., Dakua, V. K., & Sinha, B. (2007). Partial Molar Volumes, Viscosity B-Coefficients, and Adiabatic Compressibilities of Sodium Molybdate in Aqueous 1,3-Dioxolane Mixtures from 303.15 to 323.15 K. *Int J Thermophys, 28*, 1275–1284. doi:10.1007/s10765-007-0220-0

Sano, H., & Tachiya, M. (1979). Partially diffusion-controlled recombination. ,. *The Journal of Chemical Physics, 71*(3), 1276-1282. doi:10.1063/1.438427

Sawale, R. T. (2016). Molar Refraction and Polarizability of Antiemetic drug 4-amino-5-chloro-N-(2-(diethylamino) ethyl)-2 methoxybenzamide hydrochloride monohydrate in {Aqueous-Sodium or Lithium Chloride}Solutions at 30oC. *Journal of Applied Pharmaceutical Science,, 6*(03), 120-124. doi:10.7324/JAPS.2016.60321

Saxena, R. P. (2015). Introduction of ultrasonic interferometer and experimental techniques for determination of ultrasonic velocity, density, viscosity and various thermodynamic parameters. *International Journal of Applied Research, 1*(9), 562-569.

Shakeel, M., & Mahmood, K. (2020). Use of Masson's and Jones–Dole equations to study different types of interactions of three pharmacologically important drugs in ethanol. *Journal of the Chinese Chemical Society, 67*(9), 1552-1562. doi:10.1002/jccs.202000128

Shoup, D. A. (1981). Diffusion-controlled bimolecular reaction rates. The effect of rotational diffusion and orientation constraints. *Biophysical Journal, 36*(03), 697-714.

Snyder, S. A. (2006). "Perchlorate and chlorate in dietary supplements and flavor enhancing ingredients. *Analytica Chimica Acta, 567*(1), 26-32.

Spitzer , J., Singh, P., & Olofsson., I. (1978). Apparent molar heat capacities and volumes of aqueous electrolytes at 25°C: Cd(ClO4)2, Ca(ClO4)2, Co(ClO4)2, Mn(ClO4)2, Ni(ClO4)2, and Zn(ClO4)2 . *J Solution Chem, 7*, 623-630. doi:10.1007/BF00646039

Tank , P., Sharma , R., & Sharma, A. (2019). Viscometric Studies of Cu (II) surfactants derived from mustard oil in benzene at 303.15 K. Tenside Surfactants Detergents. *56*(2), 158-163. doi:10.3139/113.110601

Ultrasonic Velocity and Density Studies of Solutions of Maleic Acid and Tartaric Acid in Water at T = (298.15 and 308.15) K. (2010). *nt J Thermophys, 31*, 585–594. doi:DOI 10.1007/s10765-010-0736-6

Zhang , C., Xiao, S., Shen, Z., & Li, R. (2020). Effects of oxidation treatment by KClO 3/H 2 SO 4 systems on the chemical, crystal and microscopic structures of polyacrylonitrile fibers. ,. *New Journal of Chemistry, 44*(19), 7876-788. doi:10.1039/d0nj00442a

IJCSPUB.ORG ISSN : 2250-1770
INTERNATIONAL JOURNAL OF CURRENT SCIENCE (IJCSPUB)
IJCS PUBLICATION (IJCSPUB.ORG) An International Open Access, Peer-reviewed, Refereed Journal

# Synthesis and Characterization of Novel thiocarbohydrazide Derivatives of Disubstituted N,N-Dimethylaminomaleimides

**Sunita A. Chaudhari (Patil)[1]*, Vasant M. Patil[2], Satish M. Chavan[3], Sambhaji V. Patil[4], Vishwanath R. Patil[2]**
*[1]Directorate of Forensic Science Laboratory, Vidya Nagari Kalina, Mumbai-400098 to the Government, Home Department, Maharashtra State, India.
[2]Department of Chemistry, University of Mumbai, Kalina Campus, Vidya Nagari, Mumbai- 400098, Maharashtra, India.
[3]Department of Chemistry, R.N.C. Arts, J.D.B. Commerce & N.S.C. Science College, Nashik Road, 422101, Maharashtra, India.
[4]Maratha Vidya Prasarak Samaj's Arts, Science and Commerce College, Ozar (Mig), Tal-Niphad, Dist-Nashik, Maharashtra, India

***Abstract:*** The compound 1a-c was reacted with bromine in DMF to obtained dibromo succinimide **2a-c**. The compound **2a-c** were reacted with *N,N*-dimethyl amine as a base followed by dehydrohalogenation to obtain 3-bromo-1-(4-chlorophenyl)-1H-pyrrole-2,5-dione **3a-c** as an intermediate compound, further on Vilsmeier Haack formylation afforded compound **4a-c** with good yields. The condensation of 1-(4-halophenyl)-4-(dimethylamino)-2,5-dihydro-2,5-dioxo-1H-pyrrol-3-carbaldehyde **4a-c** with thiocarbohydrazide hydrochloride in ethanol in presence of acetic acid furnished compound **5a-c** with 78 % yield. All the synthesized compounds were well characterised by spectral and analytical techniques. The synthesised compounds were evaluated for their insecticidal activity.

***Keywords*:** Dibromosccinimide, *N,N*-dimethylamine, Vilsmeier Haack formylation, thiocarbohydrazide

## I. Introduction

Maleimide and its derivatives are synthesized from maleic anhydride and amines followed by dehydration [1]. Maleimides are an important class of substrates for biological and chemical applications. In biological applications they are used as chemical probes of protein structure [2], as immunoconjugates for cancer therapy [3] or as new herbicides and pesticides [4]. Cyclic imide [5, 6] shows potent analgesic action. Kalgutkar et al. [7] have demonstrated that some N-substituted maleinimides inhibit the prostaglandin endoperoxide synthase (PGHS). Frederic Zentz et. al [8] reported the in vitro antibacterial and cytotoxic activities of 3-substituted succinimides. Maleimides shows a wide range of biological activities such as antibacterial and antifungal [9], antiprotozoal [10], antiangiogenic [11], analgesic [12], antistress agents [13], cytotoxic, DNA binding and apoptotic inducing activity [14]. Thiocarbohydrazone [15] is the closest structural analogue of thiosemicarbazone. Thiocarbohydrazide is the hydrazide derivatives of thiocarbonic acid. Thiocarbohydrazide is seen to be the final member of the structural sequence thiourea, thiosemicarbazide [16], thiocarbohydrazide [17], and to have close links with thiocarbamic [18] and thiocarbazic acids [19] Thiocarbohydrazide derivatives have attracted much attention in recent years due to their application in the synthesis of heterocyclic compounds [20], synthesis of transition metal complexes [21], and pharmacological studies [22]. Such moiety shows biological activities like antibacterial, antifungal, cytotoxicity, anti-inflammatory, analgesic, antitubercular and antiviral activities. [23]. The derivatives of which are recommended as effective antitubercular antiviral properties. Thiocarbohydrazides of the aromatic series exhibits high antiviral and antimicrobial activity [24].

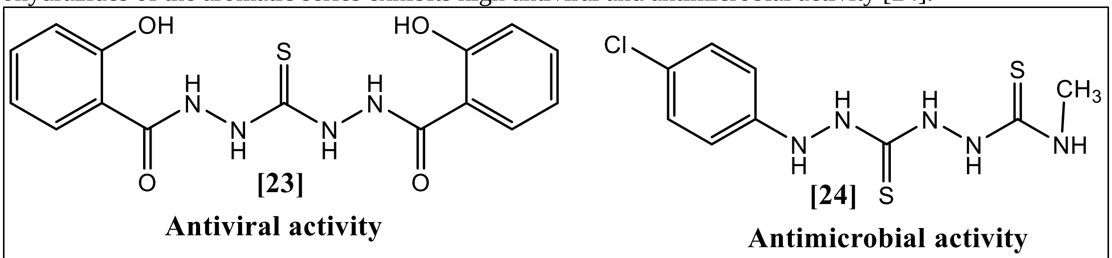

**[23]** **Antiviral activity** **[24]** **Antimicrobial activity**

## II MATERIALS AND METHODS:

Melting points were determined on a Gallenkamp melting point apparatus, Mod.MFB-595 in open capillary tube and are uncorrected. FT-IR spectra were recorded on Schimadzu FTIR-408 instrument in KBr pellets. $^{1}$H and $^{13}$C spectra were recorded on Varian XL 500 spectrometer (500MHz) in CDCl3and DMSO. Chemical shifts are reported in ppm with respect to tetra methyl silane as an internal standard. Elemental analyses were carried out on Hosli CH analyzer and are within ± 0.4 of theoretical percentages. The progress of the reaction was monitored by thin layer chromatography (TLC, 0.2 mm silica gel 60 F254, Merck plates) and visualized using UV light (254 and 366 nm) for detection. All commercial grade chemicals were purchased from S.D. Fine Chemicals, India and used without further purification while solvents were purified by standard literature procedures.

## III RESULTS AND DISCUSSION:

The compound **1a-c** were reacted with bromine in DMF at 25-27 $^{0}$C for 1- 3 hrs. to obtained trans 3,4-dibromo-1-(4-halophenyl)-1H-pyrrole-2,5-diones **2a-c**. The compound was reacted with *N*,*N*-dimethyl amine as a base followed dehydrohalogenation afforded 1-(4-halophenyl)-3-(dimethylamino)-1H-pyrrole-2,5-dione **3a-c**.Installation of an amino functionality at C-3 position in **3a-c** should increase nucleophilicity at C-4 position. The compound 1-(4-halophenyl)-3-(dimethylamino)-1H-pyrrole-2,5-dione **3a-c** on Vilsmeir Haack Formylation with bromine in DMF at 0$^{o}$C for 30 min. to furnished compound 1-(4-halophenyl)-4-(dimethylamino)-2,5-dihydro-2,5-dioxo-1H-pyrrole-3-carbaldehydes **4a-c** with good yield**. (Scheme-1).**

Further condensation of 1-(4-halophenyl)-4-(dimethylamino)-2,5-dihydro-2,5-dioxo-1H-pyrrole-3-carbaldehydes **4a-c** with thiocarbanohydrazide hydrochloride in ethanol in presence of acetic acid at 50$^{o}$C furnished orange coloured solid compound (1E)-1-((1-(4-halophenyl)-4-(dimethylamino)-2,5dihydro-2,5-dioxo-1*H*-pyrrole-3-yl)methylene)thiocarbohydrazide **5a-c** with 78 % yield. [25] All the synthesized compounds were well characterized by spectral and analytical techniques. **(Scheme 2)**

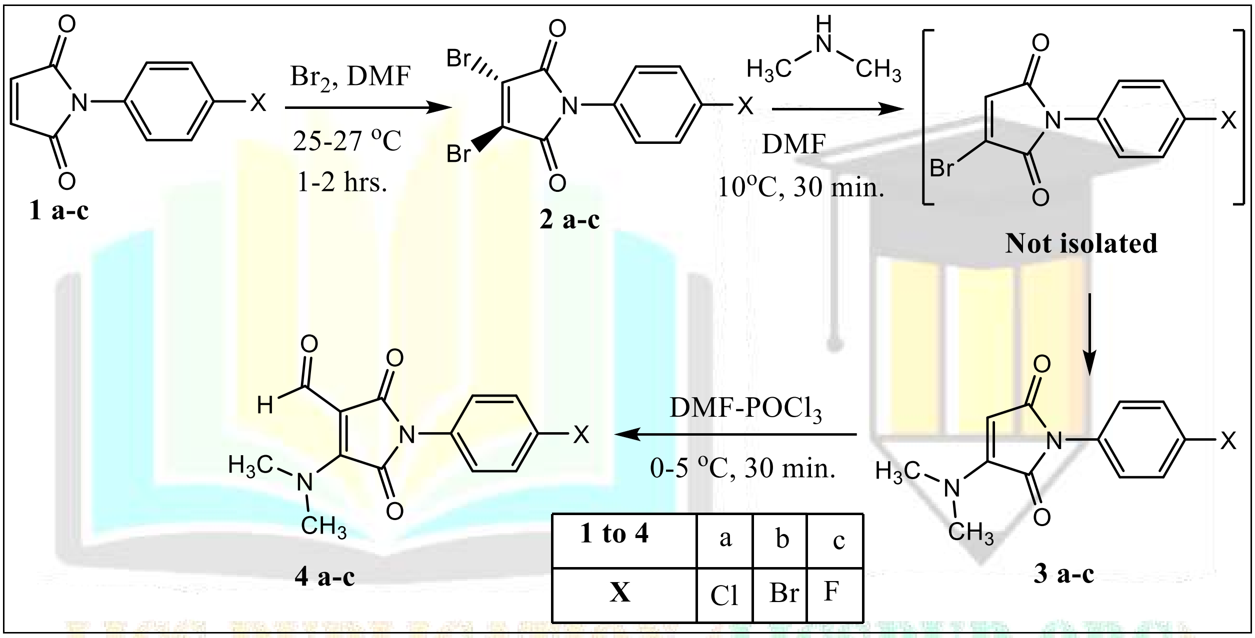


| 1 to 4 | a | b | c |
|---|---|---|---|
| X | Cl | Br | F |

**Scheme 1: Synthesis of substituted 2,5-dihydro-2,5-dioxo-1H-pyrrole-3-carbaldehydes, 4a-c**

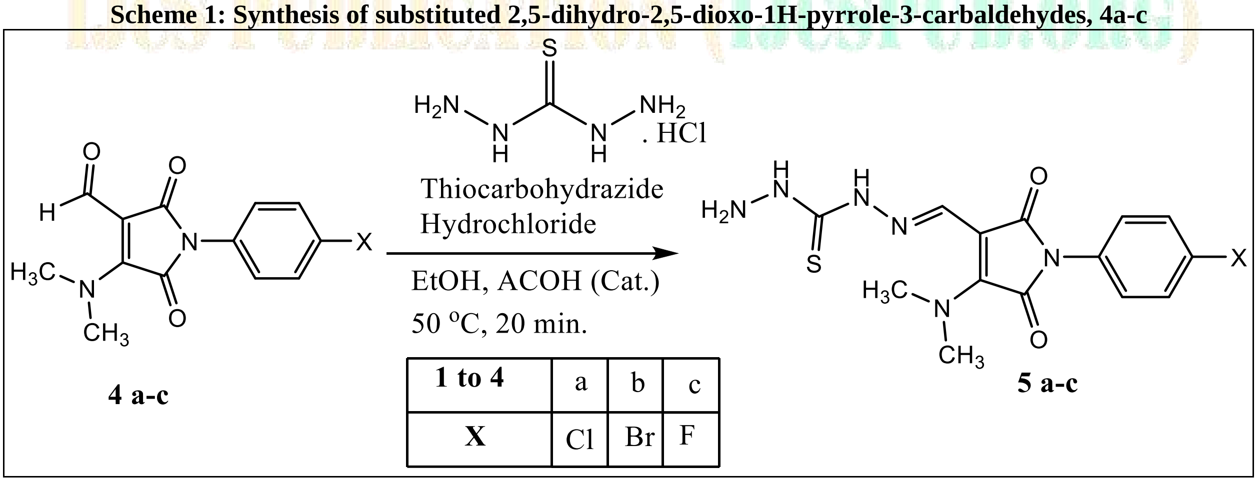


| 1 to 4 | a | b | c |
|---|---|---|---|
| X | Cl | Br | F |

**Scheme 2: Substituted 2,5dihydro-2,5-dioxo-1*H*-pyrrole-3-yl)methylene)thiocarbohydrazide, 5a-c**

The IR spectra of **4a** showed the characteristics conjugated aldehyde carbonyl stretching frequency at 1708-1711 cm-1, (C-Cl) stretching at 1619-1630 cm$^{-1}$ and (H-C=O) at 2782- 2795 cm-1. The 1H NMR spectrum ($CDCl_3$) of this solid showed broad singlet at 3.83 δ for six protons of two methyl group. The multiples appeared at 7.25-7.60 δ corresponded to four aromatic proton of benzene ring and a broad singlet at 9.73 δ corresponding to a proton of H-C=O group. $^{13}$C NMR spectrum ($CDCl_3$) of this solid showed singlet at 41.7 and 51.9 δ corresponded to the carbon of two methyl group. The aromatic carbon appears at their respective position. The signal appeared at 165.68 and 169.80 δ corresponded to two carbonyl carbon of amide group. The signal appeared at 183.30 δ corresponded to carbonyl carbon of aldehyde.

The compound **5a** obtained was characterized by spectral and analytical data. The orange solid showed sharp bands at 1758, 1697, 3393, 3385, 1613 & 1278 cm$^{-1}$ corresponding to C=O, C=O, N-H, N-H, C=N and C=S respectively in its IR spectrum. The $^{1}$H NMR spectrum (DMSO-$d_6$) of this solid showed broad singlet at 3.68 δ for six protons of two methyl group. The broad singlet appeared at 3.45 δ corresponded to two protons of $-NH_2$ group. The singlet at 7.18 δ for one proton of N=C-H group and singlet appeared at 8.20 δ corresponded to two proton of $-NH_2$ group. The doublet appeared at 7.41 δ and 7.60 δ corresponded to four aromatic proton of benzene ring and a broad singlet at 11.55 δ and 11.23 δ corresponding to a proton of two N-H group. The $^{13}C$ NMR spectrum (DMSO-$d_6$) of this solid showed signal at 44.80 and 53.7 δ corresponded to the carbon of two methyl group. The aromatic carbon appears at their respective position. The signal appeared at 163.28 and 169.55 δ corresponded to two carbonyl carbon of amide group. The peak appears at 178.25 δ corresponded to carbonyl carbon of thiocarbamide.

## IV EXPERIMENTAL:

***General procedure for synthesis of 4a-c:***

1-(4-halophenyl)-1H-pyrrole-2,5-dione **1a-c** (0.01 mol) in DMF (8mL) was vigorously stirred at room temp. The mixture of bromine (0.011mol) in DMF was added drop wise at 25 ºC and stirred for 1-3 hrs. with constant stirring, white solid separated was then filtered, washed with cold water, dried and recrystalised using ethanol to obtain compound **2a-c.** [25]

To a solution of trans-3,4-dibromo-1-(4-halophenyl)pyrrolidine-2,5-dione **2a-c** (0.01mol) in DMF (10 mL), N,N-dimethylamine (0.03 mol) was added drop wise at 10 $^0$C and stirred for 30 min. The reaction mixture was poured over crushed ice. The golden yellow solid separated was filtered and recrystalized from ethanol to obtained compound **3a-c** respectively.[26]

Vilsmeier Haack adduct prepared from DMF (0.012 mol) and $POCl_3$ (0.05 mol) at 0ºC was added to a solution of **3a-c** (0.01 mol) in 2ml DMF, reaction mixture was then stirred at 0-5ºC for 30 min. The reaction mixture was poured into cold water. The yellow product separated on neutralization with aqueous $NaHCO_3$ solution was filtered, washed with cold water, dried and purified by column chromatography, to obtained compound **4a-c** respectively.[27]

***Synthesis of 1-(4-chlorophenyl)-4-(dimethylamino)-2,5-dihydro-2,5-dioxo-1H-pyrrole-3-carbaldehydes, 4a***

M.P. (ºC):187-189, Yield (%):83, Color: Yellow solid; IR(KBr)( ν): 2795, 2782, 1711, 1708, 1630, 1619 $cm^{-1}$;$^1$H NMR ($CDCl_3$) δ:3.83(S,6H,2 xCH3 ), 7.25- 7.60(m,4H,Ar-H),9.73(S, 1H, CHO),$^{13}$C NMR ($CDCl_3$) δ:41.70, 51.90, 57.77, 97.18, 127.71(2C,S), 129.23(2C,S), 133.91, 148.06, 165.68, 169.80,183.30, MS(m/z,%); 294 [M+] and 296 [M+2]; *Analysis Calculated for* $C_{13}H_{11}ClN_2O_2S$ Calcd: C(56.45),H(3.97),N (10.26),Found: C(55.64), H(4.51),N(11.68).

***Synthesis of 1-(4-bromophenyl)-4-(dimethylamino)-2,5-dihydro-2,5-dioxo-1H-pyrrole-3-carbaldehydes, 4b***

M.P. (ºC):194-196, Yield (%): 81, Color: Yellow solid; IR(KBr)( ν):2888, 2790, 1785, 1737, 1675 $cm^{-1}$;$^1$H NMR ($CDCl_3$) δ:3.71( S, 6H, 2 x CH3 ),7.25- 7.55(m, 4H, Ar-H), 9.83(S, 1H, CHO),$^{13}$C NMR ($CDCl_3$) δ: 45.60, 50.10, 57.78, 97.66, 126.90(2C,S) 129.43(2C,S) 133.70, 148.60, 163.85,169.88, 185.10,MS (m/z,%); 339 [M+] and 341 [M+2]; Analysis Calculated for $C_{13}H_{11}BrN_2O_2S$; Calcd: C(48.32), H(3.43), N (8.67), Found: C(48.08), H(3.63), N(8.86).

***Synthesis of 1-(4-flurophenyl)-4-(dimethylamino)-2,5-dihydro-2,5-dioxo-1H-pyrrole-3-carbaldehydes, 4c***

M.P. (ºC):176-178, Yield (%): 84, Colour: Yellow solid; IR (KBr) ( ν):2878, 2780, 1780, 1727, 1673 $cm^{-1}$, $^1$H NMR ($CDCl_3$)δ:3.73(S,6H,2 x CH3 ),7.20- 7.50(m,4H,Ar-H), 9.81(S, 1H,CHO),$^{13}$CNMR($CDCl_3$) δ 42.60, 48.70, 58.73, 98.16, 126.70 (2C,S), 129.63 (2C,S), 133.90, 148.20, 163.45, 169.58, 182.10, MS (m/z,%): 277 [M+] and 279 [M+2]; Analysis Calculated for $C_{13}H_{11}FN_2O_2S$ Calcd: C(47.37),H(3.51),N (8.61),Found: C(49.08), H(3.65),N(8.89).

***General procedure for synthesis of (5a-c)***

The compound **4a-c (**0.01mol) in ethanol (10ml), catalytic amount of acetic acid was added. The reaction mixture was stirred for 20 min. till we get clear solution. To this mixture thiocarbohydrazide hydrochloride solution (0.01mol) was added while stirring. The temperature of reaction mixture was maintained at 50 $^0$C for 20 min. The orange solid separate out; the solid separated was collected and then filtered to afford compounds **5a-c** respectively.[28]

***Synthesis of 1-((1-(4-chlorophenyl)-4-(dimethylamino)-2,5-dihydro-2,5-dioxo-1H-pyrrole-3-yl) methylene)thiocarbohydrazide, 5a***

M.P. (ºC):188-189, Yield (%):76, Colour: Orange solid; IR(KBr)(ν): 1755, 1699, 3391, 3388, 1618, 1276 $cm^{-1}$;$^1$H NMR (500MHz,DMSO-$d_6$) δ:3.68( S,6H,2 x CH3 ),7.18(S,1H,=C-H),7.41-7.60(dd,4H,Ar-H), 8.20(S,2H,NH2), 3.45(bs,1H,N-H), 3.41(bs,1H,N-H) ppm; $^{13}$C NMR (125 MHz,DMSO-$d_6$) δ:44.80, 53.70, 97.83,127.75(2C,S) 129.53(2C,S), 129.76, 133.96,148.26,163.28, 169.55, 178.25 ppm MS(m/z,%); 366[M+] and 368[M+2], Analysis Calculated for $C_{14}H_{15}ClN_6O_2S$ Calcd: C(50.08),H(4.20),N (20.86),Found: C(49.86), H(4.43),N(21.03)

***Synthesis of 1-((1-(4-bromophenyl)-4-(dimethylamino)-2,5-dihydro-2,5-dioxo-1H-pyrrole-3-yl) methylene)thiocarbohydrazide, 5b***

M.P. ($^0$C):202-204, Yield (%): 74, Color: Orange solid; IR (KBr) (ν): 1763,1695 ,3389, 3392, 1644, 1278 $cm^{-1}$; $^1$H NMR (500MHz,DMSO-$d_6$) δ:3.78( S, 6H,2 x CH3 ), 7.18 (S, 1H,=C-H),7.40-7.55(dd, 4H, Ar-H), 8.28(S, 2H, NH2), 11.53 (bs,1H,N-H)ppm, 11.50 (bs,1H,N-H)ppm $^{13}$C NMR (125 MHz,DMSO-$d_6$) δ:47.65, 56.09, 97.56, 127.46(2C,S) 129.66(2C,S), 129.68, 133.91, 148.36, 163.56, 169.57, 182.82 ppm MS(m/z,%); 411[M+] and 413[M+2], Analysis Calculated for $C_{14}H_{15}BrN_6O_2S$ Calcd: C(50.58), H(4.34), N (22.82), Found: C(48.88), H(4.46),N(21.66)

***Synthesis of 1-((1-(4-fluorophenyl)-4-(dimethylamino)-2,5-dihydro-2,5-dioxo-1H-pyrrole-3-yl) methylene)thiocarbohydrazide, 5c***

M.P. (ºC):180-182,Yield (%): 78, Colour: Orange solid; IR (KBr) (ν): 1755, 1688, 3378, 3383, 1635, 1288 $cm^{-1}$; $^1$H NMR (500MHz,DMSO-$d_6$) δ: 3.81( S,6H,2 x CH3 ),7.23(S, 1H,=C-H), 7.36-7.53(dd, 4H, Ar-H), 8.25(S, 2H, NH2), 11.21 (bs, 1H, N-H) ppm, 11.36(bs, 1H, N-H) ppm; $^{13}$C NMR (125 MHz,DMSO-$d_6$) δ:46.56, 51.09, 97.85, 127.71(2C,S), 129.23(2C,S), 129.63, 133.91, 148.06, 163.58, 169.51, 182.12 ppm MS(m/z,%); 349[M+] and 351[M+2]; Analysis Calculated for $C_{14}H_{15}FN_6O_2S$ Calcd: C(50.08),H(4.20),N (20.86),Found: C(49.86), H(4.43),N(21.03)

## V CONCLUSION:

Herein we synthesized novel thiocarbohydrazone derivatives of disubstituted *N,N*-dimethyl maleimides with 78 % yield. The main advantage of our protocol are clean, easy operational and simplicity of reaction. Here we describe the synthesis of thiocarbohydrazide derivatives of 1-(4-halophenyl)-4-(dimethylamino)-2,5-dihydro-2,5-dioxo-1H-pyrrole-3-carbaldehydes **4a-c** by nucleophilic condensation of 1-(4-halophenyl)-3-(dimethylamino)-1H-pyrrole-2,5-dione **3a-c** by Vilsmeier Haack Formylation. The compound 1-(4-halophenyl)-4-(dimethylamino)-2,5-dihydro-2,5-dioxo-1H-pyrrole-3-carbaldehydes **4a-c** were further reacting with thiocarbohydrazide hydrochloride to obtained thiocarbohydrazones (1E)-1-((1-(4-halophenyl)-4-(dimethylamino)-2,5dihydro-2,5-dioxo-1*H*-pyrrole-3-yl)methylene)thiocarbohydrazide **5a-c** with good yield. All the synthesized compounds were well characterized by spectral and analytical techniques and are new addition to the family of heterocyclic compounds.

## VI ACKNOWLEDGMENT:

Authors are thankful to M.V.P.Samaj's and Principal K. T. H. M. College, Nasik and Hon. Dean, faculty of Chemistry, University of Mumbai for infrastructural facilities. We also thankful to Hon. Shri. Sandeep Bishnoi, IPS (Director of General- Legal and Technical) and Dr. Mrs. S. V. Ghumatkar ( Joint-Director and I/C Director), Directorate of forensic science laboratory, Vidynagari, Kalina, Mumbai for continuous support and encouragement.

## VIII REFERENCES

[1] M. P. Cava, A. A. Deana, K. B. Muth & M. *J.* Mitchell, **1973,** *Org. Synthesis*,**,** *5***,** 944.
[2] J. E. Corrie, **1994**, *J. Chem. Soc. Perkin Trans. 1*, 29-75
[3] K. D. Janda, J. A. Ashley, T. M Jones, D. A. McLeod, D. M. Schloeder, & M. I. Weinhouse, 1 9 9 0 , *J. Am. Chem. Soc.* , 112, 8886.
[4] G. Matocsy, M. Nadasi, V. Adriska. *Pesticide Chemistry, Akademiai Kiadó, Budapest* **1988 ,** 675- 689
[5] A. D. Andricopulo, A. W. Filho, R. A. Correˆ a, A. Santos, R. J. Nunes, R. A. Yunes, V. Cechinel Filho, *Pharmazie*, **1998**, *53*, 493- 494.
[6] V. C. Filho, T. Pinheiro, R. J. Nunes, R. A. Yunes, E. Queiroz, E. O. Lima, *Quı´mica Nova*, **1996**, *19*, 590-593.
[7] A. S. Kalgutkar, B. C. Crews, L. J. Marnett,1996,*J. Med. Chem.*, *39*, 1692-1703.
[8] F. Zentz , R. L.Guillou , R. Labia, D. Sirot, B. Linard, A. L. Valla, 2004,*Farmaco, II,* 59, 879–886.
[9] S.N. Lopez, M. Sortino, A. Escalante, F. Campos, R. Correa, V. C. Filho, R.J. Nunes, S.A. Zacchino, A. Forsch. 2003, *Drug. Res. Chem. Abstr*., 53, 280-288.
[10] Y. Durust, H. Karakus, M. Kaiser, D. Tasdemir,2012, *Eur. J. Med. Chem.*, *48,* 296-304.
[11] N. Acero, M.F. Brana, L. Anorbe, G. Dominguez, D. Munoz-Mingarro, F. Mitjans, J. Piulats, 2012, *Eur. J. Med. Chem*. 48, 108-113.
[12] F. Mahle, T. Guimaraes, A. Meira, R. Correa, R. Cruz, R. Nunes, V. Cechinel-Filho, F.Campos-Buzzi, 2010, *Eur. J. Med. Chem*, 45, 4761-4768.
[13] R. Badru, P. Anand, B. Singh, 2012, *Eur. J. Med. Chem*. 48, 81-91.
[14] A. Alaa , M. A. Aziz, 2007, *Eur. J. Med. Chem*. 42, 614-626.
[15] A. B. Aly, E. E. Brown, M. Ashraf, E. Mohamed and R.Mohamed, 2009, *ARKIVOC*, 1,150-197.
[16] L. F. Audrieth, E. S. Scott, and P. S. Kippur, 1954, *J. Org. Chem.*,19, 733.
[17] L. F. Audrieth and B. A. Ogg,1951, *"The Chemistry of Hydrazine," John Wiley and Sons, Inc., New York, N. Y.***,** , 213.
[18] R. G. Dubenko and P. S. Pelkis, *Zh.1963, Obshch. KHm.*, 33, 290.
[19] E. P. Nesynov and P. S. Pelkis, 1964, *Ibid.*,34, 2672.
[20] M. S. Chande, M. A. Pankhi, S. B. Ambhaikar, 2000, *Indian J. Chem.* 39B, 603.
[21] O. V. Mikhailov, M. A. Kazymova, T. A. Shumilova, G. A. Chmutova, S. E. Solovieva, 2005, *Transition Met. Chem*. 30, 299.
[22] M. M. Suni, V. A. Nair, C. P. Joshua,2001, *Tetrahedron*, 57, 2003.
[23] M. J. Pal, N. K. Sharma & K. K. Jha.,2011, *Jor. Adv. Sci Res***,** 2,2, 35-44.
[24] K. Marina , M. Anastssia, M. Panagiotis , P. Nicole, P. G. Spyroula, P. Christophe, W. Myriam W, D. C. Erik,2002 *Farmaco***,** 57, 253 257
[25] A. I. Vogel, Textbook of Practical Organic Chemistry, 4th Edition, ELBS and Longman, London, **1978.**
[26] Patil N. S.; Deshmukh G. B.; Mahale K.M.; Gosavi K. S. and Patil S. V.,2015, Ind. J. Chem. 54B, 2:272-78.
[27] Chaudhari (Patil) S.A., Patil V. M., Chavan S, Dingore K, Patil S. V., Toche R. B., Jachak M. N., 2016, J.Pharm, Chem. Bio. Sci, 4(2): 262-270.
[28] S. A. Chaudhari (Patil), V. M. Patil, S. M. Chavan, S. V. Patil, V. R. Patil 2020, WJPR, 9(11), 910-918
[29] S. A. Chaudhari (Patil), V. M. Patil, K. A. Mahale, S. V. Patil, V. R. Patil, 2022, WJPR,11(1), 1306-1314

International Journal of Advance and Applied Research (IJAAR)
Peer Reviewed Bi-Monthly
ISSN – 2347-7075
Impact Factor –7.328
Vol.2Issue-13May-Jun2022

# पर्यावरणवादी इतिहास लेखन: एक अभ्यास

**सहा,प्रा.सौ.नंदिनी देशमुख[1] डॉ.शशिकांत गोकुळ साबळे[2]**

[1]आर.एन.सी.आर्ट्स,जे.डी.बी.कॉम. एन.एस.सी.सायन्स कॉलेज नाशिकरोड, नाशिक

[2]आर.एन.सी.आर्ट्स,जे.डी.बी.कॉम. एन.एस.सी.सायन्स कॉलेज नाशिकरोड, नाशिक

Email: nandinibdeshmukh.24@gmail.com

Email-sabale.uma@gmail.com

घोषवारा :

नैसर्गिक आपत्तीमुळे मानवी जीवन त्याचबरोबर जीवनमूल्ये स्थावर संपत्ती आणि सामाजिक नियमांचे देखील हानी होते. त्यामुळे पर्यावरण वादी इतिहासात एक नवीन दृष्टी ने आपण निसर्गाला, राज्याकडे व समाजाकडे वेगळया दृष्टिकोनातून पाहू शकतो. इतिहास ही जरी स्वतंत्र ज्ञानशाखा असली तरी इतिहास लेखन करताना अनेक सामाजिक व शास्त्रीय शाखेचा संबंध येतो. इतिहासाच्या अभ्यासात भूगोल या ज्ञान शाखेची महत्त्वाची भूमिका आहे.स्थळ व काळ ही इतिहासाची प्रमुख परिणामे आहेत. नैसर्गिक स्थिती पर्वत, नद्या, हवामान, जंगले, समुद्र इत्यादी घटक मानवी जीवनाचे स्वरूप बदलतात.इतिहास लेखनातील नवीन विचार प्रवाह म्हणजे पर्यावरणवादी इतिहास 'एन्व्हायरमेंटल हिस्ट्री' याचा अभ्यास केला जाणार आहे. सद्यस्थितीत नैसर्गिक हानी जी मानवाकडून होत आहे याची फार महत्त्वाची भूमिका मानवी जीवनात प्रवासात ठरते.

बीज शब्द : पर्यावरणवादी इतिहास

प्रस्तावना :

मानवी कल्याण व विकास हा पर्यावरणाशी संबंधित असतो. इतिहास म्हणजे मानवी जीवनाच्या भूतकालीन घटनांचा कालक्रम अभ्यासला जातो. इतिहास मानवी घटकांचा अभ्यास करणारी एक ज्ञान शाखा मानली जाते. गतकालीन मानवी जीवनाची माहिती इतिहासा द्वारे होते. प्रागैतिहासिक काळापासून मानवाने जी प्रगती केली त्या प्रगतीचा संबंध बदलत्या पर्यावरणाशी येतो.

'Envormental History and Disaster History' या इतिहासातील नव्याने उदयास आलेल्या ज्ञान शाखा आहेत. नैसर्गिक आपत्ती, भूकंप, दुष्काळ ,चक्रीवादळ, पूर या संकटांनी प्राचीन संस्कृतीचा ऱ्हास झाला याचे इतिहासात दाखले आहेत. उदाहरणार्थ द्वारका नगरीचे अवशेष, ग्रीक बॅबिलोनियन संस्कृती, सिंधू संस्कृती. कोट्यावधी वर्षापूर्वीच्या झालेल्या भौगोलिक बदलाच्या विपरीत परिणामाला तत्कालीन जीवसृष्टी पक्षी, प्राणी जीवजंतू इत्यादी सामोरे जावे लागले.

प्रत्येक काळ मग तो प्राचीन मध्ययुगीन आधुनिक काळात मानवी जीवन व प्राणी जीवनाला नैसर्गिक आपत्तीला सामोरे जावे लागले पण सृष्टीच्या नियमाप्रमाणे उत्पत्ती स्थिती व लय याप्रमाणे सृष्टी जीवन व समाज जीवन पुनर्निर्मित झालेले दिसते. प्राचीन संस्कृतीचा उदय आणि विकास हा नद्यांच्या काठीच झालेला आहे. उदाहरणार्थ इजिप्त संस्कृती नाईल नदीकाठी मेसोपोटेमियन टायग्रीस व युफ्रेटिस सिंधू संस्कृती सिंधू रावी नदी या संस्कृतीचा उदय विकास व ऱ्हाससाठी पर्यावरणाची भूमिका महत्त्वाची ठरते.

उद्दिष्टे :

'पर्यावरणवादी इतिहास लेखन एक अभ्यास' यासंदर्भात पुढील उद्दिष्टे ठेवली आहेत.

१) पर्यावरण इतिहास म्हणजे काय?
२) पर्यावरण वादी इतिहासाची उत्पत्ती
३) पर्यावरण आणि मानवी संस्कृतीचा परस्पर संबंध
४) बदलत्या पर्यावरणाचा सांस्कृतिक जीवनाचा होणारा परिणाम
५) भविष्यात नैसर्गिक आपत्तीतून इतिहास कालीन संस्कृतिक ठेव्याची जपणूक करण्यासाठी सामाजिक जीवनाची निर्मिती करणे सामाजिक मन तयार करणे

विषयाचे महत्व :

भूतकाळातही या घटना जशा घडल्या त्यांची कारणे महत्त्वाचा शोध घेण्याचा प्रयत्न या पेपर मध्ये केला जाणार आहे. पर्यावरण वादी नवीन विचार प्रवाहातून इतिहास व भूगोल संबंध पर्यावरणाचा व सामाजिक व आर्थिक जीवनावर होणारा परिणाम अभ्यास करण्याचा प्रयत्न केला जाईल.

व्याप्ती व मर्यादा :

शोध निबंधाची व्याप्ती ही पर्यावरणवादी इतिहासलेखन या विचारपुरती मर्यादित आहे.

संशोधनपद्धती :

सादर शोध निबंध अभ्यासतांना दुय्यम साधनसामुग्रीवर आधारित आहे.पुस्तके. विविध मासिके,विविध लेख,शासकीय संकेतस्थळाच्या सहाय्याने मांडणी केली आहे.

गृहीतके :

पर्यावरणाच्या बदलाचा मानवाच्या सर्वांगीण जीवनावर परिणाम होतो.

विषय विस्तार :

विसाव्या शतकात युरोपमध्ये अनेक प्रभावशाली कल्पनांचा उगम झाला . इटलीमध्ये मायक्रो हिस्ट्री विकसित झाली तर ब्रिटनमध्ये मानववंश शास्त्रीय सामाजिक इतिहास प्रभावी होता . फ्रान्समध्ये अनल्स दृष्टिकोन विकसित झाला. पर्यावरण इतिहासाने प्रथम आकार घेतला तो संयुक्त राष्ट्रात इसवी सन 1970 ते 1980 च्या दशकात पर्यावरणीय इतिहास क्षेत्रात अमेरिकेने प्रभाव प्राप्त केला इसवी सन 1980 पासूनच पर्यावरणीय इतिहास जगाच्या कानाकोपऱ्यात भरभराटीला आला .

पर्यावरणीय इतिहास एक ज्ञान प्रवाह आहे. या विचार प्रवाहात मानवी आणि सामाजिक संबंधांवर होणाऱ्या परिणामाची चर्चा केली जाते .निसर्ग आणि पर्यावरणातील मानवी संबंधांवर परिणाम करणाऱ्या ऐतिहासिक घटना चा दीर्घकालीन प्रभाव समजून घेण्याचा प्रयत्न या विचारधारेत केला जातो . भूतकालातील पृथ्वीच्या पर्यावरणावर होणारे हे परिणाम आणि त्यामुळे निसर्गात होणारे बदल समजून घेण्याचा एक मार्ग म्हणजे पर्यावरण इतिहास पर्यावरणीय इतिहासकार मानव व त्यांनी निर्माण केलेल्या संस्थांच्या बदलाचे मूल्यमापन करतात .उदाहरणार्थ राज्य, राजेशाही. वसाहती चे साम्राज्य, पर्यावरणीय इतिहास केवळ समाज आणि अर्थव्यवस्थेतील बदल पहात नाही तर या बदलांचा नैसर्गिक वातावरण वरील परिणाम चा अभ्यास करते. या बदलत्या घटनाचा ऐतिहासिक घटनाक्रम दर्शवितो. डोनाल्ड कस्टर "द एँड्स ऑफ द अर्थ " या पुस्तकात लिहितात पर्यावरण इतिहास आपल्याला भूतकाळाकडे पाहण्याचा एक नवीन मार्ग देतो आणि या विचारात आपला दृष्टिकोन बदलण्याची क्षमता आहे. पर्यावरणीय इतिहासात मानवी स्थलांतराच्या प्रभावाचा अभ्यास केला जातो.

सामाजिक इतिहास लेखनात इतिहासलेखन क्षेत्रात क्रांती घडवून आणली. विशाल साम्राज्याचा महत्त्वाकांक्षा आणि साम्राज्य विस्ताराच्या योजनेमुळे पृथ्वीच्या वातावरणाची किती हानी झाली हे पर्यावरणी इतिहासावरून दिसून येते . भारतात रामचंद्र गुहा यांनी पर्यावरणाचा दृष्टिकोनातून समाजाचा अभ्यास केला . संस्कृतीच्या वाटचालीत होणारे बदल म्हणजे पर्यावरणाची परिणीती होय. पर्यावरणाचा बदलाने सारे सामाजिक व राजकीय तसेच जैविक संदर्भात बदल होतात.

हवामान बदलले सामाजिक स्थित्यंतरे, चालीरीती, खानपानाच्या सवयी ,यातील बदलांचा अभ्यास पर्यावरणी इतिहासात होतो. इतिहासात पूर्वी राजकीय संघर्ष लढाया यांना महत्त्व होते इतिहासात सामाजिक वर्तन हे देखील महत्त्वाचे आहे सामाजिक वर्तन त्याच्या जैविक व घटकांवर व पर्यावरणावर अवलंबून असते भोवतालच्या परिस्थितीवर व्यक्तीचे वर्तन आणि निर्णय प्रक्रिया अवलंबून असते एकाच वेळी माणसे परस्परविरोधी वर्तन करताना दिसतात शांतता निर्माण करण्याची प्रयत्न व दहशतवादी विचार जैविक व अजैविक घटकांमधील प्रक्रियेत सामाजिक इतिहास व सांस्कृतिक इतिहास समजून घेण्यासाठी पर्यावरणवादी दृष्टिकोन असणाऱ्या अभ्यास पद्धती रूढ झाल्या उदाहरणात ध्रुवीय प्रदेश, विषुववृत्तीय प्रदेश यांच्या हवामानाचा तेथील मानवी जीवनावर, संस्कृती, परंपराचा अभ्यास पद्धतीत मोडतो.

मानवी जीवन व भौतिक जग क्षणोक्षणी बदलत असते याचा अभ्यास इतिहासात केला जावा अशा विचार रामचंद्र गुहा यांनी मांडला इतिहासाचा अर्थशास्त्र, समाजशास्त्र ,मानसशास्त्र या विद्याशाखेशी असणारा अन्योन्य संबंध अभ्यासला जातो तसेच निसर्ग शास्त्राचा व इतिहासाचा अतूट संबंध इतिहासकार अभ्यासू लागले. गतकालीन मानवी जीवनाचा सामाजिक स्थित्यंतराचा व विकासाचा अभ्यास प्रकृति विज्ञानाच्या दृष्टिकोनातून इतिहासकार अभ्यासू लागेल. मानव हा निसर्गाचा अविभाज्य घटक आहे निसर्ग विज्ञान निसर्गातील भिन्न घटक परस्पर संबंधाच्या अध्ययनाचे शास्त्र आहे. जर्मन शास्त्रज्ञ हेकेल १८६६ मध्ये 'इकॉलॉजी' या शब्दाची व्याख्या करताना डार्विनचा 'ओरिजिन ऑफ स्पेसीज' या ग्रंथाच्या संदर्भात हे केलेले विधान म्हणजे डार्विनच्या सिद्धांतानुसार जीवन संघर्षाच्या प्रक्रियेतील सर्व संबंधित घटकांच्या परस्पर संबंधाचा अभ्यास म्हणजे परिस्थिती होय.

निसर्गाचा उपयोग मानवी प्रगतीसाठी मानव अनादी काळापासून करताना दिसून येतो. औद्योगीकरण आत्यंतिक नागरीकरण तांत्रिक व वैज्ञानिक विकल्पाने निसर्गाचा अतिरेकी वापरामुळे निसर्गातील संतुलन नष्ट होऊन पर्यावरण दूषित होते यामुळे वनस्पती पक्षी प्राण्यांच्या जाती नष्ट होताना दिसतात या दुष्परिणामामुळे मानवी जीवन ती संपुष्टात येण्याची धोके निर्माण झाले आहे.

१९६२मध्ये श्रीमती रॅचेल कार्सन या अमेरिकन विदुषी पर्यावरणाला धोका दर्शवणारे 'द सायलेंट स्प्रिंग' हे पुस्तक पर्यावरण चळवळीचा आधार ग्रंथ मानला जातो. निसर्गातील बदलाचा परिणाम मानवी जीवन पद्धतीत होतो उदाहरणार्थ मानवाने वस्तीसाठी डोंगर, झाडी नष्ट केली या मानवी कृतीमुळे निसर्ग बदलला . भारतीय अभ्यासकांनी ऐतिहासिक पुराव्याच्या आधारे पुरातन नैसर्गिक परिस्थितीचे आडाखे बांधले. पुण्याच्या डेक्कन कॉलेज, पुरातत्व विभाग नागपूर विद्यापीठ, पुरातत्त्वशास्त्र प्राचीन मानव जीवन व तत्कालीन नैसर्गिक परिस्थिती यांच्या परस्परावलंबी विषयांवर प्रकाश टाकण्यास उपयुक्त ठरते डॉ. म.के. ढवळीकर यांनी 'पुरातत्त्वविद्या' या ग्रंथात निसर्ग आणि इतिहास यांचा अन्य संबंधाचे स्पष्टीकरण केले प्राचीन इतिहास कालीन काही प्रश्न उत्तरे नैसर्गिक स्थित्यंतरे सापडतात.उदा. सिंधू संस्कृतीचा अंत आणि सरस्वती नदीचा ऱ्हास या प्रश्नांची उत्तरे नैसर्गिक स्थितीत शोधली जातात सिंधू संस्कृतीच्या ऱ्हासाची कारणे सांगताना नैसर्गिक कारणे शोधली तर आर. एल. रेक्स यांनी वॉटर वेदर अँड प्री हिस्टरी या ग्रंथात व्यक्त केली आहेत. सिंधू नदीच्या महापुरामुळे मोहनजोदडो शहर नष्ट झाले .पण हा पुर अतिवृष्टी मध्ये मुळे नव्हे तर भूकंपाने झाल्याचे मत . रेक्स मांडले आहे. सरस्वती नदीच्या ऱ्हासाचे कारण रेक्स देताना म्हणतात इ.सवी. पूर्व तिसऱ्या सहस्त्रकात यमुना नदीचे पाणी सरस्वती नदी पडायचे, पण ते इसवी सन पूर्व दुसऱ्या सहस्त्रकात ते गंगा नदीत पडू लागले, त्यामुळे ही नदी लुप्त झाली. बदलते नद्यांचे प्रवाह, जंगलतोड इत्यादीमुळे जल जीवनात बदल झाला.

ऐतिहासिक साहित्य, वैदिक ,साहित्य, पुराणग्रंथ, महाकाव्यात देखील प्राणी जीवन व मानवी जीवनात या बाबतचे उल्लेख आढळतात यावरून नैसर्गिक परिस्थितीचा अंदाज येतो.

एकंदरीत मानवी जीवनाच्या निसर्गाचा अति निकट संबंध येतो बदलत्या नैसर्गिक परिस्थिती चा मानवी जीवनावर होणारा परिणाम अभ्यासतांना निसर्गाची हानी मानवाचे जीवन विस्कळीत करताना दिसून येते. त्यामुळे निसर्ग संवर्धन व रक्षणाची महत्त्व मानवाला समजावे यासाठी अनेक संस्था प्रयत्न करताना दिसतात चिपको आंदोलनाचे प्रवर्तक सुंदरलाल बहुगुणा यांनी ही निसर्गाच्या रक्षणासाठी व संवर्धनाच्या विचाराचा प्रभावीपणे विचार मांडला आहे.

ज्या ऐतिहासिक साधनांच्या आधारे विशेषता उत्खलीत साधने ज्या वस्तू वास्तू यांचा समावेश होतो ती ऐतिहासिक साधने जपण्याची संवर्धनाची गरज आहे. कारण या वस्तू वास्तू नैसर्गिक आपत्तीमुळे नष्ट होतांना दिसून येतात. याबाबत सामाजिक मन व सामाजिकजाणीव निर्माण करणे महत्त्वाचे ठरते. नैसर्गिक बदलाला जसा मानव कारणीभूत आहे तसेच मानवी जीवन प्राणीजीवन निसर्गाचे रक्षण व संवर्धन करणे हा दृष्टिकोन महत्त्वाचा आहे, म्हणून इंग्लंडमध्ये एन्व्हायरमेंट अँड हिस्ट्री या नावाचे नियतकालिक जॉन क्लॉक व पीटर कोटस यांनी संपादन केले आहे. भारतातही रामचंद्र गुहा सारखे इतिहासकार या दृष्टिकोनातून लिखाण करतांना दिसून येतात.

पर्यावरणासंबंधीच्या बदलांचा विचार करताना स्थानिक बदल महत्त्वाचे असतात. पर्यावरणाच्या अभ्यासात भूशास्त्र, पुराजीवशास्त्र, हवामानशास्त्र, सागरविज्ञान, इतिहास व पुरातत्त्व शास्त्रचा उपयोग होतो. पर्यावरणीय इतिहास लेखनातून स्थानिक बदलाबरोबर जागतिक पातळीवर होणाऱ्या बदलांचा विचार केला जातो.

प्रादेशिक इतिहास लेखनात देखील प्रादेशिक पर्यावरणीय बदलाचा इतिहास लिहिला जाऊ शकतो. उदा. महाराष्ट्राचे प्रागैतिहासिक पर्यावरण यांच्या अभ्यासात दख्खन पठाराची झालेली निर्मिती. दख्खन पठाराच्या निर्मितीची प्रक्रिया सात कोटी वर्षापूर्वी सुरू झाली. या प्रक्रियेत कार्बन डायॉक्साईड वातावरणात मिसळला थंड झालेल्या लाव्हारसामुळे दख्खन पठार निर्माण झाले. कार्बन-डाय-ऑक्साईड ची वाढ मोठ्या प्रमाणात झाल्यामुळे आणि भारतीय द्वीपकल्पाच्या उत्तर गोलार्धात सरकल्यामुळे तेथील हवामानात व पर्यावरणात बदल घडून आला. तप्त लाव्हारसाखाली आधी अस्तित्वात असलेले प्राणीजीव व वनस्पती नष्ट झाल्या ,कार्बनडाय ऑक्साईडच्या वाढत्या प्रमाणामुळे तापमानात वाढ झाली.

नैसर्गिक शेती व गतकालीन मानवी जीवन म्हणजेच इतिहास यांचा परस्पर प्रभावाचा अभ्यास करताना, मानवी जीवनाचे स्वरूप नैसर्गिकस्थिती ठरविते उदा.सतत होणाऱ्या भूकंपामुळे जपानमध्ये लाकडाची व बांबूची घरे बांधतात.

डॉ.शिरीन मुसावी यांनी Man and Nature in Mughal India या ग्रंथात नैसर्गिक परिस्थितीने मोगल काळात जीवन पद्धती आणि आर्थिक व व्यापारी व्यवहाराचे बदलते स्वरूप स्पष्ट केले आहे. या संदर्भात एक उदाहरण म्हणजे गोवळकोंड्याच्या नजीकच्या जंगलात बकऱ्यांच्या पोटात मिळणारा Bezoar नावाचा मौल्यवान खडा. या बकऱ्यांना वेगळया जंगलात स्थलांतरित केल्यानंतर तो मिळत नव्हता.

नैसर्गिक शेतीचा मानवी जीवनात प्रमाणेच सर्वच प्राणी मार्गावर प्राणीमात्रावर परिणाम होतो याचाही अभ्यास पर्यावरणीय इतिहास लेखनात करता येतो.प्राचीन काळातील घराच्या बांधकामावरून साहित्यावरून येथील हवामानाचा व वस्ती चा वस्ती ची माहिती मिळते मानवी पशूच्या सांगण्यावरून त्याचे स्थलांतर अभ्यासता येते.

निष्कर्ष :

या नवा प्रवाहातून खालील निष्कर्ष काढता येतील.

१.पर्यावरणाच्या रक्षणातून संस्कृतीची जपणूक होते.
२. इतिहासलेखनातील हा नवा विचार सामाजिकशास्त्रे व विज्ञानाशी सांगड घालतांना दिसतो.
३.या दृष्टीकोनातील इतिहासलेखन सर्वांगीण इतिहास लेखन ठरते.
४.आजही आदिवासी समाजजीवन निसर्गाशी जोडून आपली संस्कृती जपतांना दिसते.
५.बदलत्या ग्रामीण व नागरी समाजाच्या अभ्यास करता येतो.
६.ऐतिहासिक ठेवा जो वस्तू व वस्तूच्या स्वरुपात आहे.याची बदलत्या पर्यावरणामुळे होणारी हानी कशी टाळता येईल यासाठी समाजात जागरुकता निर्माण केली जाऊ शकते.
७.निसर्ग जगाला तर मानवी समाज जगू शकतो हा संदेश या पर्यावरणवादी दृष्टीकोनातून देता येतो.

संदर्भ साधने :

१. J.R.Nell-Intercultural center (ICC), Geogetown University, Washington D.C.
२.कोठेकर शांता इतिहास तंत्र आणि तत्वज्ञान श्री.साईनाथ प्रकाशन नागपूर.
३.देव प्रभाकर इतिहासलेखनशास्त्र,
४..Guha Ramchandra –Envioronmentalism A Global History.
५..Institute of Historical Studies: 2018 page No.166, 67 kolkata.
६.Roy Tirthankar,' Natural Disasters and Indian History'.
७.ढवळीकर म.के.,राज्यसाहित्य संस्कृती, महाराष्ट्र,१९७९,मुंबई.
८.महाराष्ट्र इतिहास आणि संस्कृती, पर्यालोचन भारतीय इतिहास संकलन समिती,महाराष्ट्र,पुणे पान.न.१२
९.पवार जयसिंगराव,विज्ञान,तंत्रज्ञान आणि प्रगती, फडके प्रकाशन कोल्हापूर.

International Journal of Advance and Applied Research
www.ijaar.co.in
ISSN – 2347-7075 Impact Factor – 7.328
Peer Reviewed Bi-Monthly
Vol.4 No.1 Jan – Feb 2023

# Assessment of Child Malnutrition Status: A Study of Tribal Population in Nashik District (Maharashtra)

**Jyoti Anilkumar Pathare[1] Anilkumar Ramdas Pathare[2] Sudarshan Annasaheb Aher[3] Vijay Jaysing Dalvi[4]**
[1]Assistant Professor, Department of Geography, HPT Arts and RYK Science College, Nashik
[2]Professor, Department of Geography, RNC Arts, JDB Commerce and NSCScience College, Nashik road, Nashik
[3]Research Assistant, Department of Geography, RNC Arts, JDB Commerce and NSC Science College, Nashik road, Nashik
[4]Associate Professor, Department of Geography, Rajarshi Shahu Mahavidyalaya (Autonomous) Latur
***Corresponding Author-* Jyoti Anilkumar Pathare**
**DOI- 10.5281/zenodo.7546665**

**Abstract:**

The present paper is an attempt to evaluate malnutrition among children in tribal areas. For this purpose, 210 tribal children from the 0-5 age group have been selected from villages in Nashik District. The authors use data from the Primary Survey 2022 to present age-specific patterns of child mortality among the tribal population. The analysis shows four clear findings. First, a disproportionately high number of child deaths are concentrated among the tribal population, especially in the 0-5 age group and in those tehsils where there is a high concentration of the tribal population. Second, the gap in mortality between tribal children and the rest really appears after the age of one. In fact, before the age of one, tribal children faced more or less similar odds of dying as other children. However, these odds will significantly reverse later. This calls for a shift in attention from infant mortality or in general under-five mortality to factors that cause a wedge between tribal children and the rest between the ages of one and five. Third, the analysis goes contrary to the conventional narrative of poverty being the primary factor driving differences in mortality outcomes. Fourth, poverty and malnutrition exacerbate the risk of infants and children contracting various infection diseases like diarrhea and pneumonia, and heighten the probability of death, particularly among children with low birth weight. There is a close relationship between malnutrition and child death. In Nashik district, 24 percent of children die per 1000 live births before five years of age.

**Key words:** Mortality, Malnutrition, Tribal, Age group 0-5, Children

**Acknowledgement:**
Authors are very much thankful to *Indian Council of Social Science Research (Ministry of Human Resource Development) for the financial assistance for a MRP, File No. 02/37/2021-22/ICSSR/RP/MN.* This paper is part of said project.

**Introduction:**

The aim of this paper is to examine the extent of malnutrition among tribal children in Nashik district. Thirty years ago, the world made a commitment to protect and fulfil children's rights as enshrined in the Convention on the Rights of the Child. Among the most fundamental of these rights is the right of every child to survive (United Nations, 1989). While substantial progress in child survival has been made since then, the failure to fully meet that commitment reverberates today for millions of children: In 2018 alone, 5.3 million children died before reaching their fifth birthday. Globally, out of the total children aged under-five years, almost 165 million were stunted (height for age) and 52 million were wasted (weight for height). The prevalence of underweight has decreased from 26.5 percent to 17.6 percent in 1990-2015 (De Onis M, 2004). The United Nations International Children's Emergency Fund (UNICEF) world-level estimates for wasting were 7.5 percent. Malnutrition is a major cause of child mortality and is widely recognized as a public health problem in developing countries including India. India has a very high burden of childhood stunting as 61 million (37 percent) of the 165 million stunted children aged under five years globally are Indian children (De Onis M, (2012). Approximately 43 percent of children are underweight (weight for age); one, out of every five children is wasted, and almost half of the children are stunted. Under the Millennium Development Goal -1 (MDG-1), one of the key indicators was to reduce the proportion of malnourished children through the reduction in poverty and hunger and to halve the prevalence of underweight children by 2015. Goal 2 of Sustainable Development Goals (SDGs) aims to end hunger and all forms of malnutrition by 2030. Nearly, almost half of all deaths in children of age under 5 are attributable to under nutrition, resulting in an unnecessary loss of around 3 million young lives worldwide every year (UNICEF, 2018).

Various factors are responsible for malnutrition; different authors have addressed the issues of Malnutrition of Children. Found that the proportions of children having low birth weight are at higher risk among women who are not educated. Nutrition status has been found to be positively associated with infant feeding practices. It is found that children who take exclusive breastfeeding have fewer chances of malnutrition (Rathaur VK, 2018). The optimal use of nutritious food feeding is healthy for child growth and development (Chaudhary SR, 2018). Infectious diseases like diarrhea, pneumonia, and measles increase the risk of mortality among those children who are stunted, underweight and wasted children (Black RE, 2013). Practices of personal hygiene and sanitation are fundamental to avoid stunting among children and are useful for the growth and development of children (Rah, 2015). The prevalence of malnutrition was found to be high among the tribal population due to their poor condition. Parents working in agriculture, and non-agricultural areas similarly who are below the poverty line and having Antyodya card and no schooling these are factors that lead to high malnutrition among the children (Kamath SM, 2017). Evidence suggests that the level of stunted children has declined from 52 percent in 1992–93 to 38 percent by 2015-16 but the prevalence of wasted had increased from 17 percent to 28 percent during this period, as reported in National Family Health Survey (NFHS 4). Moreover, in 2016, India accounted for 62 million stunted children, 40 percent of the global share of stunting in Maharashtra (UNICEF, 2018).

Over the last few years report of death of tribal children due to malnutrition has been pouring in the Maharashtra state. This has become a recurring phenomenon despite the governmental and NGOs effort to eradicate the problem. For instance, deaths of tribal children in Melghat, Dharni block of Amravati district, the tribal areas of Chandrapur, Yavatmal, Thane, Amravati, Nashik and Gadchiroli in recent years have created a cause of concern (Sonowal C.J, 2010).

While considering the above aspects, we decided to conduct a study on the prevalence of malnutrition in different tribal tehsils of Nashik district and what socio-demographic and economic factors are responsible for it. The current study also aims to explain the factors contributing to child malnutrition in the study area. The contributing factors that clarify this childhood malnutrition are most glaring in comparative and nationally representative ways and may support policymakers in their endeavours to diminish it. Very few studies have emphasized the mounting childhood under nutrition in different countries including India. To our knowledge, there exists no available literature explaining the child malnutrition in Nashik district.

**Study Area:**

Nashik district is a tribal dominated district in Maharashtra state. It is one of the growing districts despite uneven topography and dynamic nature. It is located in the north-west of Maharashtra state. The study region extends from $19^0$ 33' to $20^0$ 52' North latitudes and $73^0$ 16' to $74^0$ 56' East longitudes (Fig. No.1). The study region spreads over 15530 square kilometres, and ranks fifth in Maharashtra state, accounting for 5.04 percent area. The population of Nashik district is 6,107,187 as per Census 2011. Nashik is the $4^{th}$ most populous district out of the total 35 districts in Maharashtra and it is the $11^{th}$ most populous district in India.


**Fig. 1: Study Area**

**Objective of the Study:**

The present study aims to assess the health status of tribal children in tribal communities. Therefore, following objectives have been considered for this study.

i. To assess child malnutrition status of target population.

**Data Sources and Methodology:**

On the basis of information on occurrence of malnutrition cases among the tribal children, seven tribal tehsils, namely Igatpuri, Trimbakeshwar, Peth, Surgana, Dindori, Kalwan and Baglan of Nashik district were selected for the study.

Out of seven tehsils, the tribal villages, where the tribal population is 100 percent, have been taken into consideration. Twenty-one tribal villages were chosen for sample collection. For the study, various villages in tehsils such as hills, plains, Riverside, roadside, forest, and so on are chosen. Villages with households with children from 0 to 5 years of age were preferred for the study of malnutrition. 210 children were assessed for this study. A personal meeting and interview method were also adopted for getting socio-economic information from the head of the family.

From each of these selected villages, ten families were selected for in-depth studies. The criteria for selecting such families were based on the presence of less than 5 years old children and expectant mothers and also the presence of malnourished children as revealed by the local Anganwadi workers' records. It is worth mentioning that the level of malnourishment was based on Anganwadi workers' data. Some of those data were cross-examined and were found to be similar to our assessment. Therefore, extensive measurements were not carried out. The prevalence of malnourishment was universally accepted. Consequently, the influencing factors were studied in detail to get a conclusion on the issue.

The selected households were surveyed using random sampling survey method schedules. The schedules included space for demographic data like age, sex, education, occupation, seasonal migration, age at marriage, land holding pattern etc. Anthropometric indices like weight for age and weight for heights, etc. were considered for determination of stages and status of malnutrition among the children. Based on preliminary data collected with the help of household survey schedules, some families were selected for intensive case studies and interviews. Observations based on certain criteria were carried out to gain insight into the problems defined for the study.

Height and weight measurements were recorded following the standard techniques. The weight was measured using Salter's scale with light clothing and without shoes. Zero error was checked and adjusted before measurements. The height of the child was recorded with the help of non-stretchable measuring tape. The new WHO Child

Growth Standards for children under 5 years (2006) were used as reference for median. Nutritional status of children were assessed according to weight for age, height for age, weight for height and BMI for age and sex by Standard Deviation classification recommended by WHO. Children below -2 SD of the reference median on any of these indices were considered as undernourished and termed as underweight, stunted and wasted respectively. Children below -3 SD were considered to be severely undernourished. All the children whose weights were more than $85^{th}$ percentiles (BMI) for the age and sex were considered as overweight and more than $95^{th}$ percentiles (BMI) for the age and sex were considered obese.

The Z - Score Method has been applied to find out tribal child malnutrition status among scheduled tribes in the study area.

To calculate the tribal child malnutrition status, the Z-score values of different parameters (as per the WHO guidelines) have been computed using the following formula. Score value of the parameter X for the $i^{th}$ tahsil =

$$\boldsymbol{Z} = \frac{Xi - \bar{X}}{STDX} X10$$

Whereas;

Xi =X parameter of $i^{th}$ tahsil

$\dot{X}$ = Mean value of X tahsils

STD= Standard Deviation of X Parameter

The z-score (more commonly referred to as a standard score) is a very useful statistic because it; Allows us to calculate the probability of a score occurring within our normal distribution, Enables us to compare two scores that are from different normal distributions and Z-scores are a way to compare results from a test to a 'normal' population. Results from tests or surveys have thousands of possible results and units. However, those results can often seem meaningless (Deviant, 2010).

**Results:**

Table No. 1 and Fig. No. 2, 3 and 4 shows the malnutrition status among the tribal children in study region of Nashik district. As shown in Table No.1 and Fig. No.2, 60 children (28.5 percent) children lie in Moderate Acute Malnutrition grade (severely underweight)(-2SD). In the study region MAM tribal children are found in the Kalwan and Dindori tehsils. This Moderate Acute Malnutrition is known as MAM. Children in this group are more vulnerable to illness and have increase threat of death or they could move to next severe acute malnutrition (SAM) where risk of death is higher. 62 children (29.5 percent) lie in Mild Malnutrition Grade (underweight) (-1SD) where they are close to normal growth but far from adequate weight. In the study region MMG tribal children are found in the Igatpuri and Trimbakeshwar tehsils. Require weight for the age group 0 to 5 to obtain normal growth ranges between 2.56 kg to 14.8 Kg but unfortunately only 90 children (42.8 percent) out of 210 children fall in this Normal growth group (not underweight).

The data presented in Table No.1 and Fig. No.2 shows that, height (wasting) of tribal children. Out of 210 sample 14.3 percent (30) children were found in -3SD group which indicates (severely wasted) Severe Acute Malnutrition (SAM). In the study region SAM tribal children are found in the Igatpuri tehsil. 58 percent (122) children are in -2SD category which reflects (wasted) Moderate Acute Malnutrition (MAM).In the study region MAM tribal children are found in the Kalwan, Dindori, Peint and Trimbakeshwar tehsils. Only Surgana and Baglan tehsils 27.6 percent (58) children were found normal according to their height for age.

**Table No. 1 : Malnutrition status of tribal children in study region of Nashik district (Z score in percent)**

| Sr. No. | Tahsil Name | Under weight | Wasting | Stunning |
|---|---|---|---|---|
| 1 | Baglan | 14.84 | 14.58 | 14.91 |
| 2 | Dindori | 12.23 | 13.61 | 12.34 |
| 3 | Igatpuri | 12.64 | 12.22 | 12.62 |
| 4 | Kalwan | 12.51 | 14.05 | 12.46 |
| 5 | Peint | 15.76 | 14.01 | 16.58 |
| 6 | Surgana | 17.99 | 17.31 | 16.81 |



Jyoti Anilkumar Pathare, Anilkumar Ramdas Pathare, Sudarshan Annasaheb Aher, Vijay Jaysing Dalvi

| | | | | |
|---|---|---|---|---|
| 7 | Trimbakeshwar | 14.02 | 14.21 | 14.29 |
| **Total** | | **100** | **100** | **100** |

**Source:** Computed by Researcher

Findings in Table no.1 and Fig. No. 4 reveal that the 30 (14.4 percent) Children fell in -3SD category (severely stunning) Severe Acute Malnutrition (SAM).In the study region SAM tribal children are found in the Dindori tehsil.92 (43.8percent) children come in -2SD category (stunning) Moderate Acute Malnutrition (MAM).In the study region SAM tribal children are found in the Igatpuri, Trimbakeshwar and Kalwan tehsils. The 90 (42.8percent) children shows normally nourishment.

Table No. 2 and Fig. No. 5 reveal that the 28.57 percent children in study area were observed as Severe Malnutrition grade. In the study region Severe Malnutrition tribal children are found in the Igatpuri and Dindori tehsils.29.52 percent children in study area were observed as Poor Malnutrition grade. In the study region Poor Malnutrition tribal children are found in the Kalwan and Trimbakeshwar tehsils. Overall nutritional status depicts that only 41.90 percent children have Neutral grade.

As per the above results, tribal child malnutrition was found to be statistically significant. The higher proportion of malnutrition was also seen among children whose mothers were illiterate as compared to those with educated mothers.

**Table No. 2 : Malnutrition status of tribal children in study region of Nashik district (Under weight, wasting and stunning)**

| Malnutrition Status | Z score in percent |
|---|---|
| Sever | 28.57 |
| Poor | 29.52 |
| Neutral | 41.90 |
| **Total** | **100** |

**Source :** Computed by Researcher


Fig. No. 2 : Malnutrition status (underweight) of tribal children



Jyoti Anilkumar Pathare, Anilkumar Ramdas Pathare, Sudarshan Annasaheb Aher, Vijay Jaysing Dalvi

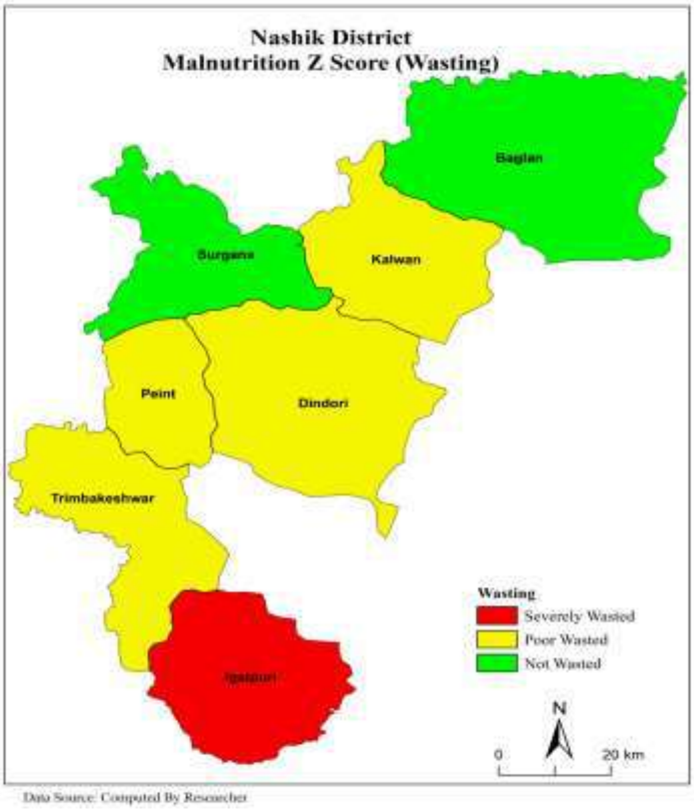


Fig. No. 3 : Malnutrition status (wasting) of tribal children

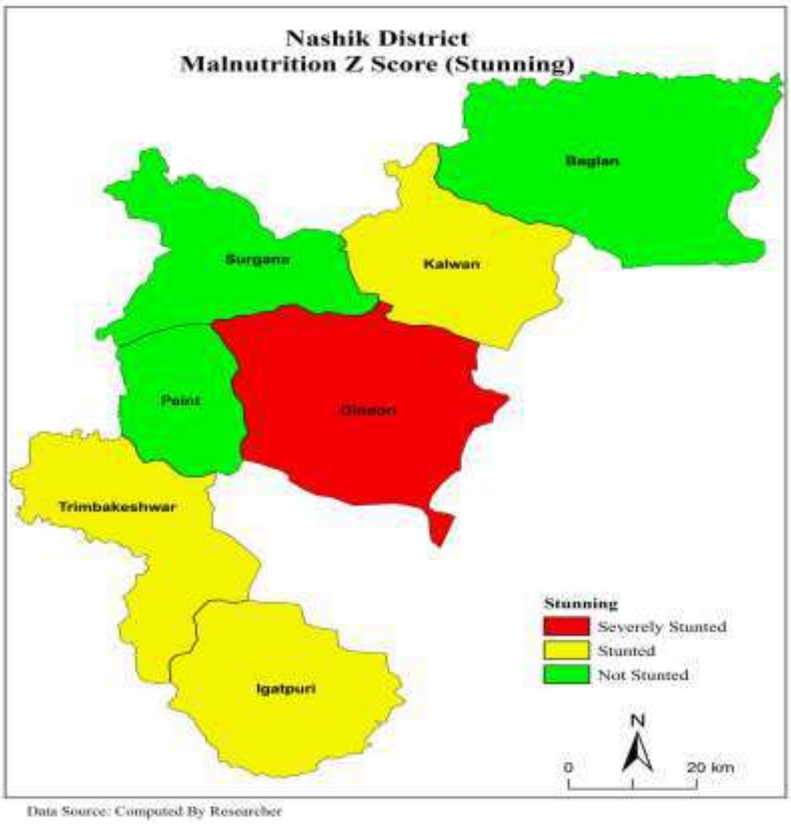


Fig. No. 4: Malnutrition status (stunning) of tribal children



Jyoti Anilkumar Pathare, Anilkumar Ramdas Pathare, Sudarshan Annasaheb Aher, Vijay Jaysing Dalvi


Fig. No. 5 : Malnutrition status of tribal children

Malnutrition has chronically remained a major public health problem among tribal child population in study region of Nashik district. Nutritional status among children below five years is betterin other eight tehsils than study regions (seven tehsils) of Nashik district because of all demographic and socioeconomic indicators are better than the study regions of Nashik district. The study, in general, revealed that malnutrition is an important public health problem where the prevalence of underweight, wasting and stunning was 14.33, 14.30 and 14.29percent, respectively. Place of residence, household, economic status, woman's employment and woman's age are important determinants of nutrition among women. We found that under nutritionist heavily concentrated among tribal region. Socio-economic status like limited access to health services, household food insecurity and the likelihood of poor environmental conditions such as access to clean water, sanitation, and hygiene increase the likelihood of illness. Women of low economic status have the highest prevalence of under-nutrition, which may be due to food insecurity in these households that negatively impacts the nutritional status of women as well as child. It was also observed that educational status of the mother positively affected the nutritional status of children. Educated mothers are more aware of their child's health and have a superior shot of utilizing the health services as compared to the illiterate ones. This study, also revealed that underweight was significant lyhigher among children whose mothers were illiterate compared with children whose mothers had secondary and higher education. Mothers education level was associated with progressively effective management of limited household resources, lower fertility, improved health promoting behaviour, better utilization of health-care services, and child- caring practices.

The present study also found an association between food restrictions and special food fed and malnutrition among the tribal children. A higher percentage of sweets and chocolate consumption among the tribal children was observed among malnourished children as compared to normal children. The higher risk of malnutrition among tribal children who ate more sweets or chocolate might be due to the lack of intake of nutritious food which is required for growth of the child.

**Conclusion**

In the present study the prevalence of underweight, wasting and stunning was found to be14.33, 14.30 and 14.29percent, respectively. Malnutrition was found to be higher among the children of illiterate parents; children belonged to Scheduled Tribes, born with low birth weight, having higher birth order, more number of siblings, those with incomplete immunization status and inappropriate feeding practices.

**Recommendation**

Maternal education had significant effect on child's nutritional status. So, there is a strong need for their formal and informal education regarding available services for their children and make those services acceptable too. The compromised nutritional status of the mother is a direct determinant in producing a low birth weight baby, thus encouraging the improvement in the nutritional status of women during ANC period is essential. Faulty feeding practices worsens the nutritional status of children. Therefore, mothers need to be educated regarding the benefits of exclusive breast feeding during initial 6 months of life

**References**

1. Black RE, Victora CG, Walker SP, (2013) Maternal and child under nutrition and overweight in low-income and middle-income countries, P. 427-451.
2. Chaudhary SR, Govil S, Lala MK, Yagnik HB (2018) Infant and young child feeding index and its association with nutritional status: a cross-sectional study of urban slums of Ahmedabad.
3. De Onis M, Blossner M, Borghi E, Frongillo EA, Morris R. (2004) Estimates of global prevalenceof childhood underweight in 1990 and 2015, p. 291.
4. De Onis M, Brown D, Blossner M, Borghi E. (2012) Levels and Trends in Child Malnutrition, UNICEF-WHO-The World Bank Joint Child Malnutrition Estimates.
5. Kamath SM, Venkatappa KG, Sparshadeep EM, (2017) Impact of nutritional status on cognitionin institutionalized orphans: a pilot study.
6. Rammohan M, Kalantar-Zadeh K, Liang A, Ghossein C. (2015) Megestrol acetate in a moderatedose for the treatment of malnutrition-inflammation complex in maintenancedialysis patients, p. 345-355.
7. Rathaur VK, Pathania M, Pannu C, (2018) Prevalent infant feeding practices among themothers presenting at a tertiary care hospital in Garhwal Himalayan region,Uttarakhand, India. J Fam Med Prim Care, p. 45.
8. Rushikesh P. Khadsea, Himanshu Chaurasia, (2020) Nutrition status and inequality among children in different geographicalregions of Maharashtra, India, Clinical Epidemiology and Global Health, P. 128-137.
9. Sonowal C.J, (2010) Factors Affecting the Nutritional Health of Tribal Children inMaharashtra, Kamla-Raj 2010, Ethno Med, 4(1): 21-36.
10. UNICEF (2018) Malnutrition in children, Available at: https://data.unicef.org/topic/nutrition/malnutrition/; 2018.
11. United Nations (1989) Convention on the Rights of the Child, Treaty Series, vol. 1577, p. 3.
12. Yadav SS, Yadav ST, Mishra P, Mittal A, Kumar R, Singh J. (2016) An Epidemiological Study of Malnutrition Among Under Five Children of Rural and Urban Haryana, Journal of clinical and diagnostic research: JCDR. 2016 Feb;10(2):LC07.

Advances and Applications in Mathematical Sciences
Volume 22, Issue 2, December 2022, Pages 503-526


# PYTHON: POWERFUL TOOL FOR SOLVING SPACE-TIME FRACTIONAL TRAVELING WAVE EQUATION

**KRISHNA GHODE, KALYANRAO TAKALE, SHRIKISAN GAIKWAD and KIRANKUMAR BONDAR**

Department of Mathematics
B. K. Birla College of Arts
Science and Commerce, Kalyan
Thane-421301, (M.S.), India

Department of Mathematics
RNC Arts, JDB Commerce and
NSC Science College, Nashik Road
Nashik-422101, (M. S.), India
E-mail: kalyanraotakale1@gmail.com

Department of Mathematics
New Atrs, Commerce and Science College
Ahmadnagar-414001, (M. S.), India
E-mail: sbgmathsnagar@gmail.com

Department of Mathematics
Government Vidarbha Institute
of Science and Humanities
Amravati 444604, (M.S.), India
E-mail: klbondar75@rediffmail.com

**Abstract**

The aim of this paper is to investigate the solution of space-time fractional traveling wave equation by Crank-Nicolson finite difference method using Python Programme. Also, we prove the scheme is unconditionally stable and convergent. Furthermore, we develop the Python programme for the proposed scheme and estimate the error. Finally, we obtain the numerical solutions of some test problems and simulated graphically by a Python programme.

2020 Mathematics Subject Classification: 35L05, 26A33, 65M06.

Keywords: Fractional traveling wave equation, Caputo derivative, Grunwald-Letnikov derivative, stability, Python etc.

*Corresponding author; E-mail: ghodekrishna@gmail.com

Received September 17, 2021; Accepted January 1, 2022

## 1. Introduction

In recent years, fractional differential equations are becoming a significant implement in the analysis and modeling of scientific problems in a broad array of fields such as physics, engineering, biology, finance, economics and earthquakes study etc. [2, 6, 9, 11, 10, 17]. There has been increasing attention in the description of physical and chemical processes using equations involving fractional derivatives and integrals. The study of fractional differential equations has been a highly focused in recent years. But most of the fractional differential equations do not have exact solutions. Traveling wave analysis is the most significant approach to study linear and non-linear partial differential equations. This study leads to various types of solutions such as soliton solutions, periodic solutions, kink solutions, cuspons solutions, compacton solutions, peakon solutions etc. [18]. The traveling wave solutions of fractional order partial differential equations are useful to analyses the mechanisms of phenomena as well as further application in various fields. Though, finding traveling wave solutions is not a straightforward task at all, therefore researchers are preferring finite difference schemes.

The finite difference approximations for derivatives are one of the simplest and the efficient method to solve fractional order partial differential equations [1, 3, 14, 13, 16]. Therefore, in this connection we develop the Crank-Nicolson finite difference scheme for space time fractional traveling wave equation and obtain its solution using Python programme. Recently, many researchers have shifted from compiled languages to interpreted problem solving environments, such as MATLAB, Maple, Octave, $R$ etc. [5, 12, 15]. The Python is now rising as a potentially competitive replacement to MATLAB, Octave, and other similar environments [4, 7]. The popularity of Python is because of simple and clean syntax of the commands, incorporation of simulation and visualization, interactive execution of commands with instantaneous feedback and lots of built-in functions available and work efficiently on arrays in compiled code. Now a days, researchers are using Python due to its simplicity, wealth of available support and the NumPy package, which provides contiguous multi-dimensional array structures with a large library of array operations.

The plan of the paper is as follows: In section 2, the Crank-Nicolson finite difference scheme is developed for space-time fractional traveling wave equation. The section 3 is devoted for stability of the scheme and the question of convergence is proved in section 4. The last section is devoted for Python programme and numerical solution of the space-time fractional traveling wave equations.

We consider the following space-time fractional traveling wave equation

$$\frac{\partial^{\alpha} V}{\partial t^{\alpha}} = C^2 \frac{\partial^{\beta} V}{\partial x^{\beta}}, \; t \in [0, T], \; x \in [0, L], \; 1 < \alpha \leq 2, \; 1 < \beta \leq 2 \tag{1.1}$$

subject to the initial conditions:

$$V(x, 0) = f(x), \; \frac{\partial}{\partial t} V(x, 0) = g(x), \; x \in [0, L] \tag{1.2}$$

and boundary conditions:

$$V(0, t) = 0, \; V(L, t) = 0, \; t > 0 \tag{1.3}$$

where $V(x, t)$ is the displacement of wave at position $x$ and time $t$, and $C$ is the velocity of wave. The Caputo time fractional derivative of order $\alpha$ is defined as follows [8],

$$\frac{\partial^{\alpha} V}{\partial t^{\alpha}} = \frac{1}{\Gamma(m - \alpha)} \int_0^t (t - \zeta)^{m-\alpha-1} \frac{\partial^m V(x, \zeta)}{\partial \zeta^m} d\zeta$$

where $m$ is a integer such that $m - 1 < \alpha \leq m$. The right shifted Grunwald-Letnikov space fractional derivative of order $\beta$ is defined as follows [8],

$$\frac{\partial^{\alpha} V}{\partial t^{\alpha}} = \lim_{M \to \infty} \frac{1}{h^{\beta}} \sum_{l=0}^{M} \frac{\Gamma(l - \beta)}{\Gamma(-\beta)\Gamma(l + 1)} V(x - (l - 1)h, t).$$

## 2. Finite Difference Scheme

In this section, we discretized the space-time fractional traveling wave equation (1.1)-(1.3) using Crank-Nicolson finite difference scheme. Let $x_i = ih, i = 0, 1, 2, \ldots, M$ and $t_n = nk, n = 0, 1, 2, \ldots, N$, where $h = \frac{L}{M}$

and $k = \frac{T}{M}$. Let $V_i^n$ be the numerical approximation of $V(x, t)$ at point $(ih, nk)$, where $h$ and $k$ are spatial and temporal sizes respectively. We discretized the Caputo time fractional derivative as follows:

$$\left(\frac{\partial^\alpha V}{\partial t^\alpha}\right)_{(x_i,\, t_{n+1})} = \frac{1}{\Gamma(2-\alpha)} \int_0^{t_{n+1}} (t_{n+1} - \zeta)^{1-\alpha} \frac{\partial^2 V(x_i, \zeta)}{\partial \zeta^2} d\zeta$$

$$= \frac{1}{\Gamma(2-\alpha)} \sum_{j=0}^{n} \int_{jk}^{(j+1)k} \eta^{1-\alpha} \frac{\partial^2 V(x_i, t_{n+1} - \eta)}{\partial \eta^2} d\eta$$

$$= \frac{1}{\Gamma(2-\alpha)} \sum_{j=0}^{n} \left( \frac{V_i^{n-j+1} - 2V_i^{n-j} + V_i^{n-j-1}}{k^2} + O(k) \right)$$

$$\times \int_{jk}^{(j+1)k} \eta^{1-\alpha} d\eta$$

$$= \frac{k^{2-\alpha}}{\Gamma(3-\alpha)} \sum_{j=0}^{n} \left( \frac{V_i^{n-j+1} - 2V_i^{n-j} + V_i^{n-j-1}}{k^2} + O(k) \right)$$

$$\times ((j+1)^{2-\alpha} - j^{2-\alpha})$$

$$= \frac{k^{-\alpha}}{\Gamma(3-\alpha)} \sum_{j=0}^{n} (V_i^{n-j+1} - 2V_i^{n-j} + V_i^{n-j-1})((j+1)^{2-\alpha} - j^{2-\alpha})$$

$$+ \frac{k^{2-\alpha}}{\Gamma(3-\alpha)} O(k) \sum_{j=0}^{n} ((j+1)^{2-\alpha} - j^{2-\alpha})$$

$$= \frac{k^{-\alpha}}{\Gamma(3-\alpha)} \sum_{j=0}^{n} (V_i^{n-j+1} - 2V_i^{n-j} + V_i^{n-j-1})((j+1)^{2-\alpha} - j^{2-\alpha})$$

$$+ \frac{k^{2-\alpha}}{\Gamma(3-\alpha)} (n+1)^{2-\alpha} O(k)$$

As $(n+1)k$ is finite, then above formula can be rewritten as

$$\left(\frac{\partial^{\alpha} V}{\partial t^{\alpha}}\right)_{(x_i,\, t_{n+1})} =$$

$$\frac{k^{-\alpha}}{\Gamma(3-\alpha)} \sum_{j=0}^{n} (V_i^{n-j+1} - 2V_i^{n-j} + V_i^{n-j-1})((j+1)^{2-\alpha} - j^{2-\alpha}) + O(k) \tag{2.1}$$

where

$$b_j = (j+1)^{2-\alpha} - j^{2-\alpha},\ j = 0, 1, 2, \ldots, n$$

We use the right shifted Grunwald formula to discretized the space fractional derivative as follows [8]:

$$\frac{\partial^{\beta} V}{\partial t^{\beta}} = \frac{1}{h^{\beta}} \sum_{l=0}^{i+1} w_l V_{i-l+1}^{n} + O(h) \tag{2.2}$$

where

$$w_l = \frac{\Gamma}{\Gamma(-\beta)\Gamma(l+1)},\ l = 0, 1, 2, \ldots, M.$$

which called the normalized Grunwald weights. They can be found by the recursive formula:

$$w_0 = 1,\ w_l = w_{l-1}\left(1 - \frac{\beta+1}{l}\right)$$

Now, putting (2.1) and (2.2) in equation (1.1), we obtain the Crank-Nicloson type numerical approximation of space-time fractional traveling wave equation (1.1) as follows:

$$\frac{k^{-\alpha}}{\Gamma(3-\alpha)} \sum_{j=0}^{n} b_j (V_i^{n-j+1} - 2V_i^{n-j} + V_i^{n-j-1}) = C^2 \frac{1}{2h^{\beta}}$$

$$\left[\sum_{l=0}^{i+1} w_l V_{i-l+1}^{n+1} + \sum_{l=0}^{i+1} w_l V_{i-l+1}^{n}\right]$$

$$\sum_{j=0}^{n} b_j (V_i^{n-j+1} - 2V_i^{n-j} + V_i^{n-j-1}) = \frac{C^2 \Gamma(3-\alpha) k^{\alpha}}{2h^{\beta}} \left[ \sum_{l=0}^{i+1} w_l V_{i-l+1}^{n+1} + \sum_{l=0}^{i+1} w_l V_{i-l+1}^{n} \right]$$

We simplify the above equation and obtain

$$V_i^{n+1} - 2V_i^n + V_i^{n-1} + \sum_{j=1}^{n} b_j (V_i^{n-j+1} - 2V_i^{n-j} + V_i^{n-j-1})$$

$$= r \left[ \sum_{l=0}^{i+1} w_l V_{i-l+1}^{n+1} + \sum_{l=0}^{i+1} w_l V_{i-l+1}^{n} \right]$$

where $r = \dfrac{C^2 \Gamma(3-\alpha) k^{\alpha}}{2h^{\beta}}$.

$$V_i^{n+1} - r \sum_{j=1}^{i+1} w_l V_{i-l+1}^{n+1} = 2V_i^n + V_i^{n-1} - \sum_{j=1}^{n} b_j (V_i^{n-j+1} - 2V_i^{n-j} + V_i^{n-j-1})$$

$$+ r \sum_{l=0}^{i+1} w_l V_{i-l+1}^{n} \qquad (2.3)$$

The initial conditions are approximated as follows:

$$V(x_i, 0) = f(x_i) \text{ implies } V_i^0 = f(x_i), \; i = 1, 2, \ldots, M-1 \qquad (2.4)$$

and

$$\frac{\partial}{\partial t} V(x_i, t_0) = g(x_i) \text{ implies } \frac{V_i^1 - V_i^{-1}}{2k} = g(x_i)$$

$$V_i^{-1} = V_i^1 - 2kg(x_i), \; i = 1, 2, \ldots, M-1. \qquad (2.5)$$

Also, the boundary conditions are approximated as follows:

$$V(0, t_n) = 0 \text{ implies } V_0^n = 0, \; n = 1, 2, \ldots, N-1$$

and

$$V(L, t_n) = 0 \text{ implies } V_M^n = 0, \; n = 1, 2, \ldots, N-1$$

We put $n = 0$ in equation (2.3) and using equation (2.5), we obtain

$$V_i^1 - \frac{r}{2}\sum_{l=0}^{i+1} w_l V_{i-l+1}^1 = V_i^0 + kg(x_i) + \frac{r}{2}\sum_{l=0}^{i+1} w_l V_{i-l+1}^0$$

and for $n = 1, 2, \ldots, N-1,$ we get

$$V_i^{n+1} - r\sum_{l=0}^{i+1} w_l V_{i-l+1}^{n+1} = 2V_i^n - V_i^{n-1} - \sum_{j=1}^{n-1} b_j (V_i^{n-j+1} - 2V_i^{n-j} + V_i^{n-j-1})$$

$$-2b_n(V_i^1 - V_i^0 + kg(x_i)) + r\sum_{l=0}^{i+1} w_l V_{i-l+1}^n$$

The complete discretized space-time fractional traveling wave equation with initial and boundary conditions is written as follows:

$$V_i^1 - \frac{r}{2}\sum_{l=0}^{i+1} w_l V_{i-l+1}^1 = V_i^0 + kg(x_i) + \frac{r}{2}\sum_{l=0}^{i+1} w_l V_{i-l+1}^0 \tag{2.6}$$

for $n = 0,$

$$V_i^{n+1} - r\sum_{l=0}^{i+1} w_l V_{i-l+1}^{n+1} = 2V_i^n - V_i^{n-1} - \sum_{j=1}^{n-1} b_j (V_i^{n-j+1} - 2V_i^{n-j} + V_i^{n-j-1})$$

$$-2b_n(V_i^1 - V_i^0 + kg(x_i)) + r\sum_{l=0}^{i+1} w_l V_{i-l+1}^n, \tag{2.7}$$

initial condition:

$$V_i^0 = f(x_i),\ i = 1, 2, \ldots, M-1 \tag{2.8}$$

boundary conditions:

$$V_i^n = 0,\ V_M^n = 0,\ n = 1, 2, \ldots, N-1 \tag{2.9}$$

The discretized finite difference scheme (2.6)-(2.9) can be written in matrix form as follows:

for $n = 0,$

$$AV^1 = (2I - A)V^0 + F_1 \tag{2.10}$$

for $n \geq 1$,

$$(2A - I)V^{n+1} = ((4 - b_1)I - 2A)V^n + \sum_{j=1}^{n-1}(2b_j - b_{j-1} - b_{j+1})V_i^{n-j}$$

$$- b_n V^1 + (2b_n - b_{n-1})V^0 + 2b_n kg(x_i)I, \tag{2.11}$$

initial condition:

$$V_i^0 = f(x_i),\ i = 1, 2, \ldots, M - 1 \tag{2.12}$$

boundary conditions:

$$V_i^n = 0,\ V_M^n = 0,\ n = 1, 2, \ldots, N - 1 \tag{2.13}$$

where $V^n = [V_1^n, V_2^n, \ldots, V_{M-1}^n]^T$, $F = [kg(x_1), kg(x_2), \ldots, kg(x_{M-1})]^T$, $I$ is an identity matrix of order $(n-1) \times (n-1)$ and matrix $A$ is defined as follows

$$A = (a_{ij})_{(M-1)\times(M-1)} = \begin{cases} 1 - \frac{r}{2} w_1, & j = i \\ -\frac{r}{2} w_0, & j = i + 1 \\ -\frac{r}{2} w_{i-j+1}, & j \leq i - 1 \\ 0, & j \geq i + 2 \end{cases}$$

**Lemma 2.1.** *The coefficient* $b_j$, $j = 1, 2, \ldots$ *satisfy*

(i) $b_j > 0$

(ii) $b_j > b_{j+1}$

**Lemma 2.2.** *Grunwald-Letnikov coefficients* $w_l$ *satisfy*:

(i) $w_0 = 1,\ w_1 = -\beta,\ w_2 = \frac{\beta(\beta - 1)}{2}$

(ii) $1 \geq w_2 \geq w_3 \geq \ldots \geq 0$

(iii) $\sum_{l=0}^{n} w_l < 0,\ n \geq 1.$

## 3. Stability

Let $\overline{V}_i^n$ and $V_i^n$ are exact and approximate solutions of the equation (1.1)-(1.3) respectively and $\varepsilon_i^n$ be the error at each mesh point $(x_i, t_n)$, then

$$\varepsilon_i^n = \overline{V}_i^n - V_i^n$$

From equations (2.6)-(2.7), we obtain for $n = 0$,

$$\varepsilon_i^1 - \frac{r}{2}\sum_{l=0}^{i+1} w_l \varepsilon_{i-l+1}^1 = \varepsilon_i^0 + \frac{r}{2}\sum_{l=0}^{i+1} w_l \varepsilon_{i-l+1}^0 \tag{3.1}$$

for $n \geq 1$,

$$\varepsilon_i^{n+1} - r\sum_{l=0}^{i+1} w_l \varepsilon_{i-l+1}^{n+1} = 2\varepsilon_i^n - \varepsilon_i^{n-1} - \sum_{j=1}^{n-1} b_j(\varepsilon_i^{n-j+1} - 2\varepsilon_i^{n-j} + \varepsilon_i^{n-j-1})$$

$$- 2b_n(\varepsilon_i^1 - \varepsilon_i^0) + r\sum_{l=0}^{i+1} w_l \varepsilon_{i-l+1}^n. \tag{3.2}$$

**Theorem 3.1.** *The solution of Crank-Nicolson finite difference scheme given by* (2.6)-(2.9) *developed for equation* (1.1)-(1.3) *is unconditionally stable.*

**Proof.** We denote the error vector by $E^n = (\varepsilon_1^n, \varepsilon_2^n, \ldots, \varepsilon_{M-1}^n)^T$ for $0 \leq n \leq N$. Also, we assume that

$$|\varepsilon^n| = \max_{1 \leq i \leq M-1} |\varepsilon_i^n| = \| E^n \|_\infty, \text{ for } n = 0, 1, 2, \ldots, N.$$

Using mathematical induction, we will prove that $\| E^n \|_\infty \leq K_1 \| E^0 \|_\infty$, for $n = 0, 1, 2, \ldots, N$, where $K_1$ is a positive number independent of $h$ and $k$. Now, using Lemma (2.2) and equation (3.1), we obtain

$$|\varepsilon_i^1| \leq |\varepsilon_i^1| - \frac{r}{2}\sum_{l=0}^{i+1} w_l |\varepsilon_{i-l+1}^1|$$

$$\leq |\, \varepsilon_i^1 - \frac{r}{2}\sum_{l=0}^{i+1} w_l \varepsilon_{i-l+1}^1 \,|$$

$$\leq |\, \varepsilon_i^0 - \frac{r}{2}\sum_{l=0}^{i+1} w_l \varepsilon_{i-l+1}^0 \,|$$

$$|\, \varepsilon_i^0 \,| + \frac{r}{2}\sum_{l=0}^{i+1} w_l |\, \varepsilon_{i-l+1}^1 \,| \leq \left(1 + \frac{r}{2}\sum_{l=0}^{i+1} w_l\right) |\, \varepsilon^0 \,| \leq K_1 |\, \varepsilon^0 \,|$$

$$\| E^1 \|_\infty \leq K_1 \| E^0 \|_\infty$$

Suppose that

$$\| E^q \|_\infty \leq K_1 \| E^0 \|_\infty,$$

for $q \leq n$ and $K_1$ is independent of $h$ and $k$.

Using Lemma (2.2), we have $2 - b_1 > 0,\ b_{j-1} - 2b_j > 0,\ 2b_n - b_{n-1} > 0$. Consider,

$$|\, \varepsilon_i^{n+1} \,| \leq |\, \varepsilon_i^{n+1} \,| - r\sum_{l=0}^{i+1} w_l |\, \varepsilon_{i-l+1}^{n+1} \,|$$

$$\leq |\, \varepsilon_i^{n+1} - r\sum_{l=0}^{i+1} w_l \varepsilon_{i-l+1}^{n+1} \,|$$

$$\leq |\, 2\varepsilon_i^n - \varepsilon_i^{n-1} - \sum_{l=0}^{n-1} b_j(\varepsilon_i^{n-j+1} - 2\varepsilon_i^{n-j} + \varepsilon_i^{n-j-1}) - 2b_n(\varepsilon_i^1 - \varepsilon_i^0) + r\sum_{l=0}^{i+1} w_l \varepsilon_{i-l+1}^n \,|$$

$$\leq |\, (2 - b_1)\varepsilon_i^n + \sum_{l=0}^{n-1}(2b_j - b_{j-1} - b_{j+1})\varepsilon_i^{n-j} - b_n\varepsilon_i^1 + (2b_n - b_{n-1})\varepsilon_i^0$$

$$+ r\sum_{l=0}^{i+1} w_l \varepsilon_{i-l+1}^n \,|$$

$$\le (2-b_1)|\,\varepsilon_i^n\,| + \sum_{j=1}^{n-1}(b_{j-1}+b_{j+1}-2b_j)|\,\varepsilon_i^{n-j}\,| + b_n|\,\varepsilon_i^1\,| + (2b_n - b_{n-1})|\,\varepsilon_i^0\,|$$

$$+ r\sum_{l=0}^{i+1} w_l|\,\varepsilon_{i-l+1}^n\,|$$

$$\le \left(2 - b_1 + \sum_{j=1}^{n-1}(b_{j-1}+b_{j+1}-2b_j) + b_n + 2b_n - b_{n-1} + r\sum_{l=0}^{i+1} w_l\right)|\,\varepsilon^0\,|$$

$$\le \left(2(1-b_1) + 2(2b_n - b_{n-1}) + r\sum_{l=0}^{i+1} w_l\right)|\,\varepsilon^0\,| \le K_1|\,\varepsilon^0\,|$$

Therefore, $\| E^{n+1} \|_\infty \le K_1 \| E^0 \|_\infty$, where $K_1$ is a positive constant independent of $h$ and $k$. Hence, by mathematical induction, for all $n = 1, 2, \ldots, N$, we have

$$\| E^n \|_\infty \le K_1 \| E^0 \|_\infty$$

This completes the proof. □

## 4. Convergence

In this section, we discuss the question of convergence. Let $\overline{V}_i^n$ be the exact solution of space-time fractional traveling wave equation (1.1)-(1.3) and $\tau_i^n$ be the local truncation error for $1 \le i \le M$. Then, from (2.6)-(2.9), we have

$$\tau_i^1 = \overline{V}_i^1 - \frac{r}{2}\sum_{l=0}^{i+1} w_l \overline{V}_{i-l+1}^1 - \overline{V}_i^0 - kg(x_i) - \frac{r}{2}\sum_{l=0}^{i+1} w_l \overline{V}_{i-l+1}^0 = O(h+k) \tag{4.1}$$

and for $1 \le n \le N-1$,

$$\tau_i^{n+1} = \overline{V}_i^{n+1} - r\sum_{l=0}^{i+1} w_l \overline{V}_{i-l+1}^{n+1} - 2\overline{V}_i^n + \overline{V}_i^{n-1} + \sum_{j=1}^{n-1} b_j(\overline{V}_i^{n-j+1} - 2\overline{V}_i^{n-j} + \overline{V}_i^{n-j-1})$$

$$+ 2b_n(\overline{V}_i^1 - \overline{V}_i^0 - kg(x_i)) - r\sum_{l=0}^{i+1} w_l \overline{V}_{i-l+1}^n = O(h+k) \tag{4.2}$$

**Theorem 4.1.** *Let* $\overline{V}_i^n$ *be the exact solution of* (1.1)-(1.3) *and* $\overline{V}_i^n$ *be the numerical solution of finite difference scheme* (2.6)-(2.9) *at each mesh point* $(x_i, t_n)$*. Then there exist a positive constant* $K_2$ *independent of h and k such that*

$$\| \overline{V}_i^n - V_i^n \| \le K_2(h+k), 1 \le n \le N.$$

**Proof.** Let $e_i^n$ be the error at each mesh point $(x_i, t_n)$, then

$$\| e_i^n \| = \| \overline{V}_i^n - V_i^n \|$$

Now, we denote the error vector by $e^n = (e_1^n, e_2^n, \ldots, e_{M-1}^n)^T$ for $1 \le n \le N$ and local truncation error vector by $\tau^n = (\tau_1^n, \tau_2^n, \ldots, \tau_{M-1}^n)^T$ for time level $n$. From equations (4.1)-(4.2), we get

$$e_i^1 - \frac{r}{2}\sum_{l=0}^{i+1} w_l e_{i-l+1}^1 = e_i^0 + \frac{r}{2}\sum_{l=0}^{i+1} w_l e_{i-l+1}^0 + \tau_i^1 \tag{4.3}$$

for $n \ge 1$,

$$e_i^{n+1} - r\sum_{l=0}^{i+1} w_l e_{i-l+1}^{n+1} = 2e_i^n - e_i^{n-1} - \sum_{j=1}^{n-1} b_j(e_i^{n-j+1} - 2e_i^{n-j} + e_i^{n-j-1})$$

$$+ 2b_n(e_i^1 - e_i^0) + r\sum_{l=0}^{i+1} w_l e_{i-l+1}^n + \tau_i^{n+1}. \tag{4.4}$$

Using mathematical induction, we will prove that $\| e^n \|_\infty \le K_2(h+k)$. For $n = 1$, we have

$$| e_i^1 | \le | e_i^1 | - \frac{r}{2}\sum_{l=0}^{i+1} w_l | e_{i-l+1}^1 |$$

$$\leq | e_i^1 - \frac{r}{2}\sum_{l=0}^{i+1} w_l e_{i-l+1}^1 |$$

$$\leq | e_i^0 - \frac{r}{2}\sum_{l=0}^{i+1} w_l e_{i-l+1}^0 + \tau_i^1 | \leq \left[1 + \frac{r}{2}\sum_{l=0}^{i+1} w_l\right] | e_i^0 | + | \tau_i^1 | \leq | \tau_i^1 | \leq K_2(h+k)$$

Therefore, $\| e^1 \|_\infty \leq K_2(h+k)$, where $K_2$ is independent of $h$ and $k$. Suppose that

$$\| e^q \|_\infty \leq K_2(h+k),$$

for $q \leq n$ and $K_2$ is independent of $h$ and $k$. Consider,

$$| e_i^{n+1} | \leq | e_i^{n+1} | - r\sum_{l=0}^{i+1} w_l | e_{i-l+1}^{n+1} |$$

$$\leq | e_i^{n+1} - r\sum_{l=0}^{i+1} w_l e_{i-l+1}^{n+1} |$$

$$\leq | 2e_i^n - e_i^{n-1} - \sum_{l=0}^{n-1} b_j (e_i^{n-j+1} - 2e_i^{n-j} + e_i^{n-j-1}) - 2b_n(e_i^1 - e_i^0)$$

$$+ r\sum_{l=0}^{i+1} w_l e_{i-l+1}^n + \tau_i^{n+1} |$$

$$\leq | (2-b_1)e_i^n + \sum_{l=0}^{n-1} (2b_j - b_{j-1} - b_{j+1}) e_i^{n-j} - b_n e_i^1 + (2b_n - b_{n-1}) e_i^0$$

$$+ r\sum_{l=0}^{i+1} w_l e_{i-l+1}^n + \tau_i^{n+1} |$$

$$\leq (2-b_1) | e_i^n | + \sum_{j=1}^{n-1} (b_{j-1} + b_{j+1} - 2b_j) | e_i^{n-j} | + b_n | e_i^1 | + r\sum_{l=0}^{i+1} w_l | e_{i-l+1}^n | + | \tau_i^{n+1} |$$

$$\leq \left(2 - b_1 + \sum_{j=1}^{n-1}(b_{j-1} + b_{j+1} - 2b_j) + b_n + r\sum_{l=0}^{i+1} w_l\right) K_2'(h+k) + |\tau_i^{n+1}|$$

$$\leq \left(2(1 - b_1) + 2(2b_n - b_{n-1}) + r\sum_{l=0}^{i+1} w_l\right) K_2'(h+k) + |\tau_i^{n+1}| \leq K_2(h+k)$$

Therefore, $\| e^{n+1} \|_\infty \leq K_2(h+k)$.

Hence, by mathematical induction, for all $n = 1, 2, \ldots, N$, we have

$$\| e^n \|_\infty \leq K_2(h+k)$$

This completes the proof. □

## 5. Python Programme

In this section, we develop the Python programme-CN for Crank-Nicolson finite difference scheme (2.6)-(2.9) to solve space-time fractional traveling wave equation (1.1)-(1.3) numerically. We compute $\overline{V}_i^n$ at each grid point $(x_i, t_n)$ using the scheme (2.6)-(2.9). The algorithm is given below:

1. Compute $V_i^0 = f(x_i)$, $i = 0, 1, 2, \ldots, M$.

2. Compute $V_i^1$, $i = 0, 1, 2, \ldots, M$.

3. Compute $V_i^{n+1}$, for each $n = 1, 2, \ldots, N-1$, $i = 0, 1, 2, \ldots, M$.

Now, we develop the Python programme-CN for complete discretized scheme (2.6)-(2.9) as follows:

Inputs:

f - initial displacement

g - initial velocity

C - velocity of wave

L - spatial length

T - end time

h - space step size

k - temporal step size

a - fractional order α of time derivative

b - fractional order β of space derivative

t1 - time level, at which solution has to be estimate

Output of Python programme CN is the approximate value of vector $V(x_i, t1)$.

```
import math
import numpy as np
import scipy.linalg
def CN(f,g,C,T,L,a,b,h,k,t1):
r=(C**2*math.gamma(3-a)*k**a)/(2*h**b)
N=int(round(T/k))
M=int(round(L/h))
t=np.linspace(0,N*k,N+1)
x=np.linspace(0,M*h,M+1)
V=np.zeros((N+1,M+1))
for i in range(0,M+1):
V[0][i]=f(x[i])
A1 = np.zeros((M-1, M-1))
A2 = np.zeros((M-1, M-1))
b1 = np.zeros(M-1)
b2 = np.zeros(M-1)
w = np.zeros(M+1)
w[0]=1
for l in range(1,M+1):
```

```
w[l]=w[l-1]*(1-((1+b)/l))
for i in range(0,M-1):
A1[i][i]=1-(r/2)*w[1]
for i in range(0,M-2):
A1[i][i+1]=-(r/2)*w[0]
for i in range(1,M-1):
for j in range(0,i):
A1[i][j]=-(r/2)*w[i-j+1]
for i in range(1,M):
s=0
for l in range(0,i+2):
s=s+w[l]*V[0][i-l+1]
b1[i-1]=V[0][i]+k*g(x[i])+(r/2)*s
V[1][1:M]=scipy.linalg.solve(A1, b1)
V[1][0]=0;V[1][M]=0
for i in range(0,M-1):
A2[i][i]=1-r*w[1]
for i in range(0,M-2):
A2[i][i+1]=-r*w[0]
for i in range(1,M-1):
for j in range(0,i):
A2[i][j]=-r*w[i-j+1]
for n in range(1,N):
for i in range(1,M):
s1,s2=0,0
for j in range(1,n):
```

```
s1=s1+((j+1)**(2-a)-j**(2-a))*(V[n-j+1][i]-2*V[n-j][i]+V[n-j-1][i])
s1=s1+2*((n+1)**(2-a)-(n)**(2-a))*(V[1][i]-V[0][i]-k*g(x[i]))
for l in range(0,i+2):
s2=s2+w[l]*V[n][i-l+1]
b2[i-1]=2*V[n][i]-V[n-1][i]-s1+r*s2
V[n+1][1:M]=scipy.linalg.solve(A2, b2)
V[n+1][0]=0;V[n+1][M]=0
t1=int(t1/k)
return(x,V[t1])
```

**Numerical experiment 1.** We consider the following space-time fractional traveling wave equation:

$$\frac{\partial^{\alpha} V}{\partial t^{\alpha}} = C^2 \frac{\partial^{\beta} V}{\partial x^{\beta}}, \ (x, t) \in \Omega = [0, 1] \times [0, 1] \tag{5.1}$$

with initial conditions:

$$V(x, 0) = \sin(2\pi x), \ \frac{\partial}{\partial t} V(x, 0) = 0, \ x \in [0, 1] \tag{5.2}$$

and boundary conditions,

$$V(0, t) = 0, \ V(1, t) = 0, \ t \in (0, 1] \tag{5.3}$$

The exact solution to this problem for $\alpha = 2, \beta = 2$ and $C = 1$ as follows:

$$V(x, t) = \sin(2\pi x)\cos(2\pi t)$$

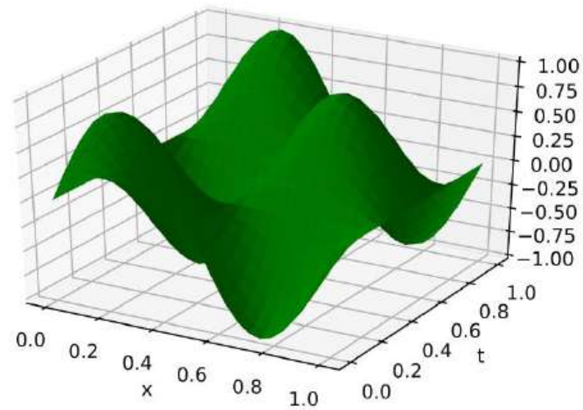


**Figure 1.** Periodic solution of traveling wave equation.

Using the python programme-CN, we estimate the value of $V(x, t)$ for any time level $t_n$. Let $\varepsilon(h, k)$ be the maximum error between exact and numerical solutions with temporal and spatial grid sizes $k$ and $h$ respectively. The temporal and spatial order of convergence are computed using

$$\text{temporal order } = \log_2\left(\frac{\varepsilon(h, 2k)}{\varepsilon(h, k)}\right), \text{ spatial order } = \log_2\left(\frac{\varepsilon(2h, k)}{\varepsilon(h, k)}\right).$$

In Table 1, we obtain the maximum error and order of convergence in temporal direction at time $t = 1$ with $h = 2^{-10}$.

**Table 1.** Maximum errors and temporal orders of convergence at $t = 1$, $h = 2^{-10}$.

| $k$ | Maximum error | Order |
|---|---|---|
| $2^{-5}$ | 0.264489 | – |
| $2^{-6}$ | 0.142758 | 0.89 |
| $2^{-7}$ | 0.074186 | 0.94 |
| $2^{-8}$ | 0.037816 | 0.97 |
| $2^{-9}$ | 0.019091 | 0.98 |
| $2^{-10}$ | 0.009592 | 0.99 |

In Table 2, we obtain the maximum error and order of convergence in spatial direction at

**Table 2.** Maximum errors and spatial orders of convergence at $x = 0.9999$, $k = 2^{-10}$.

| $h$ | Maximum error | Order |
|---|---|---|
| $2^{-2}$ | 0.999371 | – |
| $2^{-3}$ | 0.706478 | 0.50 |
| $2^{-4}$ | 0.382055 | 0.88 |
| $2^{-5}$ | 0.194462 | 0.97 |
| $2^{-6}$ | 0.097388 | 0.99 |
| $2^{-7}$ | 0.048439 | 1.00 |

$x = 0.9999$ with $k = 2^{-10}$.

From Table 1 and 2, we observe that the proposed finite difference scheme is first-order accurate in temporal as well as spatial direction. The order of convergence obtained in the numerical results agreed to the theoretical analysis. In Figure 2, we compare the exact and numerical solutions obtained by the Crank-Nicolson scheme and observe that the numerical solution is enormously agreed with the exact solution.

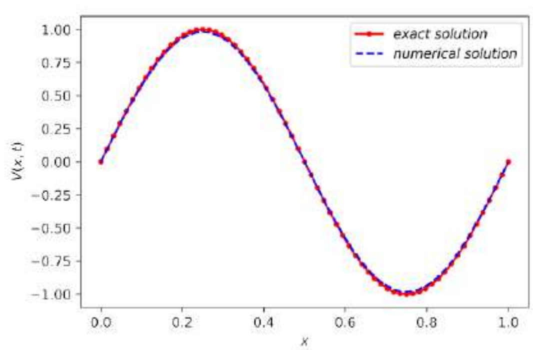


**Figure 2.** Comparison between exact and the numerical solutions with the parameters $h = 2^{-6}$, $k = 2^{-9}$, $t = 1$, $C = 1$.

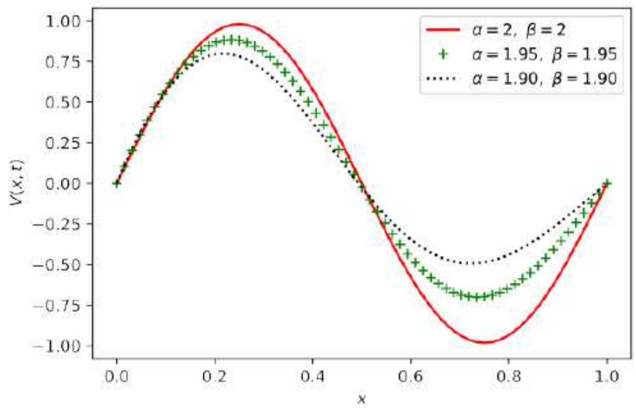


**Figure 3.** Comparison of the numerical solutions with the parameters $h = 2^{-6}$, $k = 2^{-9}$, $t = 1$, $C = 1$.

From Figure 3, we observed that the obtained solutions are stable and sufficiently approximate to the exact solutions and therefore, we conclude that the proposed scheme gives accurate results and stable solutions. Hence, Python is a powerful tool to obtain the numerical solutions of space-time fractional traveling wave equation.

**Numerical experiment 2.** We consider the following space-time fractional traveling wave equation:

$$\frac{\partial^{\alpha} V}{\partial t^{\alpha}} = C^2 \frac{\partial^{\beta} V}{\partial t^{\beta}},\ (x, t) \in \Omega = [0, 1] \times [0, 1]$$

subject to initial conditions:

$$V(x, 0) = 0,\ \frac{\partial}{\partial t} V(x, 0) = 2\pi C \sin(2\pi x),\ x \in (0, 1]$$

and boundary conditions,

$$V(0, t) = 0,\ V(1, t) = 0,\ t \in (0, 1]$$

The exact solution to this problem for $\alpha = 2, \beta = 2$ is $V(x, t) = \sin(2\pi x)\sin(2C\pi t)$. In Table 3 and 4, we obtain the order of convergence in temporal and spatial directions respectively.

**Table 3.** Maximum errors and temporal orders of convergence at $t = 0.75,\ h = 2^{-8}$.

| $k$ | Maximum error | Order |
|---|---|---|
| $2^{-6}$ | 0.106548 | – |
| $2^{-7}$ | 0.055491 | 0.94 |
| $2^{-8}$ | 0.028306 | 0.97 |
| $2^{-9}$ | 0.014285 | 0.98 |
| $2^{-10}$ | 0.007166 | 0.99 |
| $2^{-11}$ | 0.003580 | 1.00 |

**Table 4.** Maximum errors and spatial orders of convergence at $x = 0.9999,\ k = 2^{-10}$.

| $h$ | Maximum error | Order |
|---|---|---|
| $2^{-2}$ | 1.107705 | – |
| $2^{-3}$ | 0.723289 | 0.61 |
| $2^{-4}$ | 0.383607 | 0.91 |
| $2^{-5}$ | 0.194308 | 0.98 |
| $2^{-6}$ | 0.097193 | 0.99 |
| $2^{-7}$ | 0.048326 | 1.00 |

From these tables, it can be seen that the proposed finite difference scheme is first-order accurate in temporal as well as spatial direction.

In Figure 4, we obtain the numerical solutions using proposed finite difference scheme for different values of $t$ for $\alpha = 1.9,\ \beta = 1.8$.

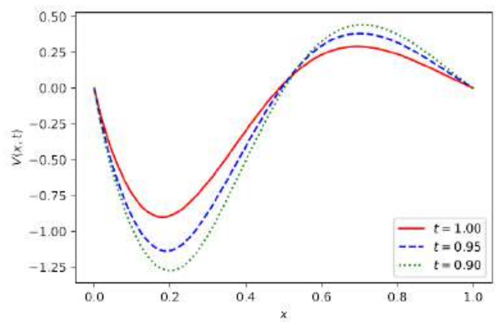


**Figure 4.** Behavior of the numerical solutions with the parameters $\alpha = 1.9$, $\beta = 1.8$, $h = 2^{-6}$, $k = 2^{-9}$, $C = 1$.

From Figure 4, we observe that solutions obtained by proposed scheme are stable and converges appropriately to the solution obtained at $t = 1$. In Figure 5, we obtain the numerical solutions for different values of $\alpha$ and $\beta$ at $t = 0.7$.

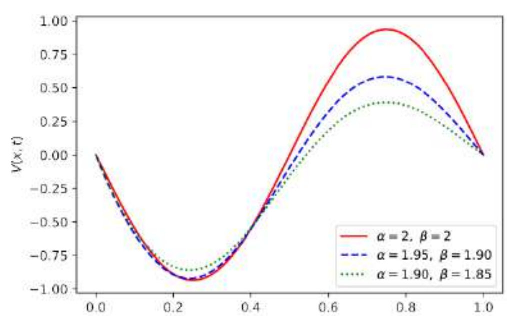


**Figure 5.** Behavior of the numerical solutions with the parameters $h = 2^{-6}$, $k = 2^{-9}$, $C = 1$, $t = 0.7$.

We observe that solutions obtained by proposed scheme are converges to the solution obtained for $\alpha = 2$, $\beta = 2$.

## 6. Conclusions

(i) We develop the Crank-Nicolson finite difference scheme for space-time fractional traveling wave equation.

(ii) Furthermore, we proved that the developed scheme is unconditionally stable and convergent.

(iii) We successfully develop a python programme for space-time fractional traveling wave equation and obtain the numerical solutions of the test problems and estimate the error.

(iv) Also, we found that the finite difference scheme is numerically stable and the results are compatible with our theoretical analysis.

(v) Finally, we conclude that Python is a powerful tool for obtaining the numerical solutions of space-time fractional traveling wave equation because the numerical results are very close to the exact solutions.

## References

[1] Elham Afshari, Behnam Sepehrian and Ali Mohamad Nazari, Finite difference method for solving the space-time fractional wave equation in the Caputo form, Fractional Differential Calculus 1 (2015), 55-63.

[2] R. Hilfer, Applications of Fractional Calculus in Physics, World Scientific, March 2000.

[3] Suryakant Jogdand, Sharvari Kulkarni and Kalyanrao Takale, On fractional order crank-nicolson finite difference scheme for space-time fractional convection diffusion equation, International Journal of Research and Analytical Reviews 6(1) (2019), 50-55.

[4] Hans Petter Langtangen and Svein Linge, Finite Difference Computing with PDEs: A Modern Software Approach, volume 16 of Texts in Computational Science and Engineering, Springer International Publishing, Cham, 2017.

[5] Jichun Li and Yi-Tung Chen, Computational partial differential equations using MATLAB. 2020. OCLC: 1127853350.

[6] Yuri Luchko, Fractional wave equation and damped waves, Journal of Mathematical Physics 54(3) (2013), 031505.

[7] Sam Morley, Applying math with python: practical recipes for solving computational math problems using Python programming and its libraries, Packt Publishing, Birmingham Mumbai, 2020.

[8] Igor Podlubny, Fractional differential equations: an introduction to fractional derivatives, fractional differential equations, to methods of their solution and some of their applications, Number V. 198 in Mathematics in science and engineering, Academic Press, San Diego, 1999.

[9] Arsen Pskhu and Sergo Rekhviashvili, Fractional Diffusion {Wave Equation with Application in Electrodynamics, Mathematics 8(11) (2020) 20-86.

[10] Fathalla A. Rihan, Numerical Modeling of Fractional-Order Biological Systems, Abstract and Applied Analysis 1 (2013), 1-11.

[11] Enrico Scalas, Rudolf Goreno and Francesco Mainardi, Fractional calculus and continuous-time finance, Physica A: Statistical Mechanics and its Applications 284(1-4) (2000), 376-384.

[12] Karl A. Seeler, Finite Difference Methods and MATLAB, In System Dynamics, Springer New York, New York, NY (2014), 467-517.

[13] G. W. Shrimangale, T. L. Holambe and K. C. Takale, Fractional order crank-nicolson finite difference scheme for time-space fractional radon diffusion equation in charcoal medium, International Journal of Research and Analytical Reviews 6(1) (2019), 831-836.

[14] G. D. Smith, Numerical solution of partial differential equations: finite difference methods, Oxford applied mathematics and computing science series, Clarendon Press; Oxford University Press, Oxford [Oxfordshire] : New York, 3rd ed. edition, 1985.

[15] Roelof J. Stroeker and Johan F. Kaashoek, Discovering Mathematics with Maple, Birkhauser Basel, Basel, 1999.

[16] K. C. Takale, V. R. Nikam and S. R. Kulkarni, Fractional order finite difference scheme for space fractional diffusion equation, Engineering and Automation Problems 3 (2014), 120-124.

[17] Yanfei Wang, Yaxin Ning and Yibo Wang, Fractional Time Derivative Seismic Wave Equation Modeling for Natural Gas Hydrate, Energies 13(22) (2020), 5901.

[18] Abdul-Majid Wazwaz, Partial differential equations and solitary waves theory, Nonlinear physical science, Higher Education Press Springer, Beijing Berlin, 2009.

Advances and Applications in Mathematical Sciences
Volume 22, Issue 2, December 2022, Pages 407-433


# CRANK-NICOLSON METHOD FOR TIME FRACTIONAL DRUG CONCENTRATION EQUATION IN CENTRAL NERVOUS SYSTEM

**UTTAM KHARDE, KALYANRAO TAKALE and SHRIKRISHNA GAIKWAD**

Department of Mathematics
S.N. Arts, D.J.M. Commerce
and B.N.S. Science College (Autonomous)
Sangamner-422605(M.S.), India

Department of Mathematics
R.N.C. Arts, J.D.B. Commerce
and N.S.C. Science College
Nashik Road, Nashik-422101, (M.S.), India
E-mail: kalyanraotakale1@gmail.com

Department of Mathematics
New Arts, Commerce and Science College
Ahmednagar-414001, (M.S.), India
E-mail: sbgmathsnagar@gmail.com

## Abstract

Recently, the treatment of central nervous system (CNS) diseases is a major problem in modern clinical world. Now, there are many drugs available that treat symptoms rather than the disease, therefore, new drugs and new techniques of treatment are needed. In human, cerebrospinal fluid (CSF) is easily accessible fluid that can be used to predict the drug concentration in CNS target site. This process can be represented by mathematical model of drug concentration equation with the help of integer order partial derivatives, but fractional order modeled scribes the drug concentration at CNS target site more precisely. Therefore, the purpose of this paper is to develop the fractional order Crank-Nicolson finite difference scheme to solve the time fractional drug concentration equation, formulated with Caputo fractional derivative. Also, we prove that the scheme is unconditionally stable and convergent. As an application of

2020 Mathematics Subject Classification: 26A33, 34A08, 97N40.
Keywords: Fractional Differential Equation, Caputo Derivative, Crank-Nicolson Finite Difference Scheme, CNS, Python.
*Corresponding author; E-mail: uttamkharde@gmail.com
Received June 2, 2021; Accepted December 14, 2021

this scheme, numerical solutions of fractional order drug concentration equation in the central nervous system is examined to verify the stability and these solutions are simulated graphically using Python.

## 1. Introduction

Fractional calculus is a newly developed branch of mathematics which deals with the study of derivatives and integrations of arbitrary order. In recent years, many areas of applied science and technology have used fractional order approach to describe certain phenomena and processes. Fractional order mathematical models describing the physical phenomena are appears in many applications of sciences, such as the fractional diffusion equation [24], fractional subdiffusion equation [31], fractional wave equation [6, 24], fractional Boussinesq's equation [28], fractional heat equation, fractional viscoelastic theory [2], etc. The arbitrary order mathematical model provides better physical analysis rather than integer order model, because it provides results at any inter-mediate stage by considering all the inputs starting from initial stage rather than only previous stage [12]. Many dynamical models of physics, engineering, biomedical, fluid dynamics, hydrology, etc. [4, 3, 7, 12, 15, 18, 19, 21] are modeled by fractional order partial differential equations. Now a days, due to its tremendous applications in various fields, a remarkable attention has been given to find its exact and approximate solution. Due to non-local nature of fractional derivative, many fractional differential equations do not have exact solutions. Therefore, to solve the fractional differential equations, numerical techniques are more demanding. To develop numerical methods for solving fractional differential equations, which are accurate and timely efficient is the primary challenge to researchers. We observed that the fractional derivatives in Caputo sense is more feasible to analyze the physical problem and it allowed to deal with integer-order initial and boundary conditions [7]. Finite difference method is one of the more effective and commonly used method to solve fractional differential equations. In the literature [9, 10, 11, 14, 17, 20, 23, 25, 26, 28], finite difference method is successfully used to obtain the numerical solutions of fractional differential equations.

Now a days, Pharmacokinetics is the branch of Pharmacology which study the drug absorption, distribution, metabolism and excretion in human body [13]. In Pharmacology, one of the significant challenge is the development of drugs targeting disease of the central nervous system (CNS). Due to medical ethics, direct measurement of brain concentration is restricted and due to presence of bloodbra in barrier (BBB), the prediction of target site concentration of CNS drug is more complicated [32]. Many researchers [9, 29, 30, 32] in pharmacology has developed a physiologically based pharmacokinetics modeling describing a drug concentration in CNS. The Advection-Diffusion equation describes the evolution of a concentration profile due to diffusion and advection simultaneously [1]. A mathematical modeling describing the drug concentration in CNS based on Advection-Diffusion equation is studied in [5]. In this context, we study the fractional order drug concentration equation in the central nervous system. Furthermore, we develop the Crank-Nicolson fractional order finite difference scheme for fractional order drug concentration equation and obtain its approximate solution. There are many numerical techniques developed for solving fractional differential equations using mathematical softwares [6, 10, 16]. We observed that, Python is a high level multi-purpose programming language having large number of mathematical tools. Recently, Python is used for teaching as well as research in various branches of applied mathematics. Therefore, in this connection we develop Python programme to obtain the numerical solution of the drug concentration equation by the proposed scheme.

We organized the paper as follows: In section 2, we develop the fractional order Crank-Nicolson finite difference scheme for time fractional drug concentration equation. Section 3 is devoted for stability of the solution obtained by the scheme. In section 4, convergence of the scheme is discussed up to the length. In section 5, the approximate solution of the time fractional drug concentration equation is computed and it is simulated graphically by Python. We consider the time fractional drug concentration equation with initial and boundary conditions as follows

$$\frac{\partial^{\alpha} c(x, t)}{\partial t^{\alpha}} = -v \frac{\partial c(x, t)}{\partial x} + D \frac{\partial^2 c(x, t)}{\partial x^2}, \; 0 < \alpha \leq 1, \; 0 \leq x \leq L, \; 0 \leq t \leq T \quad (1.1)$$

$$\text{initial condition: } c(x, 0) = 0, \; 0 < x < L \quad (1.2)$$

$$\text{boundary conditions: } c(0, t) = g(t), \; \frac{\partial c(L, t)}{\partial x} = 0, \; t \geq 0 \quad (1.3)$$

where $c(x, t)$ is the drug concentration in CSF space at time $t$ and place $x$, $v$ is the flow velocity and $D$ is the diffusion coefficient. We discretized time fractional order derivative in the Caputo sense.

The Caputo derivative of order $\alpha$ is defined as follows [22, 23]

$$\frac{\partial^{\alpha} c(x, t)}{\partial t^{a}} = \frac{1}{\Gamma(1-\alpha)} \int_0^t (x - \tau)^{-\alpha} \frac{\partial c(x, \tau)}{\partial \tau} d\tau, \; 0 < \alpha \leq 1 \tag{1.4}$$

where $\Gamma(\cdot)$ is the gamma function defined as

$$\Gamma(\alpha) = \int_0^{\infty} e^{-x} x^{\alpha - 1} dx. \tag{1.5}$$

## 2. Finite Difference Scheme

In this section, we develop the fractional order Crank-Nicolson finite difference scheme for time fractional drug concentration equation (1.1)-(1.3). For this, we define $x_i = i\Delta x$, $i = 0, 1, 2, 3, \ldots, M$ and $t_k = k\Delta t$, $k = 0, 1, 2, 3, \ldots, N$, where $\Delta x = \frac{L}{M}$ and $\Delta t = \frac{T}{N}$. Let $c(x_i, t_k)$, $i = 0, 1, 2, 3, \ldots, M$ and $k = 0, 1, 2, 3, \ldots, N$, be the exact solution of time fractional drug concentration equation (1.2)-(1.3) at mesh point $(x_i, t_k)$ and let $c_i^k$ be the numerical approximation at point $(x_i, t_k)$. The time fractional drug concentration equation with initial and boundary conditions (1.1)-(1.3) is discretized by using the second order accurate central difference formula for space derivative and finite difference formula for the time fractional derivative for each interior grid point $(i\Delta x, k\Delta t)$. At time level $t = t_{k+1}$, the Caputo time fractional derivative of order $\alpha$ is discretized as follows

$$\begin{aligned}\left(\frac{\partial^{\alpha} c}{\partial t^{\alpha}}\right)_{(x_i, t_{k+1})} &= \frac{1}{\Gamma(1-\alpha)} \int_0^{t_{k+1}} (t_{k+1} - s)^{-\alpha} \frac{\partial c(x_i, s)}{\partial s} \\ &= \frac{1}{\Gamma(1-\alpha)} \sum_{j=0}^{k} \int_{t_j}^{t_{j+1}} (t_{k+1} - s)^{-\alpha} \left[\frac{c_i^{j+1} - c_i^j}{\Delta t} + O(\Delta t)\right] ds\end{aligned}$$

$$= \frac{1}{\Gamma(1-\alpha)} \sum_{j=0}^{k} \left[ \frac{c_i^{j+1} - c_i^j}{\Delta t} + O(\Delta t) \right] \int_{t_j}^{t_{j+1}} (t_{k+1} - s)^{-\alpha} ds$$

$$= \frac{1}{\Gamma(1-\alpha)} \sum_{j=0}^{k} \left[ \frac{c_i^{j+1} - c_i^j}{\Delta t} + O(\Delta t) \right] \left[ \frac{(k-j+1)^{1-\alpha} - (k-j)^{1-\alpha}}{(1-\alpha)(\Delta t)^{\alpha-1}} \right]$$

$$= \frac{(\Delta t)^{-\alpha}}{\Gamma(2-\alpha)} \sum_{j=0}^{k} [c_i^{k-j+1} - c_i^{k-j} + O(\Delta t)][(j+1)^{1-\alpha} - j^{1-\alpha}]$$

$$= \frac{(\Delta t)^{-\alpha}}{\Gamma(2-\alpha)} \sum_{j=0}^{k} [c_i^{j+1} - c_i^{k-j} + O(\Delta t)] b_j$$

$$= \frac{(\Delta t)^{-\alpha}}{\Gamma(2-\alpha)} \sum_{j=0}^{k} b_j [c_i^{j+1} - c_i^{k-j}] + \frac{(\Delta t)^{-\alpha}}{\Gamma(2-\alpha)} \sum_{j=0}^{k} b_j O(\Delta t)$$

where $b_j = (j+1)^{1-\alpha} - j^{1-\alpha}$, $j = 0, 1, 2, 3, \ldots, k$.

Since, $k\Delta t \leq T$ is finite, the above equation can be written as,

$$\left( \frac{\partial^\alpha c}{\partial t^\alpha} \right)_{(x_i, t_{k+1})} = \frac{(\Delta t)^{-\alpha}}{\Gamma(2-\alpha)} [c_i^{k+1} - c_i^k] + \frac{(\Delta t)^{-\alpha}}{\Gamma(2-\alpha)} \sum_{j=1}^{k} b_j [c_i^{k-j+1} - c_i^{k-j}] + O(\Delta t). \tag{2.1}$$

Furthermore, the space derivatives $\frac{\partial c}{\partial x}$ is disretized as follows

$$\left( \frac{\partial c}{\partial x} \right)_{(x_i, t_{k+1})} = \frac{c_{i+1}^k - c_{i-1}^k}{2\Delta x} + O(\Delta x) \tag{2.2}$$

The space derivative $\frac{\partial^2 c}{\partial x^2}$ is discretized by using second order central difference scheme as follows

$$\left( \frac{\partial^2 c}{\partial x^2} \right)_{(x_i, t_{k+1})} = \frac{\delta_x^2 c_i^{k+1} + \delta_x^2 c_i^k}{2}$$

$$\therefore \left(\frac{\partial^2 c}{\partial x^2}\right)_{(x_i, t_{k+1})} = \frac{1}{2\Delta x^2}[c_{i-1}^{k+1} - 2c_i^{k+1} + c_{i+1}^{k+1} + c_{i-1}^{k} - 2c_i^{k} + c_{i+1}^{k}] + O(\Delta x^2) \quad (2.3)$$

where $\delta_x$ is the central difference operator.

Now, using equations (2.1), (2.2) and (2.3) in equation (1.1), we obtain

$$\frac{(\Delta t)^{-\alpha}}{\Gamma(2-\alpha)}[c_i^{k+1} - c_i^k] + \frac{(\Delta t)^{-\alpha}}{\Gamma(2-\alpha)}\sum_{j=1}^{k} b_j[c_i^{k-j+1} - c_i^{k-j}]$$

$$= \frac{-v}{2\Delta x}[c_{i+1}^k - c_{i-1}^k] + \frac{D}{2\Delta x^2}[c_{i-1}^{k+1} - 2c_i^{k+1} + c_{i+1}^{k+1} + c_{i-1}^{k} - 2c_i^{k} + c_{i+1}^{k}]$$

This gives, $[c_i^{k+1} - c_i^k] + \sum_{j=1}^{k} b_j[c_i^{k-j+1} - c_i^{k-j}]$

$$= -v\frac{(\Delta t)^{\alpha}\Gamma(2-\alpha)}{2\Delta x}[c_{i+1}^k - c_{i-1}^k]$$

$$+ D\frac{(\Delta t)^{\alpha}\Gamma(2-\alpha)}{2\Delta x^2}[c_{i-1}^{k+1} - 2c_i^{k+1} + c_{i+1}^{k+1} + c_{i-1}^{k} - 2c_i^{k} + c_{i+1}^{k}]$$

By taking $\mu = v\frac{(\Delta t)^{\alpha}\Gamma(2-\alpha)}{2\Delta x}$ and $r = D\frac{(\Delta t)^{\alpha}\Gamma(2-\alpha)}{2\Delta x^2}$, we get

$$[c_i^{k+1} - c_i^k] + \sum_{j=1}^{k} b_j[c_i^{k-j+1} - c_i^{k-j}] = -\mu[c_{i+1}^k - c_{i-1}^k]$$

$$+ r[c_{i-1}^{k+1} - 2c_i^{k+1} + c_{i+1}^{k+1} + c_{i-1}^{k} - 2c_i^{k} + c_{i+1}^{k}]$$

$$-rc_{i-1}^{k+1} + (1+2r)c_i^{k+1} - rc_{i+1}^{k+1} = (r+\mu)c_{i-1}^k + (1-2r)c_i^k + (r-\mu)c_{i+1}^k$$

$$-\sum_{j=1}^{k} b_j(c_i^{k-j+1} - c_i^{k-j}) \quad (2.4)$$

After simplification, for $k = 0, 1, 2, 3, \ldots, N,$ we obtain

$$-rc_{i-1}^{k+1} + (1+2r)c_i^{k+1} - rc_{i+1}^{k+1} = (r+\mu)c_{i-1}^k + (1-2r-b_1)c_i^k + (r-\mu)c_{i+1}^k$$

$$-\sum_{j=1}^{k}(b_j - b_{j+1})c_i^{k-j} + b_k c_i^0. \tag{2.5}$$

Now, put $k = 0$ in equation (2.4), we get

$$-rc_{i-1}^{k+1} + (1+2r)c_i^1 - rc_{i+1}^1 = (r+\mu)c_{i-1}^0 + (1-2r)c_i^0 + (r-\mu)c_{i+1}^0. \tag{2.6}$$

Finally, the initial condition $c(x, 0) = 0\,(0 < x < L)$ is approximated as follows:

$$c_i^0 = 0,\ i = 1, 2, 3, \ldots, M. \tag{2.7}$$

Also, the boundary conditions $c(0, t) = g(t)$ and $\frac{\partial c(L, t)}{\partial x} = 0\,(t \geq 0)$ are approximated as follows

$$c(0, t_k) = g(t_k) \text{ implies } c_0^k = g(t_k),\ k = 0, 1, 2, 3, \ldots, N \tag{2.8}$$

and

$$\frac{\partial c(L, t_k)}{\partial x} = 0 \text{ implies } \frac{c_{M+1}^k - c_{M-1}^k}{2\Delta x} = 0$$

This gives,

$$c_{M+1}^k = c_{M-1}^k,\ k = 0, 1, 2, 3, \ldots, N. \tag{2.9}$$

Thus, the complete discretized time fractional drug concentration equation with initial and boundary condition is as follows

$$-rc_{i-1}^1 + (1+2r)c_i^1 - rc_{i+1}^1 = (r+\mu)c_{i-1}^0 + (1-2r)c_i^0 + (r-\mu)c_{i+1}^0, \text{ for } k = 0 \tag{2.10}$$

$$-rc_{i-1}^{k+1} + (1+2r)c_i^{k+1} - rc_{i+1}^{k+1} = (r+\mu)c_{i-1}^k + (1-2r-b_1)c_i^k + (r-\mu)c_{i+1}^k$$

$$+\sum_{j=1}^{k}(b_j - b_{j+1})c_i^{k-j} + b_k c_i^0, \text{ for } k \geq 1 \tag{2.11}$$

$$\text{initial condition: } c_i^0 = 0,\ i = 1, 2, 3, \ldots, M \tag{2.12}$$

$$\text{boundary conditions: } c_0^k = g(t_k),\ c_{M+1}^k = c_{M-1}^k,\ k = 0, 1, 2, 3, \ldots, N \tag{2.13}$$

where $\mu = v\frac{(\Delta t)^{\alpha}\Gamma(2-\alpha)}{2\Delta x}$, $r = D\frac{(\Delta t)^{\alpha}\Gamma(2-\alpha)}{2\Delta x^2}$, $b_j = (j+1)^{1-\alpha} - j^{1-\alpha}$,

$j = 1, 2, 3, \ldots$ and $k = 0, 1, 2, 3, \ldots, N$, $i = 1, 2, 3, \ldots, M$.

Therefore, the discretized fractional order Crank-Nicolson finite difference scheme (2.10)-(2.13) can be expressed in matrix form as follows

$$AC^1 = BC^0 + S^0, \text{ for } k = 0 \tag{2.14}$$

$$AC^{k+1} = FC^k + \sum_{j=1}^{k-1}(b_j - b_{j+1})C^{k-j} + b_k C^0 + S^k, \text{ for } k \geq 1 \tag{2.15}$$

$$\text{initial condition: } c_i^0 = 0, i = 1, 2, 3, \ldots, M \tag{2.16}$$

$$\text{boundary conditions: } c_0^k = g(t_k), c_{M+1}^k = c_{M-1}^k, k = 0, 1, 2, 3, \ldots, N \tag{2.17}$$

where $C^k = (c_1^k, c_2^k, c_3^k, \ldots, c_M^k)^T$, $S^k = ((r+\mu)g(t_k) + rg(t_{k+1}), 0, 0, \ldots, 0)^T$ is a constant matrix,

$$A = \begin{pmatrix} 1+2r & -r & & & & & \\ -r & 1+2r & -r & & & & \\ & \ddots & \ddots & \ddots & & & \\ & & -r & 1+2r & -r & & \\ & & & \ddots & \ddots & \ddots & \\ & & & & -r & 1+2r & -r \\ & & & & & -2r & 1+2r \end{pmatrix}$$

$$B = \begin{pmatrix} 1-2r & r-\mu & & & & & \\ r+\mu & 1-2r & r-\mu & & & & \\ & \ddots & \ddots & \ddots & & & \\ & & r+\mu & 1-2r & r-\mu & & \\ & & & \ddots & \ddots & \ddots & \\ & & & & r+\mu & 1-2r & r-\mu \\ & & & & & 2r & 1-2r \end{pmatrix}$$

and

$$F = \begin{pmatrix} 1-2r-b_1 & r-\mu & & & & & \\ r+\mu & 1-2r-b_1 & r-\mu & & & & \\ & \ddots & \ddots & \ddots & & & \\ & & r+\mu & 1-2r-b_1 & r-\mu & & \\ & & & \ddots & \ddots & \ddots & \\ & & & & r+\mu & 1-2r-b_1 & r-\mu \\ & & & & & 2r & 1-2r-b_1 \end{pmatrix}$$

## 3. Stability

In this section, we discuss the stability of solution of the fractional order Crank-Nicolson finite difference scheme (2.10)-(2.13) developed for the time fractional drug concentration equation (1.1)-(1.3) with initial and boundary conditions.

**Lemma 3.1.** *The eigenvalues of* $M \times M$ *tri-diagonal matrix*

$$\begin{pmatrix} a & b & & & & & \\ c & a & b & & & & \\ & \ddots & \ddots & \ddots & & & \\ & & c & a & b & & \\ & & & \ddots & \ddots & \ddots & \\ & & & & c & a & b \\ & & & & & c & a \end{pmatrix}$$

*are given as*

$$\lambda_s = a + 2\sqrt{bc}\cos\left(\frac{s\pi}{M+1}\right),\ s = 1, 2, 3, \ldots, M$$

*where* $a$, $b$ *and* $c$ *are either real or complex numbers* [25].

**Lemma 3.2.** *If* $\lambda_j(A)$, $j = 1, 2, 3, 4, \ldots, M-1$ *represent eigenvalues of a matrix* $A$, *then following conditions are hold*

(i) $\lambda_j(A) \geq 1$

(i) $\| A^{-1} \|_2 \leq 1$, *where* $\| \cdot \|_2$ *is the second norm of matrix.*

**Proof.** By the Gerschgorin's circle theorem [25], if $\lambda$ is a eigenvalue of a square matrix $[a_{ij}]$ then $\lambda$ is in at least one of the following disc

$$| \lambda - a_{ij} | \leq \sum_{l=1,\, l \neq j}^{M} a_{lj},\ l = 1, 2, 3, \ldots, M. \tag{3.1}$$

Thus, each eigenvalue $\lambda$ of a square matrix $[a_{ij}]$ satisfy at least one of the following inequality

$$| \lambda | \leq \sum_{i=1}^{M} | a_{ij} | \tag{3.2}$$

$$| \lambda | \geq | a_{ij} | - \sum_{i=1,\, i \neq j}^{M} | a_{ij} | \tag{3.3}$$

Now, we use inequality (3.3) to prove the condition (i) for the matrix $A$ as

$$| \lambda_1(A) | \geq | (1 + 2r) + (-r) | = 1 + r \geq 1$$

$$| \lambda_2(A) | \geq | (1 + 2r) + (-r) + (-r) | = 1$$

$$| \lambda_3(A) | \geq | (1 + 2r) + (-r) + (-r) | = 1$$

$$\vdots$$

$$| \lambda_M(A) | \geq | (1 + 2r) + (-r) + (-r) | = 1$$

Thus, $| \lambda_j | \geq 1,\ j = 1, 2, 3, \ldots, M.$

To prove condition (ii), we have

$$\| A \|_2 = \max_{1 \leq j \leq M} | \lambda_j(A) |.$$

Therefore, from condition (i), we get

$$\| A \|_2 \geq 1.$$

Hence,

$$\| A^{-1} \|_2 \leq 1$$

This complete the proof. □

**Lemma 3.3.** *The discretized fractional order Crank-Nicolson finite difference scheme with initial and boundary conditions* (2.10)-(2.13) *is* *solvable for each time step unconditionally.*

**Proof.** To prove the solvability of equations (2.10) and (2.12), it is enough to prove that matrix $A$ is invertible [8, 27]. We observed that, the first and last row of matrix $A$ is diagonally dominant. For other rows, the diagonal element is $1 + 2r$ and the sum of the absolute values of the non-diagonal element in the same row is,

$$|(-r)| + |(-r)| = 2r.$$

Hence, for each row, we have $1 + 2r > 2r$. Thus, matrix $A$ is strictly diagonally dominant. Hence, matrix $A$ is invertible. This shows that the solvability of the finite difference scheme. □

**Lemma 3.4.** *If* $\lambda_s(B)$ *and* $\lambda_s(F)$ *represents the eigenvalues of* $B$ *and* $F$ *respectively, then following conditions are hold*

(i) $|\lambda_s(B)| \leq 1, |\lambda_s(F)| \leq 1, s = 1, 2, 3, \ldots, M$

(ii) $\| B \|_2 \leq 1, \| F \|_2 \leq 1, s = 1, 2, 3, \ldots, M.$

**Theorem 3.5.** *The solution of the fractional order Crank-Nicolson finite difference scheme* (2.10)-(2.13) *for time fractional drug concentration equation* (1.1)-(1.3) *is unconditionally stable.*

**Proof.** To prove the developed finite difference scheme is unconditionally stable, we will prove that

$$\| C^n \|_2 \leq K \| C^0 \|_2, n = 1, 2, 3, \ldots$$

where $K$ is positive integer independent of $x$ and $t$.

For $n = 1$, from equation (2.14), we obtain

$$C^1 = A^{-1}BC^0 + A^{-1}S^0$$

$$\therefore \| C^1 \|_2 \leq \| A^{-1} \|_2 \| B \|_2 \| C^0 \|_2 + \| A^{-1} \|_2 \| S^0 \|_2$$

$$\leq \| C^0 \|_2 + \| S^0 \|_2$$

$$\leq \| C^0 \|_2 + K_1 \| C^0 \|_2, \text{ where } \| S^0 \|_2 = K_1, \text{ a constant.}$$

Thus, result is true for $n = 1$.

For $n \leq k,$ let us assume that

$$\| C^k \|_2 \leq K \| C^0 \|_2.$$

Now, for $n = k + 1,$ from equation (2.15), we obtain

$$C^{k+1} = A^{-1}FC^k + A^{-1}\sum_{j=1}^{k-1}(b_j - b_{j+1})C^{k-j}b_k C^0 + A^{-1}S^K.$$

$$\therefore \| C^{k+1} \|_2 \leq \| C^k \|_2 + \sum_{j=1}^{k-1}(b_j - b_{j+1})\| C^{k-j} \|_2 + b_k \| C^0 \|_2 + \| S^K \|_2$$

$$= \| C^k \|_2 + [(b_1 - b_2)\| C^{k-1} \|_2 + (b_2 - b_3)\| C^{k-2} \|_2 + \ldots + (b_{k-1} - b_k)\| C^1 \|_2]$$

$$+ b_k \| C^0 \|_2 + \| S^k \|_2$$

$$\leq K_1 \| C^0 \|_2 + [(b_1 - b_2) + (b_2 - b_3) + \ldots + (b_{k-1} - b_k)]K_2 \| C^0 \|_2 + b_k \| C^0 \|_2 + K_3$$

$$\leq [K_1 + b_1 + (1 - K_2)b_k]\| C^0 \|_2 + K_3 \| C^0 \|_2$$

$$= K \| C^0 \|_2.$$

Hence, by induction, for all $n$, we have

$$\| C^n \|_2 \leq K \| C^0 \|_2$$

where $K$ is a positive number independent of $x$ and $t$.

Therefore, this shows that the scheme is unconditionally stable.

This complete the proof. □

## 4. Convergence

In this section, we discuss the convergence of the scheme. Let $\Omega$ be the region $[0, L] \times [0, T]$. We introduce the vector, $\overline{C}^k = (\bar{c}(x_0, t_k), \bar{c}(x_1, t_k), \bar{c}(x_2, t_k), \ldots, \bar{c}(x_M, t_k))^T$ of size $M + 1,$ which represent the exact solution of the time fractional drug concentration equation (1.1)-(1.3) at time level $t_k$.

Let $\tau^k = (\tau_1^k, \tau_2^k, \tau_3^k, \ldots, \tau_M^k)^T$ be the vector of truncation error at time level $t_k$. Since $\overline{C}^k$ is the exact solution of the equation (1.1)-(1.3), we have

$$A\overline{C}^1 = B\overline{C}^0 + S^0 + \tau^1, \text{ for } k = 0. \tag{4.1}$$

$$A\overline{C}^{k+1} = F\overline{C}^k + \sum_{j=1}^{k-1}(b_j - b_{j+1})\overline{C}^{k-j} + b_k\overline{C}^0 + S^k + \tau^{k+1}, \text{ for } k \geq 1. \tag{4.2}$$

**Lemma 4.1.** *The coefficient* $b_j$, $j = 0, 1, 2, 3, \ldots$ *satisfy the following conditions*

(i) $b_j > 0$

(ii) $b_j > b_j + 1$.

**Theorem 4.2.** *The fractional order Crank-Nicolson finite difference scheme* (2.10)-(2.13) *for time fractional drug concentration equation* (1.1)-(1.3) *is unconditionally convergent*.

**Proof.** We set, $E^k = \overline{C}^k - C^k = (e_1^k, e_2^k, e_3^k, \ldots, e_M^k)^T$ be the error vector in the solution at time level $t_k$. Furthermore, we assume that $| e_l^k | = \max_{1\leq i\leq M}| e_i^k | = \| E^k \|_\infty$ and $\tau_l^k = \max_{1\leq i\leq M}| \tau_i^k |$, for $l = 1, 2, 3, \ldots$

Then, using equation (2.10), we obtain

$$| e_l^1 | = | -re_{i-1}^1 + (1 + 2r)e_i^1 - re_{i+1}^1 |$$

$$\leq (r + \mu)| e_{i-1}^0 | + (1 - 2r)| e_i^0 | + (r - \mu)| e_{i+1}^0 | + | \tau_l^1 |$$

$$\leq (r + \mu + 1 - 2r + r - \mu)\max_{1\leq i\leq M}| e_i^0 | + \max_{1\leq i\leq M}| \tau_i^1 |$$

$$= \| E^0 \|_\infty + \max_{1\leq i\leq M}| \tau_i^1 |$$

$$\therefore \| E^1 \|_\infty \leq \| E^0 \|_\infty + \max_{1\leq i\leq M}| \tau_i^1 |$$

Now, from equation (2.11), we obtain

$$| e_l^{k+1} | = | -re_{i-1}^{k+1} + (1 + 2r)e_i^{k+1} - re_{i+1}^{k+1} |$$

$$\leq (r+\mu)|e_{i-1}^{k}| + (1-2r-b_1)|e_i^k| + (r-\mu)|e_{i+1}^{k}| + \sum_{j=1}^{k-1}(b_j - b_{j+1})|e_i^{k-j}|$$

$$+ b_k|e_i^0| + |\tau_l^{k+1}|$$

$$= (r+\mu)|e_{i-1}^{k}| + (1-2r-b_1)|e_i^k| + (r-\mu)|e_{i+1}^{k}| + (b_1 - b_2)|e_i^{k-1}|$$

$$+ (b_2 - b_3)|e_i^{k-2}| + \ldots + (b_{k-1} - b_k)|e_i^1| + b_k|e_i^0| + |\tau_i^{k+1}|$$

$$= [(r+\mu) + (1-2r-b_1) + (r-\mu)]|e_l^k| + [(b_1 - b_2) + (b_2 - b_3) + \ldots + (b_{k-1} - b_k)]$$

$$|e_l^k| + b_k|e_l^k| + \max_{1\leq i\leq M}|\tau_i^{k+1}|$$

$$= \| E^k \|_\infty + \max_{1\leq i\leq M}|\tau_i^{k+1}|.$$

This is true for every $k$, therefore we have

$$\| E^{k+1} \|_\infty \leq \| E^k \|_\infty + \max_{1\leq i\leq M}|\tau_i^{k+1}|$$

Hence, by induction, we get

$$\| E^{n+1} \|_\infty \leq \| E^n \|_\infty + \max_{1\leq i\leq M}|\tau_i^{n+1}|$$

As $\| E^0 \|_\infty = 0,$ implies $\| E^n \|_\infty = 0.$

Therefore, $\| E^{n+1} \|_\infty \leq \max_{1\leq i\leq M}|\tau_i^{n+1}|.$

Since $\max_{1\leq i\leq M}|\tau_i^{n+1}| \to 0$ as $(\Delta x, \Delta t) \to (0, 0),$ implies that $\| E^{n+1} \|_\infty \to 0$ uniformly on $\Omega$ as $(\Delta x, \Delta t) \to (0, 0).$

Therefore, this shows that for any $x$ and $t$, as $(\Delta x, \Delta t) \to (0, 0),$ the vector $C^n$ converges to $\overline{C}^n.$

Hence, this complete the proof. □

## 5. Python Programme

In this section, we develop the algorithm for solving the discretized scheme (2.10)-(2.13) using Python programme. Here we compute $c_i^k$ at each mesh point $(x_i, t_k)$ using the proposed scheme by Python. The algorithm for the scheme (2.14)-(2.17) is as follows

(i) Define $g(t_k)$ for each $k = 0, 1, 2, 3, \ldots, N$.

(ii) Compute the matrix $A$, $B$ and $F$.

(iii) Compute $C^0$ and $S^0$, then compute $C^1$.

(iv) Compute $S^1$. Then using $C^1$, compute $C^2$.

(v) Compute $S^k$. Then compute $C^{k+1}$ for each $k = 2, 3, 4, \ldots, N$.

Now, we develop the python programme DCE for complete discretized scheme (2.14)-(2.17) as follows:

Inputs:

g - boundary condition at x=0.

C - drug concentration

L - spatial length

T - end time

D - diffusion coefficient of drugs

mu - μ

a - fractional order α of time derivative

t1 - time at which solution to be estimated.

Output of Python programme DCE is the approximate value of vector $C(x_i, t_k)$.

```
import scipy

from scipy import *

import math

from math import *
```

```
def g(k):
    return(c(0,t))
import numpy as np
def DCE(g,v,L,T,dx,dt,D,a,t1):
    r=dt**a*D*math.gamma(2-a)/(2*dx**2)
    mu=v*dt**a*math.gamma(2-a)/(2*dx)
    N=int(round(T/dt))
    M=int(round(L/dx))
    t=np.linspace(0,N*dt,N+1)
    x=np.linspace(0,M*dx,M+1)
    A = np.zeros((M+1, M+1))
    A[0, 0] = 1+2*r
    A[0, 1]=-r
    A[M,M-1]=-2*r
    A[M, M] = 1+2*r
    for i in range(1, M):
        A[i, i-1] = -r
        A[i, i] = 1+2*r
        A[i, i+1] = -r
B=np.zeros((M+1,M+1))
B[0,0]=1-2*r
B[0,1]=r-mu
B[M,M-1]=2*r
B[M,M]=1-2*r
for i in range(1,M):
   B[i, i-1] = r+mu
```

```
    B[i, i] = 1-2*r
    B[i, i+1] = r-mu
F=np.zeros((M+1,M+1))
F[0,0]=1-2*r-((1+1)**(1-a)-1**(1-a))
F[0,1]=r-mu
F[M,M-1]=2*r
F[M,M]=1-2*r-((1+1)**(1-a)-1**(1-a))
for i in range(1,M):
    F[i, i-1] = r+mu
    F[i, i] = 1-2*r-((1+1)**(1-a)-1**(1-a))
    F[i, i+1] = r-mu
C=np.zeros((N+1,M+1))
S0=np.zeros(M+1)
S0[0]=(r+mu)*g(t[0])+r*g(t[1])
b0=B@C[0]+S0
C[1]=scipy.linalg.solve(A,b0)
S1=np.zeros(M+1)
S1[0]=(r+mu)*g(t[1])+r*g(t[2])
b1=F@C[1]+S1
C[2]=scipy.linalg.solve(A,b1)
for k in range(2,N):
    ek=(k+1)**(1-a)-k**(1-a)
    Sk=np.zeros(M+1)
    Sk[0]=(r+mu)*g(t[k])+r*g(t[k+1])
    sum=np.zeros(M+1)
    for j in range(1,k):
```

```
        sum=sum+((j+1)**(1-a)-j**(1-a)-(j+2)**(1-a)+(j+1)**(1-a))*C[k-j]
    bk=F@C[k]+sum+ek*C[0]+Sk
    C[k+1][:]=scipy.linalg.solve(A,bk)
t1=int(t1/dt)
return(x,C[t1])
```

## 6. Numerical Solutions

In this section, we obtain the approximate solution of time fractional drug concentration equation (1.1)-(1.3) by a developed fractional order Crank-Nicolson finite difference scheme (2.10)-(2.13).

### 6.1 Test Problem 1. Steady State Concentration

In pharmacology, the steady state of drug is an important fundamental concept. Steady-state is a situation during which the concentration of drug in the body is stable. In the treatment of CNSdisease, understanding of steady-state is important for choosing the right dose and determining the dosing interval to achieve a desire steady-state concentration. This is the situation corresponds to where maintenance dose is given in order to keep the drug concentration constant in the brain ECF [5]. If the concentration in brain ECF remains constant, then we will obtain the drug concentration in the CSF changes along the CSF space by the following drug concentration equation

$$\frac{\partial^{\alpha} c(x, t)}{\partial t^{a}} = -\upsilon \frac{\partial c(x, t)}{\partial x} + D \frac{\partial^{2} c(x, t)}{\partial x^{2}}, \; 0 < \alpha \leq 1, \; 0 \leq x \leq 8, \; t \geq 0$$

$$\text{initial condition: } c(x, 0) = 0, \; 0 \leq x < 8$$

$$\text{boundary conditions: } c(0, t) = 3, \; \frac{\partial c(8, t)}{\partial x} = 0 \, (t \geq 0).$$

The exact solution of the problem for $\alpha = 1$ is given as [5]

$$c(x, t) = \frac{3}{2}\left( erfc\left(\frac{x - \upsilon t}{2\sqrt{Dt}}\right) + e^{\frac{\upsilon x}{D}} erfc\left(\frac{x + \upsilon t}{2\sqrt{Dt}}\right)\right).$$

With the help of Python programme DCE, we calculate the drug concentration $c(x, t)$ for anytime $t_k$. The numerical solutions of the time fractional drug concentration equation obtained by developed scheme for $\alpha = 1.0, 0.9, 0.8$ with the parameters $\upsilon = 0.5, D = 0.7, \Delta x = 0.01$ and $\Delta t = 0.001$ is represented graphically in Figure 1. Furthermore, we simulate the numerical solution of the time fractional drug concentration equation for different values of $x$ in Figure 2. The exact solution and numerical solution for $\alpha = 1$ with the parameters $\upsilon = 0.5, D = 0.7, \Delta x = 0.01$ and $\Delta t = 0.001$ at time $t = 2$ are shown in Table 1. We observed that the magnitude of the error of exact solution and numerical solution is of $O(\Delta t + (\Delta x)^2)$.

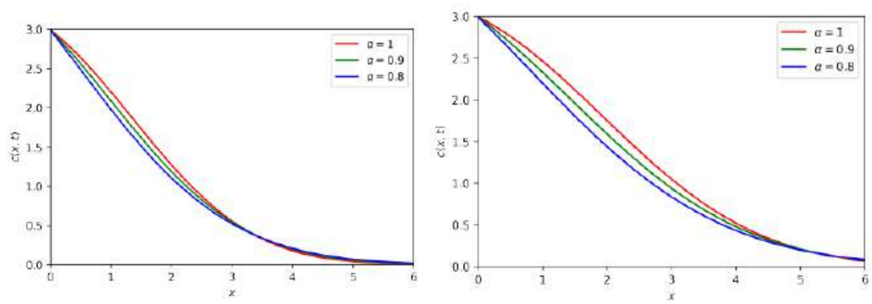


(a) $t = 2$ (b) $t = 3$

**Figure 1.** Drug concentration profile with the parameters $\upsilon = 0.5$, $D = 0.7, \Delta x = 0.01, \Delta t = 0.001$ and $\alpha = 1.0, 0.9, 0.8$.

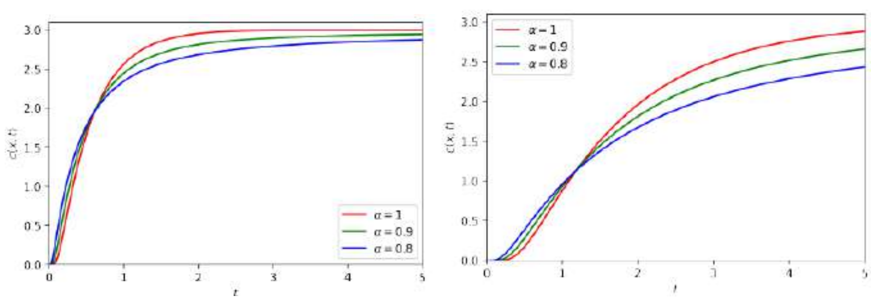


(a) $x = 1$ (b) $x = 2$

**Figure 2.** Numerical solution of steady state concentration for $x = 1$ and $x = 2$ with the parameters $\upsilon = 0.5, D = 0.7, T = 5, \Delta x = 0.01$ and $\Delta t = 0.001$.

**Table 1.** Comparision of exact solution and numerical solution for $\alpha = 1$, $t = 2$, $v = 0.5$, $D = 0.7$, $\Delta x = 0.01$ and $\Delta t = 0.001$.

| $x$ | Exact Solution | Numerical Solution | Error $e_i^k = \| \bar{c}_i^k - c_i^k \|$ |
|---|---|---|---|
| 0.0 | 3.0 | 2.993907278649013 | 0.006092721350987151 |
| 0.5 | 2.6456568378800114 | 2.637640626024081 | 0.0080162118559306 |
| 1.0 | 2.210862045444807 | 2.2016244916677286 | 0.009237553777078578 |
| 1.5 | 1.7395672793993147 | 1.7300687648213946 | 0.009498514577920059 |
| 2.0 | 1.2820481022496093 | 1.2732489286656066 | 0.008799173584002729 |
| 2.5 | 0.8812918247063797 | 0.8739078798391523 | 0.007383944867227377 |
| 3.0 | 0.5631456958949884 | 0.5575140861890188 | 0.0056316097059696535 |
| 3.5 | 0.33360708628476354 | 0.3296952147891131 | 0.003911871495650421 |
| 4.0 | 0.1828205165043782 | 0.1803422974511022 | 0.0024782190532759985 |
| 4.5 | 0.09251994640668684 | 0.0910867844617443 | 0.0014331619449425431 |
| 5.0 | 0.04317739107570287 | 0.042420349641816124 | 0.0007570414338867459 |
| 5.5 | 0.018560555515715397 | 0.01819513741539206 | 0.00036541810032333574 |
| 6.0 | 0.007342283849504758 | 0.007181092835093199 | 0.00016119101441155938 |

### 6.2 Test Problem 2. Elimination Phase

The elimination phase of drug is the case corresponds to the drug being present in the CSF in the lateral ventricles at some concentration $c_0$ [5]. At $t = 0$, the injection is stopped and the elimination begins. This case is relevant for concentration-time profile on coarse time scale. Since the drug aggregation happens quite fast in the case of intravenous injection, it will not visible on such a time-scale and we will see only elimination phase in the plot. This phenomenon is study by the following time-fractional drug concentration equation

$$\frac{\partial^\alpha c(x, t)}{\partial t^\alpha} = -v \frac{\partial c(x, t)}{\partial x} + D \frac{\partial^2 c(x, t)}{\partial x^2}, \; 0 < \alpha \leq 1, \; x \leq 6, \; t \geq 0$$

$$\text{initial condition: } c(x, 0) = 0, \; 0 < x < 6$$

boundary conditions: $c(0, t) = 3e^{-t}$, $\dfrac{\partial c(6, t)}{\partial x} = 0 (t \geq 0).$

The exact solution of the problem for $\alpha = 1$ is given as [5]

$$c(x, t) = \frac{3}{2} e^{-t} \left( e^{\frac{(v-y)x}{2D}} erfc\left( \frac{x - yt}{2\sqrt{Dt}} \right) + e^{\frac{(v+y)x}{2D}} erfc\left( \frac{x + yt}{2\sqrt{Dt}} \right) \right)$$

where $y = \sqrt{v^2 - 4D}$. The numerical solutions of the time fractional drug concentration equation obtained by developed scheme for $\alpha = 1.0, 0.9, 0.8$ with the parameters $v = 1, D = 0.2, \Delta x = 0.01$ and $\Delta t = 0.001$ are represented graphically in Figure 3 by Python programme DCE. Furthermore, we simulate the numerical solutions of the time fractional drug concentration equation for different values of $x$ in Figure 4. In Table 2, we compare the exact solution and numerical solution of the time fractional drug concentration equation for $\alpha = 1$ with the parameters $v = 1, D = 0.2,$ $\Delta x = 0.01$ and $\Delta t = 0.001$ at time $t = 2$. Moreover, we observe that the error in the calculation is of $O(\Delta t + (\Delta x)^2)$.

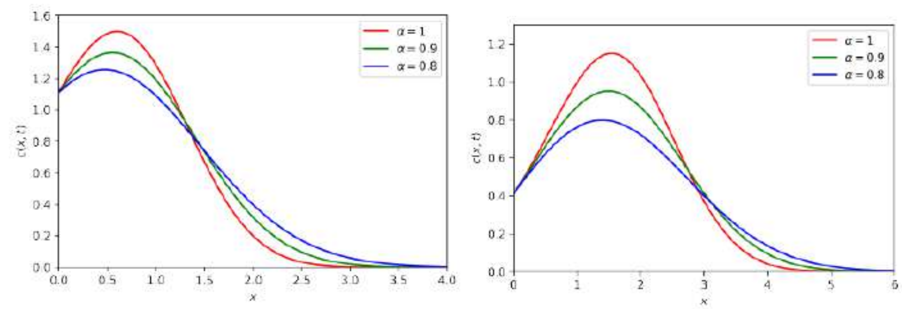

(a) $t = 1$ (b) $t = 2$

**Figure 3.** Drug concentration profile with the parameters $v = 1, D = 0.2,$ $\Delta x = 0.01, \Delta t = 0.001$ and $\alpha = 1.0, 0.9, 0.8.$

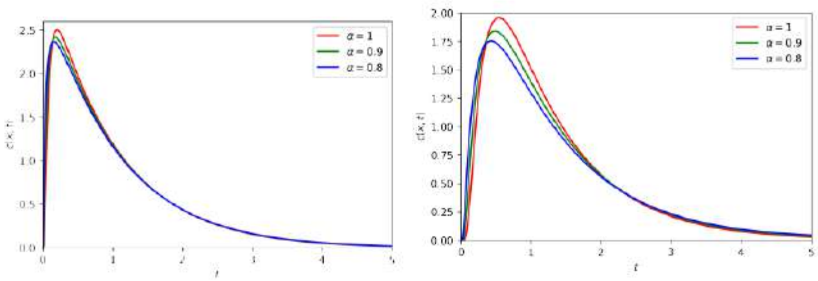


(a) $x = 0.2$ (b) $x = 0.5$

**Figure 4.** Numerical solution for drug elimination for $x = 0.2$ and $x = 0.5$ with the parameters $v = 1$, $D = 0.2$, $t = 5$, $\Delta x = 0.01$ and $\Delta t = 0.001$.

**Table 2.** Comparision of exact solution and numerical solution for $\alpha = 1$, $t = 2$, $v = 1$, $D = 0.2$, $\Delta x = 0.01$ and $\Delta t = 0.001$.

| $x$ | Exact Solution | Numerical Solution | Error $e_i^k = \lVert \bar{c}_i^k - c_i^k \rVert$ |
|---|---|---|---|
| 0.0 | 0.40600584970983805 | 0.4108789821823356 | 0.004873132472497543 |
| 0.5 | 0.690643252642077 | 0.6969777675627705 | 0.006334514920693479 |
| 1.0 | 0.9910421336946248 | 0.9965539539700895 | 0.005511820275464707 |
| 1.5 | 1.147116277674832 | 1.1484516174662687 | 0.0013353397914366294 |
| 2.0 | 1.0385500472139912 | 1.0343063307369158 | 0.004243716477075443 |
| 2.5 | 0.72077795551975 | 0.7133503723003761 | 0.007427583219373868 |
| 3.0 | 0.37847592991323475 | 0.3718015170776765 | 0.006674412835558252 |
| 3.5 | 0.14906463756342395 | 0.14515526386486594 | 0.003909373698558011 |
| 4.0 | 0.04377805649358062 | 0.04219236700542997 | 0.0015856894881506461 |
| 4.5 | 0.009547713552140515 | 0.009091836821831855 | 0.0004558767303086599 |
| 5.0 | 0.0015417744244616016 | 0.001447866329388511 | 9.390809507309065e-05 |
| 0.0 | 0.40600584970983805 | 0.4108789821823356 | 0.004873132472497543 |
| 0.5 | 0.690643252642077 | 0.6969777675627705 | 0.006334514920693479 |

**6.3 Test Problem 3.** Drug Aggregation

The drug aggregation corresponds to the case in which drug is given continuously over a longer period of time [5]. The drug reaches the CSF at time $t = 0$ and no drug was present in the brainECF and CSF before that. The injection is continued long enough in order to reach the steady state concentration and is not stopped within the period of time considered. This phenomenon is study by the following time-fractional drug concentration equation

$$\frac{\partial^{\alpha} c(x, t)}{\partial t^{\alpha}} = -v \frac{\partial c(x, t)}{\partial x} + D \frac{\partial^2 c(x, t)}{\partial x^2},\ 0 < \alpha \leq 1,\ x \leq 5,\ t \geq 0$$

$$\text{initial condition: } c(x, 0) = 0,\ 0 < x < .$$

$$\text{boundary conditions: } c(0, t) = 3e^{-t},\ \frac{\partial c(5, t)}{\partial x} = 0(t \geq 0).$$

The exact solution of the problem for $\alpha = 1$ is given as [5]

$$c(x, t) = \frac{3}{2}\left( erfc\left(\frac{x - vt}{2\sqrt{Dt}}\right) + e^{\left(\frac{vx}{D}\right)} erfc\left(\frac{x + vt}{2\sqrt{Dt}}\right)\right.$$

$$\left. - e^{-t}\left( e^{\frac{(v-y)x}{2D}} erfc\left(\frac{x - yt}{2\sqrt{Dt}}\right) + e^{\frac{(v+y)x}{2D}} erfc\left(\frac{x + yt}{2\sqrt{Dt}}\right)\right)\right)$$

where $y = \sqrt{v^2 - 4D}$. With the help of developed python programme DCE, the numerical solutions of the time fractional drug concentration equation for $\alpha = 1.0,\ 0.9,\ 0.8$ with the parameters $v = 1,\ D = 0.2,\ \Delta x = 0.01$ and $\Delta t = 0.001$ is represented graphically in Figure 5. Furthermore, we simulate the numerical solutions of the time fractional drug concentration equation for different values of $x$ in Figure 6. In the Table 3, we compare the exact solution and numerical solution at time $t = 3$ for $\alpha = 1$ with the parameters $v = 1,\ D = 0.2,\ \Delta x = 0.01$ and $\Delta t = 0.001$. We observe that the magnitude of the error between the exact solution and numerical solution is of $O(\Delta t + (\Delta x)^2)$.

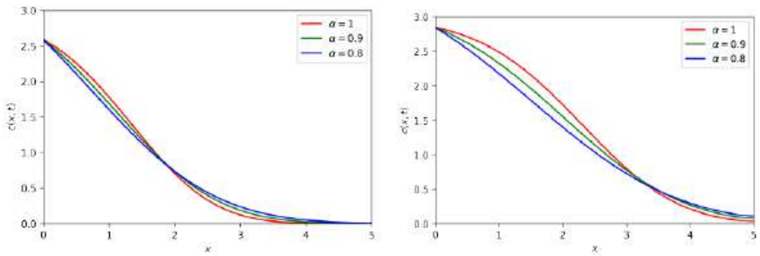


(a) $t = 2$ (b) $t = 3$

**Figure 5.** Drug concentration profile with the parameters $\upsilon = 1$, $D = 0.2$, $\Delta x = 0.01$, $\Delta t = 0.001$ and $\alpha = 1.0, 0.9, 0.8$.

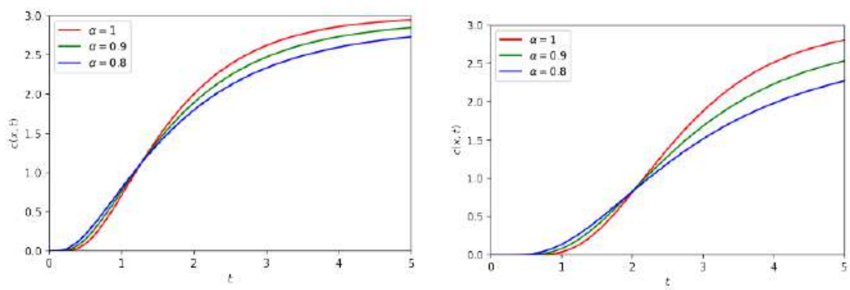


(a) $x = 1$ (b) $x = 2$

**Figure 6.** Numerical solution for drug aggregation for $x = 1$ and $x = 2$ with the parameters $\upsilon = 1$, $D = 0.2$, $\Delta x = 0.01$ and $\Delta t = 0.001$.

**Table 3.** Comparision of exact solution and numerical solution for $\alpha = 1$, $t = 3$, $\upsilon = 1$, $D = 0.2$, $\Delta x = 0.\ 01$ and $\Delta t = 0.001$.

| $x$ | Exact Solution | Numerical Solution | Error $e_i^k = \| \bar{c}_i^k - c_i^k \|$ |
|---|---|---|---|
| 0.0 | 2.8506387948964083 | 2.8486584009974187 | 0.0019803938989895187 |
| 0.5 | 2.717400152250943 | 2.7140190061622556 | 0.0033811460886887448 |
| 1.0 | 2.495369092986084 | 2.490061111986018 | 0.005307981000065798 |
| 1.5 | 2.1654336714236244 | 2.157966519981535 | 0.007467151442089204 |
| 2.0 | 1.7376742713960167 | 1.7284649530934093 | 0.009209318302607405 |
| 2.5 | 1.2617161036485738 | 1.251930562993927 | 0.009785540654646763 |

| | | | |
|---|---|---|---|
| 3.0 | 0.8126564196023055 | 0.8038171392485197 | 0.008839280353785783 |
| 3.5 | 0.4565234712200368 | 0.44980441741804056 | 0.006719053801996222 |
| 4.0 | 0.22062447196653884 | 0.21636491470986893 | 0.004259557256669905 |
| 4.5 | 0.09072778152906447 | 0.08873837701972355 | 0.001989404509340917 |
| 5.0 | 0.03147838582653009 | 0.040396872611049295 | 0.008918486784519203 |

## 7. Conclusion

(i) We successfully develop the fractional order Crank-Nicolson finite difference scheme for the time fractional drug concentration equation in the central nervous system.

(ii) The stability and convergence of the developed scheme are both investigated.

(iii) Furthermore, we successfully develop the Python programme for the time fractional drug concentration equation in the central nervous system.

(iv) The performance and efficiency of the developed scheme is numerically tested using some numerical experiments. We observe that the error in the calculation is $O((\Delta t)^{2-\alpha} + (\Delta x)^2)$.

(v) Finally, we conclude that Python is a very powerful tool for obtaining the numerical solutions of the time fractional drug concentration equation.

## References

[1] José Francisco Gómez Aguilar and Margarita Miranda Hernández, Space-Time Fractional Diffusion-Advection Equation with Caputo Derivative, Abstract and Applied Analysis (2014), 1-8.

[2] Teodor M. Atanackovic, Fractional Calculus with Applications in Mechanics, ISTE Ltd/JohnWiley and Sons Inc, Hoboken, NJ, 2013.

[3] Teodor M. Atanacković, Stevan Pilipović, Bogoljub Stanković and Dusan Zorica, Fractional Calculus with Applications in Mechanics: Vibrations and Diffusion Processes, John Wiley and Sons, Inc., Hoboken, USA, January 2014.

[4] Isa Abdullahi Baba, A fractional-order bladder cancer model with BCG treatment effect, Computational and Applied Mathematics 38(2) 37 March 2019.

[5] Laila Kristin Gabriel, A Mathematical Model for Estimating Drug Concentrations in Human Brain Fluid, Mathematisch Instituut, Universiteit Leiden, page 78, September 2016.

[6] Krishna Ghode, Kalyanrao Takale and Shrikisan Gaikwad, New technique for solving time fractional wave equation: Python, Journal of Mathematical and Computational Science 11(5) (2021), 5327-5343.

[7] R. Hilfer, Applications of Fractional Calculus in Physics, World Scientific, March 2000.

[8] Mark Hayden Holmes, Introduction to Numerical Methods in Differential Equations, Texts in Applied Mathematics, Springer-Verlag, New York, 2007.

[9] Sunil S. Jambhekar and Philip J. Breen, Basic Pharmacokinetics, Pharmaceutical Press, May 2009.

[10] Suryakant Jogdand, Kalyanrao Takale and V. C. Borkar, Fractional Order Finite Difference Scheme for Soil Moisture Diffusion Equation and its Applications, IOSR Journal of Mathematics 5(4) (2013), 12-18.

[11] Suryakant Jogdand, Kalyanrao Takale and A. Jagtap, Finite difference approximation for space fractional soil moisture diffusion equation and its application, IOSR Journal of Mathematics 8(4) (2013), 1-8.

[12] Hardik Joshi and Brajesh Kumar Jha, Fractional-order mathematical model for calcium distribution in nerve cells, Computational and Applied Mathematics 39(56), 2020.

[13] Bertram G. Katzung, Basic and Clinical Pharmacology, McGraw-Hill Medical, New York, 2012.

[14] M. Yu Kokurin, S. I. Piskarev and M. Spreafico, Finite-Difference Methods for Fractional Differential Equations of Order 1/ 2, Journal of Mathematical Sciences 230(6) (2018), 950-960.

[15] T. A. M. Langlands, B. I. Henry and S. L. Wearne, Fractional cable equation models for anomalous electro diffusion in nerve cells: Infinite domain solutions, Journal of Mathematical Biology 59(6) (2009), 761-808.

[16] Hans Petter Langtangen and Svein Linge, Finite Difference Computing with PDEs: A Modern Software Approach, Volume 16 of Texts in Computational Science and Engineering, Springer International Publishing, Cham, 2017.

[17] Changpin Li and Fanhai Zeng, Finite difference methods for fractional differential equations, International Journal of Bifurcation and Chaos 22(04) (2012), 1230014 pp 28.

[18] Richard L. Magin, Fractional calculus models of complex dynamics in biological tissues, Computers and Mathematics with Applications 59(5) (2010), 1586-1593.

[19] Kolade Matthew Owolabi and Abdon Atangana, Numerical Methods for Fractional Differentiation, Springer Series in Computational Mathematics, Springer Singapore, 2019.

[20] M. Ozisik, Helcio Orlande, Marcelo Colaco and R. M. Cotta, Finite Difference Methods in Heat Transfer: Second Edition, CRC Press, January 2017.

[21] Carla M. A. Pinto and J. A. Tenreiro Machado, Fractional model for malaria transmission under control strategies, Computers and Mathematics with Applications 66(5) (2013), 908-916.

[22] Igor Podlubny, Fractional Differential Equations: An Introduction to Fractional Derivatives, Fractional Differential Equations, to Methods of Their Solution and Some of Their Applications, Elsevier, October 1998.

[23] S. G. Samko, A. A. Kilbas and O. I. Marichev, Fractional Integrals and Derivatives: Theory and Applications, Gordon and Breach Science Publishers, Switzerland; Philadelphia, Pa., USA, 1993.

[24] W. R. Schneider and W. Wyss, Fractional diffusion and wave equations, Journal of Mathematical Physics 30(1) (1989), 134-144.

[25] G. D. Smith, Numerical Solution of Partial Differential Equations: Finite Difference Methods, Oxford Applied Mathematics and Computing Science Series, Oxford University Press, Oxford, New York, third edition, December 1985.

[26] Bhausaheb R. Sontakke and Abhijeet S. Shelke, Approximate scheme for time fractional diffusion equation and its applications, Global Journal of Pure and Applied Mathematics 13(8) (2017), 14.

[27] K. C. Takale, D. B. Dhaigude and V. R. Nikam, Douglas Higher Order Finite Difference Scheme for One Dimensional Pennes Bioheat Equation, International Journal of Advanced Engineering and Application (2011), 5.

[28] Kalyanrao Takale, Fractional Order Finite Difference Scheme for Space Fractional Boussinesq's Equations and its Applications, Int. Jr. of Mathematical Sciences and Applications 3(1) (2013), 343-353.

[29] Joost Westerhout, Bart Ploeger, Jean Smeets, Meindert Danhof and Elizabeth C. M. de Lange, Physiologically Based Pharmacokinetic Modeling to Investigate Regional Brain Distribution Kinetics in Rats, The AAPS Journal 14(3) (2012), 543-553.

[30] Joost Westerhout, Dirk-Jan van den Berg, Robin Hartman, Meindert Danhof and Elizabeth C. M. de Lange, Prediction of methotrexate CNS distribution in different species – influence of disease conditions, European Journal of Pharmaceutical Sciences 57 (2014), 11-24.

[31] Lifei Wu, Xiaozhong Yang and Yanhua Cao, An alternating segment Crank Nicolson parallel difference scheme for the time fractional sub-diffusion equation, Advances in Difference Equations (1) (2018), 287.

[32] Yamamoto Yumi et al., Predicting Drug Concentration-Time Profiles in Multiple CNS Compartments Using a Comprehensive Physiologically-Based Pharmacokinetic Model: PBPK Model for Brain Target-Site Concentrations, CPT: Pharmacometrics and Systems Pharmacology 6(11) (2017), 765-777.

B. Rushi Kumar · S. Ponnusamy · Debasis Giri ·
Bhavani Thuraisingham · Christopher W. Clifton ·
Barbara Carminati
Editors

# Mathematics and Computing

## ICMC 2022, Vellore, India, January 6–8

Springer

*Editors*
B. Rushi Kumar
Department of Mathematics
School of Advanced Sciences
Vellore Institute of Technology
Vellore, Tamil Nadu, India

Debasis Giri
Department of Information Technology
Maulana Abul Kalam Azad University of Technology
Haringhata, West Bengal, India

Christopher W. Clifton
Department of Computer Science
Purdue University
West Lafayette, IN, USA

S. Ponnusamy
Department of Mathematics
Indian Institute of Technology Madras
Chennai, Tamil Nadu, India

Bhavani Thuraisingham
Department of Computer Science
The University of Texas at Dallas
Richardson, TX, USA

Barbara Carminati
Department of Theoretical and Applied Sciences
University of Insubria
Varese, Italy

ISSN 2194-1009 ISSN 2194-1017 (electronic)
Springer Proceedings in Mathematics & Statistics
ISBN 978-981-19-9306-0 ISBN 978-981-19-9307-7 (eBook)
https://doi.org/10.1007/978-981-19-9307-7

Mathematics Subject Classification: 97R20, 94C15, 90B50, 93C10, 94D05, 05C90, 12D05, 92E20



This Springer imprint is published by the registered company Springer Nature Singapore Pte Ltd.
The registered company address is: 152 Beach Road, #21-01/04 Gateway East, Singapore 189721, Singapore

# Contents

# Crank-Nicolson Finite Difference Scheme for Time-Space Fractional Diffusion Equation

**Kalyanrao C. Takale and Veena V. Sangvikar (Kshirsagar)**

**Abstract** This paper aims in developing the Crank-Nicolson type of finite difference scheme for space-time fractional order diffusion equation (TSFDE) with a non-linear term. The proof for scheme to be unconditionally stable and also convergent is been discussed. Further, an application in terms of numerical solution is solved and graph simulated using Mathematica.

**Keywords** Finite difference scheme · Caputo derivative · Space-time fractional diffusion equation · Stableness of scheme · Convergence · Mathematica software

## 1 Introduction

Recently, fractional order partial differential equations have been widely used by researchers to represent any physical phenomina and study its minute and diversed applications in science and technology, fluid mechanics, control systems, biology, viscoelasticity, physics, dynamical systems, etc. [4, 12, 14]. Major benefit that the fractional derivatives provide is that of being a best estimate for minute elaboration of memory as well as hereditary properties of different processes and involved materials [6, 9, 13]. But, it is very difficult to tackle partial differential equations of fractional order for exact solution. Researchers find variety of essential dynamical systems, exhibit fractional order behaviour which could change with space, time or both space-time and hence the analytical solution becomes difficult. This provoked many researchers to develop numerical methods.

We consider the space-time fractional heat-transfer/diffusion equation. The space-time fractional equation of diffusion is obtained using the standard equation of diffusion by replacing second order derivative in space variable by fractional derivative of order $\beta$, $1 < \beta < 2$ [3, 13] and the first order derivative in time variable by frac-

K. C. Takale
Department of Mathematics, NSC Bytco Science College, Nashik, MS, India

V. V. Sangvikar (Kshirsagar) (✉)
School of Mathematics and Statistics, MIT World Peace University, Pune, MS, India
e-mail: kshirsagar.v.p@gmail.com



B. Rushi Kumar et al. (eds.), *Mathematics and Computing*, Springer Proceedings in Mathematics & Statistics 415, https://doi.org/10.1007/978-981-19-9307-7_54

tional derivative of order $\alpha$, $0 < \alpha < 1$. Thus, we develop the time-space fractional Crank-Nicolson finite difference scheme for diffusion equation with a non-linear source term.

The following space-time fractional equation of diffusion (TSFDE) with a non-linear term is considered.

$$\frac{\partial^{\alpha} U(x,t)}{\partial t^{\alpha}} = d\frac{\partial^{\beta} U(x,t)}{\partial x^{\beta}} + f(U,x,t),\ 0 < x < L,\ t > 0 \tag{1}$$

$$initial\ condition : U(x,0) = \phi(x),\ 0 \leq x \leq L \tag{2}$$

$$boundary\ conditions : U(0,t) = U_L,\ U(L,t) = U_R,\ 0 \leq t \leq T \tag{3}$$

where diffusion coefficient $d > 0$, $0 < \alpha \leq 1$, $1 < \beta \leq 2$.

Below are few definitions of fractional derivatives which would be useful for our subsequent development of scheme [7, 9–11, 13].

**Definition 1.1** The definition of Caputo time fractional derivative of order $\alpha$, $(0 < \alpha \leq 1)$ is

$$\frac{\partial^{\alpha} U(x,t)}{\partial t^{\alpha}} = \begin{cases} \frac{1}{\Gamma(1-\alpha)} \int_0^t \frac{\partial U(x,t)}{\partial \xi} \frac{d\xi}{(t-\xi)^{\alpha}}, & 0 < \alpha < 1 \\ \frac{\partial U(x,t)}{\partial t}, & \alpha = 1 \end{cases}$$

**Definition 1.2** The definition of Grunwald-Letnikov space fractional derivative of order $\beta$, $(1 < \beta \leq 2)$ is

$$\frac{\partial^{\beta} U(x,t)}{\partial x^{\beta}} = \frac{1}{\Gamma(-\beta)} \lim_{N \to \infty} \frac{1}{h^{\beta}} \sum_{j=0}^{N} \frac{\Gamma(j-\beta)}{\Gamma(j+1)} U(x-(j-1)h,t)$$

where $\Gamma(.)$ is the gamma function.

The paper is planned in the following way: In Sect. 2, the Crank-Nicolson finite difference scheme is advanced for one dimensional time-space fractional order equation of diffusion. The schemes stability is discussed in Sect. 3 and the convergence is proved in Sect. 4. In the last session we have the numerical solution of the time-space fractional equation of diffusion which is graphically represented using Mathematica software.

## 2 Finite Difference Scheme

We now develop fractional order Crank-Nicolson type finite difference scheme for time-space fractional equation of diffusion [8, 15–19]. We consider following time-space fractional diffusion equation having non-linear term along with initial and boundary conditions.

$$\frac{\partial^\alpha U(x,t)}{\partial t^\alpha} = d\frac{\partial^\beta U(x,t)}{\partial x^\beta} + f(U,x,t),\ 0 < x < L,\ t > 0 \quad (4)$$

$$initial\ condition : U(x,0) = \phi(x),\ 0 \le x \le L \quad (5)$$

$$boundary\ conditions : U(0,t) = U_L\ and\ U(L,t) = U_R,\ 0 \le t \le T \quad (6)$$

where $0 < \alpha \le 1$; $1 < \beta \le 2$ and d is diffusivity constant. For the implicit numerical approximation scheme, we define $h = \frac{(x_R - x_L)}{N} = \frac{L}{N}$ and $\tau = \frac{T}{N}$ the space and time steps respectively, such that $t_k = k\tau$; k = 0, 1,...,N be the integration time $0 \le t_k \le T$ and $x_i = x_L + ih$ for i = 0,1, ...., N. Let $U(x_i, t_k)$, $i = 1, 2, ...N$, $k = 1, 2, ...n$, be the exact solution of the fractional partial differential equation (4)–(6) at the node point $(x_i, t_k)$. Let $U_i^k$ be the numerical approximation to $U(x_i, t_k)$. We discretise the time fractional derivative of equation (4) by the following scheme:

$$\begin{aligned}
\frac{\partial^\alpha U(x_i,t_{k+1})}{\partial t^\alpha} &\approx \frac{1}{\Gamma(1-\alpha)}\int_0^{t_{k+1}} \frac{1}{(t_{k+1}-\xi)^\alpha}\frac{\partial U(x_i,\xi)}{\partial \xi}d\xi \\
&= \frac{1}{\Gamma(1-\alpha)}\sum_{j=0}^{k}\frac{U(x_i,t_{j+1}) - U(x_i,t_j)}{\tau}\int_{j\tau}^{(j+1)\tau}\frac{d\xi}{(t_{k+1}-\xi)^\alpha} \\
&= \frac{1}{\Gamma(1-\alpha)}\sum_{j=0}^{k}\frac{U(x_i,t_{j+1}) - U(x_i,t_j)}{\tau}\int_{(k-j)\tau}^{(k-j+1)\tau}\frac{d\eta}{\eta^\alpha} \\
&= \frac{1}{\Gamma(1-\alpha)}\sum_{j=0}^{k}\frac{U(x_i,t_{k+1-j}) - U(x_i,t_{k-j})}{\tau}\int_{j\tau}^{(j+1)\tau}\frac{d\eta}{\eta^\alpha} \\
&= \frac{\tau^{1-\alpha}}{\Gamma(2-\alpha)}\sum_{j=0}^{k}\frac{U(x_i,t_{k+1-j}) - U(x_i,t_{k-j})}{\tau}[(j+1)^{1-\alpha} - j^{1-\alpha}]
\end{aligned}$$

$$\begin{aligned}
\frac{\partial^\alpha U(x_i,t_{k+1})}{\partial t^\alpha} = \frac{\tau^{-\alpha}}{\Gamma(2-\alpha)}&[U(x_i,t_{k+1}) - U(x_i,t_k)]+ \\
&\frac{\tau^{-\alpha}}{\Gamma(2-\alpha)}\sum_{j=1}^{k} b_j[U(x_i,t_{k+1-j}) - U(x_i,t_{k-j})]
\end{aligned}$$

where $b_j = (j+1)^{1-\alpha} - j^{1-\alpha},\ j = 1, 2, ..., k$.

For $\frac{\partial^\beta U(x,t)}{\partial x^\beta} = {}_0D_x^\beta U(x,t)$, we use the shifted *Grünwald* finite difference formula at all time levels as follows

$$\frac{\partial^\beta U(x_i, t_{k+1})}{\partial x^\beta} = oD_x^\beta U(x_i, t_{k+1})$$
$$= \frac{1}{h^\beta}\sum_{j=0}^{i+1} g_{\beta,j} U[x_i - (j-1)h, t_{k+1}] + O(h^2)$$

Here the *Grünwald* normalized weights are defined by

$$g_{\beta,0} = 1,\ g_{\beta,j} = \frac{\Gamma(j-\beta)}{\Gamma(-\beta)\Gamma(j+1)},\ j = 0, 1, ...$$

On substituting *Grünwald* estimates in the superdiffusion equation (4) to obtain the Crank-Nicolson type numerical approximation, the obtained finite difference equation is

$$\frac{\tau^{-\alpha}}{\Gamma(2-\alpha)}[U_i^{k+1} - U_i^k] + \frac{\tau^{-\alpha}}{\Gamma(2-\alpha)}\sum_{j=1}^{k} b_j[U_i^{k-j+1} - U_i^{k-j}] = \frac{d}{2}\,(\delta_{\beta,x}U_i^{k+1} + \delta_{\beta,x}U_i^k) + f_i^k \tag{7}$$

where $f_i^k = f(U_i^k, x_i, t_k)$ and the above operator which is a fractional partial differential, is defined as

$$\delta_{\beta,x}U_i^k = \frac{1}{h^\beta}\sum_{j=0}^{i+1} g_{\beta,j}U_{i-j+1}^k \tag{8}$$

Therefore, from (2.4) and (2.5) we get

$$\frac{\tau^{-\alpha}}{\Gamma(2-\alpha)}[U_i^{k+1} - U_i^k] + \frac{\tau^{-\alpha}}{\Gamma(2-\alpha)}\sum_{j=1}^{k} b_j[U_i^{k-j+1} - U_i^{k-j}] = \frac{d}{2h^\beta}\{\sum_{j=0}^{i+1} g_{\beta,j}U_{i-j+1}^{k+1} + \sum_{j=0}^{i+1} g_{\beta,j}U_{i-j+1}^k] + f_i^k$$

$$U_i^{k+1} - U_i^k + \sum_{j=1}^{k} b_j[U_i^{k-j+1} - U_i^{k-j}] = \frac{d\tau^\alpha\Gamma(2-\alpha)}{2h^\beta}\{\sum_{j=0}^{i+1} g_{\beta,j}U_{i-j+1}^{k+1} + \sum_{j=0}^{i+1} g_{\beta,j}U_{i-j+1}^k] + \tau^\alpha\Gamma(2-\alpha)f_i^k$$

$$U_i^{k+1} - U_i^k + \sum_{j=1}^{k} b_j[U_i^{k-j+1} - U_i^{k-j}] = r\{\sum_{j=0}^{i+1} g_{\beta,j}U_{i-j+1}^{k+1} + \sum_{j=0}^{i+1} g_{\beta,j}U_{i-j+1}^k\} + \tau^\alpha\Gamma(2-\alpha)f_i^k \tag{9}$$

$$where\ r = \frac{d\tau^\alpha\Gamma(2-\alpha)}{2h^\beta}\ \ for\ i = 0, 1, 2, ...N, k = 0, 1, 2, ...$$

After further simplification, we get

$$(1 - rg_{\beta,1})U_i^{k+1} - r\sum_{j=0, j\neq 1}^{i+1} g_{\beta,j}U_{i-j+1}^{k+1} = (1 - b_1 + rg_{\beta,1})U_i^k + \sum_{j=1}^{k-1}(b_j - b_{j+1})U_i^{k-j}$$
$$+ r\sum_{j=0, j\neq 1}^{i+1} g_{\beta,j}U_{i-j+1}^k + b_kU_i^0 + \tau^\alpha\Gamma(2-\alpha)f_i^k$$

The approximation to initial condition is as $U_i^0 = \phi(x_i),\ i = 0, 1, 2, \ldots$ The approximations to boundary conditions are as $U_0^k = U_L,\ U_N^k = U_R,\ k = 0, 1, 2, \ldots$ Hence, the complete discretised scheme to IBVP (4)–(6) is

$$(1+\beta r)U_i^1 - r\sum_{j=0, j\neq 1}^{i+1} g_{\beta,j}U_{i-j+1}^1 = (1-\beta r)U_i^0 + r\sum_{j=0, j\neq 1}^{i+1} g_{\beta,j}U_{i-j+1}^0 + \tau^\alpha\Gamma(2-\alpha)f_i^0,\ for\ k=0 \tag{10}$$

$$(1+\beta r)U_i^{k+1} - r\sum_{j=0, j\neq 1}^{i+1} g_{\beta,j}U_{i-j+1}^{k+1} = (1-r\beta-b_1)U_i^k + \sum_{j=1}^{k-1}(b_j-b_{j+1})U_i^{k-j} + r\sum_{j=0, j\neq 1}^{i+1} g_{\beta,j}U_{i-j+1}^k + b_kU_i^0 + \tau^\alpha\Gamma(2-\alpha)f_i^k,\ for\ k\geq 1 \tag{11}$$

$$initial\ condition:\ U_i^0 = \phi(x_i),\ i = 0, 1, 2, \ldots \tag{12}$$

$$boundary\ conditions:\ U_0^k = U_L,\ U_N^k = U_R,\ k = 0, 1, 2, \ldots. \tag{13}$$

where $r = \frac{d\tau^\alpha\Gamma(2-\alpha)}{2h^\beta}$, $g_{\beta,0} = 1$, $g_{\beta,1} = (-\beta)$, $g_{\beta,j} = \frac{\Gamma(j-\beta)}{\Gamma(-\beta)\Gamma(j+1)}$, and $b_j = (j+1)^{1-\alpha} - j^{1-\alpha}$, $j = 0, 1, 2, \ldots, k$. The finite-difference Eqs. (10) to (13) are expressed in the matrix form as:

$$AU^1 = BU^0 + \tau^\alpha\Gamma[2-\alpha]f_i^0 \tag{14}$$

$$AU^{k+1} = BU^k + \sum_{j=1}^{k-1}(b_j-b_{j+1})U^{k-j} + b_kU^0 + \tau^\alpha\Gamma[2-\alpha]f_i^k + D \tag{15}$$

where $U^k = (U_1^k, U_2^k, \ldots, U_{N-1}^k)^T,\ k = 0, 1, 2\ldots, N$ $A = (a_{ij})$ is a (N − 1) ordered square matrix of coefficients

$$A = \begin{pmatrix} (1+r\beta) & (-r) & & & \\ (-r)g_{\beta,2} & (1+r\beta) & (-r) & & \\ (-r)g_{\beta,3} & (-r)g_{\beta,2} & (1+r\beta) & (-r) & \\ \vdots & \vdots & \ddots & \ddots\ \ddots & \\ (-r)g_{\beta,m-1} & (-r)g_{\beta,m-2} & (-r)g_{\beta,m-3} & \cdots\ \cdots & (1+r\beta) \end{pmatrix}$$

$B = (b_{ij})$ is a (N − 1) ordered square matrix of coefficients

$$B = \begin{pmatrix} (1-b_1-r\beta) & r & & & \\ rg_{\beta,2} & (1-b_1-r\beta) & r & & \\ rg_{\beta,3} & rg_{\beta,2} & (1-b_1-r\beta) & r & \\ \vdots & \vdots & \ddots & \ddots \ddots & \\ rg_{\beta,m-1} & rg_{\beta,m-2} & rg_{\beta,m-3} & \cdots\cdots & (1-b_1-r\beta) \end{pmatrix}$$

and D is a constant column matrix given by

$$D = \begin{pmatrix} rg_{\beta,2}(U_0^k + U_0^{k+1}) \\ rg_{\beta,3}(U_0^k + U_0^{k+1}) \\ rg_{\beta,4}(U_0^k + U_0^{k+1}) \\ \vdots \\ \vdots \\ rg_{\beta,N-1}(U_0^k + U_0^{k+1}) \\ rg_{\beta,N}(U_0^k + U_0^{k+1}) + r(U_N^k + U_N^{k+1}) \end{pmatrix}$$

where $r = \frac{d\tau^\alpha \Gamma(2-\alpha)}{2h^\beta}$, $g_{\beta,j} = \frac{\Gamma(j-\beta)}{\Gamma(-\beta)\Gamma(j+1)}$, $b_j = (j+1)^{1-\alpha} - j^{1-\alpha}$, $j = 0, 1, 2, ..., k$.

The system above is of algebraic equations which will be solved using some mathematical software tool preferably Mathematica.

Next, we work on stability of solution that would be obtained from the developed time-space fractional Crank-Nicolson finite difference scheme (10)–(13) for the time-space fractional diffusion equation (TSFDE) (4)–(6).

## 3 Stability

**Lemma 3.1** *For $i = 1, 2, ..., N$, $k = 1, 2, ..., N$, $0 < \alpha \le 1$, $1 < \beta \le 2$ the coefficients $b_j$ and $g_{\beta,j}$ for $j = 0, 1, 2, ....$ satisfy*
*(i) $b_j > b_{j+1}$, $j = 0, 1, 2,...$*
*(ii) $b_0 = 1$, $b_j > 0$, $j = 0, 1, 2,...$*
*(iii) $g_{\beta,0} = 1$, $g_{\beta,1} = -\beta$, $g_{\beta,j} \ge 0\ (j \ne 1)$, $\sum_{j=0}^{\infty} g_{\beta,j} = 0$*
*(iv) We have $\sum_{j=1}^{n} g_{\beta,j} < 0$, for any positive integer $n$.*

**Definition 3.1** For $E^0$, being some initial rounding error arbitrarily, if there exists $c$ a positive number, independent of $h$ and $\tau$ such that $\|E^k\| \le c\|E^0\|$ or $\|E^k\| \le c$, then the difference approximation is stable.

**Theorem 3.2** *Solution obtained from the Crank-Nicolson finite approximation scheme defined by* (10)–(13) *is unconditionally stable.*

***Proof*** We assume that $\bar{U}_i^k$ is a vector of exact solution of TSFDE (4)–(6). Denote, $E_i^k = \bar{U}_i^k - U_i^k$ for $i = 0, 1, ...N$; $k = 0, 1, ...N$. where $E^0 = 0$ and $E^k = (\varepsilon_1^k, \varepsilon_2^k, ...., \varepsilon_{N-1}^k)^T$. Furthermore, we assume that

$$|E_l^k| = \max_{1 \le i \le N-1} |\varepsilon_i^k| = \|E^k\|_\infty, \ for\ l = 1, 2, ...$$

Therefore, from Eq. (10), we get

$$\begin{aligned}
|E_l^1| &= |(1 + r\beta)\varepsilon_i^1 - r \sum_{j=0,\, j\neq 1}^{i+1} g_{\beta,j}\varepsilon_{i-j+1}^1| \\
&\le |(1 - r\beta)||\varepsilon_i^0| + r \sum_{j=0,\, j\neq 1}^{i+1} g_{\beta,j}|\varepsilon_{i-j+1}^0| + \tau^\alpha \Gamma(2-\alpha)|f[U(x_i, t_0), x_i, t_0] - f[U_i^0, x_i, t_0]| \\
&\le |\varepsilon_i^0| + \tau^\alpha \Gamma[2-\alpha]L|U(x_i, t_0) - U_i^0| \\
&\le |\varepsilon_i^0| + \tau L|\varepsilon_i^0| \\
&\le (1 + \tau L)|E_l^0| \\
\Rightarrow \|E^1\|_\infty &\le (1 + \tau L)\|E^0\|_\infty \\
&\le e^{\tau L}\|E^0\|_\infty
\end{aligned}$$

We assume that, $|E_l^k| = \|E^k\|_\infty \le (1 + \tau L)^k \|E^0\|_\infty \le e^{k\tau L}\|E^0\|_\infty$.
From Eq. (11) we get

$$\begin{aligned}
|E_l^{k+1}| &= |(1 + r\beta)\varepsilon_i^{k+1} - r \sum_{j=0,\, j\neq 1}^{i+1} g_{\beta,j}\varepsilon_{i-j+1}^{k+1}| \\
&\le |(1 - b_1 - r\beta)\varepsilon_i^k + r \sum_{j=0,\, j\neq 1}^{i+1} g_{\beta,j}\varepsilon_{i-j+1}^k + \sum_{j=1}^{k-1}(b_j - b_{j+1})\varepsilon_i^{k-j} + b_k\varepsilon_i^0 + \\
&\qquad \tau^\alpha \Gamma[2-\alpha]f[U(x_i, t_k), x_i, t_0] - f[U_i^k, x_i, t_0]| \\
&\le (1 - b_1)|\varepsilon_i^k| + (b_1 - b_k)|\varepsilon_i^k| + b_k|\varepsilon_i^k| + \tau L|\bar{U}_i^k - U_i^k| \\
&\le (1 - b_1 + b_1 - b_k + b_k)|E_l^k| + \tau L|E_l^k| \\
&\le (1 + \tau L)|E_l^k| \\
&\le (1 + \tau L)^{k+1}\|E^0\|_\infty \\
\Rightarrow \|E^{k+1}\|_\infty &\le e^{\tau L(k+1)}\|E^0\|_\infty
\end{aligned}$$

Hence, by mathematical induction this shows that the Crank-Nicolson finite approximation scheme defined by (10)–(13) is unconditionally stable.

Proceeding further to the next section, we discuss the convergence of the approximate scheme.

## 4 Convergence

**Theorem 4.1** *Let the problem (4)–(6) has smooth solution* $U(x,t)\varepsilon C_{x,t}^{1+\alpha,2+\beta}(\Omega)$. *Let* $U_i^k$ *be the numerical approximate computed from (10)–(13). Then there exists a positive constant* $C$ *independent of* $i, k, h$ *and* $\tau$ *such that* $|U(x_i,t_k)-U_i^k| \leq cO(\tau^2+h^2)$ *for* $i = 1, 2...N-1$; $k = 1, 2, ...N$.

***Proof*** Define $e_i^k = U(x_i,t_k) - U_i^k$ for $i = 0, 1, ...N$; $k = 0, 1, ...N$. Where $E^0 = 0$ and $E^k = (e_1^k, e_2^k, ..., e_N^k)^T$. Furthermore, we assume that $|e_l^k| = \max\limits_{1\leq i\leq N-1} |e_i^k| = \|E^k\|_\infty$, $for\ l = 1, 2, ...$ and $T_l^k = \max\limits_{1\leq i\leq N-1} |T_i^k|$ then using $\sum\limits_{j=0}^{\infty} g_{\beta,j} = 0$ and $\sum\limits_{j=1}^{i+1} g_{\beta,j} < 0$, from Eq. (10), we get

$$
\begin{aligned}
|e_l^1| &= |(1+r\beta)e_l^1 - r\sum_{j=0,j\neq1}^{i+1} g_{\beta,j}e_{i-j+1}^1| \\
&\leq |(1-r\beta)||e_l^0| + r\sum_{j=0,j\neq1}^{i+1} g_{\beta,j}|e_{i-j+1}^0| + \\
&\qquad \tau^\alpha\Gamma(2-\alpha)|f[U(x_i,t_0),x_i,t_0] - f[U_i^0,x_i,t_0]| + |T_l^1| \\
&\leq |e_l^0| + \tau^\alpha\Gamma[2-\alpha]L|U(x_i,t_0) - U_i^0| + |T_l^1| \\
&\leq |e_l^0| + \tau L|e_l^0| + |T_l^1| \\
&\leq (1+\tau L)|e_l^0| + |T_l^1| \\
\Rightarrow |e_l^1| &\leq (1+\tau L)|e_l^0| + c_1O(\tau^2+h^2) \\
\Rightarrow \|E^1\|_\infty &\leq (1+\tau L)\|E^0\|_\infty + cO(\tau^2+h^2)
\end{aligned}
$$

Assume that

$$\|E^k\|_\infty \leq (1+\tau L)^k\|E^0\|_\infty + cO(\tau^2+h^2)$$

From Eq. (11), we get

$$
\begin{aligned}
|e_l^{k+1}| &= |(1+r\beta)e_l^{k+1} - r\sum_{j=0,j\neq1}^{i+1} g_{\beta,j}e_{i-j+1}^{k+1}| \\
&\leq (1-b_1-r\beta)|e_l^k| + r\sum_{j=0,j\neq1}^{i+1} g_{\beta,j}|e_{i-j+1}^k| + \sum_{j=1}^{k-1}(b_j - b_{j+1})|e_l^{k-j}| + b_k|e_l^0| + \\
&\qquad \tau^\alpha\Gamma[2-\alpha]|f[U(x_i,t_k),x_i,t_k] - f[U_i^k,x_i,t_k]| + |T_l^{k+1}| \\
&\leq (1-b_1)|e_l^k| + (b_1-b_k)|e_l^k| + b_k|e_l^k| + \tau L|U_i^k - U_i^k| + |T_l^{k+1}| \\
&\leq (1-b_1+b_1-b_k+b_k)|E_l^k| + \tau L|E_l^k| + |T_l^{k+1}| \\
&\leq (1+\tau L)|E_l^k| + c_2O(\tau^2+h^2) \\
\Rightarrow \|E^{k+1}\|_\infty &\leq (1+\tau L)^{k+1}\|E^0\|_\infty + c_1O(\tau^2+h^2) + c_2O(\tau^2+h^2) \\
&\leq (1+\tau L)^{k+1}\|E^0\|_\infty + cO(\tau^2+h^2)
\end{aligned}
$$

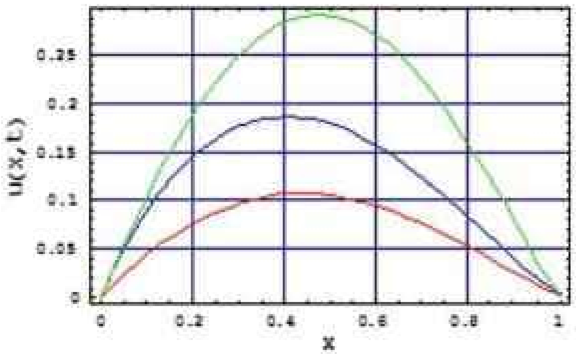


**Fig. 1** The diffusion profile with $t = 0.05$, $h = 0.1$, $\alpha = 0.7$, $\beta = 1.7(blue)$, $\alpha = 0.8$, $\beta = 1.8(red)$ *and* $\alpha = 0.9$, $\beta = 1.9(green)$

Hence, by induction we prove $\|E^k\|_\infty \leq (1 + \tau L)^k \|E^0\|_\infty + cO(\tau^2 + h^2)$, for all $k = 1, 2, ...N$.

Therefore, we observe that for any $x$ and $t$, as $(h, \tau) \to (0, 0)$, $U_i^k$ converges to $U(x_i, t_k)$. Hence proof completed (Fig. 1).

## 5 Numerical Solutions

We now obtain the numerical solution of one dimensional time-space fractional diffusion equation by the discrete scheme developed in Eqs. (10)–(13). The following time-space fractional diffusion equation with initial and boundary conditions and a non-linear term is considered.

$$\frac{\partial^\alpha U(x,t)}{\partial t^\alpha} = \frac{\partial^\beta U(x,t)}{\partial x^\beta} + \sin U;\ 0 < x < 1,\ 0 < \alpha \leq 1,\ 1 < \beta \leq 2,\ t > 0$$

$$initial\ condition : U(x, 0) = \sin \pi x,\ \ 0 \leq x \leq 1$$

$$boundary\ conditions : U(0, t) = U_L = 0,\ \ U(1, t) = U_R = 0,\ \ t > 0$$

with the diffusion coefficient $d = 1$.

The numerical solution is obtained at $t = 0.05$ by considering the parameters $\tau = 0.005$ and $h = 0.1$, which are simulated using Mathematica Software for three different values of $\alpha$ and $\beta$ that is, $\alpha = 0.7$, $\beta = 1.7(blue)$, next $\alpha = 0.8$, $\beta = 1.8(red)$ and next $\alpha = 0.9$, $\beta = 1.9(green)$ followed by the solution graphically.

**Conclusions**

(i) We have successfully developed the Crank-Nicolson fractional order finite difference scheme for time-space fractional diffusion equation in a bounded domain.
(ii) We observe that the developed scheme is unconditionally stable.
(iii) Analysis shows clearly that the finite difference scheme is numerically stable and the results are compatible with our theoretical analysis. Therefore, these solution techniques can be applicable to other fractional partial differential equations.

## References

1. Baeumer, B., Meerschaert, M.M., Mortensen, J.: Space-time fractional derivative operators. Proc. Am. Math. Soc. **133**, 2273–2282 (2005)
2. Ben Adda, F.: Geometric interpritaion of the fractional derivative. J. Fract. Calc. **11**, 21–52 (1997)
3. Diethelm, K., Ford, N.J., Freed, A.D., Luchko, Yu.: Algorithms for the fractional calculus: a selection of numerical methods. Comput. Methods Appl. Mech. Engrg. **194**, 743–773 (2005)
4. Hilfer, R.: Applications of Fractional Calculus in Physics. World Scientific, Singapore (2000)
5. Jain, M.K., Iyengar, S.R.K., Jain, R.K.: Numerical Methods for Scientific and Engineering Computation, 3rd edn. New AGE International (P) Limited, Publishers, New Delhi (1992)
6. Strikwerda, J.C.: Finite Difference Schemes and Partial Differential Equations, 2nd edn. SIAM (2004)
7. Lavoie, J.L., Osler, T.J., Tremblay, R.: Fractional derivatives and special functions. SIAM Rev. **18**(2), 240–268
8. Mainardi, F., Luchko, Yu., Pagnini, G.: The fundamental solution of the space-time fractional diffusion equation. Fract. Calc. Appl. Anal. **4**, 153–192 (2001)
9. Miller, K., Ross, B.: An Introduction to the Fractional Calculus and Fractional Differential Equations. Eiley, New York (1993)
10. Munkhammar, J.D.: Riemann-Liouville Fractional Derivatives and the Taylor-Riemann Series, UUDM Project Report (2004)
11. Murio, D.A.: On stable numerical evaluation of caputo fractional derivatives. Comput. Math. Appl. **51**, 1539–1550 (2006)
12. Nishimoto, K. (ed.): Fractional Calculus and its Applications. Nihon University, Koriyama (1990)
13. Podlubny, I.: Fractional Differential Equations. Academic Press, San Diago (1999)
14. Pskhu, A.V.: Partial Differential Equations of Fractional Order. Nauka, Moscow (2005)
15. Yang, Q., Turner, I., Liu, F.: Analytical and numerical solutions for the time and space-symmetric fractional diffusion equation. ANZIAM J. **50**(CTA 2008), C800–C814 (2009)
16. Richtmeyer, R.D., Morton, K.W.: Difference Method in Initial Value Problems, 2nd edn. Interscience, New York (1967)
17. Sankara Rao, K.: Numerical Methods for Scientist and Engineers. Printice-Hall of India, New Delhi (2004)
18. Shen, S., Liu, F.: Error analysis of an explicit finite difference approximation for the space fractional diffusion equation with insulated ends. ANZIAM J. **46**(E), C871–C887 (2005)
19. Diego Murio, A.: Implicit finite difference approximation for time fractional diffusion equations. Comput. Math. Appl. **56**, 1138–1145 (2008)

JETIR.ORG ISSN: 2349-5162 | ESTD Year : 2014 | Monthly Issue
JOURNAL OF EMERGING TECHNOLOGIES AND INNOVATIVE RESEARCH (JETIR)
An International Scholarly Open Access, Peer-reviewed, Refereed Journal

# Virtual Chemistry Practical for future owing to the pandemic

***Beg Waseem Ahamad**

Department of Chemistry
Gokhale Education Societys'
RNC Arts,JDB Commerce NSC Science College Nashik-road, Nashik
Email: begwaseem02@gmail.com

Contact- 8329628368, 9923073900

**Abstract:** The Basic Practical Chemistry course's objectives are to give students a thorough understanding of practical chemistry's underlying principles and to help them hone their fundamental experimenting skills. The in-person lab sessions are regarded as one of the most crucial components of the course for students to engage in because many students enter the course with little or no prior lab experience. Recently, academic activities all around the world came to a halt as a result of the COVID-19 epidemic, and all in-person events were cancelled as a result of strict health laws.

In contrast to theory-based courses, which continued to be taught even during the pandemic through online teaching methods, there were very few alternatives available to keep practical-based courses running during the pandemic due to the inherent difficulties of effectively delivering practical-based content through online teaching methods. Open educational resources (OER) were used to develop a collection of virtual chemical simulations and animations to help students learn during the pandemic lockdown. Through the university's learner management system and specially developed MOOCs, it was made available to students online.

**Key Words:** COVID-19, Pandemic, Virtual Chemical Laboratories, Animations and Simulations.

## Introduction:

The global COVID-19 pandemic epidemic that started in 2020 was unexpected and difficult to manage. All teachers worldwide were required to hold their classes online due to the COVID-19 pandemic. Students are completing their courses online while the majority of the instruction has been outsourced off campus. Despite this, the lab class/chemistry practical, one of the most essential elements of higher scientific education, has turned out to be challenging. 2
The relocation of experiments and laboratory activities was demanded because science and chemistry teachers had to synchronize the instruction of both theoretical and practical knowledge. The rise of information and communication technologies (ICTs) has opened up a range of options for students learning practical chemistry fundamentals through online classes. Schomann (2003)

## Objectives:

The relevance of theoretical (content) and practical (process) development is focused more than in other academic subjects, such as chemistry. 4 Improving the practical components of the course curriculum while also teaching students experimental methodologies, observations, presentation skills, and laboratory techniques is all vital, right? Students' comprehension of chemistry is greatly influenced by experimental chemistry labs. 5 The discovering process seems to be what gives science its fundamental excitement, and laboratory experiments illustrate the interconnections between theory and practice. Aspiring scientists benefits from lab sessions in the development of both practical abilities and a grasp of the intellectual culture of the discipline. Without being given an opportunity to apply theoretical concepts in a lab setting, many students might not understand entirely some theoretical concepts. 6 Undergraduate chemistry courses must also include laboratory-based practical components in order for students to gain practical experience and knowledge of chemistry-related experiments. In general, practical chemistry techniques that can be seen and done in a lab are simpler to understand. Technology is therefore not used all that commonly while teaching practical chemistry material.

## Methodologies:

All stakeholders in higher education obtained surveys on the benefits and drawbacks of virtual or online learning that were created in a Google form. In this study, responses are gathered and analyzed. On the basis of this, this part explores and discusses some of the perspectives of various stakeholders.

Even if technology is necessary for remote education, it is essential to think about how it can be utilized to impart knowledge to make sure it is successful. Evaluating whether or not an unique tool could be used to educate practical chemistry online was the study's main objective as a consequence. 7
While online course delivery has historically been utilized in fields of education where it is easy to execute, it has historically been used very infrequently in fields like practical chemistry.

Thanks to advancements in technology within the last few years, users can now imitate chemistry lab experiences digitally, without having to be present. Virtual reality simulations, according to the authors, are important in education because they provide students with realistic models that they can interact with to get real-world experience and a stable environment where they may repeat exercises without fear of being hurt. 2 Unquestionably, the current COVID-19 pandemic has changed the world's educational system, causing a swift shift away from traditional classroom-based instruction and toward a new type of online learning. As a result, technology was successfully used in the distribution of materials at the university level during the recent COVID-19 pandemic, according to a number of recent investigations.

Despite the widespread misperception that online education would enable academics to continue teaching regardless of their social constraints, a number of institutional, technological, and perceived barriers may limit the broad use of online content delivery systems. 8
The use of a virtual lab for education and assessment has significant downsides, and there is a scarcity of student support for it. Such restrictions have been attributed to basic impediments including a lack of required infrastructure, a technical skill gap, or even a lack of participant interest and drive. 9 Therefore, if technology is to allow effective information sharing, it is crucial that any potential restrictions be discovered and preventative measures be made to lessen their impact.

Researchers have examined students' performance in physical and virtual lab settings in research investigations. Students can benefit from virtual laboratories regardless of where they are when they participate. 10 Additionally, they contribute to reducing the amount of chemical waste generated. All of the experts suggest taking measures when adjusting or conducting additional study. Similar challenges arise for lab teachers due to the requirement to maintain social distance in crowded laboratory classes, even though restrictions are becoming less strict.

Fig 1: **Student, teacher, and parent perspectives on the advantages and disadvantages of the virtual laboratory**

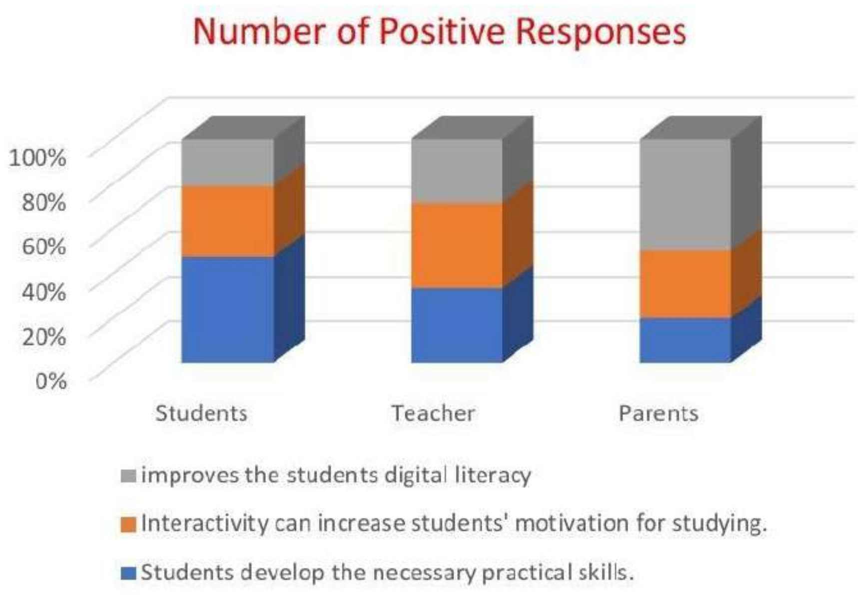


## Conclusion:

Following the first wave of the COVID-19 epidemic, academic activities were immediately resumed, and the students were welcomed back into the college to take part in the regularly planned laboratory-based practical sessions. 11 It was predicted that students who had used information and communication technologies (ICTs) to become familiar with the theory and procedures of the experiments covered in the session would complete the laboratory activity with more competency.

It is stated that, even while digital technologies have their place in the laboratory, they shouldn't completely take the place of the important activities. It should go without saying that laboratory activities must include both traditional labs and computer-assisted activities. Don't rely solely on one or the other.

## References:

1. Ferraz-Caetano, J. (2021). *Towards Digital Laboratories*. 464–474. https://doi.org/10.4018/978-1-7998-6533-9.CH023

2. Wijenayake, L. A., & Iqbal, S. S. (2021). Going virtual with practical chemistry amidst the COVID-19 pandemic lockdown: significance, constraints and implications for future. *Asian Association of Open Universities Journal*, *16*(3), 255–270. https://doi.org/10.1108/AAOUJ-09-2021-0102

3. Youssef, M., McKinstry, E. L., Dunne, A., Bitton, A., Brady, A. G., & Jordan, T. (2020). Developing engaging remote laboratory activities for a non majors chemistry course during covid-19. *Journal of Chemical Education*, *97*(9), 3048–3054. https://doi.org/10.1021/ACS.JCHEMED.0C00792

4. Boschmann, E. (2003). Teaching Chemistry via Distance Education. *Journal of Chemical Education*, *80*(6), 704–708. https://doi.org/10.1021/ED080P704

5. Phipps, L. R. (2013). Creating and teaching a web-based, university-level introductory chemistry course that incorporates laboratory exercises and active learning pedagogies. *Journal of Chemical*

*Education*, *90*(5), 568–573. https://doi.org/10.1021/ED200614R

6. Van Heuvelen, K. M., Daub, G. W., & Ryswyk, H. Van. (2020). Emergency remote instruction during the covid-19 pandemic reshapes collaborative learning in general chemistry. *Journal of Chemical Education*, *97*(9), 2884–2888. https://doi.org/10.1021/ACS.JCHEMED.0C00691

7. Fergus, S., Botha, M., & Scott, M. (2020). Insights Gained during COVID-19: Refocusing Laboratory Assessments Online. *Journal of Chemical Education*, *97*(9), 3106–3109. https://doi.org/10.1021/ACS.JCHEMED.0C00568

8. Kennepohl, D. (2021). Laboratory activities to support online chemistry courses: A literature review. *Canadian Journal of Chemistry*, *99*(11), 851–859. https://doi.org/10.1139/CJC-2020-0506
9. Kennepohl, D. K. (2013). Learning from blended chemistry laboratories. *Proceedings - 2013 IEEE 5th International Conference on Technology for Education, T4E 2013*, 135–138. https://doi.org/10.1109/T4E.2013.40

10. Shidiq, A. S., Permanasari, A., Hernani, & Hendayana, S. (2021). Chemistry teacher responses to learning in the COVID-19 outbreak: Challenges and opportunities to create innovative lab-work activities. *Journal of Physics: Conference Series*, *1806*(1). https://doi.org/10.1088/1742-6596/1806/1/012195

11. Waycott, J., Dalgarno, B., Kennedy, G., & Bishop, A. (2012). Making science real: Photo-sharing in biology and chemistry. *Research in Learning Technology*, *20*(2). https://doi.org/10.3402/RLT.V20I0.16151

International Journal of Advance and Applied Research
www.ijaar.co.in
ISSN – 2347-7075 Impact Factor – 7.328
Peer Reviewed Bi-Monthly
Vol.3 No.2 Sept – Oct 2022

# SYNTHESIS AND STRUCTURAL PROPERTIES OF ZINC FERRITE

**Rahul Upalaikar**
Assistant professor, Department of Physics,
R.N.C. Art's, J.D.B. Commerce and N.S.C. Science College, Nashik Road, India, 422101

***Corresponding Author***- **Rahul Upalaikar**
Email:- wankhedkarpt@gmail.com
**DOI- 10.5281/zenodo.7295619**

**Abstract-**
Powdered spinel zinc ferrite powder sample was synthesized by using sol-gel method. Structure of spinel zinc ferrite was confirmed by using X-ray diffraction. Average crystalline size and lattice parameter of powdered sample is calculated using X- ray diffraction.

**Keywords** – Zinc ferrite, X-ray diffraction

## Introduction

Ferrite nanoparticles are a large group of magnetic particles have drawn a lot of attention of many researchers due to its extensive uses in variety of disciplines from biomedical to industry. Ferrite nanoparticles are particularly used for biomedical applications due to its physiochemical properties like surface functionalization feasibility, high surface to volume ratio [1]. properties like strong magnetic anisotropy, high coercivity at room temperature, moderate saturation magnetization, good mechanical hardness, chemical stability & high resistivity makes the family of ferrites is promising material for various industrial purpose such as sensors, memory devices, refrigeration, quality filter circuit, high frequency transformers, wide band transformers, high frequency electronic circuitry, microwave applications, multilayer chip conductor [2]–[4].

Spinel ferrites have face centered cubic structure and characterized by $MFe_2O_4$ formula where M denotes the divalent metal ions like Zn, Cu, Al. Spinel ferrites can have normal spinel structure, inverse spinel structure or mixed spinel structure. In spinel structure, all metal ions occupy tetrahedral sites, whereas all $Fe^{+3}$ occupy octahedral sites. In inverse structure, all metal ions occupy octahedral site while $Fe^{+3}$ ions are distributed over both tetrahedral & octahedral sites [5]. Among family of ferrites, zinc ferrite ($ZnFe_2O_4$) having normal spinel structure is imperative due its wide applications in data recording media, adsorption, sensors, photo catalyst, lithium ion batteries, magnetic resonance imaging (MRI), biomedical applications [6]–[8] as it shows low saturation magnetization, high resistivity properties. For synthesis of zinc ferrite, many methods like co precipitation[9], hydrothermal [10], combustion [11], ball milling [12] , sol gel [13] are used.

In this paper, we reported synthesis of zinc ferrite using sol gel method & structural properties of zinc ferrite are determined using X-ray diffraction.

## Materials & methods

### Materials

For synthesis of zinc ferrite analytical grade zinc nitrate ($Zn (NO_3)_3.6H_2O$), & ferric nitrates ($Fe (NO_3)_3.9H_2O$), reagents are used without further purification. Double distilled water is used throughout the synthesis & citric acid is used as reducing agent.

### Method

For preparation of zinc ferrite, separate solutions of zinc nitrate & ferric nitrate are prepared in stoichiometric amount in double distilled water. These solutions were mixed into beaker & beaker is kept for constant stirring with heating at 150°C. Citric acid is added into beaker as a reducing agent. After 3 hours, solution is converted into viscous gel due to evaporation. Then, the gel was heated to 250°C to self -sustaining combustion to produce burned brownish zinc ferrite fluffy powder. This burned fluffy brownish powder is kept for annealing in furnace for 900°C for 4 hours & used for further characterization.

## Results and Discussion

### Structural properties

X-ray diffraction (XRD) pattern of zinc ferrite powder is shown in figure 1. From X-ray diffraction pattern, phase, crystalline size and lattice parameter of the powdered sample is obtained. The XRD pattern shows spinel structure having Fd3m space group having peaks due to (111), (200), (311), (222), (400), (422), (511) planes that fit with JCPDS card no.82-1049. Average crystalline size is calculated using Debye-Scherer formula $D = \frac{0.9\lambda}{\beta cos\theta}$ where $\lambda$ is the wavelength of X-ray radiation, $\beta$ is full width half maxima for most intense peak, $\theta$ -Bragg's angle for the most intense peak. Lattice parameter is calculated by using formula $a = d_{hkl}\sqrt{h^2 + k^2 + l^2}$ , where $d_{hkl}$ is inter-planner spacing & $hkl$ are Miller indices. Using given formula calculated value of lattice constant & average crystalline size are 8.48 °A and 27.12 nm.

## Conclusion

In the present paper, zinc ferrite is synthesized using sol-gel method & spinel structure of zinc ferrite is confirmed by using X-ray diffraction. From X-ray diffraction, calculated values of lattice constant and average crystalline size were found out to be 8.48 °A and 27.12 nm.

## References


[1] S. D. & G. Dini, "Applications of cobalt ferrite nanoparticles.pdf," p. 18, 2019.

[2] B. K. Kuanr *et al.*, "Frequency and field dependent dynamic properties of CoFe2-xAlxO4 ferrite nanoparticles," *Mater. Res. Bull.*, vol. 76, pp. 22–27, 2016, doi: 10.1016/j.materresbull.2015.11.033.

[3] R. Srivastava and B. C. Yadav, "Ferrite materials: Introduction, synthesis techniques, and applications as sensors," *Int. J. Green Nanotechnol. Biomed.*, vol. 4, no. 2, pp. 141–154, 2012, doi: 10.1080/19430892.2012.676918.

[4] M. M. Eltabey and S. A. Gharbia, "Enhancement of the magnetic properties of Ni – Cu – Zn ferrites by the non-magnetic Al 3 + -ions substitution," *J. Alloys Compd.*, vol. 509, no. 5, pp. 2473–2477, 2011, doi: 10.1016/j.jallcom.2010.11.056.

[5] J. B. Goodenough and P. E. Tannenwald, "Oxide magnetic materials," *Solid-State Electronics*, vol. 7, no. 7. pp. 556–557, 1964. doi: 10.1016/0038-1101(64)90095-4.

[6] R. M. Borade, S. B. Somvanshi, S. B. Kale, R. P. Pawar, and K. M. Jadhav, "Spinel zinc ferrite nanoparticles: An active nanocatalyst for microwave irradiated solvent free synthesis of chalcones," *Mater. Res. Express*, vol. 7, no. 1, 2020, doi: 10.1088/2053-1591/ab6c9c.

[7] X. Biotech, "Evaluation of the Zinc Ferrite Nano particles for Bio-applications," vol. 46, no. August, pp. 2–7, 2017.

[8] K. Wu, J. Li, and C. Zhang, "Zinc ferrite based gas sensors: A review," *Ceram. Int.*, vol. 45, no. 9, pp. 11143–11157, 2019, doi: 10.1016/j.ceramint.2019.03.086.

[9] L. C. Sonia, M. Victory, and S. Phanjoubam, "A Comparative Study of the Properties of Zinc Ferrite Nanoparticles Synthesized by Different Techniques for Nanofluid Preparation," *Integr. Ferroelectr.*, vol. 204, no. 1, pp. 100–111, 2020, doi: 10.1080/10584587.2019.1674978.

[10] R. Rahimi, M. Heidari-Golafzani, and M. Rabbani, "Preparation and photocatalytic application of ZnFe2O4@ZnO core-shell nanostructures," *Superlattices Microstruct.*, vol. 85, pp. 497–503, 2015, doi: 10.1016/j.spmi.2015.05.047.

[11] P. M. Prithviraj Swamy, S. Basavaraja, A. Lagashetty, N. V. Srinivas Rao, R. Nijagunappa, and A. Venkataraman, "Synthesis and characterization of zinc ferrite nanoparticles obtained by self-propagating low-temperature combustion method," *Bull. Mater. Sci.*, vol. 34, no. 7, pp. 1325–1330, 2011, doi: 10.1007/s12034-011-0323-x.

[12] S. Bid and S. K. Pradhan,

"Preparation of zinc ferrite by high-energy ball-milling and microstructure characterization by Rietveld's analysis," *Mater. Chem. Phys.*, vol. 82, no. 1, pp. 27–37, 2003, doi: 10.1016/S0254-0584(03)00169-X.

[13] A. Azam, M. Chaman, and A. H. Naqvi, "Synthesis of zinc ferrite nanoparticles by sol-gel method and their characterisation," *Int. J. Nanoparticles*, vol. 2, no. 1–6, pp. 388–393, 2009, doi: 10.1504/ijnp.2009.028773.

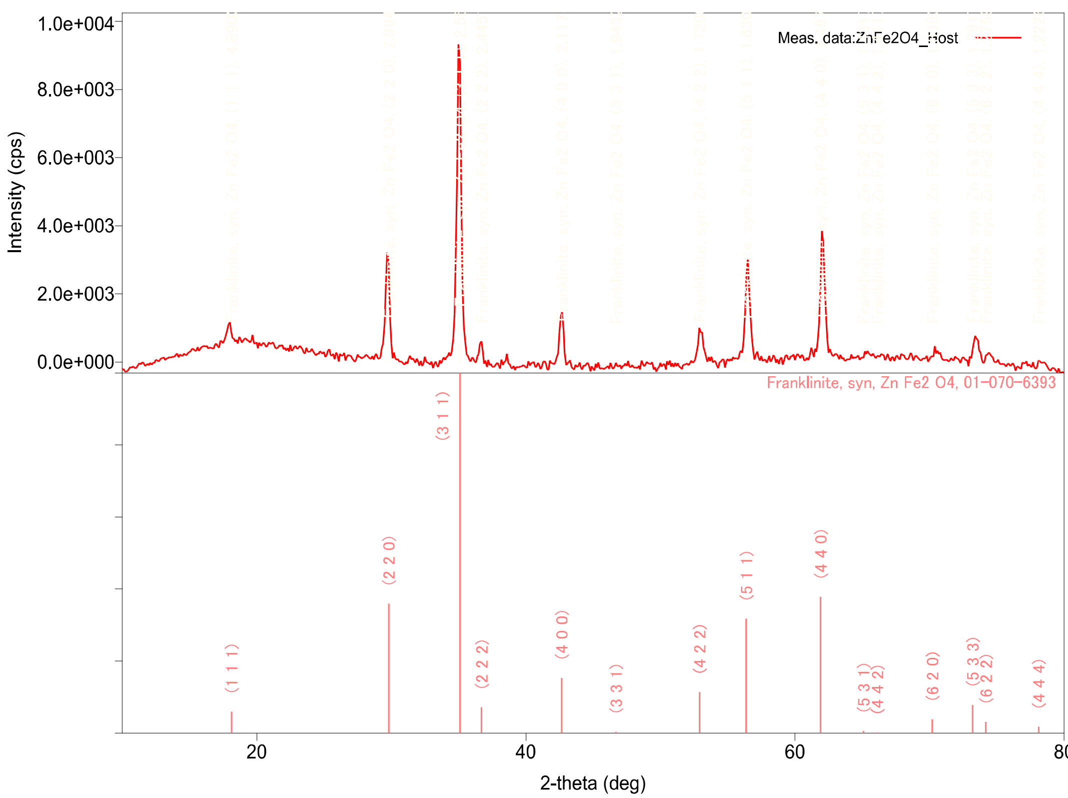


**Fgure 1**

Regular Article | Published: 17 June 2022

# Removal of Cd(II) and Pb(II) ions from water solution by $CoFe_2O_4/Al_2O_3$ nanocomposite

Ashwini S. Varpe, Mrinalini D. Deshpande, Dipak R. Tope & Ashok V. Borhade

*The European Physical Journal Plus* **137**, Article number: 705 (2022)

## Abstract

In this study, the performance of magnetic $CoFe_2O_4/Al_2O_3$ nanocomposite is evaluated towards the removal of Cd(II) and Pb(II) metal ions from the wastewater. The removal efficiency of $CoFe_2O_4/Al_2O_3$ nanocomposite is compared with the bare $CoFe_2O_4$ nanoparticles. The $CoFe_2O_4$ and its composite with $Al_2O_3$ is synthesized via sol–gel auto-combustion method. The as-prepared samples are characterized by fourier transform infrared spectroscopy (FTIR), X-ray diffraction (XRD), field emission scanning electron microscopy (FESEM), transmission electron microscope (TEM) and vibrating sample magnetometer (VSM) analysis. As compared to bare nanoparticles, the decrease in particle size, enhanced specific surface area and porosity, higher magnetization, lowering of the band gap, and uniform distribution with spherical shaped structure is observed in $CoFe_2O_4/Al_2O_3$ nanocomposite. To probe the nature of the adsorbent, various experiments are performed by considering the reaction parameters like contact time, adsorbent dose and concentration of Cd(II) and Pb(II) ions. During optimization process, it is observed that for bare $CoFe_2O_4$ nanoparticles, the maximum removal efficiency is found for Cd(II) ions 75% and for Pb(II) ions, it reaches upto 43%. In composite form, the removal efficiency for Cd(II) ions increases upto 88% and for Pb(II) ions, it is 77%. The enhanced removal efficiency is observed for the $CoFe_2O_4/Al_2O_3$ nanocomposite due to smaller particle size and increased surface area as compared to that of $CoFe_2O_4$ nanoparticles. The effect on removal efficiency is also studied with the variation of temperature. The isothermal adsorption results are well fitted to Langmuir model. The high adsorption capacity of $CoFe_2O_4/Al_2O_3$ nanocomposite as compared to $CoFe_2O_4$ makes it promising candidate for removal of heavy metal ions from aqueous solution.

## References

1. M.L. Sikosana, K. Sikhwivhilu, R. Moutloali, D.M. Madyira, Proc. Manufact. **35**, 1018 (2019)

2. K.K. Kesari, R. Soni, Q.M. Jamal, P. Tripathi, J.A. Lal, N.R. Jha, M.H. Siddiqui, P. Kumar, V. Tripathi, J. Ruokolainen, Water Air Soil Pollut. **232**, 208 (2021)

3. Z. Aghalari, H.U. Dahms, M. Sillanpa, J.E. Sosa-Hernandez, R. Parra-Saldivar, Glob. Health **16**, 13

(2020)

4. N.A. Qasem, R.H. Mohammed, D.U. Lawal, npj Clean Water **4**, 36 (2021)

5. K. Atkovska, K. Lisichkov, G. Ruseska, A.T. Dimitrov, A. Grozdanov, J. Chem. Tech. Metall. **53**, 202 (2018)

6. K.K. Kefeni, B.B. Mamba, T.A. Msagati, Sep. Purif. Technol. **188**, 399 (2017)

7. R. Suresh, S. Rajendran, P.S. Kumar, D.N. Vo, L. Cornejo-Ponce, Chemosphere **274**, 129734 (2021)

8. A. Soufi, H. Hajjaoui, R. Elmoubarki, M. Abdennouri, S. Qourzal, N. Barka, Appl. Surf. Sci. Adv. **6**, 100145 (2021)

9. K.A. Yaqoob, M. Bououdina, M.S. Akhter, B.A. Najar, J.J. Vijaya, Mater. Chem. Phys. **232**, 254 (2019)

10. P. Jain, M. Kaur, J.K. Grewal, Bull. Mater. Sci. **42**, 77 (2019)

11. R. Asadi, H. Abdollahi, M. Gharabaghi, Z. Boroumand, Adv. Powder Tech. **31**, 1480 (2020)

12. Y. Liu, Y. Zhang, J.D. Feng, C.F. Li, J. Shi, R. Xiong, J. Exp. Nanosci. **4**, 159 (2009)

13. T. Tatarchuk, M. Bououdina, W. Macyk, O. Shyichuk, N. Paliychuk, I. Yaremiy, B. Al-Najar, M. Pacia, Nanoscale Res. Lett. **12**, 141 (2017)

14. J. P. Singh, J. Y. Park, V. Singh, S. H. Kim, W. C. Lim, H. Kumar, Y. H. Kim, Lee S, Chae KH (2020) RSC Adv. 10:21259 (2020)

15. N.T.T. Loan, N.T.H. Lan, N.T.T. Hang, N.Q. Hai, D.T.T. Anh, V.T. Hau, L.V. Tan, T.V. Tran, Processes **7**, 885 (2019)

16. B. Alqassem, I. Othman, M.A. Haija, F. Banat, Catal. Commun. **150**, 106267 (2021)

17. R.S. Melo, P. Banerjee, A. Franco, J. Mater. Sci. Mater. Electron. **29**, 14567 (2018)

18. R.S. Yadav, I. Kuritka, J. Vilcakova, J. Havlica, J. Masilko, L. Kalina, J. Tkacz, J. Svec, V. Enev,

M. Hajduchova, Adv. Nat. Sci. Nanosci. Nanotechnol. **8**, 045002 (2017)

19. M.A. Maksoud, A.M. Elgarahy, C. Farrell, A.H. Al-Muhtaseb, D.W. Rooney, A.I. Osman, Coord. Chem. Rev. **403**, 213096 (2020)

20. C. Ren, X. Ding, H. Fu, C. Meng, W. Li, H. Yang, RSC Adv. **6**, 72479 (2016)

21. T. Dippong, E.A. Levei, O. Cadar, Materials **14**, 1139 (2021)

22. X. Wang, Z. Zhang, Y. Zhao, K. Xia, Y. Guo, Z. Qu, R. Bai, Nanomaterials **8**, 673 (2018)

23. X. Liu, B.P. Pichon, C. Ulhaq, C. Lefevre, J.M. Greneche, D. Begin, S. Begin-Colin, Chem. Mater. **27**, 4073 (2015)

24. H. Lu, Y. Li, Y. Wang, X. Li, J. Saudi Chem. Soc. **23**, 536 (2019)

25. N.S. Asri, E. Suharyadi, A.I.P. Conf, Proc. **2256**, 1–030022 (2019)

26. M. Yakob, H. Umar, P. Wahyuningsih, R.A. Putra, A.I.M.S. Mater, Science **6**, 45 (2019)

27. C. Ren, X. Ding, W. Li, H. Wu, H. Yang, J. Chem. Eng. Data **62**, 1855 (2017)

28. E.E. Ateia, R. Ramadan, A.S. Shafaay, Appl. Phys. A **126**, 222 (2020)

29. B.G. Fouda-Mbanga, E. Prabakaran, K. Pillay, Arab. J. Chem. **13**, 6762 (2020)

30. W. Cai, Y. Hu, J. Yu, W. Wang, J. Zhou, M. Jaroniec, RSC Adv. **5**, 7066 (2015)

31. R. Zotov, E. Meshcheryakov, A. Livanova, T. Minakova, O. Magaev, L. Isupova, I. Kurzina, Materials **11**, 132 (2018)

32. X. Li, R. Zhao, B. Sun, X. Lu, C. Zhang, Z. Wang, C. Wang, RSC Adv. **4**, 42376 (2014)

33. Q. Wang, Y. Shao, N. Guo, W. Chu, J. Chen, X. Lu, Y. Zhu, N. An, Sep. Purif. Technol. **189**, 176 (2017)

34. D.Q. Tang, D.J. Zhang, D.Y. Tang, Chem. Lett. **35**, 1238 (2006)

35. A. Yakubu, Z. Abbas, N.Z. Ibrahim, M. Hashim, Phys. Sci. Int. J. **8**, 1 (2015)

36. S. Anand, A.P. Amaliya, M.S. Janifer, S. Pauline, Modern Electron. Mater. **3**, 168 (2017)

37. E. Eidi, M.Z. Kassaee, P.T. Cummings, Res. Chem. Intermed. **44**, 1 (2018)

38. A. Shamsi, S. Hashemian, Desalina. Water. Treat. **181**, 346 (2020)

39. A.V. Borhade, S.R. Kenkrej, J. Chem. Eng. Data **62**, 596 (2017)

## Acknowledgements

Authors are greatly thankful for financial support by the Council of Scientific and Industrial Research (CSIR), New Delhi for the project EMR-II-03/1429/18. Authors acknowledges XRD facility from IR services technology, Mumbai, VSM facility from SNBNCBS, Kolkata, and UV facility from Gholap College, Pune. Authors greatfully acknowledges, Department of Chemistry, H. P. T.

Arts and R. Y. K. College Nashik, for providing experimental setup for adsorption study. Authors would like to thank Miss Mayuri Kulkarni from Chemistry Department for fruitful discussion while performing the experiments.

## Author information

### Authors and Affiliations

**Department of Physics, H.P.T. Arts and R.Y.K. Science College, Nashik, Maharashtra, 422005, India**

Ashwini S. Varpe & Mrinalini D. Deshpande

**Department of Chemistry, H.P.T. Arts and R.Y.K. Science College, Nashik, Maharashtra, 422005, India**

Dipak R. Tope & Ashok V. Borhade

### Corresponding author

Correspondence to Mrinalini D. Deshpande.

## Ethics declarations

### Conflict of interest

The authors declare that they have no known competing financial interests or personal relationships that could have appeared to influence the work reported in this paper.

## Rights and permissions

## About this article

### Cite this article

Varpe, A.S., Deshpande, M.D., Tope, D.R. *et al.* Removal of Cd(II) and Pb(II) ions from water solution by $CoFe_2O_4/Al_2O_3$ nanocomposite. *Eur. Phys. J. Plus* **137**, 705 (2022). https://doi.org/10.1140/epjp/s13360-022-02898-y

| Received | Accepted | Published |
| --- | --- | --- |
| 27 January 2022 | 28 May 2022 | 17 June 2022 |

DOI

https://doi.org/10.1140/epjp/s13360-022-02898-y

# Composite $SiO_2$:$PbCrO_4$ catalyst as an efficient heterogeneous catalyst for one pot four component synthesis of 1H-pyrazolo [1, 2-b] phthalazine-5, 10-dione derivatives

**Borhade Ashok[1]*, Shelke Yogita[2] and Tope Dipak[1]**
1. Department of Chemistry, HPT Arts and RYK Science College, (Affiliated to Savitribai Phule Pune University, Pune), Nasik (MS), INDIA
2. Department of Chemistry, K. K. Wagh Arts, Commerce and Science College, (Affiliated to Savitribai Phule Pune University, Pune), Pimpalgaon (B), Niphad, Nashik (MS), INDIA
*ashokborhade2007@yahoo.co.in

***Abstract***
*An efficient one pot four component 1H-pyrazolo [1,2-b] phthalazine-5,10-dione derivatives was synthesized by using benzaldehyde, phthalic anhydride, hydrazine hydrate and malononitrile in presence of $SiO_2$ composite $PbCrO_4$ as a catalyst. The composite $SiO_2$:$PbCrO_4$ catalyst was prepared by using hydrothermal process. The XRD, TEM and BET measurement techniques were used for characterization of catalyst.*

*The present method offers several advantages such as use of an inexpensive catalyst, high product yield, short reaction time, mild reaction condition and reusability of the catalyst.*

**Keywords:** $SiO_2$ composite $PbCrO_4$ as a catalyst, 1H-pyrazolo [1,2-b] phthalazine-5,10-dione, phthalic anhydride, hydrazine monohydrate, malononitrile.

## Introduction

Strecker[21] discovered multicomponent reactions (MCRs) in 1850 and they are becoming more important in the synthesis of various heterocyclic compounds, as well as having great potential for the synthesis of drug-like heterocyclic molecules. MCRs are a type of multicomponent reaction that may be utilized to make physiologically active molecules and they have become a contentious issue in organic and pharmaceutical chemistry.

Further research in the synthesis of heterocyclic compounds via MCR technique and environmentally friendly methodologies is essential in the drug development process. The synthesis of novel heterocyclic compounds has attracted researchers' attention in recent decades due to their large variety of applications. Heterocyclic compounds are abundant in nature and are necessary for life to exist.

Among a wide range of heterocyclic compounds, nitrogen-containing heterocyclic compounds are abundant in nature and their use in medicines, agricultural chemicals and biomaterials is gaining significant attention[4,8,10-12]. 1H-pyrazolo[1,2-b] phthalazine-5,10-diones are nitrogen-containing heterocycles with anticancer, antibacterial, antifungal, anti-inflammatory, anticonvulsant, cytotoxic, antiviral, antitumor, anticoagulant, antibiotic and antihypoglycemic properties[5,9,14,16,18,20,22,23].

Cardiotonic[14] and vasorelaxant[22] properties have also been discovered in phenazine derivatives. As a result, it is essential to design a simple approach for 1H-pyrazolo [1,2-b]phthalazine-5,10-diones.

The following conditions were used to synthesise 1H-pyrazolo [1,2-b]phthalazine-5,10-diones from one-pot three-component condensation of phthalhydrazide, malononitrile/ethyl cyanoacetate and benzaldehyde: [Bmim]OH under microwave irradiation at 100 W power and 45°C[17], triethylamine in ethanol at 50°C for 1 hour and ultrasonication at 50 KHz and 350 W output power[15] and p-TSA in ionic liquid [Bmim]Br as solvent at 100°C[7].

One-pot four component reactions involving phthalimide, hydrazine hydrate, malononitrile/ethyl cyanoacetate and benzaldehyde were also reported using basic ionic liquids such as 1,8-diazabicyclo[5,4,0]-undec-7-en-8-ium acetate[19], pyrrolidinium acetate[13] and triethyl amine as a catalyst[6]. However, conventional techniques have a number of limitations including prolonged reaction times, high temperatures, adverse reaction conditions, the use of toxic and costly catalysts and catalyst recyclability. As a result, there is scope to create environmentally friendly ways for producing 1H-pyrazolo [1,2-b]phthalazine- 5,10-diones.

In this study, we discuss the synthesis of functionalized 1H-pyrazolo[1,2-b]phthalazine-5,10-dione derivatives as a development of our study on multicomponent reactions[1-3]. Under reflux conditions, 1H-pyrazolo[1,2-b]phthalazine-5,10-dione derivatives were produced through a four-component condensation process of hydrazine monohydrate, phthalic anhydride, malononitrile and aromatic aldehydes with $SiO_2$ composite $PbCrO_4$ as catalyst (Scheme 1).

## Material and Methods

Lead oxide (PbO, Sigma-Aldrich, 99.99 %), chromium oxide ($CrO_3$, Sigma-Aldrich, 99.90 %), silicon dioxide ($SiO_2$, Merck, 99.00%) and sodium hydroxide (NaOH, Merck, 99 %) were purchased and used without purification. Similarly, organic chemicals were purchased and used without purification

**General procedure for synthesis of $PbCrO_4$ as catalyst:** In this procedure, an equimolar mixture of PbO (1mol) and $CrO_3$ (1mol) was ground to a fine powder using a mortar and pestle for 20 minutes before being calcined at 300°C for 3 hours. After milling, the resulting powder was calcined at 400 $^0$C for a second time after every two-hour interval.

For 12 hours, the temperature of the Muffle furnace was designed to increase at a rate of 10$^0$C/min from one temperature to the next. The material was cooled and ground using a mortar and pestle after being heated at 400°C for 1 hour. The ground material was then heated for another 12 hours at 600°C. Finally, $PbCrO_4$ polycrystalline powder was produced. The generated catalyst was utilized to characterize and synthesize $SiO_2$ composite $PbCrO_4$ catalysts.

**Synthesis of $SiO_2$:$PbCrO_4$ catalyst:** In a buffer solution, the required amount of $SiO_2$ (1 mol percent) and synthesized $PbCrO_4$ powder (1 mol percent) were mixed to make the $SiO_2$:$PbCrO_4$ catalyst. This reaction mixture was stirred for 1 hour and then placed in a steel-lined Teflon autoclave and heated at 120°C for 24 hours. The precipitate was filtered, rinsed with distilled water and dried for 12 hours at 100$^0$C. The polycrystalline product was placed immediately in the furnace for 4 hours of calcination at 300$^0$C. The obtained catalyst was used for characterization and synthesis of phthalazine-5,10-dione derivatives.

**General Procedure for the synthesis of 1H-pyrazolo[1,2-b]phthalazine-5,10-dione derivatives:** Phthalic anhydride (1 mmol), hydrazine (1 mmol), an aromatic aldehyde (1 mmol) and malononitrile were heated for 15-50 minutes in an oil bath at 120$^0$C. TLC was used to observe the response. After the reaction was completed, the reaction mixture was cooled to room temperature before being poured into ice water. The resulting product was filtered and rinsed with warm water with several times, then the catalyst was separated from the chemicals using ethanol. Various analytical methods were used to characterize the resulting products which were recrystallized.

**Characterization:** Various analytical methods were used to characterize the pure compounds. The XRD pattern was recorded at a scan rate of 0.17° 2θ $S^{-1}$ using a multifunctional X-ray diffractometer (Philips-1710 diffractometer with CuKα, = 1.5406). The scanning electron microscope (SEM) was used to scan the material with a high-energy electron beam. Electron micrographs were taken using a Schottky electron gun on a Hitachi SU 70 FESEM. TEM with SAED on a Phillips CM-200 microscope was used to investigate the structure and particle size of the produced materials. The $N_2$ adsorption–desorption isotherm was used to determine the BET surface area on Quantachrome Autosorb Automated Gas Sorption System Autosorb-1, NOVA-1200 and Mercury Porosimeter Autosorb-1c.

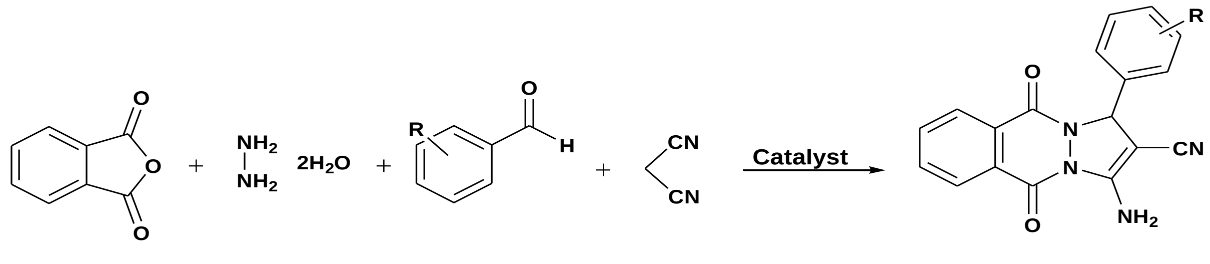


**Scheme 1: Synthesis of phthalazine-5,10-dione derivatives.**

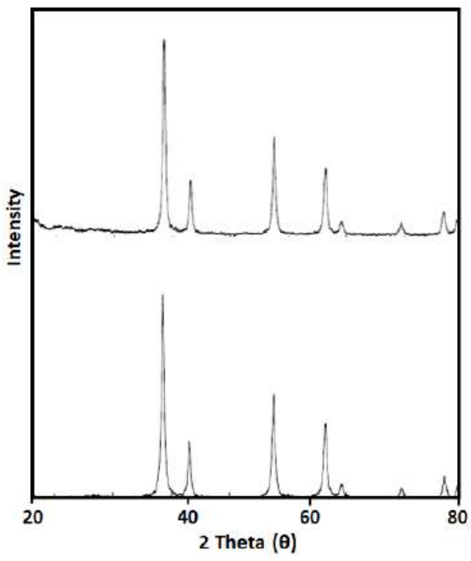


**Figure 1: XRD analysis of a) $PbCrO_4$ b) $SiO_2$:$PbCrO_4$ catalyst.**

**Spectral Data**

**3-amino-5,10-dihydro-5,10-dioxo-1-phenyl-1H-pyrazolo [1,2-b]phthalazine-2-carbonitrile (5a):** M.P.: 276-278 $^0$C; Solvent system: Hexane : Ethyl acetate (9:1), Rf value: 0.58 cm; $^1$H-NMR (400 MHz, DMSO-$d_6$) δ ppm: 7.79-7.63 (10 H, m, H-Ar and $NH_2$), 6.65 (1H, S, CH); $^{13}$C-NMR (125 MHz, DMSO-$d_6$) δ ppm: 167.56, 158.19, 143.43, 141.65, 139.23, 135.73, 131.21, 128.43, 126.21, 125.64, 123.12, 122.87, 121.09, 62.97, 60.52; EIMS: 316 (M+1) m/z.

**3-amino-1-(4-chlorophenyl)-5,10-dihydro-5,10-dioxo-1H -pyrazolo[1,2-b]phthalazine-2-carbonitrile (5b):** M.P.: 270-272 $^0$C; Solvent system: Hexane : Ethyl acetate (9:1), Rf value: 0.39 cm; $^1$H-NMR (400 MHz, DMSO-$d_6$) δ ppm: 7.98-7.65 (10 H, m, H-Ar and $NH_2$), 6.08 (1H, S, CH); $^{13}$C-NMR (125 MHz, DMSO-$d_6$) δ ppm: 170.23, 166.34, 153.32, 142.56, 138.54, 136.87, 134.43, 133.43, 132.78, 130.67, 129.54, 127.21, 124.65, 59.45, 54.87; EIMS: 351 (M+1) m/z.

**3-amino-1-(2-chlorophenyl)-5,10-dihydro-5,10-dioxo-1H -pyrazolo[1,2-b]phthalazine-2-carbonitrile (5c):** M.P.: 250-252 $^0$C; ; Solvent system: Hexane : Ethyl acetate (9:1), Rf value: 0.44 cm; $^1$H-NMR (400 MHz, DMSO-$d_6$) δ ppm: 7.85-7.63 (10 H, m, H-Ar and NH2), 6.08 (1H, S, CH); $^{13}$C-NMR (125 MHz, DMSO-$d_6$) δ ppm: 168.45, 162.42, 152.45, 142.87, 139.97, 136.37, 134.87, 134.90, 132.28, 130.52, 129.78, 126.95, 124.32, 61.53, 58.47; EIMS: 351 (M+1) m/z.

**3-amino-1-(4-flurophenyl)-5,10-dihydro-5,10-dioxo-1H-pyrazolo[1,2-b]phthalazine-2-carbonitrile (5d):** M.P.: 262-264 $^0$C; ; Solvent system: Hexane : Ethyl acetate (9:1), Rf value: 0.48 cm; $^1$H-NMR (400 MHz, DMSO-$d_6$) δ ppm: 7.87-7.78 (10H, m, H-Ar and NH2), 6.07 (1H, S, CH); $^{13}$C-NMR (125 MHz, DMSO-$d_6$) δ ppm: 170.35, 163.65, 152.56, 141.87, 138.35, 136.72, 132.43, 129.23, 127.89, 126.65, 124.38, 123.87, 122.20, 61.73, 59.38; EIMS: 336 ($M^+$) m/z.

**3-amino-1-(4-bromophenyl)-5,10-dihydro-5,10-dioxo-1 H-pyrazolo[1,2-b]phthalazine-2-carbonitrile (5e):** M.P.: 266-268 $^0$C; Solvent system: Hexane : Ethyl acetate (9:1), Rf value: 0.37 cm; $^1$H-NMR (400 MHz, DMSO-$d_6$) δ ppm: 8.03-7.94 (10H, m, H-Ar and NH2), 5.98 (1H, S, CH); $^{13}$C-NMR (125 MHz, DMSO-$d_6$) δ ppm: 169.54, 154.52, 143.17, 139.97, 135.78, 133.45, 131.32, 129.47, 128.13, 126.64, 124.59, 123.54, 122.27, 61.73, 60.38; EIMS: 396 (M+2) m/z.

**3-amino-1-(4-N,Ndimethylphenyl)-5,10-dihydro-5,10-dioxo-1H-pyrazolo[1,2-b]phthalazine-2-carbonitrile (5f):** M.P.: 222-224 $^0$C; Solvent system: Hexane : Ethyl acetate (9:1), Rf value: 0.32 cm; $^1$H-NMR (400 MHz, DMSO-$d_6$) δ ppm: 8.09-7.89 (10H, m, H-Ar and $NH_2$), 6.10 (1H, S, CH); $^{13}$C-NMR (125 MHz, DMSO-$d_6$) δ ppm: 176.76, 165.80, 154.35, 147.70, 143.80, 139.76, 136.72, 133.87, 131.23, 130.12, 129.34, 127.54, 124.27, 65.23, 62.12; EIMS: 360 (M+1) m/z.

**3-amino-1-(4-ethylaminephenyl)-5,10-dihydro-5,10-dioxo-1H-pyrazolo[1,2-b] phthalazine-2-carbonitrile (5g):** M.P.: 244-248 $^0$C; Solvent system: Hexane : Ethyl acetate (9:1), Rf value: 0.41 cm; $^1$H-NMR (400 MHz, DMSO-$d_6$) δ ppm: 7.86-7.69 (10H, m, H-Ar and NH2), 6.22 (1H, S, CH); $^{13}$C-NMR (125 MHz, DMSO-$d_6$) δ ppm: 169.67, 165.43, 154.12, 147.21, 143.76, 137.54, 133.62, 129.66, 129.13, 127.64, 126.59, 125.54, 123.27, 65.43, 62.54; EIMS: 359 (M+1) m/z.

**3-amino-1-(3-Nitrophenyl)-5,10-dihydro-5,10-dioxo-1H-pyrazolo[1,2-b]phthalazine-2-carbonitrile (5h):** M.P.: 266-268 $^0$C; Solvent system: Hexane : Ethyl acetate (9:1), Rf value: 0.43 cm; $^1$H-NMR (400 MHz, DMSO-$d_6$) δ ppm: 8.05-7.65 (10H, m, H-Ar and $NH_2$), 6.23 (1H, S, CH); $^{13}$C-NMR (125 MHz, DMSO-$d_6$) δ ppm: 175.54, 162.76, 156.54, 146.85, 139.97, 135.57, 132.69, 132.36, 129.73, 128.64, 128.59, 128.14, 122.27, 63.23, 60.31; EIMS: 362 (M+1) m/z.

**3-amino-1-(3-thiophene)-5,10-dihydro-5,10-dioxo-1H-pyrazolo[1,2-b]phthalazine-2-carbonitrile (5i):** M.P.: 244-246 $^0$C; Solvent system: Hexane : Ethyl acetate (9:1), Rf value: 0.28 cm; $^1$H-NMR (400 MHz, DMSO-$d_6$) δ ppm: 8.03-7.65 (10H, m, H-Ar and NH2), 6.21 (1H, S, CH); $^{13}$C-NMR (125 MHz, DMSO-$d_6$) δ ppm: 168.43, 163.58, 149.24, 143.32, 141.23, 139.32, 136.62, 134.78, 132.89, 130.43, 128.32, 127.54, 124.43, 64.87, 62.43 EIMS: 351 (M+1) m/z.

**3-amino-1-(4-pyridine)-5,10-dihydro-5,10-dioxo-1H-pyrazolo[1,2-b]phthalazine-2-carbonitrile (5j):** M.P.: 230-232 $^0$C; Solvent system: Hexane : Ethyl acetate (9:1), Rf value: 0.31 cm; $^1$H-NMR (400 MHz, DMSO-$d_6$) δ ppm: 7.83-7.59 (10H, m, H-Ar and NH2), 5.87 (1H, S, CH); $^{13}$C-NMR (125 MHz, DMSO-$d_6$) δ ppm: 178.34, 169.43, 154.65, 147.83, 141.90, 139.43, 135.22, 133.45, 132.34, 130.64, 127.59, 127.43, 124.28, 64.73, 60.65 EIMS: 318 (M+1) m/z.

**3-amino-1-(4-methyl phenyl)-5,10-dihydro-5,10-dioxo-1H-pyrazolo[1,2-b]phthalazine- 2-carbonitrile (5k):** M.P.: 253-255 $^0$C; Solvent system: Hexane : Ethyl acetate (9:1), Rf value: 0.45 cm; $^1$H-NMR (400 MHz, DMSO-$d_6$) δ ppm: 8.20-7.850 (10H, m, H-Ar and $NH_2$), 5.98 (1H, S, CH); $^{13}$C-NMR (125 MHz, DMSO-$d_6$) δ ppm: 162.32, 158.23, 147.23, 136.34, 135.16, 133.54, 132.62, 130.66, 129.83, 129.14, 127.59, 127.54, 124.27, 63.23, 60.28; EIMS: 330 (M+1) m/z.

## Results and Discussion

Hydrothermally synthesized products were calcined for 3 hrs at 600 $^0$C before being examined using the X-ray diffraction technique. Both products have XRD pattern indicating that they are polycrystalline in nature. The XRD pattern for pure $PbCrO_4$ (Fig. 1a) reveals 2θ as well as (hkl) planes at 25.6 (100), 28.4 (110), 33.5 (200), 34.5 (200) and 50.1 (200). These peaks in the XRD profile match well to JCPDS data (Card No. 270997) indicating that the crystals are cubic.

Figure 1b shows the XRD pattern for $SiO_2:PbCrO_4$, the 2θ with (hkl) plane of 25.9 (110), 28.7 (111), 34.5 (111), 35.5 (002), 42.4 (100), 50.3 (202), 56.3 (220), 62.4 (211), 67.85 (111), 76.54 (200). The XRD pattern demonstrates that there is no amorphous phase present, indicating that the product is strongly polycrystalline and cubic in nature.

TEM images and SAED patterns for nanocrystalline $PbCrO_4$ and $SiO_2:PbCrO_4$ products are presented in fig. 2a-b. The majority of $PbCrO_4$ crystals are cubic in form as seen in fig. 2a. $PbCrO_4$ has a particle size of 187 nm which is determined by TEM. The particle size of $SiO_2:PbCrO_4$ measured by TEM is 32.27 nm as shown in fig. 3b which also includes a TEM image and an SAED pattern for $SiO_2:PbCrO_4$. The TEM study clearly shows that the crystals are cubic in form which is compatible with the XRD analysis. Some of the crystals are large and hexagonal, while the majority are cubic in form as seen in the diagram. In catalysis, the material's surface area is important.

The usual $N_2$ adsorption/desorption isotherm and BJH pore distribution of manufactured $PbCrO_4$, $SiO_2:PbCrO_4$ are almost same in curve in the current study as shown in fig. 3a-b. A close examination of $PbCrO_4$ has the greatest surface area of 163.7 $m^2/g$, with average pore volume (Vp) and pore diameter (dp) of 0.0106 cc/g and 18.88 $A^0$ respectively. The average pore volume (Vp) and pore diameter (dp) for $SiO_2:PbCrO_4$ with surface area 187.9 $m^2/g$ were 0.0202 cc/g and 16.73 $A^0$ respectively.

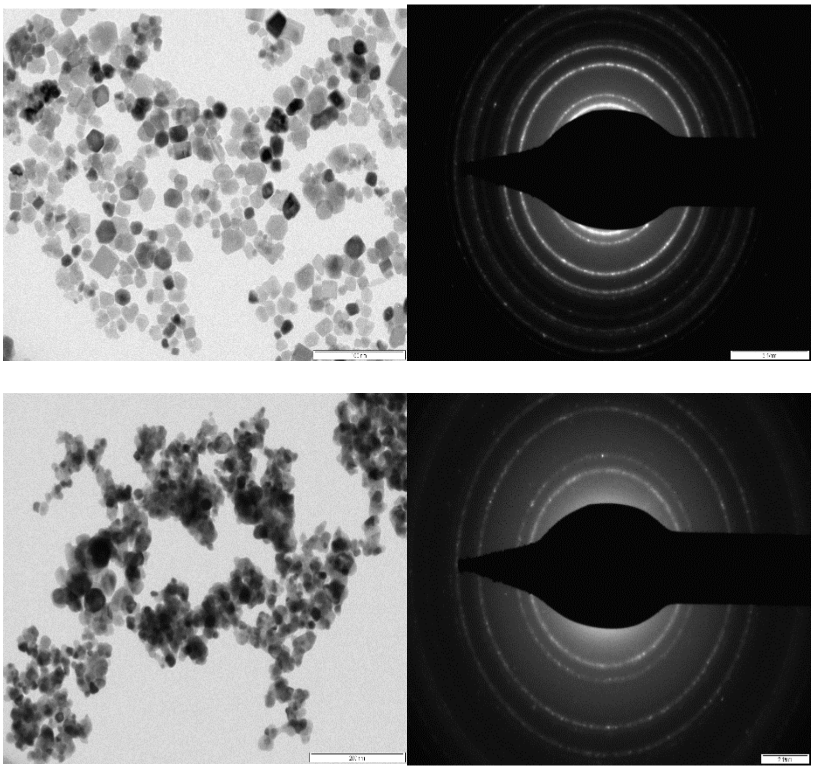

**Figure 2: TEM and SAED analysis of a) $PbCrO_4$ b) $SiO_2:PbCrO_4$ catalyst.**

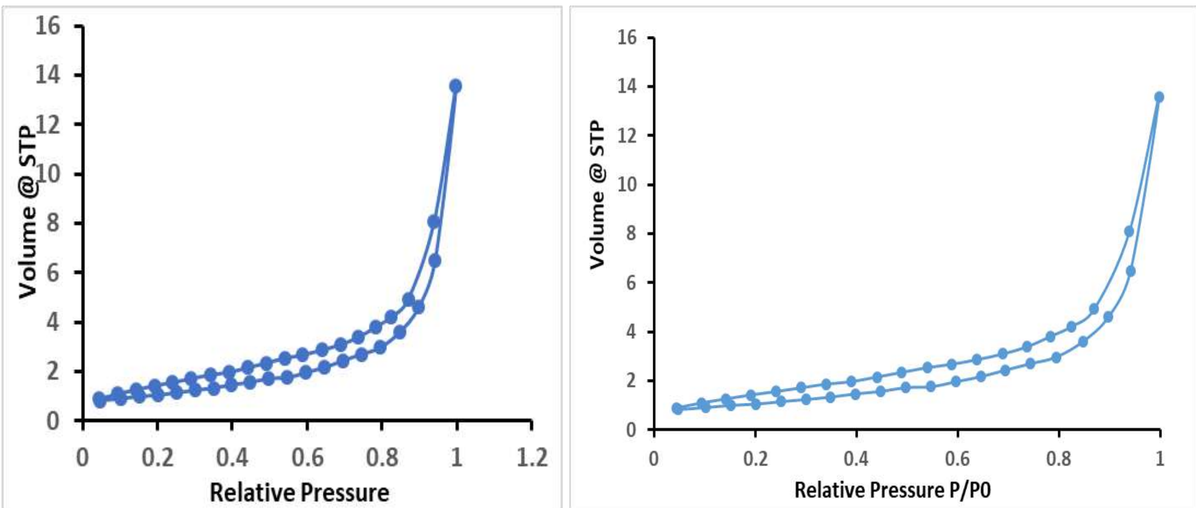


**Figure 3: BET surface area of a) $PbCrO_4$ b) $SiO_2:PbCrO_4$ catalyst.**

https://doi.org/10.25303/2705rjce1250131

**Catalytic results:** The reaction conditions were modified in order to get successful results. For the synthesis of phthalazine-5,10-dione derivatives, phthalic anhydride (1.0 mol), hydrazine hydrate (1.0 mol), malononitrile (1.0 mol), substituted benzaldehyde (1.0 mol) and $SiO_2:PbCrO_4$ (0.5 mol) were used (Scheme 1). The following reaction variables were used to optimize the reaction conditions.

For the synthesis of phthalazine-5,10-dione derivatives in methanol at reflux temperature, a blank reaction was carried out using phthalic anhydride (1.0 mol), hydrazine hydrate (1.0 mol), malononitrile (1.0 mol), substituted benzaldehyde (1.0 mol) and $SiO_2:PbCrO_4$ (0.5 mol), which generated no phthalazine-5,10- dione product even after 5 hrs. The required phthalazine-5,10-dione was obtained in 25 minutes using the same process with a catalytic amount of $SiO_2:PbCrO_4$.

We used synthesized $SiO_2$, $PbCrO_4$ and $SiO_2:PbCrO_4$ for the cyclization reaction of phthalic anhydride, hydrazine hydrate, malononitrile and p-chloro benzaldehyde (1.0 mol). $SiO_2$ decomposes the product whereas $PbCrO_4$ offered high yield but took longer time than $SiO_2:PbCrO_4$. Table 1 summarizes the findings.

We examined various mol equivalents of the catalyst relative to the quantity of phthalic anhydride to optimize the amount of catalyst necessary for the cyclization (Table 2). The cyclization rate was determined to be 90% when the reaction was carried out using 0.5 mol equivalents. The cyclization procedure was carried out in a variety of solvents including DMF, MeOH, EtOH, $CH_3CN$ and $CH_2Cl_2$, with these results clearly indicating that methanol was the best option as shown in table 3.

The rate of reaction was examined using electron-donating and electron-withdrawing substituents on the aromatic ring. As shown in table 4, electron-donating groups and electron-withdrawing substituents have an impact on the reaction, with electron-donating groups providing the corresponding phthalic anhydride in high yield with less time (Table 4, entries 5f, 5g, 5k and 5l), while electron-withdrawing substituents required a longer reaction time with low yield (Table 4, entries 5b, 5c, 5d,5e and 5h).

**Table 1**
**Effect of catalyst on reaction time and yield.**

| S.N. | Catalyst | Time (Min) | % Yield |
|---|---|---|---|
| 1 | $SiO_2$ | 50 | 46 |
| 2 | $PbCrO_4$ | 50 | 50 |
| 3 | $SiO_2:PbCrO_4$ | 35 | 89 |
| 4 | $SiO_2:PbCrO_4$ (30%) | 50 | 65 |
| 5 | $SiO_2:PbCrO_4$ (60%) | 50 | 75 |

**Table 2**
**Effect of Solvent and Temperature on reaction.**

| Entry | solvent | Temperature | Time | Yield of product % |
|---|---|---|---|---|
| 1 | Solvent Free | R.T. | 50 | 35 |
| 2 | Solvent Free | Reflux | 50 | 89 |
| 3 | MeOH | R.T. | 35 | 45 |
| 4 | MeOH | 70 | 35 | 78 |
| 5 | MeOH | Reflux | 35 | 75 |
| 6 | EtOH | Reflux | 35 | 85 |
| 7 | $CH_3CN$ | Reflux | 35 | 56 |
| 8 | DMF | Reflux | 35 | 59 |
| 9 | $CH_2Cl_2$ | Reflux | 35 | 48 |

**Table 3**
**Effect of mole percentage of catalyst.**

| Entry | Catalyst quantity (g) | Yield of product % |
|---|---|---|
| 1 | 0.2 | 56 |
| 2 | 0.4 | 67 |
| 3 | 0.6 | 74 |
| 4 | 0.8 | 89 |
| 5 | 1.0 | 86 |
| 6 | 1.2 | 78 |
| 7 | 1.4 | 65 |

**Table 4**
**Synthesis of 1H-pyrazolo [1,2-b] phthalazine-5, 10-dione derivatives using $SiO_2$:$PbCrO_4$ catalyst.**

| S.N. | Substituted benzaldehyde | Time (min) | Yield (%) |
|---|---|---|---|
| 5a | H | 50 | 78 |
| 5b | P-Cl | 35 | 89 |
| 5c | O-Cl | 45 | 85 |
| 5d | P-F | 40 | 81 |
| 5e | P-Br | 45 | 76 |
| 5f | P-N,N dimethyl | 50 | 83 |
| 5g | P-Ethyl amino | 40 | 85 |
| 5h | M-$NO_2$ | 35 | 79 |
| 5i | Thiophene 3-Carboxaldehyde | 40 | 81 |
| 5j | 3-pyridine Carboxaldehyde | 40 | 83 |
| 5k | P-OH | 60 | 71 |

**Table 5**
**Reusability of $SiO_2$:$PbCrO_4$ catalyst.**

| Run | Yield of product % |
|---|---|
| 1 | 89 |
| 2 | 89 |
| 3 | 88 |
| 4 | 87 |
| 5 | 86 |

Furthermore, it has been shown that the electrical characteristics of benzaldehyde's aromatic ring have an impact on yield and reaction timings.

The catalyst was filtered, washed with methanol and then calcined in an oven at 200°C for 2 hours to see if it could be reused. The catalysts reusability was examined on multiple times under identical reaction conditions. Table 5 shows that the catalyst was determined to be stable and reusable after five cycles with no significant decrease in activity.

A conventional leaching experiment was carried out to demonstrate that the reaction is heterogeneous. At the reaction temperature, the catalyst was filtered out and the reaction was allowed to proceed without it. Even after 12 hours of reflux, there was no change in yield, showing that no homogeneous catalyst was involved.

## Conclusion

Finally, utilizing environmentally friendly nanocrystalline silica composite $PbCrO_4$, we established a straight forward and efficient four component procedure for the synthesis of 1H-pyrazolo[1,2-b]phthalazine-2-carbonitrile in one pot. According to the findings of the catalytic activity studies, the $SiO_2$: $PbCrO_4$ catalyst has outstanding catalytic activity. Most notably, this catalyst speeds up reaction rates and increases product yields when used with solid supports.

## Acknowledgement

Authors are thankful to BCUD, Savitribai Phule Pune University, for providing literature support. Authors are also thankful to IIT SAIF, Bombay for providing the analysis.

## References

1. Borhade A., Agashe J. and Tope D., An efficient multicomponent synthesis of tetrahydropyrans using novel recyclable nanocrystalline $Y_2(CO_3)_3$ catalyst, *Russ. J. Appl. Chem.*, **90(6)**, 1005-1014 **(2017)**

2. Borhade A., Tope D., Gare G. and Dabhade G., One pot four-component synthesis of novel substituted 2-phenyl-4(3h) quinazolinones using recyclable nanocrystalline $CuMnO_3$ catalyst, *J. Korean Chem. Soc*., **61(4)**, 57-163 **(2017)**

3. Borhade A., Tope D. and Gite S., Synthesis, characterization and catalytic application of silica supported tin oxide nanoparticles for synthesis of 2, 4, 5-tri and 1, 2, 4, 5- tetrasubstituted imidazoles under solvent-free conditions, *Arab. J. Chem*., **10**, S559–S567 **(2017)**

4. Czarnik A., Guest Editorial, *Acc. Chem. Res.*, **29**, 112-113 **(1996)**

5. El-Sakka S., Soliman A. and Imam A., Synthesis, antimicrobial activity and electron impact of mass spectra of phthalazine-1,4-dione derivatives, *Afinidad*., **66**, 167-127 **(2009)**

6. Davis E.M., Zhang K., Cui Y., Kuhlenbeck H., Shaikhutdinov S. and Freund H.J., Growth of $Fe_3O_4$ (001) thin films on Pt(100): Tuning surface termination with an Fe buffer layer, *Surf. Sci.*, **636**, 42–46 **(2015)**

7. Ghahremanzadeh R., Shakibaei G. and Bazgir A., An efficient one-pot synthesis of 1Hpyrazolo[1,2-b]phthalazine-5,10-dione derivatives, *Synlett*., **8(8)**, 1129-1132 **(2008)**

8. Gupta Alok Kumar, Singh Manvendra, Marboh Eveing Stone, Anal Ajit Kumar Dubedi and Nath Vishal, Pollen grains of Longan

(Dimocarpus longan Lour.): Scanning electron microscope study, *Res. J. Biotech.*, **15(9)**, 130-132 **(2020)**

9. Hemming K., Synthesis of 1H-pyrazolo[1,2-b]phthalazine-5,10-dione derivatives using $NiFe_2O_4$ nanoparticle, *Annu. Rep. Prog. Chem. B.*, **107**, 118-137 **(2011)**

10. Horton D., Bourne G. and Smythe M., The combinatorial synthesis of bicyclic privileged structures or privileged substructures, *Chem. Rev*., **103**, 893-930 **(2003)**

11. Li. J., Zhao Y., Yuan X., Xu J. and Gong P., Synthesis and Anticancer Activities of Novel 1,4-Disubstituted Phthalazines, *Molecules*, **11(7)**, 574-682 **(2006)**

12. Kozikowski A., Comphrensive Heterocyclic Chemistry, Pergamon Press **(1984)**

13. Liu L., Lu J. and Shi M., $PhI(OAc)_2$-mediated novel 1,3-Dipolar cycloaddition of methylenecyclopropanes (MCPs), vinylidenecyclopropanes (VCPs) and methylene cyclobutane (MCB) with phthalhydrazide, *Org. Lett*., **9**, 1303 **(2007)**

14. Nomoto Y., Obase H., Takai H., Teranishi M., Nakamura J. and Kubo K., Studies on cardiotonic agents. II: Synthesis of novel phthalazine and 1, 2, 3-benzotriazine derivatives, *Chem. Pharm. Bull. (Tokyo).*, **38**, 2179-2182 **(1990)**

15. Naid M. et al, Ultrasound-assisted one-pot, three-component synthesis of 1H-pyrazolo [1, 2-b] phthalazine-5, 10-diones, *Ultrason. Sonochem*, **17(1)**, 159-61 **(2010)**

16. Pozharskii A., Soldatenkov A. and Katritzky A., Heterocycles in life and society an introduction to heterocyclic chemistry, biochemistry and applications, Heterocycles in Life and Society, 2nd ed., Wiley & Sons, New York, USA **(2011)**

17. Raghuvanshi D. and Singh K., A highly efficient green synthesis of 1H-pyrazolo[1,2-b]phthalazine-5,10-dione derivatives and their photophysical studies, *Tetrahedron Lett.*, **52**, 5702 **(2011)**

18. Ryu C., Park R. and Nho M.Y.J.H., Synthesis and antifungal activity of benzo[d]oxazole-4,7-diones, *Bioorg. Med. Chem. Lett.*, **17**, 2577 **(2007)**

19. Shaterian H. and Mohammadnia M., Mild basic ionic liquids catalyzed new four-component synthesis of 1H-pyrazolo[1,2-b]phthalazine-5,10-diones, *J. Mol. Liq.*, **173(55)**, 55-61 **(2012)**

20. Sinkkonen J., Ovcharenko V., Zelenin K.N., Bezhan I.P., Chakchir B.A., Al-Assar F. and Pihlaja K., $^{1}H$ and $^{13}C$ NMR study of 1-Hydrazino-2,3-dihydro-1H-pyrazolo[1,2-a]pyridazine-5,8-diones and -1H-pyrazolo[1,2-b]phthalazine-5,10-diones and their ring-chain tautomerism, *Eur. J. Org. Chem.*, **13**, 2046 **(2002)**

21. Strecker A., Ueber die künstliche bildung der milchsäure und einen neuen, dem glycocoll homologen körper, *Ann. Chem. Pharm.*, **75**, 27-45 **(1850)**

22. Watanabe N., Kabasawa Y., Takase Y., Matsukura M., Miyazaki K., Ishihara H., Kodama K. and Adachi H., ChemInform Abstract: 4-benzylamino-1-chloro-6-substituted phthalazines: synthesis and inhibitory activity toward phosphodiesterase, *J. Med. Chem*., **41**, 3367–3372 **(1998)**

23. Zhang L., Guan L.P., Sun X.Y., Wei C.X., Chai K.Y. and Quan Z.S., Synthesis and anticonvulsant activity of 6-alkoxy-[1,2,4]triazolo[3,4-a] phthalazines, *Chem. Biol. Drug Des.*, **73**, 313-319 **(2009)**.

(Received 01st May 2022, accepted 03rd July 2022)

*Available online at* www.derpharmachemica.com

ISSN 0975-413X
CODEN (USA): PCHHAX

**Der Pharma Chemica, 2022, 14(11): 8-13**
*(http://www.derpharmachemica.com/archive.html)*

# Synthesis of Biologically Active Compound 1,4-Dihydropyridine by using An Efficient and Versatile Silica Supported MgO Catalyst

**Dipak R Tope[1], Shilpa L. Sangle[2*], Jyoti A. Agashe[1], Yogita R. Shelke[1] and Ashok V. Borhade[1]**

[1]*Department of Chemistry, HPT Arts and RYK Science College, Nasik 422005, India*
[2]*Department of Chemistry, SSSM ASC College, Saikheda-422210, Nashik, India*

****Corresponding author:** Shilpa L. Sangle, Department of Chemistry, SSSM ASC College, Saikheda-422210, Nashik, India, **E-mail**: shilpasangle620@gmail.com*

**Received**: 10-Nov-2022, Manuscript no: dpc-22-79479, **Editor assigned**: 12-Nov-2022, PreQC No: dpc-22-79479, **Reviewed**: 26-Nov-2022, QC No: dpc-22-79479, **Revised**: 28-Nov-2022, Manuscript No: dpc-22-79479, **Published**: 05-Dec-2022, **DOI**: 10.4172/0975-413X.14.11.8-13

**ABSTRACT**

*A simple one pot synthesis has been developed for the synthesis 1,4-dihydropyridine using an efficient and reusable silica supported MgO solid catalyst by condensation of dimedone, ethyl acetoacetate, aldehyde and ammonium acetate in methanol as a solvent at room temperature. The reactions could be carried out under mild reaction conditions with very good yield of polyhydroquinoline, up to 92%. This catalyst could be recycled very easily, which makes this methodology environmentally benign.*

**Keywords:** 1,4-dihydropyridine; Multicomponent reaction; Silica supported MgO; Recyclable catalyst

## INTRODUCTION

1,4-dihydropyridine (1,4-DHP) and their derivatives have attracted considerable interest in recent times because of their promising biological activities such as vasodilators, bronchodilators, Anti-atherosclerotic, anti-tumor, neuroprotective drugs, hepatoprotective and antidiabetic agents [1]. Moreover, 1,4-DHPs exhibits several medicinal applications which include neuroprotectant [2] and platelet anti-aggregatory activity [3]. Also they have been reported for their applications in treatment of Alzheimer's diseases [4] due to their cerebral anti-schematic activity and chemo-sensitizer in tumor-therapy [5]. These examples clearly demonstrate the remarkable potential of 1,4-DHPs as a source of valuable drug candidate.

Dihydropyridines are particularly well known in pharmacology as L-type calcium channel blockers, used in the treatment of hypertension. Compared with certain other L-type calcium channel blockers (for example those of the phenylalkylamine class such as Verapamil) which have significant action at the heart, they are relatively vascular selective in their mechanism of action in lowering blood pressure.

In recent years, much attention has been focused on the synthesis of 1,4-dihydropyridyl compounds (1,4-DHPs), due to their significant biological activity. Cardiovascular agents such as nifedipine, nicardipine, amlodipine and other related derivatives are dihydropyridyl compounds, which are effective for the treatment of hypertension. 4-Aryl-1,4- dihydropyridines are analogs of NADH co-enzymes, which have been explored for their calcium channel activity and the heterocyclic rings are found in a variety of bioactive compounds such as bronchodilators, geroprotective and hepatoprotective agents. Extensive studies indicate that these compounds exhibit different medical functions, acting as neuroprotectants, antiplatelet aggregators, cerebral antiischemic agents and chemosensitizers. For these reasons, polyhydroquinoline compounds not only have attracted the attention of chemists to synthesize but also represent an interesting research challenge.

Owing to the wide range of biological and medicinal activities, the synthesis of such compounds has become an important target in recent years. In 1882, Arthur Hantzsch [6] reported first synthesis of substituted 1,4-dihydropyridines by one-pot condensation of ethyl acetoacetate, aromatic aldehydes and ammonia. The reaction was carried out in acetic acid at reflux temperature in ethanol for long period provide low to moderate yields. Recently a number of methods have been reported for the synthesis of 1,4-dihydropyridine using alum, molecular iodine, [7] $HClO_4$-$SiO_2$ [8], TMSCl [9] ceric(IV)ammonium nitrate [10] L-proline [11] ionic liquids [12] expensive metal triflate $Yb(OTf)_3$ [13] $Sc(OTf)_3$ [14] scolecite [15], ZnO-beta zeolite [16], Baker's yeast [17] and solid phase organic synthesis technique [18] All reported methods has its own merits, while some of these methods suffers from one or more drawbacks such as poor yields, longer reaction time, difficult work-up procedure and effluent pollution.

Hence development of clean, efficient and high yielding catalyst under mild reaction conditions for environmentally benign protocols is highly desired. The possibility of performing multi-component reactions with a heterogeneous catalyst could enhance their efficiency from an economic as well as ecological point of view. In continuation to our work on the applications of heterogeneous catalysts in organic transformations [19,21] we report here a convenient and efficient method for the synthesis of 1,4-dihydropyridine derivatives using silica supported MgO catalyst (Scheme 1).

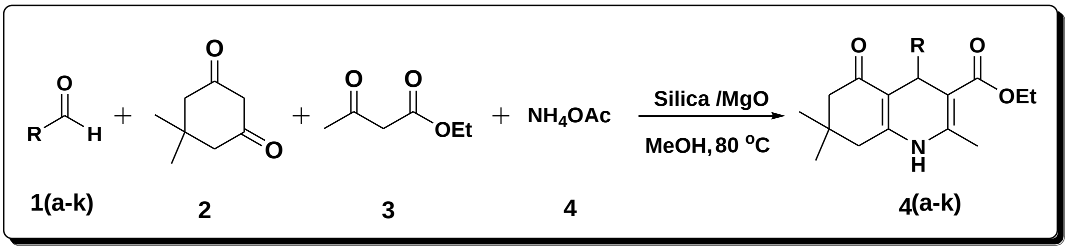


**Scheme-1**: Synthesis of 1,4-dihydropyridine derivatives using silica supported MgO catalyst.

## EXPERIMENTAL

All chemicals were employed are commercial products (Aldrich Chemical Co.) and were used without purification. All yields refer to isolated products after purification. $^1$H (300 MHz) NMR and $^{13}$C (75 MHz) NMR spectra were recorded on Varian mercury XL-300 and Bruker spectrometer instruments using TMS as internal standard. The solvent used for NMR spectra was $CDCl_3$ and DMSO-$d_6$. Infra-red spectra were taken on Shimadzu FTIR–408 on KBr pellet. The mass spectra were recorded on Shimadzu GC-MS QP trap 2010A mass spectrometer with an ionization potential of 70 eV. Column chromatography was performed on silica gel (230–400 mesh) supplied by Acme Chemical Co.

## RESULT AND DISCUSSION

### Characterization of MgO nanoparticles

The XRD pattern of Silica supported MgO nanoparticles (figure 1) have fundamental peak due to diffraction of MgO on the plane 111, 200, 311, 222, 400, 331, 420 and 422. The XRD patterns of synthesized MgO nanoparticles show single phase system with average particle size of 47 nm (Figure 1).

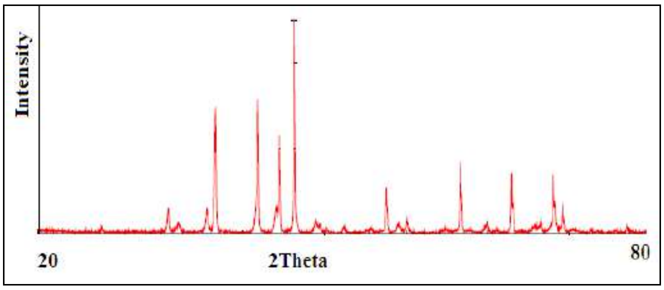


**Figure 1**: XRD Pattern of Silica supported MgO.

The XRD pattern is in agreement with cubic structure of MgO nanoparticles (JCPDS card no. 02-1102). The SEM image (figure 2) decides the morphology of MgO nanoparticles. The SEM image confirms the cubic structure of MgO nanoparticles, uniform shape and size. The elemental analysis of MgO nanoparticles confirmed by EDAX spectrum , it shows the presence of Mg and O element in the synthesized sample material.

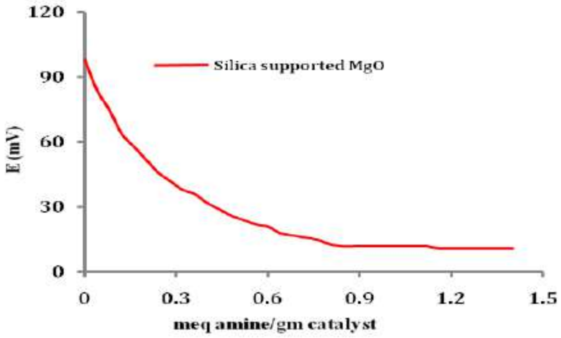


**Figure 2**: Potentiometric titration of Silica supported MgO.

The TEM image (Figure 3a) reveals that nanomaterial is of cubic structure. The dark spot in the SAED micrograph (Figure 3b) can be alluded to synthesized MgO nanoparticles as the SAED pattern. Such a spot reveals the occurrence of cubic MgO in the total agreement with XRD data. The average size of MgO nanoparticles obtained by TEM was found around 47 nm (Figure 3).

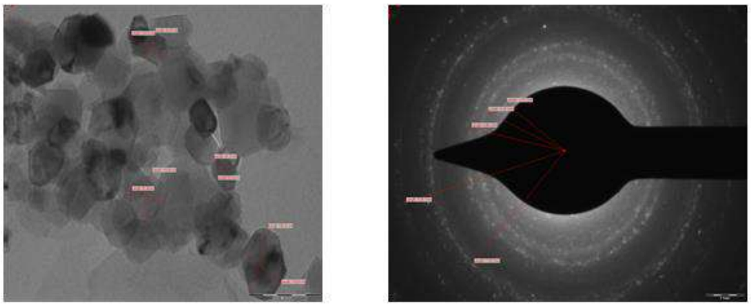

3a 3b

**Figure 3**: TEM and SAED of Silica supported MgO.

The $N_2$ adsorption-desorption isotherms and BJH pore size distribution of MgO nanoparticles (figure 4) reveals that the samples have typical IV $N_2$ adsorption-desorption isotherms with $H_1$ hysteresis. The BJH pore size distribution demonstrates that all the samples have a narrow pore diameter range. Based on the $N_2$ adsorption-desorption isotherms, the specific surface area (SBET) of CdO nanoparticles obtained from BET method is 29.71 $m^2/g$, the average pore volume (VP) and pore diameter (dp) were 0.04630 cc/g and 24.87 A° (Figure 4).

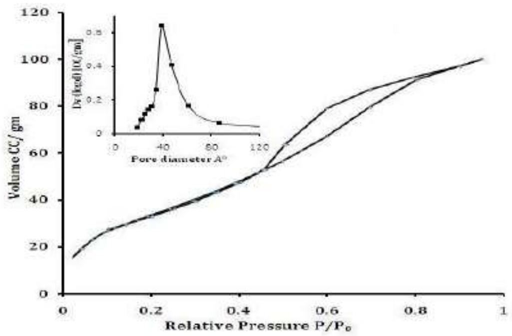


**Figure 4**: BET Surface area of Silica supported MgO.

### Catalytic results

In present work, we wish to report the one-pot multicomponent synthesis of substituted 1,4-dihydropyridines catalyzed by MgO nanoparticles as a heterogeneous solid catalyst. In a typical run, dimedone (1.1 mol), aryl aldehyde (1.3 mol), Ethyl acetoacetate (1.0 mol) and silica supported MgO (0.8 mol) nanoparticles were allowed to react in methanol at 80ºC for 25 min. The reaction mixture was directly filtered and washed with methanol. The recovered catalyst was dried and reused further in successive reactions. Filtrate was collected and evaporated under reduced pressure to afford the product. The isolated products were characterized by IR, NMR and Mass spectrometry.

### Spectral data of representative compounds

***Ethyl 1,4,5,6,7,8-hexahydro-2,7,7-trimethyl-5-oxo-4-phenylquinoline-3-carboxylate (5a):*** $^1$H NMR (300 MHz, $CDCl_3$): δ 0.94 (s, 3H), 1.09 (s, 3H), 1.14 (t, *J* = 7.3 Hz, 3H), 2.13-2.34 (m, 4H), 2.37 (s, 3H), 4.05 (q, *J* = 7.3 Hz, 2H), 5.02 (s, 1H), 5.74 (s, 1H),7.03-7.34 (m, 5H); $^{13}$C NMR (75 MHz, DMSO-$d_6$) δ 14.2,19.1, 21.3, 27.6, 36.5, 37.3, 59.8, 106.0, 113.7, 126.3, 127.8,
128.0, 143.3, 147.1, 149.2, 167.3, 194.8; IR (KBr $cm^{-1}$): 3233, 3210, 3080, 1696, 1602, 1059, 692; *m/z* = 340 $(M+H)^+$.

***Ethyl 1,4,5,6,7,8-hexahydro-2,7,7-trimethyl-4-(3-nitrophenyl)-5-oxoquinoline-3-carboxylate (5b):*** $^1$H NMR (300 MHz, $CDCl_3$): δ 0.96 (s, 3H), 1.04 (s, 3H), 1.22 (t, *J* = 7.3 Hz, 3H), 2.10-2.34 (m, 4H), 2.38 (s, 3H), 4.01 (q, *J* = 7.3 Hz, 2H), 4.96 (s, 1H), 6.32 (s, 1H), 6.74-7.38 (m, 4H); $^{13}$C

NMR (75 MHz, DMSO-$d_6$): δ 14.18, 19.32, 21.1, 27.3, 33.1, 33.90, 59.5, 105.4, 112.3, 121.2, 122.8, 128.6, 134.8, 144.6, 148.3, 149.5,151.0, 166.9, 196.0; IR (KBr in $cm^{-1}$): 3303, 2954, 1683,1610, 1167, 759; $m/z$ = 385 $(M+H)^+$.

***Ethyl 1,4,5,6,7,8-hexahydro-4-(4-methoxyphenyl)-2,7,7-trimethyl-5-oxoquinoline-3-carboxylate (5g):*** $^1$H NMR (300 MHz, $CDCl_3$): δ 0.96 (s, 3H), 1.06 (s, 3H), 1.22 (t, $J$ = 7.2 Hz, 3H), 2.10-2.26 (m, 3H), 2.34-2.40 (m, 4H), 3.77(s, 3H), 4.02 (q, $J$ =7.2 Hz, 2H), 5.08 (s, 1H), 5.85 (s, 1H), 6.71-7.24 (m, 4H); $^{13}$CNMR (75 MHz, DMSO-$d_6$) δ 14.3, 17.9, 26.3, 28.8, 32.4,35.0, 50.1, 50.4, 55.1, 59.2, 102.7, 109.5, 113.4, 128.3, 128.5,140.0, 144.9, 149.1, 156.8, 168.2, 193.8; IR (KBr in $cm^{-1}$):3281, 3199, 3080, 1708, 1607, 1224, 837; $m/z$ = 370 $(M+H)^+$.

## RESULTS AND DISCUSSION

In order to determine the most appropriate reaction conditions and evaluate the catalytic efficiency of silica supported MgO catalyst for the synthesis of 1,4-dihydropyridine, initially a model study was carried out on the synthesis of 1,4-dihydropyridine (1,4-DHP) (Scheme 1) using p-chloro benzaldehyde as a model substrate. The reaction was monitored by TLC technique using ethyl acetate-hexane (3:7 v/v) as a solvent system.

To evaluate and optimize the effectiveness of silica supported MgO with different catalyst, we tried MgO, $SiO_2$, 25%, 50% and 75% Silica supported MgO for the cyclization reaction of dimedone, ethyl acetoacetae and *p*-chlorobenzaldehyde. MgO, $SiO_2$ gave poor yield while 25%, 50%, 75% silica supported MgO gave good yield but required more time as compared to silica supported MgO (Table **1**).

**Table 1**: Effect of different catalyst on reaction time and yield.

| Entry | Catalyst | Time (min) | Yield* |
|---|---|---|---|
| 1 | MgO | 90 | 34 |
| 2 | $SiO_2$ | 65 | 79 |
| 3 | $SiO_2$/MgO | 25 | 94 |
| 4 | 75% $SiO_2$/MgO | 30 | 89 |
| 5 | 50% $SiO_2$/MgO | 50 | 81 |
| 6 | 25% $SiO_2$/MgO | 40 | 79 |

With increasing silica loading from 25% to 100%, cyclization substantially increases and it reaches a maximum (94%) at the silica content of 100%. Therefore, it shows that 100 % silica supported MgO results in higher catalytic activity. Thus, it is obvious from our studies that silica supported MgO was superior in the cyclization reaction with good yield in short reaction time. To optimize catalyst required for the cyclization, we carried out reaction using various mole equivalents of the catalyst with respective dimedone (Table 2).

**Table 2**: Effect of mole percentage of silica supported MgO.

| Entry | Amount of $SiO_2$/MgO (mol) | Time (min) | Yield* |
|---|---|---|---|
| 1. | 0.1 | 80 | 78 |
| 2. | 0.4 | 40 | 89 |
| 3. | 0.8 | 26 | 94 |
| 4. | 1.2 | 25 | 87 |

It was found that when reaction was carried out with 0.8 mol, equivalent catalyst gives 94% yield. Different solvents were studied such as DMF, methanol, ethanol, acetonitrile, dichloromethane and among the methanol were found to be the best choice (Table 3).

**Table 3**: Effect of Solvent for 1,4-dihydropyridine using silica supported MgO.

| Entry | Substituent (-X) | Time | Yield |
|---|---|---|---|
| a. | -H | 25 | 95 |
| b. | 0 | 35 | 92 |
| c. | 0 | 35 | 93 |

| | | | |
|---|---|---|---|
| d. | 2,3-$OCH_3$ | 30 | 91 |
| e. | -OH | 20 | 90 |
| f. | -Cl | 20 | 92 |
| g. | -Br | 25 | 94 |
| h. | -F | 25 | 92 |
| i. | 0 | 40 | 89 |
| j. | -CH=CH-Ph | 40 | 87 |
| k. | -$N(CH_3)_2$ | 50 | 86 |

In order to evaluate the generality of the process, several diversified examples illustrating the present method for the synthesis of 1,4-dihydropyridine was studied (Table 4).

**Table 4**: Synthesis of 1,4-dihydropyridine in the presence of silica supported MgO.

| **Sr. no.** | **Solvent** | **Time** | **Yield*** |
|---|---|---|---|
| 1 | MeOH | 25 | 94 |
| 2 | EtOH | 25 | 91 |
| 3 | DMF | 45 | 86 |
| 4 | $CH_3CN$ | 40 | 89 |
| 5 | $CH_2Cl_2$ | 60 | 69 |

The cyclization reaction dimedone was checked by treating with wide range of substituted aldehydes bearing electron donating (such as hydroxy, methoxy, methyl, N,N-dimethyl) or electron withdrawing (nitro, halides) was carried out in the presence of Silica supported MgO catalyst. The reaction of aromatic aldehyde with electron donating groups and electron withdrawing groups reacted very well. Treatment of substituted aldehydes with dimedone and ethyl acetoacetate in methanol with Silica supported MgO (0.8 mol) at 80°C temperature afforded 1,4-dihydropyridine with excellent yield. The results obtained are illustrated in table 4. All the products obtained were characterized by IR, $^1$H-NMR, $^{13}$C-NMR and Mass spectrometry.

The reusability of the catalyst was tested in the synthesis of DHPs as shown in Table **5**. The catalyst was recovered after each successive run, washed three times with acetone, dried in oven at 120°C for 3 hrs. Prior to use and tested for its activity in the subsequent run. The catalyst was tested for 5 runs. It was observed that the catalyst found to very good reusability (Table 5).

**Table 5**: Results of the reaction run in the presence of recycled catalyst.

| **Sr. no** | **Reaction run** | **time** | **Yield*** |
|---|---|---|---|
| 1 | 1 | 25 | 94 |
| 2 | 2 | 25 | 94 |
| 3 | 3 | 25 | 92 |
| 4 | 4 | 25 | 87 |
| 5 | 5 | 25 | 90 |

*All reactions (Table.1-5) are carried at 80ºC using silica supported MgO

## CONCLUSION

In conclusion, we developed an efficient and simple alternative method for the preparation of 1,4-dihydropyridine (1,4-DHP) using silica supported MgO catalyst at 80ºC. Prominent among the advantages of this new method are simple and easy workup procedure, short reaction time, good yield and use of cheap, nontoxic and easily synthesized silica supported MgO catalyst.

## REFERENCES

[1] Godfraind T, Miller R, Wibo M. Pharmacol Rev. **1986**, 38: p. 321.
[2] Klusa V. Drugs Fut. **1995**, 20: p. 135.
[3] Bretzel RG, Bollen CC, Maeser E, et al., Am J Kidney Dis. **1993**, 21: p. 53.
[4] Bretzel RG, Bollen CC, Maeser E, et al., Drugs Fut. **1992**, 17: p. 465.
[5] Boer R, Gekeler V. Drugs Fut. **1995**, 20: p. 499.
[6] Hantzsch A. Ann Chem. 215: p. 1.
[7] Ko S, Sastry MNV, Lin C, et al., Tetrahedron Lett. **2005**, 46: p. 5771.
[8] Maheswara M, Siddaiah V, Damu GLV, et al., Arkivoc. **2006**, p. 201.
[9] Sabitha G, Reddy GSKK, Reddy CS, et al., Tetrahedron Lett. **2003**, 44: p. 4129.
[10] S. Ko, C.F. Yao, Tetrahedron, 2006, 62, 7293.
[11] Karade NN, Budhewar VH, Shinde SV, et al., Lett Org Chem. **2007**, 4: p. 16.

[12] Ji SJ, Jiang ZQ, Lu J, et al., Synlett. **2004**, 831.
[13] Wang LM, Sheng J, Zhang L, et al., Tetrahedron. **2005**, 61: p. 1539.
[14] Donelson JL, Gibbs RA, De SK. J Mol Catal A: Chem. 2006, 256, 309.
[15] Gadekar LS. Bull Korean Chem Soc. **2009**, 30: p. 11.
[16] Katkar SS, Arbad BR, Lande MK. Arab J Sci and Eng. **2011**, 36: p. 39-46.
[17] Kumar A, Maurya RA. Tetrahedron Lett. **2007**, 48: p. 3837.
[18] Gordeev MF, Patel DV, Gordon PM. J Org Chem. **1996**, 61: p. 924.
[19] Shinde SV, Jadhav WN, Lande MK, et al., Catal Lett. **2008**, 125: p. 57.
[20] Gadekar LS, Katkar SS, Vidhate KN, et al., Bull Catal Soc Ind. **2008**, 7: p. 79.
[21] Cid R, Pecci G. Appl Catal. **1985**, 14: p. 15.

ISSN 1070-4280, Russian Journal of Organic Chemistry, 2023, Vol. 59, No. 4, pp. 663–673. © Pleiades Publishing, Ltd., 2023.

# A Simple, Green, and Efficient One-Pot Synthesis of Dihydropyrano[3,2-*c*]chromene Derivatives Using $MgMnO_3$@$ZrO_2$@CoO as a Core–Shell Nanocrystalline Catalyst

**Y. R. Shelke[a], V. D. Bobade[b], D. R. Tope[b], J. A. Agashe[b], and A. V. Borhade[b],***

[a] *Department of Chemistry, K. K. Wagh Arts, Commerce and Science College, Pimpalgaon (B), Affiliated to Savitribai Phule Pune University, Nashik, Maharashtra, 422209, India*

[b] *Department of Chemistry, Research Centre, H.P.T Arts and R.Y.K. Science College, Nashik, Maharashtra, 422005, India*

**e-mail: ashokborhade2007@gmail.com*

Received April 17, 2022; revised July 27, 2022; accepted August 14, 2022

**Abstract**—A rapid, clean, and highly efficient method for the synthesis of dihydropyrano[3,2-*c*]chromene derivatives by one-pot three-component condensation of aromatic aldehydes, malononitrile, and 4-hydroxycoumarin using novel $MgMnO_3$@$ZrO_2$@CoO core–shell nanocrystalline catalyst is described. The catalyst has been synthesized by hydrothermal method and characterized by XRD, SEM, TEM, and BET surface area analyses. The average particle size of the nanocrystalline catalyst was estimated by TEM scans at 50–60 nm. The BET surface area of $MgMnO_3$@$ZrO_2$@CoO was found to be 31.61 $m^2/g$, indicating that it has good catalytic properties. The catalyst can be reused for five successive runs without significant loss in activity. The advantages of the proposed method and catalyst are clean reaction, short reaction time, good yield, easy purification, and reusability and financial availability of the catalyst.

**Keywords:** dihydropyrano[3,2-*c*]chromene derivatives, $MgZrO_3$@$Fe_2O_3$@ZnO catalyst, reusable catalyst

**DOI:** 10.1134/S1070428023040152

## INTRODUCTION

Multicomponent reaction (MCRs) are a powerful tool for the synthesis of wide range organic molecules by creating carbon–carbon and carbon–heteroatom bonds in one pot [1–3]. These reactions have various advantages such as simple procedures, high bonding efficiency, low costs, and time and energy saving [4]. MCRs provide greater atom economy and selectivity than traditional multistep syntheses, as well as quick access to molecular complexity and diversity while producing fewer by-products. As a result, MCRs are becoming more vital in modern organic chemistry and are being designed to efficiently produce medicinally relevant scaffolds [5–7].

Heterogeneous catalysts are of great scientific and commercial interest due to their stability, selectivity, and high activity. There is little doubt that the catalysis community keeps a close eye on the progress in nanotechnology [8–10]. In recent years, core–shell nanoparticles have received a lot of interest because of their nanoscale dimensions and unique properties. Core–shell nanoparticles are more stable than pure magnetic particles because the shell protects the magnetic core nanoparticles from environmental degradation and also prevents agglomeration [11–14]. The production of nanoparticles of diverse materials (metallic, semiconductor, and dielectrics) has generated much interest due to their applications in catalysis, medicine, electronics, and other domains. Materials scientists are always exploring innovative ways to change the size and shape of nanoparticles in order to suit the requirements of their applications [15].

Pyrano[3,2-*c*]chromenes constitute an important family of heterocycles with a variety of biological activities, including antispasmodic, diuretic, anticoagulant, anticancer, and anti-anaphylactic action [16, 17]. Furthermore, they have been used to treat Alzheimer's disease, vascular dementia, Huntington's disease, amyotrophic lateral sclerosis, AIDS-related dementia, and Down's syndrome, as well as schizophrenia and myoclonic seizures [18]. Aminochromene derivatives also have a wide range of biological effects such as antihypertensive and anti-ischemic properties [19–21].

The three-component condensation of 4-hydroxycoumrin, aldehydes, and malononitrile for the synthesis of dihydropyrano[3,2-*c*]chromene derivatives has been carried out under various conditions by using different catalysts such as $Fe_3O_4$@GO-naphthalene-$SO_3H$ nanocatalyst [22], $Fe_3O_4$@$SiO_2$-polyacrylic acid nanocatalyst [23], MNPs@Cu nanocatalyst [24], ionic liquids [25], DABCO [26], $Mg(ClO_4)_2$ [27], $AcONH_4$ [28], DBU [29], diammonium hydrogen phosphate (DAHP) [30], $Na_2HPO_4$ [31], $K_2CO_3$ [32], (*S*)-proline [33], tetrabutylammonium bromide (TBAB) [34], 3-hydroxypropanaminium acetate (HPAA) [35], [bmim]Br [36], and potassium phthalimide-*N*-oxyl [37]. These catalysts have some drawbacks related to high costs, high reaction temperatures, low yields, the use of hazardous solvents, and the need for specialized equipment, which produced negative results.

In view of the above results, herein we used $MgMnO_3$@$ZrO_2$@CoO core–shell catalyst for the synthesis of dihydropyrano[3,2-*c*]chromenes that have a wide range of pharmacological, biological, and therapeutic effects using a simple and ecofriendly technique.

## RESULTS AND DISCUSSION

The $MgMnO_3$@$ZrO_2$@CoO core–shell catalyst was prepared as shown in Scheme 1. Initially, $MgMnO_3$ nanoparticles were synthesized by the hydrothermal process from equivalent amounts of magnesium chloride ($MgCl_2$) and manganese chloride ($MnCl_4$) in double distilled water in the presence of polyethylene glycol, followed by treatment with aqueous sodium hydroxide. Next, $MgMnO_3$@$ZrO_2$ core–shell nanoparticles were obtained by dissolving $MgMnO_3$ and $ZrO_2$ [38] (1:2) and an appropriate quantity of polyethylene glycol in double distilled water. Finally, $MgMnO_3$@$ZrO_2$ was treated with an equimolar amount of cobalt(II) oxide [38] in 2 M NaOH in the presence of polyethylene glycol. The resulting nanocatalyst was calcined for 6 h at 700°C.

**XRD analysis.** The $MgMnO_3$@$ZrO_2$@CoO core–shell catalyst was characterized by XRD, SEM, TEM, EDAX, and BET surface area analyses. Figure 1 shows the XRD patterns of $MgMnO_3$, $MgMnO_3$@$ZrO_2$, and $MgMnO_3$@$ZrO_2$@CoO. All diffraction peaks in the XRD pattern of $MgMnO_3$ (Fig. 1a) were indexed to a defect cubic spinel-type structure (JCPDS, 28-0625) with well-ordered *hkl* planes. The diffraction peaks (111), (220), (311), (222), (400), (422), (511), (440), (533), and (622) were seen at different diffraction angles of 18.07°, 30.97°, 36.08°, 36.61°, 44.34°, 53.88°, 56.17°, 64.50°, 74.18°, and 76.52°. The presence of $ZrO_2$ in $MgMnO_3$@$ZrO_2$ was confirmed by its XRD pattern (Fig. 1b) which displayed broad peaks at 28.29°, 30.37°, and 31.54°. According to the JCPDS 79-1771 card, the peak centered at 30.37° (101) is typical of the tetragonal crystalline phase, whereas those at 28.29° (111) and 31.54° (111) are representative of the monoclinic phase (JCPDS 37-1484). These findings point to a combination of tetragonal and monoclinic crystalline phases that are seen in $ZrO_2$ materials [39, 40]. Figure 1c shows the presence of $ZrO_2$ and CoO phases in the $MgMnO_3$@$ZrO_2$@CoO core–shell nanoparticle clusters suggesting that CoO was coated on the $ZrO_2$ nanoparticles. The major peaks were found at 36.92°, 44.78°, and 65.32°, corresponding to the lattice scattering planes (111), (200) and (220) for CoO crystal. Also, well-defined peaks assigned to the face-centered cubic structures were observed, which matched with the JCPDS card 071-1178 for cobalt oxide [41, 42].

**Scanning electron microscopy (SEM) analysis.** The morphology of the core–shell nanoparticles was

**Scheme 1.**

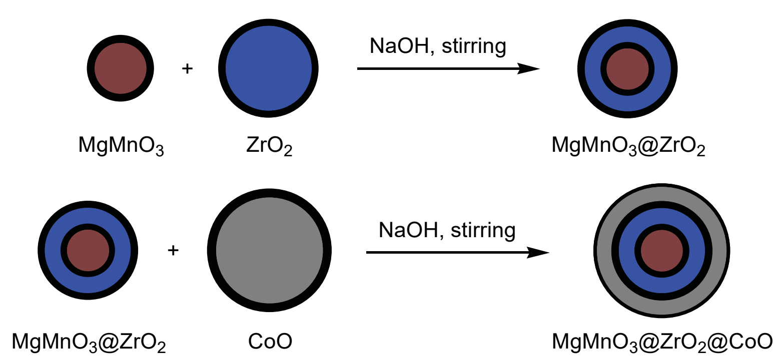

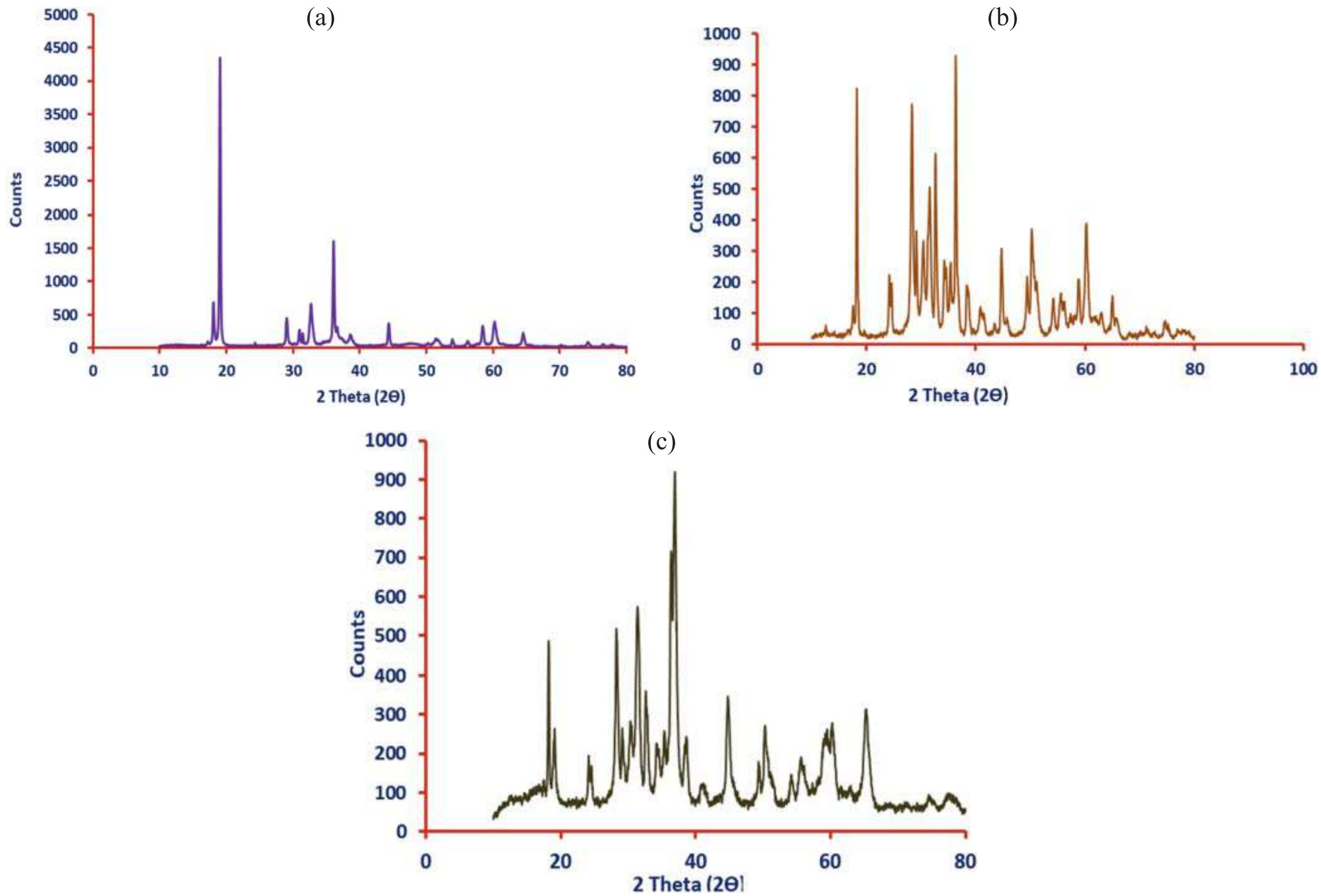


**Fig. 1.** XRD patterns of (a) $MgMnO_3$, (b) $MgMnO_3$@$ZrO_2$, and (c) $MgMnO_3$@$ZrO_2$@CoO.

examined by field-emission scanning electron microscopy (FE-SEM). Figure 2a shows the FE-SEM micrograph of pure magnesium magnate particles generated by the sol–gel process. As verified by the XRD data, cubic and octahedral morphologies can be seen with the crystal habit of spinel minerals. The $MgMnO_3$@-$ZrO_2$ crystals are larger than $MgMnO_3$ (Fig. 2b). The crystals are cubic and rectangular with sharp edges. The crystals of $MgMnO_3$@$ZrO_2$@CoO core–shell nanoparticles are smaller and are cubic and rectangular in shape (Fig. 2c).

**Energy dispersive X-ray spectroscopy (EDAX) analysis.** The elemental composition of $MgMnO_3$ coated with $ZrO_2$ and CoO was investigated by using energy-dispersive X-ray spectroscopy. Figure 2a revealed the prominent peaks for magnesium at 1.2 keV and manganese at 0.7 and 5.8 keV in the EDAX spectrum, whereas zirconium was found at 2.1 keV in $MgMnO_3$ coated with $ZrO_2$, as displayed in Fig. 2b on the same scale as for $MgMnO_3$. The EDAX spectrum of $MgMnO_3$@$ZrO_2$ covered with cobalt oxide confirmed the presence of the latter which gave peaks at 0.5, 7.1, and 7.8 keV due to Co (Fig. 2c). Thus, the presence of Mg, Mn, O, Zr, and Co with appropriate proportions in the prepared core–shell nanoparticles has been demonstrated.

**Transmission electron microscopy (TEM) analysis.** For further investigation of shape and size, TEM analysis was performed for $MgMnO_3$, $MgMnO_3$@-$ZrO_2$, and $MgMnO_3$@$ZrO_2$@CoO (Fig. 3). It is known that TEM analysis gives accurate information about the morphology of nanostructures. The TEM analysis of $MgMnO_3$ nanoparticles revealed their cubic shape and a crystal size of 40–50 nm (Fig. 3a). Figure 3b shows a typical TEM image of $MgMnO_3$@$ZrO_2$ core–shell nanoparticles prepared from zirconium oxide precursor with hexagonal structure which formed layers on the surface of the $MgMnO_3$ core after thermal degradation. The particle size is 55–60 nm. Figure 3c shows the TEM image of a double coated $MgMnO_3$ sample confirming the presence of two kinds of coating layers on the $MgMnO_3$ core. The $ZrO_2$ shell surrounds the $MgMnO_3$ core as a primary coating layer, while CoO covers the $ZrO_2$ shell as a secondary coating layer. It is

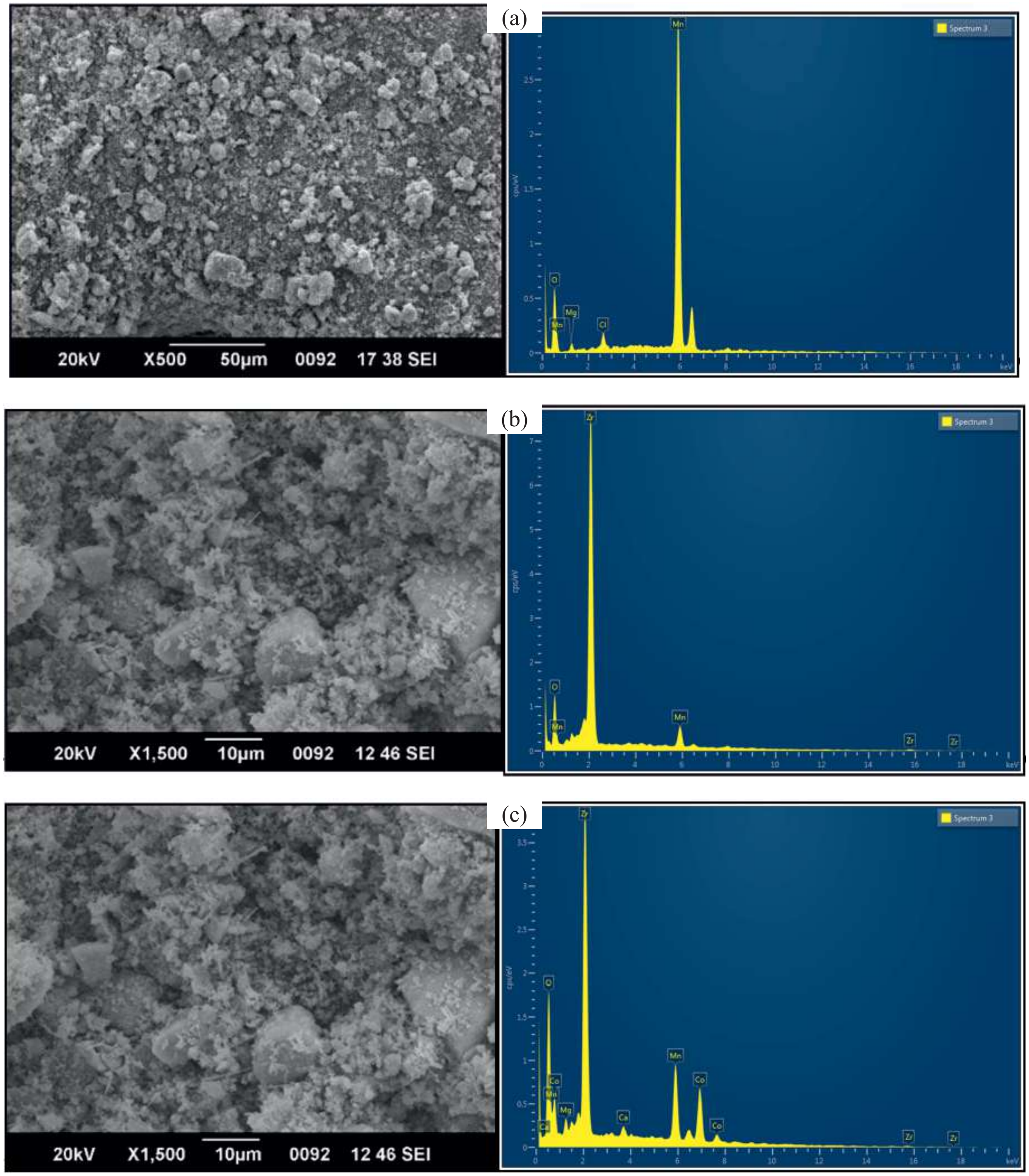


**Fig. 2.** SEM micrographs and EDAX spectra of a) $MgMnO_3$,, b) $MgMnO_3@ZrO_2$, and (c) $MgMnO_3@ZrO_2@CoO$.

seen that CoO forms a full solid coating layer on $ZrO_2$. The particle size of $MgMnO_3@ZrO_2@CoO$ is 30–35 nm.

**Brunauer–Emmett–Teller (BET) analysis.** Measurements of the specific surface area, pore size, and pore volume of core–shell nanomaterials are important since their surface characteristics are responsible for their interfacial behavior when they are used as catalysts. The surface area ($S_{BET}$), pore size, and pore volume of the synthesized catalyst were determined according to the Brunauer–Emmett–Teller (BET) method by measuring nitrogen adsorption. The $N_2$ adsorption–desorption isotherms for $MgMnO_3$, $MgMnO_3@ZrO_2$, and $MgMnO_3@ZrO_2@CoO$ are shown in Fig. 4. According to the BDDT classification, the adsorption curves in Fig. 4a–4c correspond to type III. The surface areas ($S_{BET}$), pore diameters ($d_p$), and pore volumes ($V_p$) are given in Table 1.

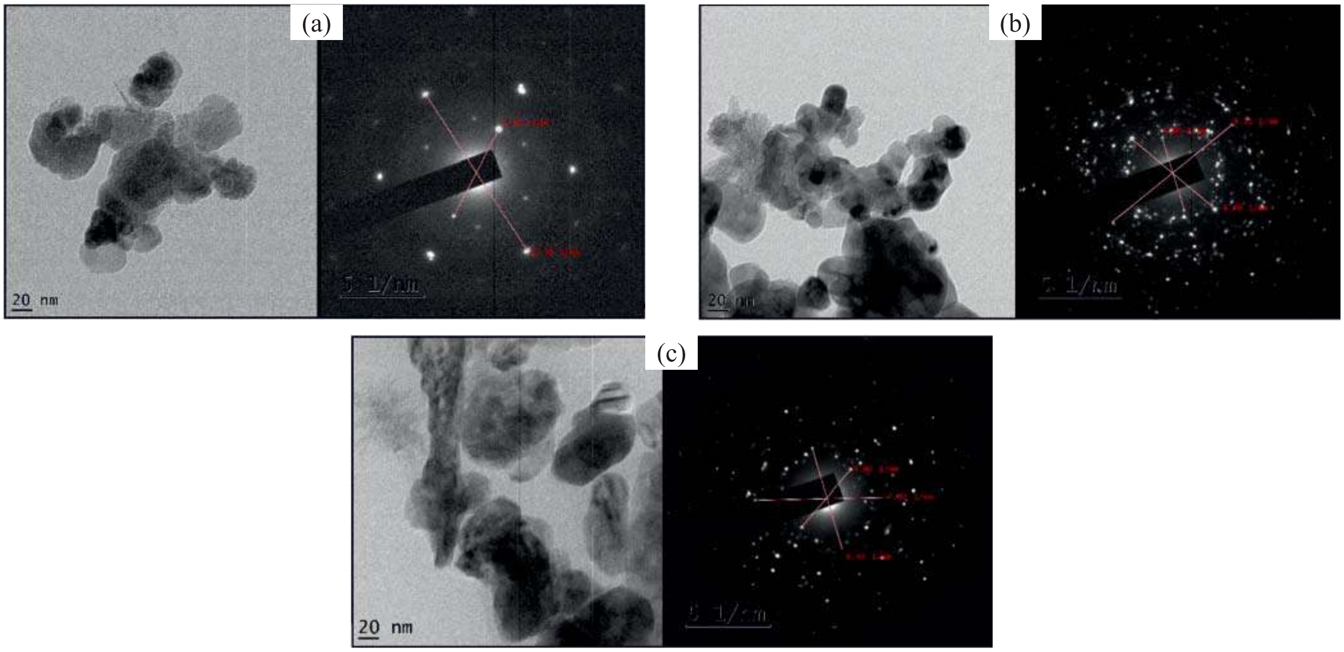


**Fig. 3.** TEM images and SAED patterns of (a) $MgMnO_3$, (b) $MgMnO_3$@$ZrO_2$, and (c) $MgMnO_3$@$ZrO_2$@CoO.

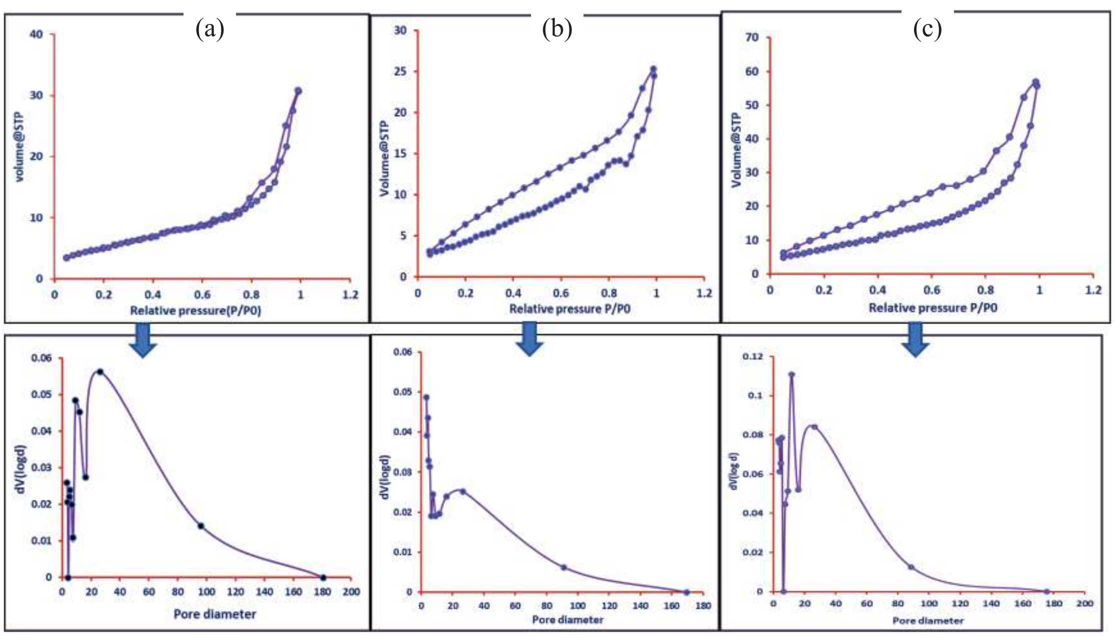


**Fig. 4.** BET Surface area analysis of (a) $MgMnO_3$, (b) $MgMnO_3$@$ZrO_2$, and (c) $MgMnO_3$@$ZrO_2$@CoO nanoparticles.

The prepared $MgMnO_3$@$ZrO_2$@CoO core–shell nanocatalyst was used in the condensation of 4-hydroxycoumarin (**1**), malononitrile (**2**), and substituted benzaldehydes **3a**–**3j** to obtain dihydropyrano[3,2-*c*]-chromene derivatives **4a**–**4j** (Scheme 2). To optimize the conditions, the condensation of 4-nitrobenzaldehyde (**3b**, 1 mmol), 4-hydroxycoumarin (**1**, 1 mmol), and malononitrile (**2**, 1.1 mmol) was selected as a model reaction. First, the catalytic efficiency of $MgMnO_3$, $MgMnO_3$@$ZrO_2$, and $MgMnO_3$@$ZrO_2$@CoO nanoparticles in the model reaction was studied. The results showed that $MgMnO_3$@$ZrO_2$@CoO efficiently catalyzed the reaction and that 0.3 g of the catalyst produced the best yield (Table 2). Neither decrease or increase of the amount of $MgMnO_3$@-$ZrO_2$@CoO affected the yield or reaction time.

Table 3 summarizes the results of studying the effects of solvent and temperature on the reaction. The

**Scheme 2.**

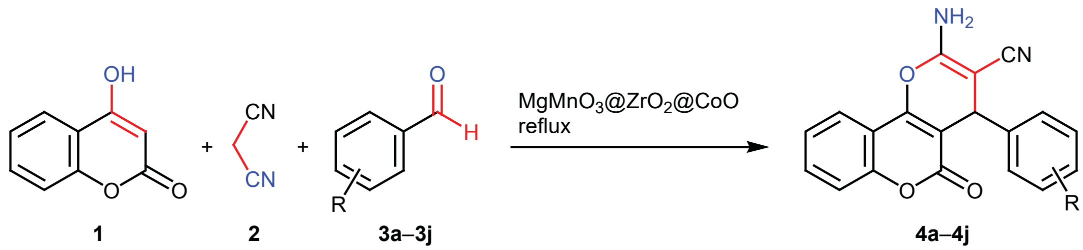


For R, see Table 4.

condensation of 4-nitrobenzaldehyde, 4-hydroxycoumarin, and malononitrile was carried out in chloroform, acetonitrile, *N*,*N*-dimethylformamide, methylene chloride, ethanol, methanol, and water. When the reaction was carried out under solvent-free conditions at room temperature, no target product was formed even after 20 min, but the yield of **4b** was 68% under reflux condition (Table 3; entry nos. 1, 2). When chloroform was used as a solvent, the yield was extremely low at the reflux temperature (Table 3, entry no. 3), the reaction time being the same. The use of a more polar solvent such as acetonitrile under reflux did not improve the yield to a significant extent (Table 3, entry no. 4). Likewise, no significant results were obtained

**Table 1.** BET surface area, pore diameter (Dp), and pore volume (Vp) of core shell nanoparticles

| Catalyst | BET surface area $S_{BET}$, m$^2$/g | Pore diameter $d_p$, nm | Pore volume $V_p$, cm$^3$/g |
|---|---|---|---|
| $MgMnO_3$ | 18.43 | 10.32 | 0.004573 |
| $MgMnO_3$@$ZrO_2$ | 15.25 | 3.385 | 0.03157 |
| $MgMnO_3$@$ZrO_2$@CoO | 31.61 | 3.386 | 0.07753 |

**Table 2.** Effect of catalyst on reaction time and yield of **4b** in 20 min

| Entry. no. | Catalyst | Amount of catalyst, g | Yield of **4b**, % |
|---|---|---|---|
| 1 | $MgMnO_3$ | 0.3 | 57 |
| 2 | $MgMnO_3$@$ZrO_2$ | 0.3 | 68 |
| 3 | $MgMnO_3$@$ZrO_2$@CoO | 0.1 | 91 |
| 4 | $MgMnO_3$@$ZrO_2$@CoO | 0.3 | 97 |
| 5 | $MgMnO_3$@$ZrO_2$@CoO | 0.5 | 92 |

**Table 3.** Effect of solvent and temperature on the yield of **4b** in 20 min

| Entry no. | Solvent | Temperature | Yield of **4b**, % |
|---|---|---|---|
| 1 | None | R.T. | No reaction |
| 2 | None | Reflux | 68 |
| 3 | Chloroform | Reflux | 29 |
| 4 | Acetonitrile | Reflux | 43 |
| 5 | Dimethylformamide | Reflux | 82 |
| 6 | Dichloromethane | Reflux | 67 |
| 7 | Methanol | Reflux | 88 |
| 8 | Ethanol | Reflux | 97 |
| 9 | Ethanol | R.T. | 34 |

**Table 4.** Synthesis of substituted dihydropyrano[3,2-*c*]chromene derivatives **4a**–**4j** using $MgMnO_3$@$ZrO_2$@CoO core–shell catalyst (ethanol, reflux)

| Compd. no. | R | Time, min | Yield, % | mp, °C |
|---|---|---|---|---|
| **4a** | 4-Cl | 20 | 91 | 267–268 [30] |
| **4b** | 4-$NO_2$ | 20 | 97 | 258–260 [30] |
| **4c** | 4-OMe | 35 | 92 | 243–245 [30] |
| **4d** | 3-$NO_2$ | 30 | 89 | 263–265 [30] |
| **4e** | 4-Me | 40 | 80 | 265–268 [30] |
| **4f** | 4-Br | 35 | 87 | 246–248 [26] |
| **4g** | 4-OH | 35 | 86 | 260–262 [24] |
| **4h** | 4-F | 35 | 87 | 260–262 [22] |
| **4i** | 4-$NMe_2$ | 30 | 91 | 214–216 [44] |
| **4j** | 2,4-$(OMe)_2$ | 45 | 89 | 236–238 [43] |

using methylene chloride or methanol (Table 3; entry nos. 5, 7). Finally, ethanol was chosen as the best solvent since it provided the maximum yield (Table 3, entry no. 8). Thus, the optimal conditions were 0.3 g of $MgMnO_3$@$ZrO_2$@CoO catalyst and ethanol as a solvent under reflux; in this case, the reaction was complete in 20 min to afford 97% of **4b**.

The scope of the three-component one-pot condensation was explored using different substituted aromatic aldehydes under the optimized conditions (Table 4). Aromatic aldehydes with both electron-withdrawing and electron-donating substituents gave high yields of the corresponding dihydropyrano[3,2-*c*]-chromene derivatives. The best yield was achieved with 4-nitrobenzaldehyde (**3b**).

Heterogeneous catalysts are advantageous since they can be easily recovered and reused. The recyclability of the catalyst was estimated by carrying out the synthesis of **4b** using recovered $MgMnO_3$@$ZrO_2$@-CoO. For each cycle, after completion of reaction, product **4b** was isolated and identified. The catalyst could be recovered by simple filtration and reused for five successive runs times without a notable change in the yield and reaction time (Fig. 5). Table 5 compares the $MgMnO_3$@$ZrO_2$@CoO core–shell catalyst with some previously reported catalysts in terms of reaction time, yield, and conditions.

## EXPERIMENTAL

Commercially available magnesium chloride ($MgCl_2$), manganese(IV) chloride ($MnCl_4$), poly-(ethylene glycol), organic compounds, and solvents (anhydrous grade) were used without further purification. Silica gel (80–120 mesh) was used for column chromatography. The melting points were measured in capillary tubes and are uncorrected. The IR spectra were recorded on a Shimadzu IR Affinity FT-IR spectrometer. The $^1H$ and $^{13}C$ NMR spectra were recorded on a Bruker spectrometer at 400 and 100 MHz, respectively, using DMSO-$d_6$ as solvent and tetramethylsilane as internal standard. The mass spectra (electron impact, 70 eV) were obtained on an Agilent Technologies 5975C GC/MS instrument.

The X-ray powder diffraction patterns were obtained by using a Rigaku Ultima IV diffractometer running at 25 kV and 25 mA with Cu $K_\alpha$ radiation (λ 0.154 nm); Bragg's scanning angle 20° to 80°. The elemental compositions and atomic weight proportions of $MgMnO_3$@$ZrO_2$@CoO were studied using a Bruker

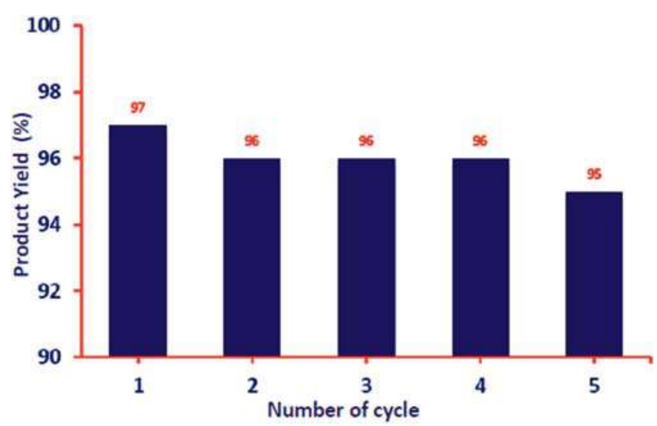


**Fig. 5.** Reusability of $MgMnO_3$@$ZrO_2$@CoO catalyst in the synthesis of 2-amino-4-(4-nitrophenyl)-5-oxo-4*H*,5*H*-pyrano[3,2-*c*]chromene-3-carbonitrile (**4b**).

**Table 5.** Comparison of the catalysts for the synthesis of dihydropyrano[3,2-*c*]chromene derivative **4b**

| Entry no. | Catalyst | Time, min | Yield, % | Reference |
|---|---|---|---|---|
| 1 | DABCO | 30 | 96 | 26 |
| 2 | $Mg(ClO_4)_2$ | 45 | 95 | 27 |
| 3 | IL-Immobilized $FeNi_3$ | 15 | 95 | 44 |
| 4 | Trisodium citrate | 35 | 88 | 45 |
| 5 | 4-Chlorophenylboronic acid | 70 | 89 | 46 |
| 6 | $MgMnO_3@ZrO_2@CoO$ | 20 | 97 | Present work |

X-Flash 613 equipment. The surface morphology and characteristics of the material were analyzed with an FEI Nova Nano SEM 450 scanning electron microscope. The crystallinity, shape, and crystal type of $MgMnO_3$ and core-shell nanostructures were studied using a JEOL/JEM 2100 transmission electron microscope (200 kV, LaB6 electron gun, resolution 0.23 and 0.14 nm). The $N_2$ adsorption–desorption isotherm used to calculate the BET surface area of the catalyst was plotted using a Quantachrome NOVA-1200 Autosorb-1 automated gas sorption system and an Autosorb-1C mercury porosimeter.

**Synthesis of $MgMnO_3$ Nanoparticles.** A 2 M solution of sodium hydroxide was gently added with vigorous stirring to a mixture of equivalent amounts of magnesium chloride ($MgCl_2$), manganese(IV) chloride ($MnCl_4$), and polyethylene glycol as a surfactant in 100 mL of double distilled water. The mixture was heated at 120°C for 24 h in a Teflon-lined steel autoclave, and the resulting gel was filtered off, repeatedly washed with double distilled water, and dried at 110°C to remove the surfactant.

**Synthesis of $MgMnO_3@ZrO_2$ core–shell nanoparticles.** A 1 M NaOH solution was added dropwise over a period of 1 h under continuous stirring to a mixture of 1 mol of $MgMnO_3$, 2 mol $ZrO_2$ [40], and 2 mL of polyethylene glycol in 100 mL of double distilled water. The resulting slurry was autoclaved for 24 h at 120°C, and the precipitate was filtered, washed twice with double distilled water, dried for 5 h at 110°C, and calcined for 6 h at 650°C to eliminate organic impurities.

**Synthesis of $MgMnO_3@ZrO_2@CoO$ core–shell nanoparticles.** A mixture of $MgMnO_3@ZrO_2$ (1 mol), cobalt(II) oxide (1 mol) [40], and 2 mL of polyethylene glycol in 100 mL of 2 M NaOH was gently stirred for 2 h. The mixture was then heated for 24 h at 120°C in a Teflon-lined steel autoclave in an oven. After completion of the reaction, the precipitate was filtered off, washed with deionized water, and dried for 4 h at 120°C. To make a fine powder, the dry product was crushed using a pestle in a mortar, and the resulting powder was calcined for 6 h at 700°C.

**General procedure for the synthesis of dihydropyrano[3,2-*c*]chromene derivatives 4a–4j.** A mixture of 4-nitrobenzaldehyde (1 mmol), 4-hydroxycoumarin (1 mmol), malononitrile (1.1 mmol), and $MgMnO_3@$-$ZrO_2@CoO$ (0.3 g) in 10 mL of ethanol was refluxed with constant stirring for a time indicated in Table 4. When the reaction was complete (TLC), the mixture was cooled to room temperature, transferred into a beaker, and diluted with distilled water. The solid product was filtered off and washed with distilled water and cold ethanol to remove unreacted starting materials and other organic contaminations. The catalyst was separated from the product by filtration using ethanol. The catalyst is insoluble in ethanol, and it could be reused by simple filtration. Compounds **4a**–**4j** were purified by recrystallization from ethanol.

**2-Amino-4-(4-chlorophenyl)-5-oxo-4*H*,5*H*-pyrano[3,2-*c*]chromene-3-carbonitrile (4a)** was synthesized from 4-chlorobenzaldehyde (**3a**, 1.1 mmol), 4-hydroxycoumarin (1.2 mmol), and malononitrile (1.1 mmol); reaction time 20 min. Yield 0.98 g (91%), dark yellow solid, mp 267–268°C. IR spectrum, ν, cm$^{-1}$: 778 (C–Cl), 1046 (C–O), 1231 (C–O), 1602 (C=C), 1650 (C=C), 1730 (C=O), 2245 (C≡N), 3122 (=C–H), 3218 and 3310 ($NH_2$). $^1$H NMR spectrum, δ, ppm: 4.98 s (1H, 4-H), 7.43 d (2H, $H_{arom}$, $J$ = 8.2, 7.4 Hz), 7.68 d (2H, $H_{arom}$, $J$ = 8.2, 7.4 Hz), 9.76 s (2H, $NH_2$). $^{13}$C NMR spectrum, $\delta_C$, ppm: 103.5, 114.4, 115.6, 116.2, 116.3, 118.2, 120.3, 122.3, 122.6, 134.3, 136.4, 138.6, 143.2, 152.5, 158.2, 161.2, 172.3 (C=O). Mass spectrum: *m*/*z* 351.23.

**2-Amino-4-(4-nitrophenyl)-5-oxo-4*H*,5*H*-pyrano[3,2-*c*]chromene-3-carbonitrile (4b)** was synthesized from 4-nitrobenzaldehyde (**3b**, 1.0 mmol), 4-hydroxycoumarin (1.1 mmol), and malononitrile

(1.1 mmol); reaction time 20 min. Yield 0.97 g (97%), dark yellow solid, mp 258–260°C. IR spectrum, ν, $cm^{-1}$:1030 (C–O), 1248 (C–O), 1345 ($NO_2$), 1653 (C=C), 1734 (C=O), 2257 (C≡N), 3217 (=C–H), 3324 ($NH_2$), 3410 ($NH_2$). $^1H$ NMR spectrum, δ, ppm: 5.12 s (1H, 4-H), 7.44 d (2H, *J* = 8.0, 7.2 Hz, $H_{arom}$), 7.85 d (2H, *J* = 8.0, 7.2 Hz, $H_{arom}$), 8.47 s (2H, $NH_2$). $^{13}C$ NMR spectrum, $\delta_C$, ppm: 102.3, 112.3, 114.5, 114.9, 118.2, 120.1, 122.2, 124.7, 126.6, 130.7, 132.1, 138.6, 148.4, 158.3, 160.2, 164.2, 176.5 (C=O). Mass spectrum: *m*/*z* 363.43.

**2-Amino-4-(4-methoxyphenyl)-5-oxo-4*H*,5*H*-pyrano[3,2-*c*]chromene-3-carbonitrile (4c)** was synthesized from 4-methoxybenzaldehyde (**3c**, 1.0 mmol), 4-hydroxycoumarin (1.1 mmol), and malononitrile (1.1 mmol); reaction time 35 min. Yield 0.93 g (92%), white solid, mp 243–245°C. IR spectrum, ν, $cm^{-1}$: 987 (C–C), 1054 (C–C), 1120 (C–C), 1431 (C–C),1656 (C–O), 1728 (C=O), 2235 (C≡N), 3309 (=C–H), 3365 ($NH_2$). $^1H$ NMR spectrum, δ, ppm: 2.8 s (3H, $OCH_3$), 5.09 s (1H, 4-H), 7.59 d (2H, *J* = 8.1, 7.3 Hz, $H_{arom}$), 7.71 d (2H, *J* = 8.1, 7.3 Hz, $H_{arom}$), 6.54 s (2H, $NH_2$). $^{13}C$ NMR spectrum, $\delta_C$, ppm: 35.7 ($OCH_3$), 103.2, 114.8, 116.4, 116.5, 119.5, 122.2, 122.5, 126.9, 128.6, 132.3, 132.9, 136.4, 142.2, 154.2, 156.7, 160.4, 172.9 (C=O). Mass spectrum: *m*/*z* 348.97.

**2-Amino-4-(3-nitrophenyl)-5-oxo-4*H*,5*H*-pyrano[3,2-*c*]chromene-3-carbonitrile (4d)** was synthesized from 3-nitrobenzaldehyde (**3d**, 1.1 mmol), 4-hydroxycoumarin (1.2 mmol), and malononitrile (1.2 mmol); reaction time 30 min. Yield 0.91 g (89%), yellow solid, mp 263–265°C. IR spectrum, ν, $cm^{-1}$: 984 (C–C),1047 (C–C), 1232 (C–O), 1342 ($NO_2$),1602 (C–O), 1632 (C–O), 1738 (C=O), 2245 (C≡N), 3123 (=C–H), 3321 ($NH_2$), 3498 ($NH_2$). $^1H$ NMR spectrum, δ, ppm: 4.87 s (1H, 4-H), 7.42 d (2H, *J* = 8.1, 7.2 Hz, $H_{arom}$), 7.54 d (2H, *J* = 8.1, 7.2 Hz, $H_{arom}$), 9.98 s (2H, $NH_2$). $^{13}C$ NMR spectrum, $\delta_C$, ppm: 104.5, 110.2, 112.4, 116.7, 118.4, 121.5, 122.8, 124.4, 128.9, 132.3, 138.4, 140.8, 142.7, 152.5, 158.6, 162.5, 172.7 (C=O). Mass spectrum: *m*/*z* 363.21.

**2-Amino-4-(4-methylphenyl)-5-oxo-4*H*,5*H*-pyrano[3,2-*c*]chromene-3-carbonitrile (4e)** was synthesized from 4-methylbenzaldehyde (**3e**, 1.2 mmol), 4-hydroxycoumarin (1.2 mmol), and malononitrile (1.1 mmol); reaction time 40 min. Yield 0.84 g (80%), white solid, mp 265–268°C. IR spectrum, ν, $cm^{-1}$: 1156 (C–O), 1234 (C–C), 1604 (C–O), 1632 (C–O), 1743 (C=O), 2232 (C≡N), 3294 (=C–H), 3310 ($NH_2$). $^1H$ NMR spectrum, δ, ppm:1.8 s (3H, $CH_3$), 4.97 s (1H, 4-H), 7.38 d (2H, *J* = 8.2, 7.4 Hz, $H_{arom}$), 7.68 d (2H, *J* = 8.2, 7.4 Hz, $H_{arom}$), 6.78 s (2H, $NH_2$). $^{13}C$ NMR spectrum, $\delta_C$, ppm: 21.2 ($CH_3$), 103.6, 113.7, 116.8, 116.9, 118.2, 121.2, 122.3, 124.8, 128.9, 131.7, 136.1, 140.6, 142.3, 152.6, 158.6, 162.2, 172.6 (C=O). Mass spectrum: *m*/*z* 332.23.

**2-Amino-4-(4-bromophenyl)-5-oxo-4*H*,5*H*-pyrano[3,2-*c*]chromene-3-carbonitrile (4f)** was synthesized from 4-bromobenzaldehyde (**3f**, 1.1 mmol), 4-hydroxycoumarin (1.0 mmol), and malononitrile (1.0 mmol) ; reaction time 35 min. Yield 0.89 g (87%), brown solid, mp 246–248°C. IR spectrum, ν, $cm^{-1}$: 835 (C–Br), 932 (C–C), 1056 (C=C), 1287 (C=C), 1458 (C–N), 1665 (C–O), 1734 (C=O), 2276 (C≡N), 3234 (=C–H), 3376 ($NH_2$), 3456 ($NH_2$). $^1H$ NMR spectrum, δ ppm:4.97 s (1H, 4-H), 7.39 d (2H, *J* = 8.2, 7.2 Hz, $H_{arom}$), 7.62 d (2H, *J* = 8.0, 7.2 Hz, $H_{arom}$), 6.98 s (2H, $NH_2$). $^{13}C$ NMR spectrum, $\delta_C$, ppm: 104.6, 111.4, 113.6, 116.3, 119.6, 122.1, 122.9, 126.7, 128.4, 130.4, 134.4, 142.1, 146.8, 162.2, 162.8, 166.8, 172.3 (C=O). Mass spectrum: *m*/*z* 396.

**2-Amino-4-(4-hydroxyphenyl)-5-oxo-4*H*,5*H*-pyrano[3,2-*c*]chromene-3-carbonitrile (4g)** was synthesized from 4-hydroxybenzaldehyde (**3g**, 1.1 mmol), 4-hydroxycoumarin (1.0 mmol), and malononitrile (1.0 mmol); reaction time 35 min. Yield 0.88 g (86%), white solid, mp 260–262°C. IR spectrum, ν, $cm^{-1}$: 856 (C–H), 1123 (C–C), 1221 (C–C), 1440 (C–O),1634 (C–O), 1734 (C=O), 2234 (C≡N), 3181 (=C–H), 3298 and 3380 ($NH_2$). $^1H$ NMR spectrum, δ, ppm: 5.23 s (1H, 4-H), 7.43 d (2H, *J* = 8.1, 7.3 Hz, $H_{arom}$), 7.72 d (2H, *J* = 8.1, 7.3 Hz, $H_{arom}$), 6.87 s (2H, $NH_2$). $^{13}C$ NMR spectrum, $\delta_C$, ppm: 104.8, 110.1, 110.5, 111.9, 112.2, 118.1, 118.2, 120.7, 122.6, 122.9, 128.1, 128.6, 138.4, 148.3, 150.2, 154.2, 172.5 (C=O). Mass spectrum: *m*/*z* 334.65.

**2-Amino-4-(4-fluorophenyl)-5-oxo-4*H*,5*H*-pyrano[3,2-*c*]chromene-3-carbonitrile (4h)** was synthesized from 4-fluorobenzaldehyde (**3h**, 1.2 mmol), 4-hydroxycoumarin (1.1mmol), and malononitrile (1.1 mmol); reaction time 35 min. Yield 0.90 g (87%), yellow solid, mp 260–262°C. IR spectrum, ν, $cm^{-1}$: 775 (C–F), 875 (C–H), 1012 (C–C), 1131 (C–C), 1267 (C–C),1621 (C–O), 1732 (C=O), 2234 (C≡N), 3317 (=C–H), 3424 ($NH_2$). $^1H$ NMR spectrum, δ, ppm: 4.95 s (1H, 4-H), 7.32 d (2H, *J* = 8.0, 7.2 Hz, $H_{arom}$), 7.58 d (2H, *J* = 8.0, 7.2 Hz, $H_{arom}$), 6.98 s (2H, $NH_2$). $^{13}C$ NMR spectrum, $\delta_C$, ppm: 104.6, 108.3, 110.5, 110.9, 111.2, 112.8, 113.2, 114.7, 116.6, 126.7, 128.1, 128.6, 148.9, 149.3, 162.2, 166.8, 172.5 (C=O). Mass spectrum: *m*/*z* 336.78.

**2-Amino-4-[4-(dimethylamino)phenyl]-5-oxo-4*H*,5*H*-pyrano[3,2-*c*]chromene-3-carbonitrile (4i)** was synthesized from 4-(dimethylamino)benzaldehyde (**3i**, 1.0 mmol), 4-hydroxycoumarin (1.1 mmol), and malononitrile (1.1 mmol); reaction time 30 min. Yield 0.91 g (91%), dark yellow solid, mp 214–216°C. IR spectrum, ν, $cm^{-1}$: 895 (C–H), 1123 (C–C), 1276 (C–C), 1434 (C–N),1631 (C–O), 1742 (C=O), 2243 (C≡N), 3307 (=C–H), 3376 and 3390 ($NH_2$). $^1H$ NMR spectrum, δ, ppm: 2.8 s (6H, $CH_3$), 5.23 s (1H, 4-H), 7.30 d (2H, *J* = 8.2, 7.3 Hz, $H_{arom}$), 7.56 d (2H, *J* = 8.2, 7.3 Hz, $H_{arom}$), 6.78 s (2H, $NH_2$). $^{13}C$ NMR spectrum, $\delta_C$, ppm: 45.3 ($CH_3$), 103.6, 110.1, 112.1, 112.9, 116.2, 118.8, 120.2, 122.4, 124.6, 128.8, 130.6, 136.2, 142.4, 152.1, 156.2, 160.2, 172.5 (C=O). Mass spectrum: *m*/*z* 362.32.

**2-Amino-4-(2,4-dimethoxyphenyl)-5-oxo-4*H*,5*H*-pyrano[3,2-*c*]chromene-3-carbonitrile (4j)** was synthesized from 2,4-dimethoxybenzaldehyde (**3j**, 1.1 mmol), 4-hydroxycoumarin (1.2 mmol), and malononitrile (1.1 mmol); reaction time 45 min. Yield 0.90 g (89 %), yellow product, mp 236–238°C. IR spectrum, ν, $cm^{-1}$: 1134 (C–C), 1435 (C–N), 1542 (C–O), 1632 (C–O), 1747 (C=O), 2242 (C≡N), 3189 (=C–H), 3284 and 3381 ($NH_2$). $^1H$ NMR spectrum, δ, ppm: 3.24 s (6H, $CH_3O$), 5.02 s (1H, 4-H), 7.44 d (2H, *J* = 8.0, 7.2 Hz, $H_{arom}$), 7.85 d (2H, *J* = 8.0, 7.2 Hz, $H_{arom}$), 9.79 s (2H, $NH_2$). $^{13}C$ NMR spectrum, $\delta_C$, ppm: 35.6 ($CH_3$), 103.6, 110.5, 112.8, 112.9, 116.2, 118.3, 120.2, 122.6, 124.6, 132.2, 136.2, 140.2, 142.8, 152.3, 157.2, 162.6, 172.2 (C=O). Mass spectrum: *m*/*z* 378.23.

## CONCLUSIONS

The synthesis of novel $MgMnO_3@ZrO_2@CoO$ core–shell catalyst by simple hydrothermal method has been reported for the first time. The catalyst was used for the one-pot three-component synthesis of dihydropyrano[3,2-*c*]chromene derivatives from 4-hydroxycoumarin, malononitrile, and substituted benzaldehydes. The salient features of this study include the use of easily available materials, higher yields, shorter reaction time, cleaner reaction conditions, and catalyst reusability. With reference to our study, this method is a useful alternative to many other complicated reactions reported so far.

## ACKNOWLEDGMENTS

The authors thank S. P. Pune University (Pune, Maharashtra) for financial support, and SAIF Cochin (Kerala, India) for supporting analytical studies.

## CONFLICT OF INTEREST

The authors declare no conflict of interest.

## REFERENCES

1. Domlin g, A., *Chem. Rev*., 2006, vol. 106, p. 17. https://doi.org/10.1021/cr0505728
2. Ugi, I., *Adv. Synth. Catal*., 1997, vol. 339, p. 499. https://doi.org/10.1002/prac.19973390193
3. Terrett, N.K., Gardner, M., Gordon, D.W., Kobylecki, R.J., and Steele, J., *Tetrahedron*, 1995, vol. 51, p. 8135. https://doi.org/10.1016/0040-4020(95)00467-M
4. Dömling, A. and Ugi, I., *Angew. Chem., Int. Ed*., 2000, vol. 39, p. 3168. https://doi.org/10.1002/1521-3773(20000915)39:18<3168::AID-ANIE3168>3.0.CO;2-U
5. Kandhasamy, K. and Gnanasambandam, V., *Curr. Org. Chem*., 2009, vol. 13, p. 1820. https://doi.org/10.2174/138527209789630514
6. Bienaymé, H., Hulme, C., Oddon, G., and Schmitt, P., *Chem. Eur. J*., 2000, vol. 6, p. 3321. https://doi.org/10.1002/1521-3765(20000915)6:18<3321::AID-CHEM3321>3.0.CO;2-A
7. Müller, T.J.J., *Science of Synthesis, Multicomponent Reactions I*, Stuttgart: Georg Thieme, 2014, vol. 1. https://doi.org/10.1055/b-003-125816
8. Borhade, A.V., Tope, D.R., Gare, G.D., and Dabhade, G.B., *J. Korean Chem. Soc*., 2017, vol. 61, p. 157. https://doi.org/10.5012/jkcs.2017.61.4.157
9. Tope, D.R., Patil, D.R., and Borhade, A.V., *J. Chem. Pharm. Res*., 2012, vol. 4, p. 2501.
10. Borhade, A.V., Uphade, B.K., and Tope, D.R., *J. Chem. Sci*., 2013, vol. 125, p. 583. https://doi.org/10.1007/s12039-013-0396-8
11. Szabó, D.V. and Vollath, D., *Adv. Mater*., 1999, vol. 11, p. 1313. https://doi.org/10.1002/(SICI)1521-4095(199910)11:15<1313::AID-ADMA1313>3.0.CO;2-2
12. Dumitrache, F., *Diamond Relat. Mater*., 2004, vol. 13, p. 362. https://doi.org/10.1016/j.diamond.2003.10.022
13. Borhade, A.V., Tope, D.R., Agashe, J.A., and Kushare, S.S., *J. Water Environ. Nanotechnol*., 2021, vol. 6, p. 164. https://doi.org/10.22090/jwent.2021.02.006
14. Borhade, A.V., Tope, D.R., Agashe, J.A., and Kushare, S.S., *J. Water Environ. Nanotechnol*., 2021, vol. 6, p. 306. https://doi.org/10.22090/jwent.2021.538176.1427
15. Larios, E., Calderón, L., Guerrero, K., Pinedo, E., Maldonado, A., and Tanori, J., *J. Dispersion Sci. Technol*., 2012, vol. 33, p. 1360. https://doi.org/10.1080/01932690903294147

16. Green, G.R., Evans, J.M., and Vong, A.K., *Comprehensive Heterocyclic Chemistry II*, Katritzky, A.R., Rees, C.W., and Scriven, E.F.V., Eds., Oxford: Pergamon, 1996, vol. 5, p. 469. https://doi.org/10.1016/B978-008096518-5.00112-X
17. Foye, W.O. and Dall'Acqua, F., *Principi di chimica farmaceutica*, Padova: Piccin, 1991, 2nd ed., p. 416.
18. Konkoy, C.S., Fick, D.B., Cai, S.X., Lan, N.C., and Keana, J.F.W., US Patent no. 6800657B2, 2004.
19. Burgard, A., Lang, H., and Gerlach, U., *Tetrahedron*, 1999, vol. 55, p. 7555. https://doi.org/10.1016/S0040-4020(99)00376-2
20. Evans, J.M., Fake, C.S., Hamilton, T.C., Poyser, R.H., and Showell, G.A., *J. Med. Chem*., 1984, vol. 27, p. 1127. https://doi.org/10.1021/jm00375a007
21. Evans, J.M., Fake, C.S., Hamilton, T.C., Poyser, R.H., and Watts, E.A., *J. Med. Chem*., 1983, vol. 26, p. 1582. https://doi.org/10.1021/jm00365a007
22. Khaleghi-Abbasabadi, M. and Azarifar, D., *Res. Chem. Intermed*., 2019, vol. 45, p. 2095. https://doi.org/10.1007/s11164-018-03722-y
23. Mohammaadi, P. and Sheibani, H., *Mater. Chem. Phys*., 2019, vol. 228, p. 140. https://doi.org/10.1016/j.matchemphys.2018.11.058
24. Wanzheng, M.A., Ebadi, A.G., Sabil, M.S., Javahershenasd, R., and Jimenez, G., *RSC Adv*., 2019, vol. 9, p. 12801. https://doi.org/10.1039/c9ra01679a
25. Ramin, G.V., Jafar, M., Yaser, M., and Azadeh, S., *Curr. Org. Synth*., 2017, vol. 6, p. 904. https://doi.org/10.2174/1570179414666170203150629
26. Jain, S., Rajguru, D., Keshwal, B.S., and Acharya, A.D., *Int. Scholarly Res. Not*., 2013, vol. 2013, article ID 185120. https://doi.org/10.1155/2013/185120
27. Emtiazi, H. and Amrollahi, M.A., *Bulg. Chem. Commun*., 2017, vol. 49, p. 478.
28. Kanakaraju, S., Prasanna, B., Basavoju, S., and Chandramouli, G.V.P., *Arab. J. Chem*., 2017, vol. 10, p. S2705. https://doi.org/10.1016/j.arabjc.2013.10.014
29. Khurana, J.M., Nand, B., and Saluja, P., *Tetrahedron*, 2010, vol. 66, p. 5637. https://doi.org/10.1016/j.tet.2010.05.082
30. Abdolmohammadi, S. and Balalaie, S., *Tetrahedron Lett*., 2007, vol. 48, p. 3299. https://doi.org/10.1016/j.tetlet.2007.02.135
31. Shitole, B.V., Shitole, N.V., and Kakde, G.K., *Orbital: Electron. J. Chem*., 2019, vol. 9, p. 131. https://doi.org/10.17807/orbital.v11i3.1396
32. Kidwai, M. and Saxena, S., *Synth. Commun*., 2006, vol. 36, p. 2737. https://doi.org/10.1080/00397910600764774
33. Mohammadi, A.S., and Balalaie, S., *Tetrahedron Lett*., 2007, vol. 48, p. 3299. https://doi.org/10.1016/j.tetlet.2007.02.135
34. Khurana, J.M. and Kumar, S., *Tetrahedron Lett*., 2009, vol. 50, p. 4125. https://doi.org/10.1016/j.tetlet.2009.04.125
35. Shaabani, A., Samadi, S., Badri, Z., and Rahmati, A., *Catal. Lett*., 2005, vol. 104, p. 39. https://doi.org/10.1007/s10562-005-7433-2
36. Tavakoli-Hoseini, N., Heravi, M.M., Bamoharram, F.F., and Davoodnia, A., *Asian J. Chem*., 2011, vol. 23, p. 3599.
37. Dekamin, M.G., Eslami, M., and Maleki, A., *Tetrahedron*, 2013, vol. 69, p. 1074. https://doi.org/10.1016/j.tet.2012.11.068
38. Borhade, A.V., Tope, D.R., and Agashe, J.A., *J. Mater. Sci.: Mater. Electron*., 2018, vol. 29, p. 7551. https://doi.org/10.1007/s10854-018-8747-3
39. Heshmatpour, F. and Aghakhanpour, R.B., *Powder Technol*., 2011, vol. 205, p. 193. https://doi.org/10.1016/j.powtec.2010.09.011
40. Singh, A.K. and Nakate, U.T., *Sci. World J*., 2014, vol. 2014, article ID 349457. https://doi.org/10.1155/2014/349457
41. Pudukudy, M., Yaakob, Z., Narayanan, B., Gopalakrishnan, A., and Tasirin, S.M., *Superlattices Microstruct*., 2013, vol. 64, p. 15. https://doi.org/10.1016/j.spmi.2013.09.012
42. Yuan, Y., Ye, F., and Li, S., *Mater. Lett*., 2006, vol. 60, p. 3175. https://doi.org/10.1016/j.matlet.2006.02.062
43. Hekmatshoar, R., Majedi, S., and Bakhtiari, K., *Catal. Commun*., 2008, vol. 9, p. 307. https://doi.org/10.1016/j.catcom.2007.06.016
44. Safaei-Ghomi, J., Eshteghal, F., and Shahbazi-Alavi, H., *Polycyclic Aromat. Compd*., 2020, vol. 40, p. 13. https://doi.org/10.1080/10406638.2017.1348368
45. Zheng, J. and Li, Y.-Q., *Arch. Appl. Sci. Res*., 2011, vol. 3, no. 2, p. 381.
46. Pendalwar, S.S., Chakrawar, A.V., Chavan, A.S., and Bhusare, S.R., *Der. Pharma. Chem*., 2016, vol. 8, no. 10, p. 143.

Research Article | Published: 25 February 2023

# Enhanced photocatalytic performance of $CdFe_2O_4/Al_2O_3$ nanocomposite for dye degradation

Ashwini S. Varpe, Mrinalini D. Deshpande, Dipak R. Tope & Ashok V. Borhade

*Environmental Science and Pollution Research* **30**, 52549–52560 (2023)



## Abstract

In the present work, $CdFe_2O_4/Al_2O_3$ magnetic nanocomposite photocatalyst is successfully synthesized by simple sol-gel auto-combustion method. The role of this sample is studied as a photocatalyst. The influence of $Al_2O_3$ concentration with $CdFe_2O_4$ on the photocatalytic property is also studied. We have considered three weight percentage of $Al_2O_3$, 5%, 10%, and 20% with $CdFe_2O_4$. All the samples are characterized with X-ray diffraction (XRD), Brunauer-Emmett-Teller (BET), Fourier transform infrared spectroscopy (FTIR), field emission scanning electron microscopy (FESEM), transmission electron microscopy (TEM) with selected area electron diffraction (SAED), vibrating sample magnetometer (VSM), UV-Visible, and photoluminescence (PL) spectroscopy techniques. The 10% composite sample showed the lower particle size, higher surface area, enhanced porosity, higher saturation magnetization, and considerable band gap as compared to that of 5% and 20% $CdFe_2O_4/Al_2O_3$ as well as bare $CdFe_2O_4$ nanoparticles. The photocatalytic activity of the sample is evaluated towards the degradation of the xylenol orange (XO) dye under UV light. The degradation process of the dye is monitored spectrophotometrically. The performance in terms of removal efficiency is studied by varying the contact time, dye concentration and amount of catalyst. Among the three concentrations of $Al_2O_3$, the 10% weight concentration of $Al_2O_3$ with $CdFe_2O_4$ is found to be the optimal concentration and showed the higher degradation rate. After 30 min photocatalytic reaction, the degradation rate is 92.29% for 10% $CdFe_2O_4/Al_2O_3$ and for bare $CdFe_2O_4$, it is 85.79%. This work provides a new reference for designing $Al_2O_3$-based spinel ferrite nanocomposites and their role in wastewater management.

## Data availability

The data used to support the findings of this study are included within the article.

## References

Abbas N, Rubab N, Sadiq N, Manzoor S, Khan M, Garcia J, Aragao I, Tariq M, Akhtar Z, Yasmin G (2020) Aluminum-doped cobalt ferrite as an efficient photocatalyst for the abatement of methylene blue. Water 12:2285

Bhatkhande D, Pangarkar VG, Beenackers AA (2001) Photocatalytic degradation for environmental applications - a review. J Chem Tech Biotech 77:102

Borade RM, Somwanshi SB, Pawar KSB, RP JKM (2020) Spinel zinc ferrite nanoparticles: an active nanocatalyst for microwave irradiated solvent free synthesis of chalcones. Mater Res Express 7:016116

Chaker H, Attar AE, Djennar M, Fourmentin S (2021) A statistical modeling optimization approach for efficiency photocatalytic degradation of textile azo dye using cerium-doped mesoporous ZnO : a central composite design in response surface methodology. Chem Eng Res Design 171:198. https://doi.org/10.1016/j.cherd.2021.05.008

Chen YN, Liu T, Zhang Q, Shang C, Wang H (2017) Nanostructured biogel templated synthesis of $Fe_3O_4$ nanoparticles and its application for catalytic degradation of xylenol orange. RSC Adv 7:758. https://doi.org/10.1039/C6RA24926D

Chiu YH, Change TF, Chen CY, Sone M, Hsu YJ (2019) Mechanistic insights into photodegradation of organic dyes using heterostructure photocatalysts. Catalyst 9:430

Danish M, Tayyab M, Akhtar A, Altaf AA, Kausar S, Ullah S, Iqbal M (2021) Effect of soft template variation on the synthesis, physical, and electrochemical properties of $Mn_3O_4$ nanomaterial. Inorg. Nanometal Chem 51:359

Dippong T, Andrea Levei E, Cadar O (2021) Recent advances in synthesis and applications of $MFe_2O_4$ (m = Co, Cu, Mn, Ni, Zn) nanoparticles. Nanomaterials 11:1:1560. https://doi.org/10.3390

Dutta SK, Akhter M, Ahmed J, Amin MK, Dhar PK (2022) Synthesis and catalytic activity of spinel ferrites: a brief review. Biointer. Res. Appl. Chem. 12:4399

Fang MM, Shao JX, Huang XG, Wang JY, Chen W (2020) Direct Z-scheme $CdFe_2O_4$/g-$C_3N_4$ hybrid photocatalysts for highly efficient ceftiofur sodium photodegradation. J Mater Sci Tech 56:133. https://doi.org/10.1016/j.jmst.2020.01.054

Golsefidi MA (2017) Influence of the surfactant, capping agent and reductant agent on the morphology and size of $CdFe_2O_4$ nanoparticles. J Mater Sci Mater Electronics 28:6345. https://doi.org/10.1007/s10854-016-6318-z

Harish NK, Bhojya Naik HS, Prashanth Kumar PN, Vishwanath R, Yashvanth Kumar GS (2013) Optical and photocatalytic properties of $CdFe_2O_4$ nanocatalysts: potential application in water treatment under solar light irradiation. Arch Appl Sci Res 5:42

Kadier Ilyas AR, Huzaifah M, Harihastuti N, Sapuan S, Harussani M, Azlin M, Yuliasni R, Ibrahim R, Atikah M, Wang J, Chandrasekhar K, Islam M, Sharma S, Punia S, Rajasekar A, Asyraf M, Ishak M (2021) Use of industrial wastes as sustainable nutrient sources for bacterial cellulose (BC) production: mechanism, advances, and future perspectives. Polymers 13:3365

Kefeni KK, Mamba BB (2020) Photocatalytic application of spinel ferrite nanoparticles and nanocomposites in wastewater treatment : review. Sustain Mater Tech 23:e00140

Kharisov BI, Rasika Das HV, Kharissova OV (2019) Mini-review: ferrite nanoparticles in the catalysis. Arab J Chem 12:1234

Kirankumar VS, Sumathi S (2020) A review on photodegradation of organic pollutants using spinel oxide. Mater Today Chem 18:100355

Kusuma K, Manju M, Ravikumar C, Nagaswarupa H, Amulya M, Anilkumar M, Avinash B, Gurushantha K, Ravikantha N (2020) Photocatalytic and electrochemical sensor for direct detection of paracetamol comprising $\gamma$-aluminium oxide nanoparticles synthesized via sonochemical route. Sensors Inter 1:100039

Li Z, Wang H, Wei X, Liu X, Yang Y, Jing W (2016) Preparation and photocatalytic performance of magnetic $Fe_3O_4@TiO_2$ core-shell microsphere supported by silica aerogels from industrial fly ash. J Alloys Comp 659:240

Liu G, Feng M, Tayyab M, Gong J, Zhang M, Yang M, Lin K (2021) Direct and efficient reduction of perfluorooctanoic acid using bimetallic catalyst supported on carbon. J Hazard Mater 412:125224. https://doi.org/10.1016/j.jhazmat.2021.125224

Liu Y, Zhu Q, Tayyab M, Zhou L, Lei J, Zhang J (2021) Single-atom Pt loaded zinc vacancies ZnO-ZnS induced type-V electron transport for efficiency photocatalytic $H_2$ evolution. Solar RRL 5:2100536

Mapossa AB, Mhike W, Adalima JL, Tichapondwa S (2021) Removal of organic dyes from water and wastewater using magnetic ferrite-based titanium oxide and zinc oxide. Catalyst 11:1543

Moreno YP, Silva WL, Stedile FC, Radtke C, Santos JHZ (2021) Micro and nanodomains on structured silica/titania photocatalysts surface evaluated in RhB degradation: effect of structural properties on catalytic efficiency. Appl Surf Sci Adv 3:10055. https://doi.org/10.1016/j.apsadv.2021.100055

Naik M, Naik H, Nagaraju G, Vinuth M, Vinu K, Rashmi S (2018) Effect of aluminium doping on structural, optical, photocatalytic and antibacterial activity on nickel ferrite nanoparticles by sol–gel auto-combustion method. J Mater Sci Mater Electron 29:20395

Nasseri M, Moghadam S, Kazemnejadi M, Allahresani A (2020) Cu/Ni-doped sulfated zirconium oxide immobilized on $CdFe_2O_4$ NPs: a cheap, sustainable and magnetically recyclable inorgano-catalyst for the efficient preparation of $\alpha$-aminonitriles in aqueous media. Res Chem Intermed 46:4233

Patil SB, Naik HSB, Nagaraju G, Shiralgi Y (2018) Sugarcane juice facilitated eco-friendly synthesis of solar light active CdFe2O4 nanoparticles and its photocatalytic application. Eur Phys J Plus 133:229. https://doi.org/10.1140/epjp/i2018-12063-5

Plocek J, Hutlova A, Niznansky D, Bursik J, Rehspringer J, Micka Z (2003) Preparation of $ZnFe_2O_4/SiO_2$ and $CdFe_2O_4/SiO_2$ nanocomposites by sol-gel method. J Non-Cryst Solid 315:70

Ragab SS, Badawy AA, Nazar HA (2019) A green approach to the synthesis of 2,3-diaminophenazine using a photocatalytic system of $CdFe_2O_4/TiO_2$ nanoparticles. J Chin Chem Soc 66:719. https://doi.org/10.1002/jccs.201800355

Sagadevan S, Pal K, Chowdhury ZZ, Hoque ME (2017) Structural, optical and dielectric investigation of $CdFe_2O_4$ nanoparticles. Mater Res Express 4:075025. https://doi.org/10.1088/2053-1591/aa77b5

Salehi K, Bahmani A, Shahmoradi B, Pordel MA, Kohzadi S, Gong Y, Guo H, Shivaraju HP, Rezaee R, Pawar RR, Lee SM (2017) Response surface methodology optimization approach for degradation of Direct Blue 71 dye using CuO-ZnO nanocomposite. Int J Environ Sci Technol 14:2067. https://doi.org/10.1007/s13762-017-1308-0

Shahid M (2020) Fabrication of magnesium substituted cadmium ferrite nanoparticles decorated Graphene-Sheets with improved photocatalytic activity under visible light irradiation. Cera Inter 46:10861. https://doi.org/10.1016/j.ceramint.2020.01.098

Shi W, Liu X, Zhang T, Wang Q, Zhang L (2015) Magnetic nano-sized cadmium ferrite as an efficient catalyst for the degradation of Congo red in the presence of microwave irradiation. RSC Adv 5:51027. https://doi.org/10.1039/C5RA07591B

Shindhal T, Rakholiya P, Varjani S, Pandey A, Ngo H, Guo W, Ng H, Taherzadeh M (2021) A critical review on advances in the practices and perspectives for the treatment of dye industry wastewater. Bioengineered 12:70

Somwanshi SB, Somwanshi SB, Kharat PB (2020) Nanocatalyst: a brief review on synthesis to applications. J Phys Conf Series 1644:012046

Tang DQ, Zhang DJ, Tang DY, Ai H (2006) Fabrication of magnetic core-shell $CoFe_2O_4/Al_2O_3$ nanoparticles as immobilized metal chelate affinity support for protein adsorption. Chem Lett 35:1238. https://doi.org/10.1246/c1.2006.1238

Tetteh EK, Ezugbe EO, Asante-Sackey E, Armh EK, Rathilal S (2021) Response surface methodology: photocatalytic degradation kinetics of basic blue 41 dye using activated carbon with $TiO_2$. Molecules 26:1068. https://doi.org/10.3390/molecules26041068

Varpe AS, Deshpande MD (2020) Study of structural, optical, and dielectric properties of sol-gel derived $ZnFe_2O_4$-$Al_2O_3$ composite nanoparticles. J Sol-Gel Sci Tech 96:1. https://doi.org/10.1007/s10971-020-05408-7

Viswanathan B (2018) Photocatalytic degradation of dyes: an review. Current Cata 7:1

Zhang D, Wang Q, Wang L, Zhang L (2015) Magnetically separable $CdFe_2O_4$/graphene catalyst and its enhanced photocatalytic properties. J Mater Chem A 3:3576. https://doi.org/10.1039/C4TA05419A

Zhang J, Guo Q, Liu Y, Cheng Y (2012) Preparation and characterization of $Fe_2O_3/Al_2O_3$ using the solution combustion approach for chemical looping combustion. Int Eng Chem Res 51:12773. https://doi.org/10.1021/ie301804c

Zhu AD (2011) Synthesis of porous $Fe_3O_4$ nanospheres and its application for the catalytic degradation of xylenol orange. J Phys Chem 115:18923. https://doi.org/10.1021/jp200418j

## Funding

This work was supported by the Council of Scientific and Industrial Research (CSIR), New Delhi, India, for the project EMR-II-03/1429/18.

## Author information

### Authors and Affiliations

**Department of Physics, H.P.T. Arts and R.Y.K. Science College, Nashik, 422005, Maharashtra, India**

Ashwini S. Varpe & Mrinalini D. Deshpande

**Department of Chemistry, H.P.T. Arts and R.Y.K. Science College, Nashik, 422005, Maharashtra, India**

Dipak R. Tope & Ashok V. Borhade

### Contributions

ASV conducted the experimental work and drafted the initial manuscript. MDD supervised the work equally. DRT and AVB equally contributed in catalytic experiments. All authors contributed to the final manuscript.

Corresponding author

Correspondence to Mrinalini D. Deshpande.

## Ethics declarations

### Consent to participate

All authors agree to participate in the editing of the paper.

### Consent for publication

All authors agree to publish this manuscript in your journal.

### Conflict of interest

The authors declare no competing interests.

## Additional information

Responsible Editor: Sami Rtimi

Publisher’s note



## Supplementary Information

ESM 1

(PDF 328 KB)

## Rights and permissions



## About this article

### Cite this article

Varpe, A.S., Deshpande, M.D., Tope, D.R. *et al.* Enhanced photocatalytic performance of $CdFe_2O_4/Al_2O_3$ nanocomposite for dye degradation. *Environ Sci Pollut Res* **30**, 52549–52560 (2023). https://doi.org/10.1007/s11356-022-24834-4

| Received | Accepted | Published |
|---|---|---|
| 08 July 2022 | 14 December 2022 | 25 February 2023 |

Issue Date

April 2023

DOI

https://doi.org/10.1007/s11356-022-24834-4

Keywords

**Spinel ferrites nanocomposite**

**Sol-gel auto-combustion** **Photocatalyst**

**Dye degradation**

# Pau Lawrence Dunbar's *Harriet Beecher Stowe* and *We Wear the Masks* Represent the Life of Slaves Post Abolishment of Slavery

**OPEN ACCESS**

Manuscript ID:
ENG-2022-11026079

Volume: 11

Issue: 2

Month: March

Year: 2023

P-ISSN: 2320-2645

E-ISSN: 2582-3531

Received: 18.12.2022

Accepted: 17.02.2023

Published: 01.03.2023

Citation:
Aware, Rupali, and Swapnil Satish Alhat. "Pau Lawrence Dunbar's *Harriet Beecher Stowe* and *We Wear the Masks* Represent the Life of Slaves Post Abolishment of Slavery." *Shanlax International Journal of English*, vol. 11, no. 2, 2023, pp. 1–3.

DOI:
https://doi.org/10.34293/english.v11i2.6079



**Rupali Aware**
*LVH College, Savitribai Phule Pune University, Nashik, Pune, India*

**Swapnil Satish Alhat**
*Lecturer, Department of English*
*LVH College, Savitribai Phule Pune University, Nashik, Pune, India*
*https://orcid.org/0000-0002-3668-6484*

**Abstract**
*In all the civilizations there has existed slavery of one or the other form and it had acceptance from the contemporary society. If you are a slave then there is nothing you can do about it you will have to bear it meekly. The American slaves were different, they were brought there from some other continent and their look and physique were also different than the Europeans settled in America, thereof their rights were ignored and assumed that they did not have any rights. Nonetheless when the slavery was abolished from America there was revolt and civil war took place. But no one thought about the slave's livelihood post abolition of slavery and this is where Dunbar comments upon. His poetry throughs lights on this aspect of the former slaves and their kids, they were free but did not have any skill or way of livelihood. In this present paper I would endeavour to trace this aspect of Dunbar's poets.*

**Keywords: Slavery, Abolition, Harried Beecher Stowe, We Wear the Mask, Impact of Slavery**

## Introduction

Slavery is an undeniable reality of the American Society. How so ever America project herself as an inclusive, developed and fighting for human rights but she cannot do away from her history. Many movies are made and novels have been written describing about the lives of slaves during slavery, their suffering and atrocities done on them but not much literature is available on how the life of slaves post abolishment of slavery. Paul Laurence Dunbar's most of the poems voices the lives of slaves post abolishment of slavery.

## Representation of Life of Slaves Post Abolishment of Slavery

### Harried Beecher Stowe

She told the story, and the whole world wept
At wrongs and cruelties it had not known
But for this fearless woman's voice alone.
She spoke to consciences that long had slept:
Her message, Freedom's clear reveille, swept
From heedless hovel to complacent throne.
Command and prophecy were in the tone,
And from its sheath the sword of justice leapt.
Around two peoples swelled a fiery wave,

But both came forth transfigured from the flame.
Blest be the hand that dared be strong to save,
And blest be she who in our weakness came-
Prophet and priestess! At one stroke she gave
A race to freedom, and herself to fame.
-(http://utc.iath.virginia.edu/africam/afpo33at.html)

In the poem *Harriet Beecher Stowe* Dunbar shows his gratitude towards Stowe. It was Stowe's ***Uncle Tom's Cabin*** (1952) informed the whole world the dark side of the slavery and the lives of slaves. She was the first one to boldly write about the slaves and their plights furthermore directly or indirectly her novel made the impact not only on common people but likes of Abraham Lincoln, who was determined to abolish slavery from the American soil.

In the poem Dunbar never mentions the name of Harriet Beecher Stowe rather he uses pronoun she. He says that it was she who told the story and the world came to know about slave's plights. When she had written the novel the slaves might not have had the idea that a lady was speaking on their behalf because most of the slaves were illiterate. Hence, Dunbar, through this poem, shows the gratitude of all the slaves. He also saluted the courage of Stowe for speaking her mind: *But for this fearless woman's voice alone, / She spoke to consciences that long had slept:*

Freedom is the most important thing for the humans but for many years no one paid any heed towards the freedom of the slaves, they were given inhumanly treatment, did not consider as human. It was Stowe who gave the message of freedom but her message was not accepted by everyone. The Southern States of contemporary America revolted against the abolition of the slavery and the civil war took place. After the Civil War there emerged a new America, totally transformed and transfigured: *Around two peoples swelled a fiery wave,/ But both came forth transfigured from the flame.*

In the last four lines Dunbar shows the gratefulness on behalf of the all the former slaves. He says that she should be blessed as she has shown courage to talk about us, she came to rescue us when no one wouldn't. He further gives her the status of Prophet, the saviour of slaves, who freed them from the shackles of slavery. Stowe did not fight for the slaves she just wrote a novel describing the life of slaves and that was enough, the slaves got their freedom:

*Blest be the hand that dared be strong to save,*
*And blest be she who in our weakness came-*
*Prophet and priestess! At one stroke she gave*
*A race to freedom, and herself to fame.*

Dunbar in this poem seems to thanking Stowe on behalf of the all the former slaves, because they were not aware that a lady wrote a novel about them and that novel triggered the movement against the slavery. Here he also acknowledges Stowe for speaking for them.

**We Wear the Mask**

We wear the mask that grins and lies,
It hides our cheeks and shades our eyes,—
This debt we pay to human guile;
With torn and bleeding hearts we smile,
And mouth with myriad subtleties.
Why should the world be over-wise,
In counting all our tears and sighs?
Nay, let them only see us, while
We wear the mask.
We smile, but, O great Christ, our cries
To thee from tortured souls arise.
We sing, but oh the clay is vile
Beneath our feet, and long the mile;
But let the world dream otherwise,
We wear the mask!
-(https://www.poetryfoundation.org/poems/44203/we-wear-the-mask)

*We Wear the Mask* describes the lives of the Slaves Post Abolishment. The speaker of the poem apprises us about how the former slaves were living their life. Were they happy they got freedom? And people in general were also very curious to know about the status of the life that now they were no longer slaves they were free, so how were they enjoying their freedom?

So the speaker informs us that they all wear the Mask of happiness when someone asks them about their lives and they lie with those people faking smile because they had to do it to show the world that they were happy after the abolishment of the slavery. Did their lives changed? No! because the abolishment just gave them freedom, what about jobs? They had neither education nor any skills for employment, they just got independence, they were just free. This pangs of life, their suffering they cannot afford to show to the world because the world was under the impression that they were slaves earlier and now they are free, but none thought about their livelihood. Therefore, to hide their plight and sorrow they wear the mask of Happiness and Lie, to hide their inner pain: *This debt we pay to human guile*; / *With torn and bleeding hearts we smile,.*

They do not want that world be more concerned about us.They were free now and can think of themselves thus people must not be worried our lives. Yes they wanted freedom from the inhumanly treatment but they also wanted some kind of work for their livelihood, no one paid heed to that:What would be their life once they got free? Hence the speaker says:…*let them only see us, while / We wear the mask.*

In the last stanza of the poem the speaker prays to Christ and wishes that the world was blind to their inner feelings and needs but they hope that Christ would not be, he must be aware of their pain and plight. They are aware of the struggle of their life and also that they will have to fight their own battle of life hence they hide their feelings and pretend to be happy.

**Conclusion**

Paul Lawrence Dunbar was the first-generation poet post-Abolition era. He was well aware of the impact of slavery and its abolishment on the mind of the former slaves and their kids. Therefore, there in undercurrent of this in his works. The former slaves were in dilemma whether to be grateful and celebrate their freedom or to die of hunger and displacement. In the present paper the researcher attempted to trace the life and sentiments of erstwhile slaves reflected through the Dunbar's poem.

**References**

Baldwin, Emma. "We Wear the Mask by Paul Laurence Dunbar." *Poem Analysis*, https://poemanalysis.com/paul-laurence-dunbar/we-wear-masks

Best, Felton O'Neal. *Crossing the Color Line: A Biography of Paul Laurence Dunbar, 1872-1906*. Ohio State University, 1992.

Blount, Marcellus Jr. *Broken Tongues: Figures of Voice in Afro-American poetry*. Yale University, 1987.

Burton, Orville Vernon. "Debates Over Slavery and Abolition: An Interpretative and Historiographical Essay." *Slavery and Anti-Slavery: A Transnational Archive*. Cengage Learning, 2009.

Corfman, Allisa. "Harriet Beecher Stowe by Paul Laurence Dunbar." *Poem Analysis*, https://poemanalysis.com/paul-laurence-dunbar/harriet-beecher-stowe

Dunbar, Paul Lawrence. "We Wear the Mask." *Poetry Foundation*, https://www.poetryfoundation.org/poems/44203/we-wear-the-mask

Dunber, Paul Lawrence. "Harriet Beecher Stowe." *Bartleby.com*, https://www.bartleby.com/248/1640.html

Franklin, John Hope, and Alfred A. Moss. *From Slavery to Freedom: History of African Americans*. McGraw-Hill, 1994.

*Merriam-Webster's Dictionary of American Writers*. Merriam-Webster, 2001.

Swapnil's Analysis. "Analysis of Harried Beecher Stowe by Paul Lawrence Dunbar/@Swapnil's Analysis." *YouTube*, 2021, https://www.youtube.com/watch?v=i2Xaj-LI-os&t=313s

**Author Details**

**Rupali Aware,** *MA II Student, LVH College, Savitribai Phule Pune University, Nashik, Pune, India*

**Swapnil Satish Alhat,** *Lecturer in English, LVH College, Savitribai Phule Pune University, Nashik, Pune, India*
***Email ID***: *www.swapnilalhat@gmail.com, runimatingmind2022@gmail.com*